SHEAR-FLEXURE-AXIAL LOAD INTERACTION IN RECTANGULAR CONCRETE BRIDGE PIERS WITH OR WITHOUT FRP WRAPPING

by

AHMED HAMID ABDULRAHMAN AL-RAHMANI

B.S., American University of Sharjah, 2010
M.S., Kansas State University, 2012

AN ABSTRACT OF A DISSERTATION

submitted in partial fulfillment of the requirements for the degree

DOCTOR OF PHILOSOPHY

Department of Civil Engineering
College of Engineering

KANSAS STATE UNIVERSITY
Manhattan, Kansas

2015

Abstract

Recent applications in reinforced concrete columns, including strengthening and extreme loading events, necessitate the development of specialized nonlinear analysis methods to predict the confined interaction domain of axial force, shear, and bending moment in square and slightly rectangular concrete columns. Fiber-reinforced polymer (FRP) materials are commonly used in strengthening applications due to their superior properties such as high strength-to-weight ratio, high energy absorption and excellent corrosion resistance. FRP wrapping of concrete columns is done to enhance the ultimate strength due to the confinement effect, which is normally induced by steel ties. The existence of the two confinement systems changes the nature of the problem. Existing research focused on a single confinement system. Also, very limited research on rectangular sections was found in the literature. In this research, a model to estimate the combined behavior of the two systems in rectangular columns is proposed. The calculation of the effective lateral pressure is based on Lam and Teng model and Mander model for FRP wraps and steel ties, respectively. The proposed model introduces load eccentricity as a parameter that affects the compression zone size, and in turn the level of confinement engagement. Full confinement corresponds to zero eccentricity, while unconfined behavior corresponds to infinite eccentricity. The model then generates curves for eccentricities within these boundaries. The numerical approach developed has then been extended to account for shear interaction using the simplified modified compression field theory adopted by AASHTO LRFD Bridge Design Specifications 2014. Comparisons were then performed against experimental data and Response-2000, an analytical analysis tool based on AASHTO 1999 in order to validate the interaction domain generated. Finally, the developed models were implemented in the confined analysis software “KDOT Column Expert” to add FRP confinement effect and shear interaction.

SHEAR-FLEXURE-AXIAL LOAD INTERACTION IN RECTANGULAR CONCRETE BRIDGE PIERS WITH OR WITHOUT FRP WRAPPING

by

AHMED HAMID ABDULRAHMAN AL-RAHMANI

B.S., American University of Sharjah, 2010
M.S., Kansas State University, 2012

A DISSERTATION

submitted in partial fulfillment of the requirements for the degree

DOCTOR OF PHILOSOPHY

Department of Civil Engineering
College of Engineering

KANSAS STATE UNIVERSITY
Manhattan, Kansas

2015

Approved by:

Major Professor
Hayder Rasheed

Copyright

Abstract

Recent applications in reinforced concrete columns, including strengthening and extreme loading events, necessitate the development of specialized nonlinear analysis methods to predict the confined interaction domain of axial force, shear, and bending moment in square and slightly rectangular concrete columns. Fiber-reinforced polymer (FRP) materials are commonly used in strengthening applications due to their superior properties such as high strength-to-weight ratio, high energy absorption and excellent corrosion resistance. FRP wrapping of concrete columns is done to enhance the ultimate strength due to the confinement effect, which is normally induced by steel ties. The existence of the two confinement systems changes the nature of the problem. Existing research focused on a single confinement system. Also, very limited research on rectangular sections was found in the literature. In this research, a model to estimate the combined behavior of the two systems in rectangular columns is proposed. The calculation of the effective lateral pressure is based on Lam and Teng model and Mander model for FRP wraps and steel ties, respectively. The proposed model introduces load eccentricity as a parameter that affects the compression zone size, and in turn the level of confinement engagement. Full confinement corresponds to zero eccentricity, while unconfined behavior corresponds to infinite eccentricity. The model then generates curves for eccentricities within these boundaries. The numerical approach developed has then been extended to account for shear interaction using the simplified modified compression field theory adopted by AASHTO LRFD Bridge Design Specifications 2014. Comparisons were then performed against experimental data and Response-2000, an analytical analysis tool based on AASHTO 1999 in order to validate the interaction domain generated. Finally, the developed models were implemented in the confined analysis software “KDOT Column Expert” to add FRP confinement effect and shear interaction.

Table of Contents

List of Figures

List of Tables

Acknowledgements

First and foremost, all praise be to Allah the exalted, the creator, and the Lord of the universe.

I would like to express my deepest gratitude to my advisor, Dr. Hayder Rasheed, for the opportunity to study under his mentorship. His continuous help, support and guidance were the factors that led to this research's success and completion. Gratitude is also extended to the members of the supervisory committee: Dr. Asad Esmaeily, Dr. Hani Melhem, Dr. Yacoub Najjar, Dr. Youqi Wang, and Dr. Christopher Sorensen.

Financial support provided by Kansas State University Transportation Center is acknowledged. I would also like to thank the members of the Civil Engineering departments at Kansas State University, including faculty, staff and students. I would like to express my genuine appreciation to all my precious friends for being there for me. Thank you, from the deepest corners of my heart, for being my friends.

Last but not least, my sincere appreciation goes to my parents; whose relentless support and loving care throughout my life were the major factors in making my ongoing educational journey a success.

Dedication

This dissertation is dedicated to my parents for their love, endless support and encouragement. Thank you from the bottom of my heart for being there for me.

Section I: Combined FRP/Transverse Steel Confinement in Rectangular Concrete Columns

Chapter 1 - Introduction

Background

Columns are structural members that are essential to most structures. Columns transfer loads mainly through axial compression. Recently, the need to increase the strength of reinforced concrete columns has become the subject that all civil engineers are interested to tackle. Of the many proposed solutions, Fiber-Reinforced Polymer (FRP) materials have attracted attention due to their superior properties such as high strength-to-weight ratio, high energy absorption and excellent corrosion resistance. FRP wrapping of concrete columns is done to enhance the capacity and ductility of the column due to the confinement effect, which is normally induced by steel ties. The analysis of columns under extreme loading events requires accounting for all possible factors that contribute to the column's ultimate capacity, including the confinement effect. The existence of the two confinement systems changes the nature of the problem, thus necessitating specialized nonlinear analysis to obtain the column's ultimate capacity. There is a need to develop a model that predicts the behavior of the combined confinement system, and provides engineers with reliable predictions for the ultimate capacity of confined concrete columns.

Objectives

This part of the study aims to estimate the capacity of rectangular reinforced concrete columns confined with steel ties and FRP wraps. To achieve that, a model to estimate the combined behavior of the two systems is proposed. The calculation of the effective lateral pressure is based on Lam and Teng model and Mander model for FRP wraps and steel ties, respectively. The proposed model introduces load eccentricity as a parameter that affects the compression zone, and in turn the level of confinement engagement. Full confinement corresponds to zero eccentricity, while unconfined behavior corresponds to infinite eccentricity. The model then generates curves for eccentricities within these boundaries. Generalization of the moment of area approach is utilized based on proportional loading, finite layer procedure and the secant stiffness approach, to generate interaction diagrams for these columns accounting for the combined confinement effect.

Scope

This section consists of seven chapters that cover all the aspects involved in this study. The first chapter provides a brief introduction to the background and objectives of the study, in addition to the scope. Chapter two comprises reviews of previous work found in the literature related to models and experiments. Chapter three covers the finite element analysis that was conducted as a preliminary study. Chapter four covers the confined analysis of rectangular columns subjected to biaxial bending and axial compression. It includes the description of the proposed model and the formulations derived. Chapter five reports the results obtained from this study, including comparisons with experiments and a parametric study, in addition to the discussion. Chapter six presents KDOT Column Expert, the software that was developed to facilitate the confined analysis using the proposed approach. Chapter seven summarizes the conclusions of this study and provides recommendations for further future research work.

Chapter 2 - Literature Review

Confinement Models in Rectangular Columns

FRP Confinement Models

In this section, a review of selected models proposed for rectangular columns confined with FRP only is presented chronologically.

Mirmiran et al. (1998) and Samaan et al. (1998)

Mirmiran et al. (1998) investigated the effect of column parameters on FRP-confined concrete. One of the parameters they investigated was the shape effect. They proposed a modified confinement ratio (MCR) for noncircular sections. MCR is defined as follows:

$$MCR = \frac{2r_c}{D}\left(\frac{f_l}{f'_{co}}\right) \quad \textbf{(2-1)}$$

$where\ r_c = radius\ of\ rounded\ corners$

$D = largest\ dimension\ of\ noncircular\ section, confirmed\ by\ Lam\ and\ Teng\ (2003)$

$f_l = confinement\ pressure$

$f'_{co} = unconfined\ concrete\ strength$

Samaan and his coauthors (1998) presented an empirical model to predict the behavior of concrete columns confined with FRP tubes only. Mirmiran et al. (1998) used the same equation for the compressive strength of confined concrete (f_{cc}) in columns wrapped with FRP, as follows:

$$f_{cc} = f'_{co} + 6f_l^{0.7}(MPa) = f'_{co} + 3.38f_l^{0.7}(ksi) \quad \textbf{(2-2)}$$

Including the modification for the shape, the final compressive strength equation is obtained as follows:

$$f_{cc} = f'_{co} + 12\frac{r_c}{D}f_l^{0.7}(MPa) = f'_{co} + 6.76\frac{r_c}{D}f_l^{0.7}(ksi) \quad \textbf{(2-3)}$$

The authors noted that the MCR value affects the second branch of the bilinear response curve. They observed that an ascending second branch was not achieved for specimens with MCR < 0.15. For this case, the post peak stress (f_{ccu}) can be obtained as follows:

$$f_{ccu} = (0.169 \ln MCR + 1.32)f_{cc} \quad \textbf{(2-4)}$$

Otherwise, for cases with MCR > 0.15, the authors recommended using Samaan et al. (1998) model to predict the stress-strain relationship. This model was based on the four-

parameter relationship developed by Richard and Abbott (1975). The expression for the stress-strain relationship is as follows:

$$f_c = \frac{(E_1 - E_2)\varepsilon_c}{\left(1 + \left(\frac{(E_1 - E_2)\varepsilon_c}{f_o}\right)^n\right)^{1/n}} + E_2\varepsilon_c \quad \textbf{(2-5)}$$

$where\ f_c, \varepsilon_c = confined\ axial\ stress\ and\ strain\ of\ concrete, respectively$

$E_1, E_2 = slope\ of\ the\ first, second\ branch\ of\ the\ curve, respectively$

$n = transition\ zone\ curve\ shape\ parameter$

$f_o = intercept\ stress\ (between\ E_2\ and\ stress\ axis)$

The first slope (E_1) depends mainly on the unconfined concrete properties due to the passive nature of the FRP confinement. It is obtained from the expression provided by Ahmad and Shah (1982), which is as follows:

$$E_1 = 3950\sqrt{f_c'}\ (MPa) = 47.586\sqrt{1000f_c'}\ (ksi) \quad \textbf{(2-6)}$$

The second slope (E_2) depends mainly of the FRP, and thus is a function of its stiffness. The following expression is used to evaluate its value:

$$E_2 = 245.61(f_c')^{0.2} + 1.3456\frac{E_f t_f}{D}\ (MPa) = 52.411(f_c')^{0.2} + 1.3456\frac{E_f t_f}{D}\ (ksi) \quad \textbf{(2-7)}$$

The intercept stress (f_o) is obtained as a function of both the unconfined strength and the confining pressure as follows:

$$f_o = 0.872f_c' + 0.371f_l + 6.258\ (MPa) = 0.872f_c' + 0.371f_l + 0.908(ksi) \quad \textbf{(2-8)}$$

Finally, the ultimate confined strain (ε_{ccu}) is calculated from the slope of the second curve as follows:

$$\varepsilon_{ccu} = \frac{f_{cc} - f_o}{E_2} \quad \textbf{(2-9)}$$

Campione and Miraglia (2003)

Campione and Miraglia (2003) presented an analytical model to predict the behavior of concrete columns confined with FRP only under concentric compression. This model considered only square sections with and without rounded corners. The authors analyzed the force equilibrium in the section, and obtained the following expressions for the confining pressure:

$$f_l = \frac{2tf_r}{b_c} \; for\ square\ sections\ with\ rounded\ corners \quad \textbf{(2-10)}$$

$$f_l = \frac{\sqrt{2}t_f f_u}{b_c} k_i \; for\ square\ sections \quad \textbf{(2-11)}$$

$where\ t_f = FRP\ thickness$

$b_c = core\ width$

$f_u = ultimate\ FRP\ strength$

The stress in FRP for rounded sections (f_r) is obtained from the following equation:

$$f_r = f_u \left(1 - \frac{\sqrt{2}}{2} k_i\right) \frac{2r_c}{b_c} + k_i \frac{\sqrt{2}}{2} \quad \textbf{(2-12)}$$

$where\ k_i = shape\ reduction\ factor = 0.2121$

Due to the reduced confinement efficiency in square sections when compared to circular sections, the authors proposed an effectiveness coefficient (k_e) to scale down the confinement pressure (f_l) and then determined the effective confinement pressure (f_l') as expressed in the following equation:

$$f_l' = k_e f_l \quad \textbf{(2-13)}$$

For a square section with rounded corners, the factor is obtained as follows:

$$k_e = \frac{\left(b_c^2 - 4\left(r_c^2 - \frac{\pi r^2}{4}\right)\right) - \frac{2}{3}(b_c - 2r_c)^2}{b_c^2 - 4\left(r_c^2 - \frac{\pi r_c^2}{4}\right)} \quad \textbf{(2-14)}$$

The derivation of the factor assumed a value of 1.0 for circular sections and 1/3 for square sections without rounded corners. Finally, after calculating all of the parameters indicated previously, the confined compressive strength is obtained from the following equation:

$$f_{cc} = f_c' + 2f_l' \quad \textbf{(2-15)}$$

Additionally, Campione and Miraglia considered the determination of the ultimate confined strain in their model (2003). They based their method on the energy balance approach proposed by Mander et al. (1988). They extended the approach to account for the presence of FRP in the section. The energy balance is established by equating the ultimate strain energy per unit volume spent to break the FRP (U_{st}) to the difference in area between the confined (U_{cc}) and the unconfined (U_{co}) concrete stress-strain curves, in addition to the energy required to maintain the yielding of the longitudinal steel (U_{sl}). This is expressed in the following equation:

$$U_{st} = U_{cc} + U_{sl} - U_{co} \quad \textbf{(2-16)}$$

Below are the expressions for each energy term:

$$U_{st} = \rho_f A_c \int_0^{\varepsilon_{us}} f_{st} d\varepsilon_{st} \quad \textbf{(2-17)}$$

$$U_{cc} = A_c \int_0^{\varepsilon_{cu}} f_c d\varepsilon_c \quad \textbf{(2-18)}$$

$$U_{sl} = \rho_{cc} A_c \int_0^{\varepsilon_{cu}} f_{sl} d\varepsilon_{sl} \quad \textbf{(2-19)}$$

$$U_{co} = A_c \int_0^{2\varepsilon_o} f_{uc} d\varepsilon_c \quad \textbf{(2-20)}$$

Substituting back in the first equation, the ultimate strain could be determined if the full constitutive materials' relations were known. The authors then derived a simplified approximate method to determine the ultimate confined strain by neglecting the longitudinal steel contribution. In the end, the following expression was given for the ultimate confined strain (ε_{ccu}):

$$\varepsilon_{ccu} = \varepsilon_{co} + \rho_f \frac{f_r^2}{E_f(f_c' + k_e f_l)} \quad \textbf{(2-21)}$$

Finally, for the stress-strain relationship, the authors based their model on the Pinto and Giuffre model (1970). The relationship is as follows:

$$\frac{f_c}{f_c'} = \beta \frac{\varepsilon_c}{\varepsilon_{co}} + \frac{\left((1-\beta)\frac{\varepsilon_c}{\varepsilon_{co}}\right)}{\left(1 + \left(\frac{\varepsilon_c}{\varepsilon_{co}}\right)^R\right)^{1/R}} \quad \textbf{(2-22)}$$

$where\ \beta = strain\ hardening\ ratio = \frac{E_2}{E_1}$

$E_h = \frac{f_{cc} - f_c'}{\varepsilon_{cu} - \varepsilon_{co}}$

$E_1 = first\ branch\ modulus$

$E_2 = second\ branch\ modulus$

$R = transition\ curve\ factor = 3$

The authors concluded by stating that this relation provided good predictions for cases with effective confinement. Good predictions were not expected for cases where the presence of FRP has negligible effect on the strength.

Pulido et al. (2002)

Pulido and his coauthors (2002) presented a simplified model to predict the behavior of concrete columns confined with FRP only subjected to pure axial compression. The model consists of two linear segments that define the stress-strain relationship. The first point is taken to be the origin. The second point is defined at the break point which corresponds to an axial strain of 0.002. The stress at the point (f_{co}) is calculated as follows:

$$f_{co} = 57000\sqrt{f_c'}\varepsilon_{co}\ (psi) = 4700\sqrt{f_c'}\varepsilon_{co}\ (MPa) \quad \textbf{(2-23)}$$

$where\ \varepsilon_{co} = strain\ at\ break\ point = 0.002$

In order to determine the ultimate point, the lateral pressure (f_l) needs to be calculated first. Lateral pressure for rectangular sections is obtained as follows:

$$f_l = K_e\left(\frac{E_f\varepsilon_f t_f}{d} + \frac{E_f\varepsilon_f t_f}{b}\right) \quad \textbf{(2-24)}$$

$where\ K_e = shape\ factor = 0.75$

$b, d = width\ and\ depth\ of\ the\ section, respectively$

$E_f = modulus\ of\ elasticity\ of\ FRP$

$\varepsilon_f = strain\ of\ FRP\ in\ the\ fibers\ direction$

$t_f = thickness\ of\ FRP$

The ultimate point consists of the ultimate confined strength and the ultimate confined strain. The ultimate confined compressive strength (f_{cc}) is obtained using the following empirical equation:

$$f_{cc} = f_c' + 5.5f_l^{0.7}(ksi) = f_c' + 9.8f_l^{0.7}(MPa) \quad \textbf{(2-25)}$$

The ultimate confined strain (ε_{ccu}) is computed based on the following empirical equation:

$$\varepsilon_{ccu} = \frac{\varepsilon_{CF}}{0.09 - 0.23\ln\left(\frac{f_l}{f_c'}\right)} \quad \textbf{(2-26)}$$

$where\ \varepsilon_{CF} = ultimate\ FRP\ strain\ taken\ as\ 50\%\ of\ the\ measure\ utlimate\ strain$

The proposed model was derived for rectangular sections with no rounded corners. The model also does not consider the aspect ratio effect. A constant shape factor of 0.75 was provided for all rectangular sections.

Lam and Teng (2003)

Lam and Teng (2003) presented an empirical model to predict the behavior of concrete columns confined with FRP only under pure axial compression. Assessment performed by an ACI committee 440 task group (2007) showed that this model was the most reliable for predicting the ultimate compressive strength and strain for circular and rectangular columns. As a result, this model has been adopted by the ACI Committee 440 for use in the ACI440.2R-08 guidelines (2008). This model is discussed in detail in Chapter 4 - .

FRP-Transverse Steel Combined Confinement Models

In this section, a review of selected models proposed for rectangular columns confined with transverse steel and FRP is presented chronologically.

Restrepol and De Vino (1996)

Restrepol and De Vino (1996) presented a model to predict the behavior of concrete columns confined with both transverse steel and FRP. They based the transverse steel confinement part in their model on the model of Mander et al. (1988). Based on the amount of transverse steel along each axis, the lateral confining pressure is calculated. As for the FRP, the lateral confining pressures were calculated as follows:

$$f_{lfx} = \rho_{fx} k_{ef} f_f \quad \textbf{(2-27)}$$

$$f_{lfy} = \rho_{fy} k_{ef} f_f \quad \textbf{(2-28)}$$

$$\rho_{fx} = \frac{2t_f}{h} \quad \textbf{(2-29)}$$

$$\rho_{fy} = \frac{2t_f}{b} \quad \textbf{(2-30)}$$

$where\ b, h = overall\ section\ width\ and\ depth, respectively$

$t_f = total\ FRP\ thickness$

$f_f = FRP\ stress\ in\ the\ transverse\ direction$

The effectiveness confinement coefficient (k_{ef}) is calculated as follows:

$$k_{ef} = \frac{A_{ef}}{A_c} \quad \textbf{(2-31)}$$

$$A_{ef} = bh - \frac{\left(w'_{fx}\right)^2 + \left(w'_{fy}\right)^2}{3} - A_s \quad \textbf{(2-32)}$$

$$A_c = bh - A_s \quad \textbf{(2-33)}$$

$where\ w'_{fx}, w'_{fy} = straight\ portion\ of\ the\ width\ and\ depth\ of\ the\ column, respectively$

$A_s = total\ area\ of\ longitudenal\ steel$

Wang and Restrepo (2001) clarified that the confining FRP stress (f_f) should be obtained from the constitutive material properties as follows:

$$f_f = \begin{cases} E_f \varepsilon_t, \text{if } 0 \le \varepsilon_t \le \varepsilon_{fu} \\ 0, if\ \varepsilon_t > \varepsilon_{fu} \end{cases} \quad \textbf{(2-34)}$$

$where\ \varepsilon_{fu} = ultimate\ tensite\ strain\ of\ FRP$

$\varepsilon_t = transverse\ strain$

In order to obtain the transverse strain, it was assumed that Poisson's ratio (ν) is 0.5. The transverse strain is then obtained by the following equation:

$\varepsilon_t = 0.5\varepsilon_a$

$where\ \varepsilon_a = axial\ strain$

After obtaining the FRP confining pressure, the total pressure due to the dual confinement is calculated as follows:

$$f_{lx} = f_{lsx} + f_{lfx} \quad \textbf{(2-35)}$$

$$f_{ly} = f_{lsy} + f_{lfy} \quad \textbf{(2-36)}$$

Finally, the compressive strength is obtained based on the iterative triaxial state of stress approach proposed by Mander et al. (1988). A closed form approximation can be made to obtain the confined compressive strength as follows:

$$f_{cc} = \alpha_1 \alpha_2 f'_c \quad \textbf{(2-37)}$$

$$where\ \alpha_1 = 1.25\left(1.8\sqrt{1 + \frac{7.94F_l}{f'_c}} - \frac{1.6F_l}{f'_c} - 1\right)$$

$$\alpha_2 = \left(\frac{1.4f_l}{F_l} - 0.6\left(\frac{f_l}{F_l}\right)^2 - 0.8\right)\sqrt{\frac{F_l}{f'_c}} + 1$$

$F_l, f_l = maximum, minimum\ lateral\ confinung\ pressures, respectively$

The model proposed by those authors predicted the confined strength only. No expressions were provided to predict the maximum confined strain or the stress-strain relationship.

Chun and Park (2002)

Chun and Park (2002) presented their Passive Confinement Model (PCM) to predict the behavior of concrete columns confined with both transverse steel and FRP. The model considers the change in the Poisson's ratio of the confined concrete. This change will affect the expansion rate of the concrete, and thus the overall confinement. They based the transverse steel confinement part in their model on the model of Mander et al. (1988). Based on the amount of transverse steel along each axis, the lateral confining pressure is calculated. The method requires an iterative procedure. The first step is to choose an axial strain value (ε_c) for which the section is to be analyzed. Next, the Poisson's ratio (ν) is calculated as follows:

$$\nu = \nu_o(1 + 1.3763x - 5.36x^2 + 8.586x^3) \leq \nu_u \quad \textbf{(2-38)}$$

$$\nu_u = -0.2305 \ln\left(\frac{f_{ld}}{f'_{co}}\right) + 0.087 \quad \textbf{(2-39)}$$

$$f_{ld} = \left(\frac{2f_{fu}t_f}{D}\right)k_e + \left(\frac{A_c}{A_g}\right)f_{lsu} \quad \textbf{(2-40)}$$

$$x = \frac{\varepsilon_c}{\varepsilon_{cc}} \quad \textbf{(2-41)}$$

$where\ f_{ld} = design\ confining\ pressure$

ε_{cc}

$= axial\ strain\ corresponding\ to\ the\ axial\ confined\ strength\ (f_{cc}) per\ Mander\ model$

$\nu_o = initial\ concrete\ Poisson's\ ratio$

$k_e = shape\ factor\ provided\ by\ Mander\ et\ al.\ (1988)$

$f_{fu} = tensile\ strength\ of\ FRP$

$t_f = thickness\ of\ FRP$

$D = section\ width$

$A_c = concrete\ area\ within\ hoops$

$A_g = gross\ concrete\ area$

$f_{lsu} = maximum\ confining\ pressure\ provided\ by\ hoops\ from\ Mander\ et\ al.\ (1988)$

The transverse strain (ε_t) is then obtained as follows:

$$\varepsilon_t = \varepsilon_f = \nu\varepsilon_c \quad \textbf{(2-42)}$$

Next, the confining pressure (f_l) is calculated as per the following equations:

$$f_l = \begin{cases} \dfrac{2\varepsilon_f E_f t_f}{D} k_e, for\ concrete\ cover \\ \dfrac{2\varepsilon_f E_f t_f}{D} k_e + f_{ls}, for\ concrete\ core \end{cases} \quad \textbf{(2-43)}$$

$where\ f_{ls} = confining\ pressure\ provided\ by\ hoops\ from\ Mander\ et\ al.$ (1988)

Now that the confining pressure has been determined, the confined strength (f_{cc}) and its corresponding strain (ε_{cc}) is computed as follows:

$$f_{cc} = f_c' \left(2.254 \sqrt{1 + 7.94 \frac{f_l}{f_c'}} - \frac{2f_l}{f_c'} - 1.254 \right) \quad \textbf{(2-44)}$$

$$\varepsilon_{cc} = \varepsilon_{co} \left(\frac{5f_{cc}}{f_c'} - 4 \right) \quad \textbf{(2-45)}$$

$where\ \varepsilon_{co} = strain\ correcponding\ to\ unconfined\ strength\ f_c' = 0.002$

The ultimate strain (ε_{cc}) is compared with the assumed strain value at the beginning. If the difference exceeds a defined tolerance (1% was defined by those authors), the new strain value is used as an initial value and the process is repeated until the desired tolerance is met. If convergence is attained, the stress-strain relationship can then be obtained from the following equation:

$$f_c = f_{cc} \frac{\varepsilon_c}{\varepsilon_{cc}} \left(\frac{n}{n - 1 + \left(\frac{\varepsilon_c}{\varepsilon_{cc}} \right)^n} \right) \quad \textbf{(2-46)}$$

$$where\ n = \frac{E_c}{E_c - \frac{f_{cc}}{\varepsilon_{cc}}}$$

It should be noted that those authors did not specify what the calculated confinement pressure (f_l) corresponded to in a noncircular section. It appears that the model only considers the confining pressure along the width of the section, and ignores the pressure provided by the FRP and transverse steel along the depth of the section.

Experimental Studies

In this section, a review of selected experiments conducted on FRP-confined square and rectangular columns is presented. Further details on the specimens' parameters and the experimental data points can be found in Table 5-1 and Table 5-2.

Bousias et al. (2004)

Bousias and his coworkers investigated the effect of bar corrosion of the effectiveness of the retrofitting of rectangular reinforced concrete columns. A total of twenty concrete columns, were prepared for testing. The specimens were all rectangular with the following dimensions: 25 x 500 millimeters (mm). Longitudinal reinforcement consisted of four 18 mm diameter bars. Rectilinear ties were used to support the bars at the corners and were made with 8 mm diameter bars. Steel properties are provided in Table 2-1. Half of the specimens were subjected to salty water exposure for 3.5 months to induce corrosion. Both CFRP and GFRP wraps were used to confine the columns. Their properties including thickness (t_f), weight, elastic modulus (E_f), failure strain (ε_f), and tensile strength (f_{fu}) are presented in Table 2-2.

Table 2-1: Steel Properties for Bousias et al. Specimens (2004).

Rebar Type	f_y (MPa)	f_u (MPa)	ε_u (%)
Longitudinal	559.5	682	13
Transverse	286	350	13

Table 2-2: FRP Properties for Bousias et al. Specimens (2004).

FRP	t_f (mm)	Weight (kg/m^2)	E_f (GPa)	ε_f (%)	f_{fu} (MPa)
CFRP	0.13	0.23	230	1.5	3450
GFRP	0.17	0.43	70	3.1	2170

Displacement control was enforced, and the specimens were loaded along the strong or the weak axes, depending on their designation. One pair of specimens was taken to be the control specimens in each the strong and the weak directions, while all the remaining specimens were wrapped with FRP. All specimens failed in flexure control. It was concluded that the FRP jackets improved the deformation capacity. Columns wrapped with FRP experienced constant axial load until failure where the load was lost immediately. It was also observed that increasing the number of CFRP wraps from two to five did not significantly improve the deformation capacity and strength. FRP confinement effectiveness was observed to marginally better in specimens which were tested along the strong axis. For specimens that failed due to FRP fracture, deformation capacity was increased by 90% in specimens tested along the strong direction while it also increased by 50% for the specimens tested along the week direction.

Harajli and Rteil (2004)

Harajli and Rteil (2004) investigated the effect of FRP confinement on seismic performance of concrete columns. A total of 12 specimens were prepared for testing. The columns had a cross-section of 150 x 300 mm. The specimens were divided into two groups based on the longitudinal reinforcement. The first group had six #4 bars, while the second group had eight #5 bars. The yield stresses were 534 megapascals (MPa) and 565 MPa for the #4 and #5 bars, respectively. All specimens had rectilinear ties made of 8 mm diameter bars. The tie spacing was 150 mm except for two specimens, in which the ties were spaced at 75 mm. The sections were confined with CFRP, with properties provided in Table 2-3.

Table 2-3: FRP Properties for Harajli and Rteil Specimens (2004).

Fiber Type	t_f (mm)	E_f (GPa)	ε_f (%)	f_{fu} (MPa)
CFRP	0.13	230	1.5	3500

A constant axial load was applied to the columns with the help of a hydraulic jack. A 100 tons dynamic capacity actuator was used to apply lateral load to the column. It was observed that splitting occurred along the spliced reinforcement. Cracks were concentrated at the column base for all specimens. In specimens with no FRP confinement, spliced reinforcement underwent significant bond deterioration, which led to significant strength degradation. CFRP wraps improved the behavior of the columns by increasing the capacity, reducing spalling and bond deterioration. It was also observed that increasing the amount of CFRP improved the seismic performance, albeit not proportionally. Finally, CFRP was shown to be more efficient in improving seismic performance compared to steel.

Memon and Sheikh (2005)

Memon and Sheikh (2005) investigated the seismic resistance of GFRP-confined columns. A total of eight columns were prepared for testing. Seven columns were retrofitted with GFRP, while a single column was used as a control specimen. The tested sections were squares with the following dimensions: 305 x 305 x 1473 mm. Longitudinal reinforcement consisted of eight 20M bars. The lateral reinforcement consisted of both rectilinear and diamond ties made with #3 bars. Steel reinforcement properties are provided in Table 2-4.The tested sections were confined with GFRP, with properties provided in Table 2-5.

Table 2-4: Steel Properties for Memon and Sheikh Specimens (2005).

Rebar Type	E_s (MPa)	f_y (MPa)	ε_y (%)	f_u (MPa)	ε_u (%)
Longitudinal	202170	465	0.23	640	20.21
Transverse	207730	457	0.22	739	14.11

Table 2-5: FRP Properties for Memon and Sheikh Specimens (2005).

Fiber Type	t_f (mm)	E_f (GPa)	ε_f (%)	f_{fu} (MPa)
GFRP	1.25	19754	2.28	450

Testing was conducted using a hydraulic jack with a capacity of 4450 kilonewtons (kN) for axial loading and an actuator with a capacity of 1000 kN for lateral loading. The specimens demonstrated an enhanced behavior when compared to unconfined sections. It was concluded that using FRP jackets was an appropriate approach to retrofitting structures and improving their performance during major earthquakes.

Wang and Hsu (2007)

Wang and Hsu (2007) investigated the axial load strength of rectangular and square reinforced compression members confined with GFRP jackets and steel hoops. A total of six columns were prepared for testing. Three columns had a square section of 300 x 300 mm, and the remaining three had a rectangular section of 300 x 450 mm. Square sections had four 20 mm diameter grade 430 steel bars with a bar at each corner. The bars were supported by rectilinear ties made of 10 mm diameter grade 300 steel bars. The rectangular section had six 20 mm grade 430 steel bars distributed uniformly. Rectilinear ties, made of 10 mm diameter grade 300 steel bars, supported bars at the corners, and connected the two bars at the midsection. Properties for the steel reinforcement are provided in Table 2-6. For each section type, there was an unconfined specimen (No FRP wraps), a section with two layers of FRP, and a section with six layers of FRP. Properties for the FRP jackets are provided in Table 2-7.

Table 2-6: Steel Properties for Wang and Hsu Specimens (2007).

Rebar Type	E_s (GPa)	f_y (MPa)	ε_u (%)
Longitudinal	200	439	6.67
Transverse	203	365	19

Table 2-7: FRP Properties for Wang and Hsu Specimens (2007).

Fiber Type	t_f (mm)	E_f (GPa)	ε_f (%)	f_{fu} (MPa)
GFRP	1.27	20.5	2	375

Testing was conducted using a 10 meganewton (MN) capacity electro-hydraulic universal testing machine. It was concluded that confinement provided by FRP has immensely improved the ultimate strength and strain. They were also efficient in impeding premature buckling of longitudinal bars. Specimens with two FRP layers failed by debonding, while specimens with six layers failed due to the splitting of the FRP at the corners. It was also observed that loading in square specimens maintained after the peak, while that was not the case for rectangular columns. The authors attributed that to the fact that FRP confinement effect is poorer is rectangular sections.

Darby et al. (2011)

Darby and his coworkers investigated the behavior of small and large-scale FRP confined rectangular under both concentric and eccentric loading. A total of 18 columns were prepared for testing. The variables in this study were the dimensions of the cross-section and the eccentricity. Of the specimens, six columns were subjected to concentric loading, while the remaining columns were loaded eccentrically. Eccentricities were chosen so that three cases occurred as follows:

- Uniform compression axial strain profile.
- Linear strain profile starting from zero along an edge to the maximum strain on the opposite edge.
- Linear strain profile with each half of the section under tension and compression.

Three sizes of square columns were tested, 150 x 150, 300 x 300, and 450 x 450 (all in mm). The smaller two sections (150x150 mm and 300x300 mm) had a bar at each corner for a total of four bars. Bars with 12 mm and 25 mm diameter were provided in the 150x150 and 300x300 mm columns, respectively. The 450x450 mm section had pairs of 25 mm diameter bars at each corner. The yield strength for all bars was 550 MPa. As for transverse reinforcement, the authors reported that minimum links were provided in the central region. The concentric

specimens were all pairs of unconfined and FRP confined columns. The eccentric specimens had pairs for only the 150x150 mm section, while the other sections were confined with FRP. The properties of FRP are provided in Table 2-8.

Table 2-8: FRP Properties for Darby et al. Specimens (2011).

Fiber Type	t_f (mm)	E_f (GPa)	ε_f (%)
CFRP	0.16	214	1.45

Displacement control was enforced, and testing was conducted using a 2000 kN, 5000 kN, and 100000 kN loading rigs for the 150x150 mm, 300x300 mm, and 450x450 mm specimens, respectively. It was observed that the confined specimens have generally failed by rupture of the FRP. Specimens subject to high eccentricities failed due to the snapping of the steel on the tension side. No size-effect was observed on the capacity or overall behavior. It was concluded that small-scale columns and large-scale columns behaved in the same way.

ACI 440 Procedure for Plotting Interaction Diagrams

In the ACI 440.2R-08 document (2008), the ACI committee 440 provides guidelines to obtain the interaction diagram for a reinforced concrete column confined with FRP. The following limitations are specified for members under combined axial compression and bending. The effective strain in the FRP jacket should not exceed the value obtained from the following equation. This limit is specified to ensure the shear integrity of the confined concrete (2008).

$$\varepsilon_{fe} \leq minimum(0.004, \kappa_\varepsilon \varepsilon_{fu})$$

Another limitation is the strength enhancement is only accepted when the actual load point (P_u, M_u) is in the compression controlled failure region. This region is defined as the area above the line connecting the origin and the balance point (C) for the unconfined interaction diagram (see Figure 2-1). They cited Bank's (2006) study which reported that strength enhancement is only considered of significance in remembers where compression failure controls.

The ACI 440 committee procedure simplifies the compression-controlled region of the interaction diagram to two bilinear curves passing through three points (points A, B, C) as shown in Figure 2-1. The points can be calculated by satisfying the strain compatibility and force

equilibrium using the Lam and Teng model (2003) earlier and adopted by ACI for stress-strain behavior of FRP-confined concrete.

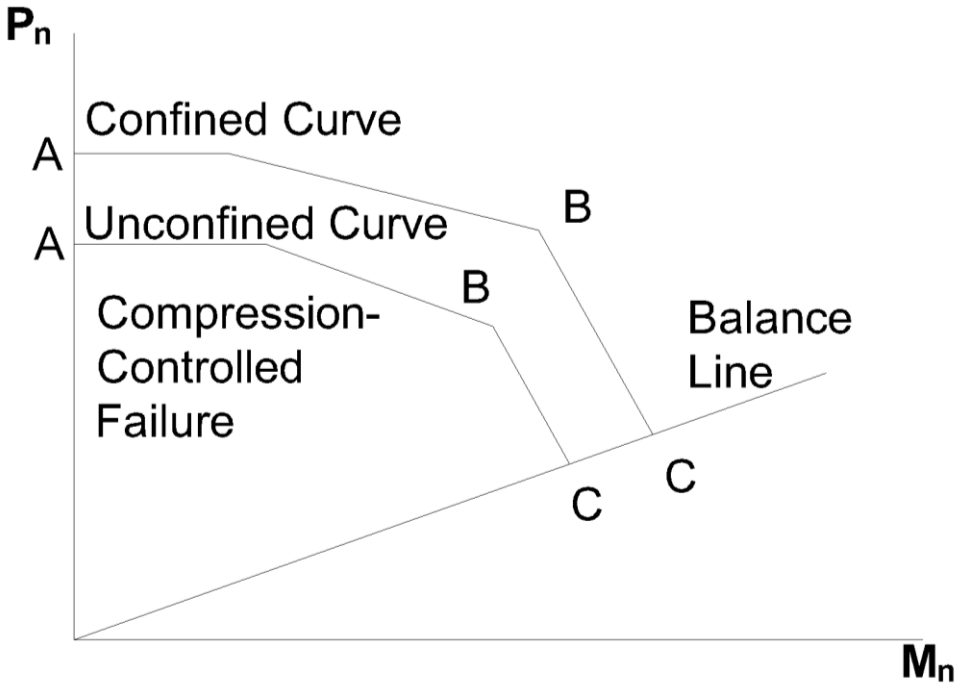

Figure 2-1: Representative ACI 440 Interaction Diagram.

Point A (P_n, 0), which is the point of pure compression, is obtained from the following formula. This formula is applicable for columns with steel ties and eccentricities less than 10% of the section's depth (0.1h).

$$P_n = 0.85[0.85f'_{cc}(A_g - A_{st}) + f_y A_{st} \quad \textbf{(2-47)}$$

Point B is obtained for a section with a strain distribution that corresponds to zero strain in the extreme tension steel fibers, and a compressive strain ε_{ccu} at the compression face. Point C is obtained for a section with a strain distribution that corresponds to a balanced failure (at which concrete compressive strain = ε_{ccu} and extreme tension steel strain = ε_y). For these two points, the coordinates are obtained by similar triangles from the prescribed strain profiles, see Figure 2-2.

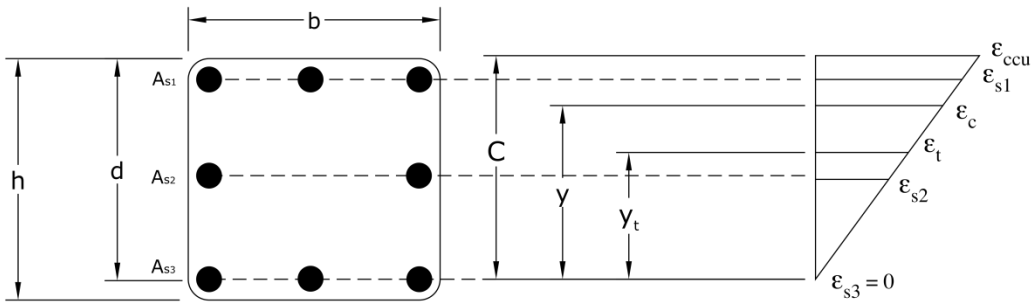

(a) Point B

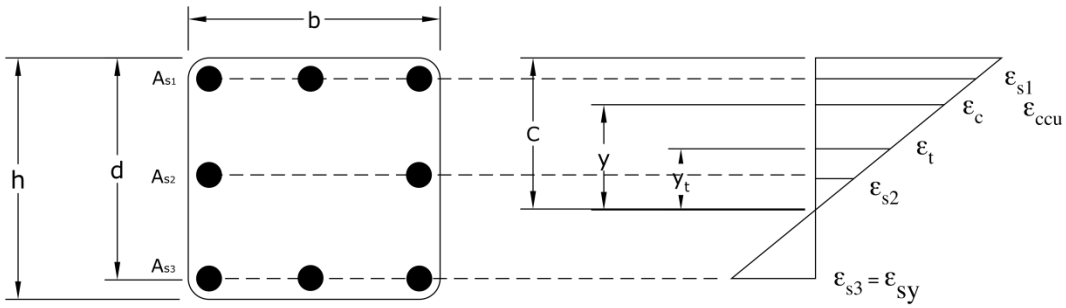

(b) Point C

Figure 2-2: Prescribed Strain Profiles for a) Point B. b) Point C.

The following equations can be used to compute the coordinates of points B and C.

$$P_n = A(y_t)^3 + B(y_t)^2 + C(y_t) + D + \sum A_{si} f_{si} \quad \textbf{(2-48)}$$

$$M_n = E(y_t)^3 + F(y_t)^3 + G(y_t)^2 + H(y_t) + I + \sum A_{si} f_{si}\, d_i \quad \textbf{(2-49)}$$

$$where: A = -\frac{b(E_c - E_2)^2}{12 f_c'} \left(\frac{\varepsilon_{ccu}}{c}\right)^2 \quad \textbf{(2-50)}$$

$$B = \frac{b(E_c - E_2)}{2} \left(\frac{\varepsilon_{ccu}}{c}\right) \quad \textbf{(2-51)}$$

$$C = -b f_c' \quad \textbf{(2-52)}$$

$$D = bc f_c' + \frac{bcE_2}{2} \varepsilon_{ccu} \quad \textbf{(2-53)}$$

$$E = \frac{-bc(E_c - E_2)^2}{16 f_c'} \left(\frac{\varepsilon_{ccu}}{c}\right)^2 \quad \textbf{(2-54)}$$

$$F = b\left(c - \frac{h}{2}\right)\frac{(E_c - E_2)^2}{12f_c'}\left(\frac{\varepsilon_{ccu}}{c}\right)^2 + \frac{b(E_c - E_2)}{3}\left(\frac{\varepsilon_{ccu}}{c}\right) \quad \textbf{(2-55)}$$

$$G = \left(\frac{b}{2}f_c' + b\left(c - \frac{h}{2}\right)\frac{(E_c - E_2)}{2}\left(\frac{\varepsilon_{ccu}}{c}\right)\right) \quad \textbf{(2-56)}$$

$$H = bf_c'\left(c - \frac{h}{2}\right) \quad \textbf{(2-57)}$$

$$I = \frac{bc^2}{h}f_c' - bcf_c'\left(c - \frac{h}{2}\right) + \frac{bc^2E_2}{3}\varepsilon_{ccu} - \frac{bcE_2}{2}\left(c - \frac{h}{2}\right)(\varepsilon_{ccu}) \quad \textbf{(2-58)}$$

In the previous equations, c is the distance between the extreme compression fiber and the neutral axis, and y_t is the vertical distance between the neutral axis and the fiber at which strain is equal to the transition strain (ε_t'). These two parameters can be obtained as follows:

$$c = \begin{cases} d \dots for\ point\ B \\ d\dfrac{\varepsilon_{ccu}}{\varepsilon_y + \varepsilon_{ccu}} \dots for\ point\ C \end{cases} \quad \textbf{(2-59)}$$

$$y_t = c\frac{\varepsilon_t'}{\varepsilon_{ccu}} \quad \textbf{(2-60)}$$

Chapter 3 - Finite Element Modeling of Rectangular Columns Subjected to Concentric Loading

As a preliminary study, confinement in rectangular concrete columns was modeled by finite element analysis. The main objectives of this study were to obtain stresses in the steel ties at different loading states, and to determine the effect of a section's aspect ratio on the stress ratio in the steel in both transverse directions. To accomplish that, a concrete slice was modeled using Abaqus FEA software (2010). Different approaches were evaluated in the preliminary models. After validation, the most appropriate approach was then used to prepare the final models used to obtain the results for this study.

Preliminary Model Definition

As a starting point, the full section was modeled in Abaqus in order ensure that the model behaves reasonably and functions properly. The geometric properties and steel specifications for the modeled slice are provided in Figure 3-1. The slice included 3 ties and had a thickness 6 inches.

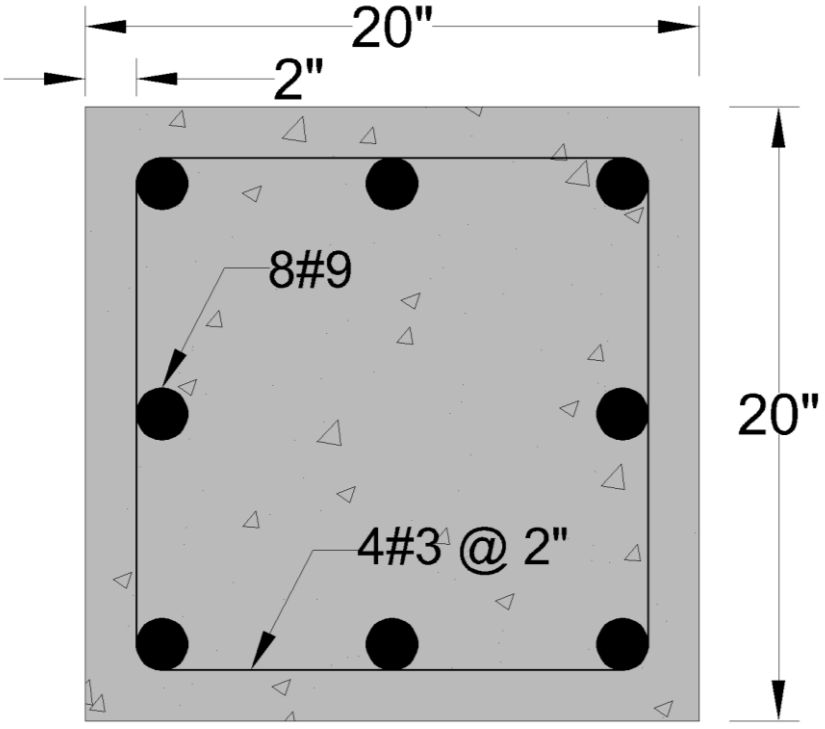

Figure 3-1: Preliminary Model Slice Details.

As for materials definition, both elastic and plastic properties were provided. For concrete, a compressive strength (f_c') of 4 kips per square inch (ksi) was assumed. Elastic parameters include the modulus of elasticity (E) and a poisson's ratio (ν). The value of poisson's ratio was taken to be 0.2, while the modulus of elasticity was calculated using the following equation provided by the ACI 318 building code (2011), was obtained to be 3605 ksi.

$$E = 57000\sqrt{f_c'}\ (in\ psi)$$

For plasticity, two separate compression and tension behavior were defined. In compression, Hognestad's parabola (1951) is used to provide the stress-strain ($\sigma - \varepsilon$) relation according to the following equation:

$$\sigma = f_c'\left(2\left(\frac{\varepsilon}{\varepsilon_o}\right) + \left(\frac{\varepsilon}{\varepsilon_o}\right)^2\right) \quad \textbf{(3-1)}$$

$where\ f_c' = concrete\ compressive\ strength$

$\varepsilon_o = strain\ at\ ultimate\ compressive\ strength = 0.002$

As for tension, the concrete's behavior was assumed to be elastic till rupture, following Hooke's law (Ugural and Fenster, 2003):

$$\sigma = E\varepsilon \quad \textbf{(3-2)}$$

After stress reaches the modulus of rupture of concrete (f_r), it is assumed that the stress drops until the strain reaches 10 times the cracking strain ($10\varepsilon_{cr}$) according to the following equation:

$$\sigma = \frac{f_r(10\varepsilon_{cr} - \varepsilon)}{9\varepsilon_{cr}} \quad \textbf{(3-3)}$$

Based on the equations provided above, the stress-strain relation is plotted in Figure 3-2.

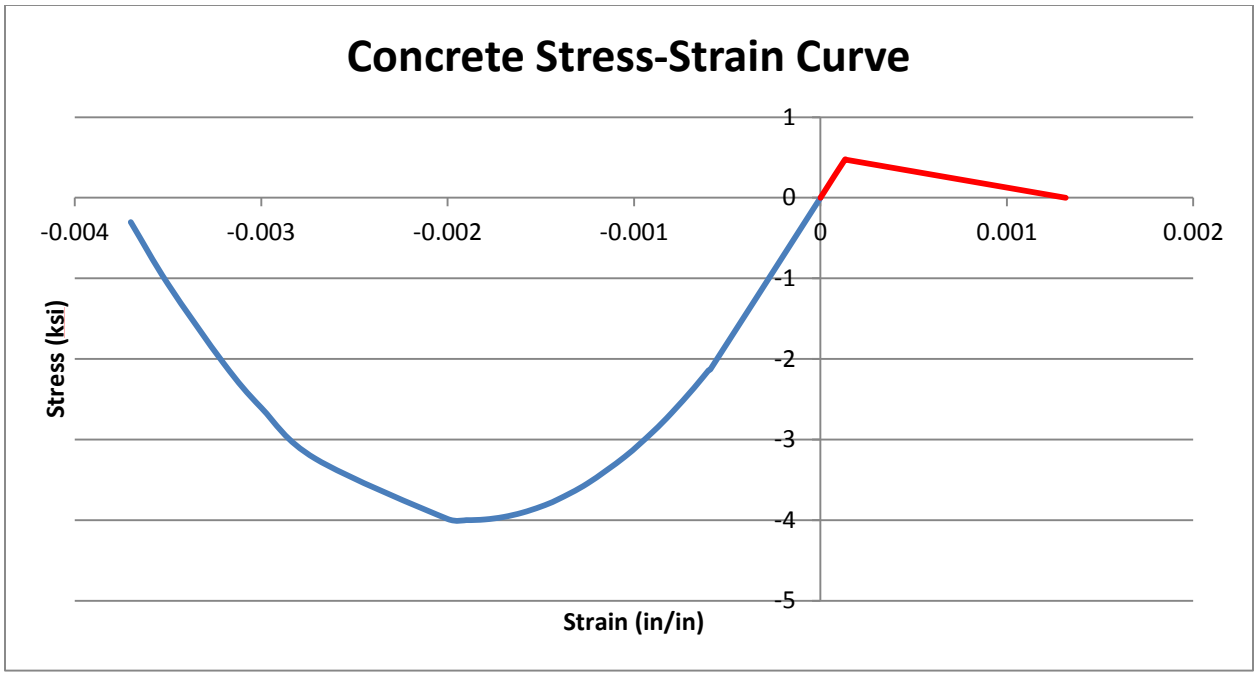

Figure 3-2: Concrete Material Model Used in Abaqus.

As for steel, it was defined as an elastic-perfectly plastic material. As a material, steel behavior in tension and compression is taken to be identical. The elastic parameters, the modulus of elasticity (E) and poisson's ratio (ν), were taken to be 29000 ksi and 0.3, respectively. Steel was assumed to be perfectly plastic after reaching yielding. The stress and strain values at yielding (f_y, ε_y) were taken to be 60 ksi and 0.16, respectively. The stress-strain relation is plotted in Figure 3-3.

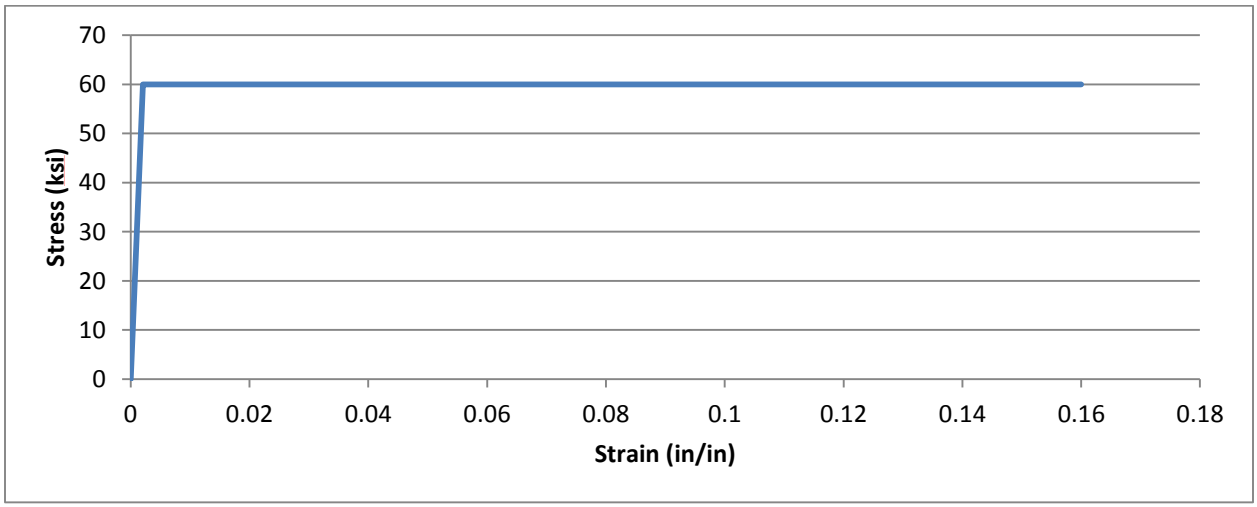

Figure 3-3: Steel Material Model Used in Abaqus.

Two types of elements were used in the analysis. Concrete was modeled using solid elements (C3D8R), which are described in Abaqus as 8-node linear bricks. Steel rebars were modeled in two different ways. In addition to solid elements, truss elements (T3D2), described by Abaqus as 2-node linear 3-D trusses, were used and compared. The comparison is provided later in this chapter. As for the mesh, Abaqus was utilized to automatically generate it. The approximate mesh size was specified as 0.5 inches. The generated mesh for the concrete slice and a bar (truss) are shown in Figure 3-4.

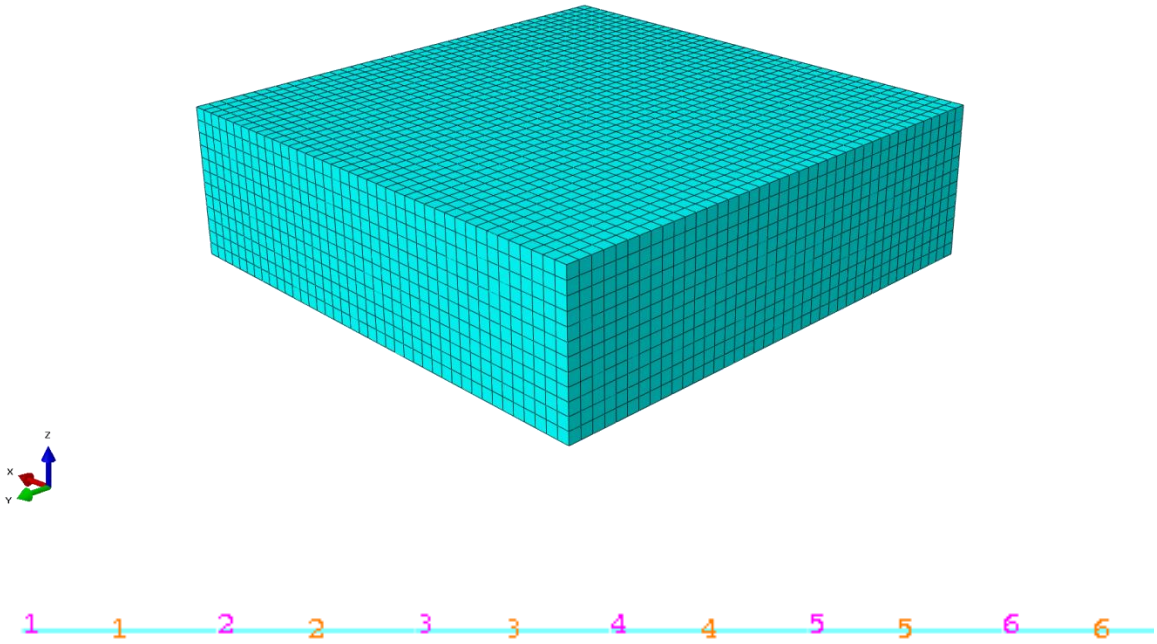

Figure 3-4: Meshes Generated by Abaqus.

In addition to the concrete and steel parts, two rigid plates were included in the model assembly. Displacement control was implemented by imposing 0.04 inches of deflection to a rigid loading plate. As for the boundary conditions, the loading plate was prevented from rotating around any axis. The rigid support plate's rotational and translational degrees of freedom were restricted in all axes. Additionally, smooth plate interaction was assumed to occur between the rigid plates and the concrete slice. This was done in Abaqus by defining tangential surface to surface interaction between the contact surfaces. The coefficient of friction was taken to be 0.001 for smooth behavior. Figure 3-5 illustrates the current model assembly in Abaqus.

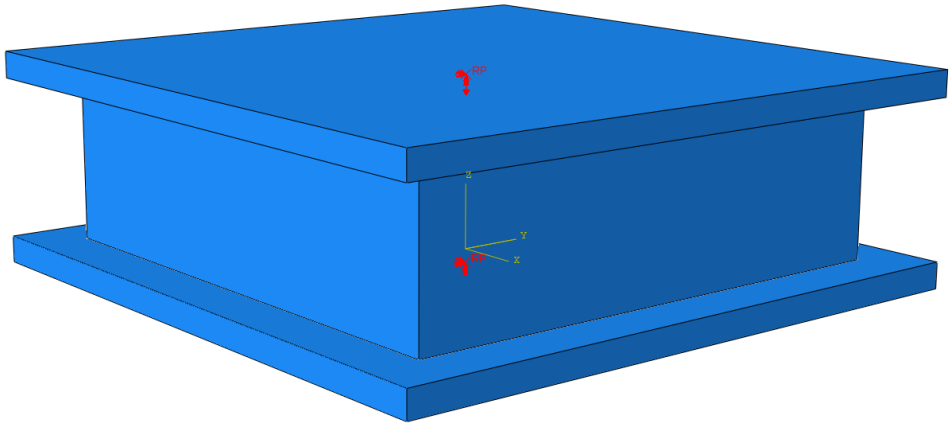

Figure 3-5: Model Assembly with Imposed Boundary Conditions.

Triaxial State of Stress Verification

In order to ensure that confinement effect is accounted for in the finite element analysis, a model of the concrete core only was created. This model utilized the concrete material model defined in the previous section. The upper surface was displaced in the z-direction. The lower surface was allowed to expand laterally, but prevented from displacement in the z-direction. To provide the confinement effect, lateral pressure corresponding to a specific tie spacing value was applied to the core, as shown in Figure 3-6. The analysis was conducted for a control case with no confinement, and two cases with tie spacing of 1 and 2 inches.

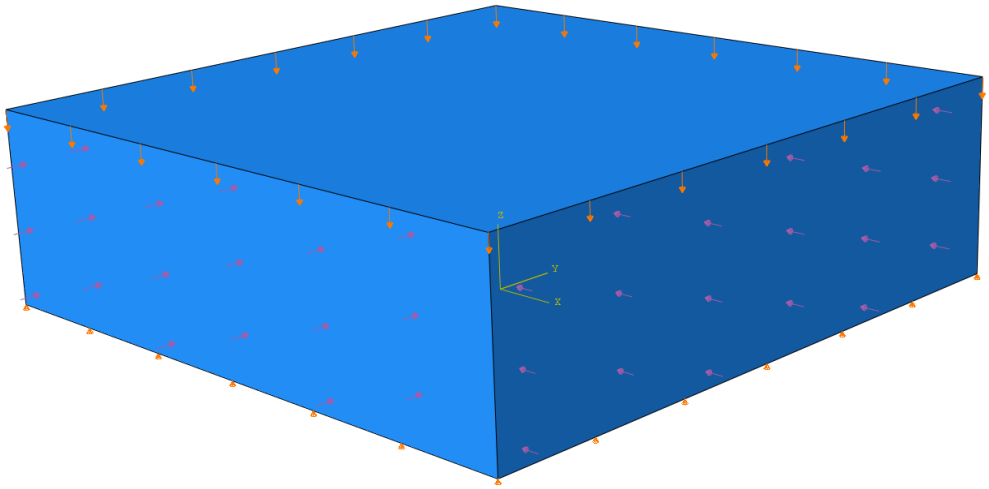

Figure 3-6: Lateral Pressures Application on the Triaxial Verification Model.

From the finite element analysis, the stress-strain curve for each case was then obtained as shown in Figure 3-7 and Figure 2-1. Additionally, Figure 3-8 shows the deformed shape of the concrete core with a tie spacing of 2 inches. The stress contour plot was obtained at the compressive strength.

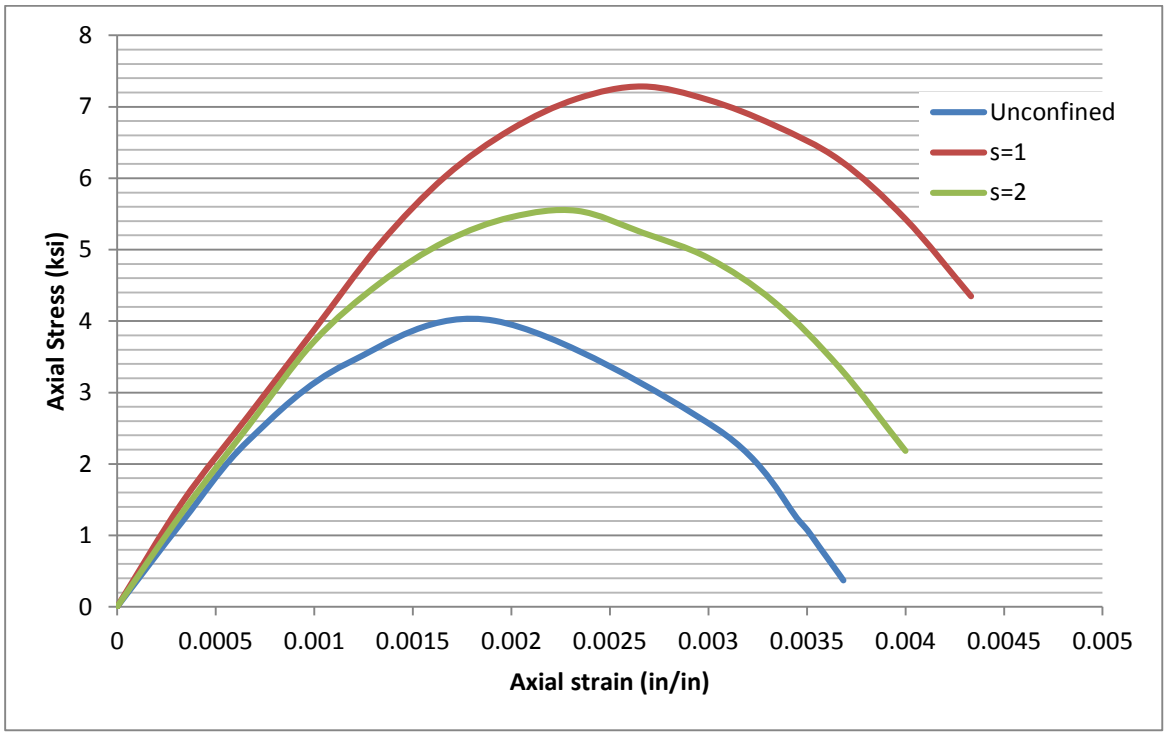

Figure 3-7: Axial Stress-Strain curves for triaxial verification model.

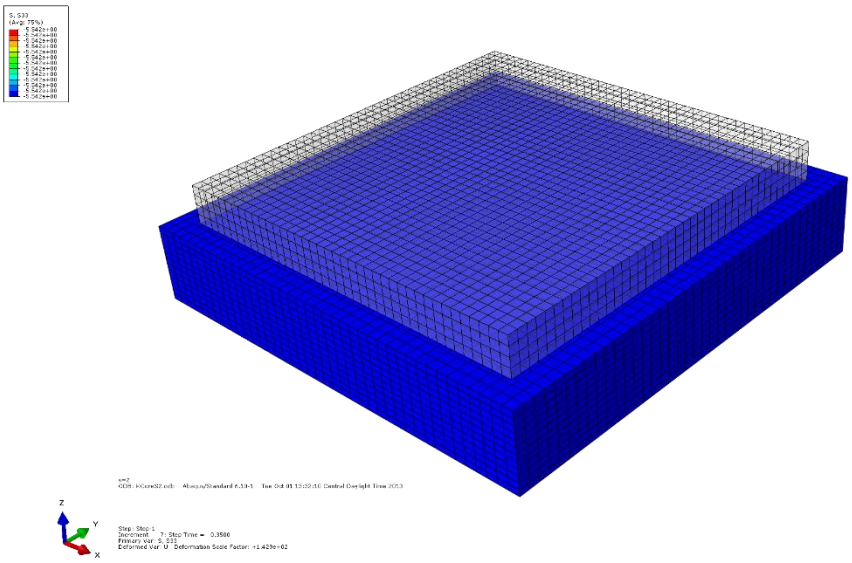

Figure 3-8: Stress contours at compressive strength for s=2 inches.

In order to validate these curves, the confined compressive strength (f_{cc}) corresponding to each tie spacing case was calculated per the Mander transverse steel confinement model (1988). Detailed explanation on this model is provided in Chapter 4 - . Also, the compressive strength was obtained from the curves in Figure 3-7 and compared with the calculated values. Table 3-1 below summarizes these results.

Table 3-1: Summary of Triaxial Validation Results.

Tie Spacing (in.)	Mander f_{cc} (ksi)	FEA f_{cc} (ksi)	Error (%)
1	5.86	5.6	4.44
2	7.45	7.3	2.01

As it can be seen in Table 3-1, the finite element analysis results provided good agreement with the compressive strength calculated using Mander's model. This indicates that Abaqus is capable of modeling confinement and allowed us to proceed with further analyses.

Modeling Approaches for Steel Reinforcement

Abaqus offers multiple ways to model steel reinforcement in the concrete. In order to determine the most appropriate approach, these approaches were tested and multiple models were created. As mentioned earlier, steel reinforcement can be modeled using either solid (3D) elements, or truss (1D) elements. As for embedment in the concrete, Abaqus offers the embedded region technique, which is a simple way to embed the reinforcement in the concrete (host region). Abaqus locates rebar nodes that lie within the concrete, and then constrains the embedded elements' degrees of freedom to those in the host. The technique can be applied to both solid and truss elements. Additionally, solid elements could be modeled in the concrete by defining surface to surface interaction between the contact surfaces of the concrete and the steel. This approach necessitates removing the concrete at the locations where the steel bars are intended to be manually. In summary, the following approaches for reinforcement modeling were evaluated:

- Approach 1: Solid elements for steel with surface to surface interaction.
- Approach 2: Truss elements for steel with the embedded region technique.
- Approach 3: Solid elements for steel with the embedded region technique.

The first case of solid elements with surface to surface interaction is illustrated in Figure 3-9. For this case, the mesh for the steel cage which consists of the longitudinal bars and the ties were merged. The grooves created by the manual removal of concrete are also shown.

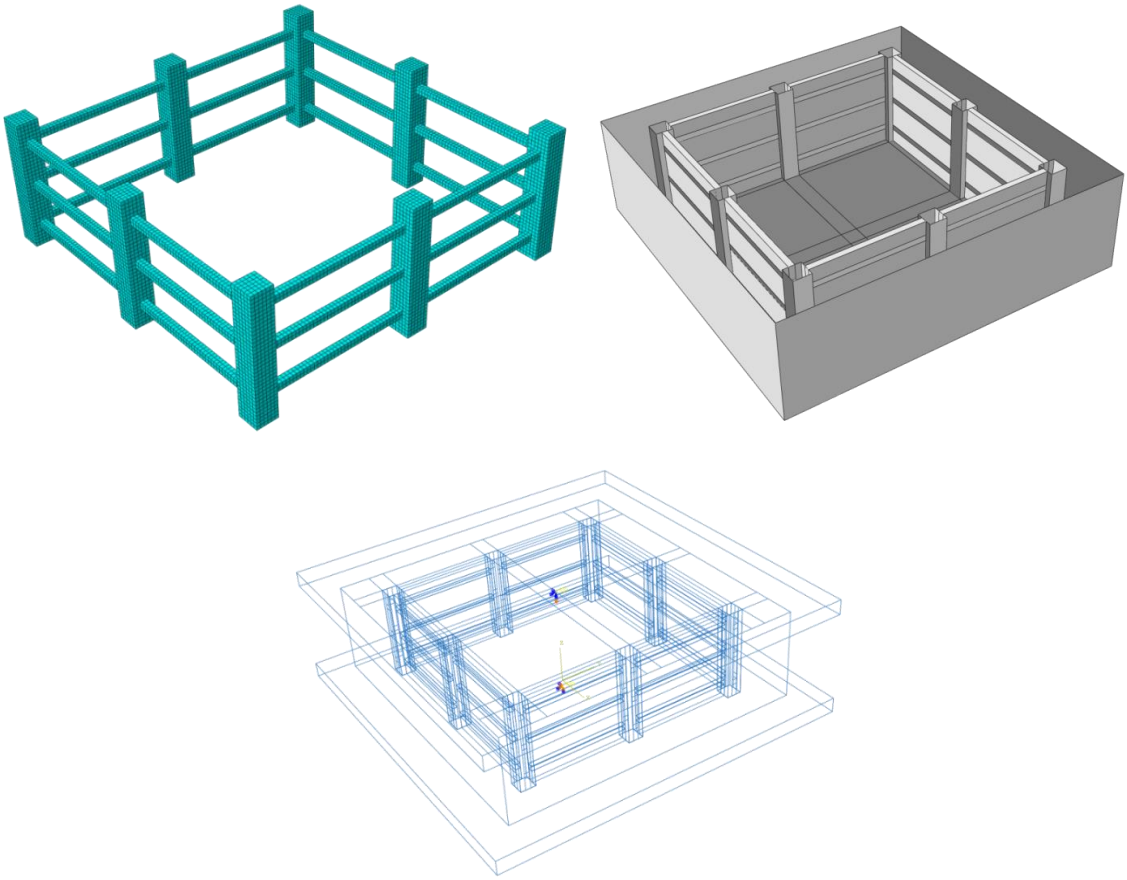

Figure 3-9: Approach 1 A) Steel Cage Mesh B) Inner View of Concrete Grooves C) Wire-Frame View of the Whole Model.

Next, approaches 2 and 3 are illustrated in Figure 3-10. This approach is simpler due to the fact that Abaqus takes care of the process, and manual concrete removal is not required.

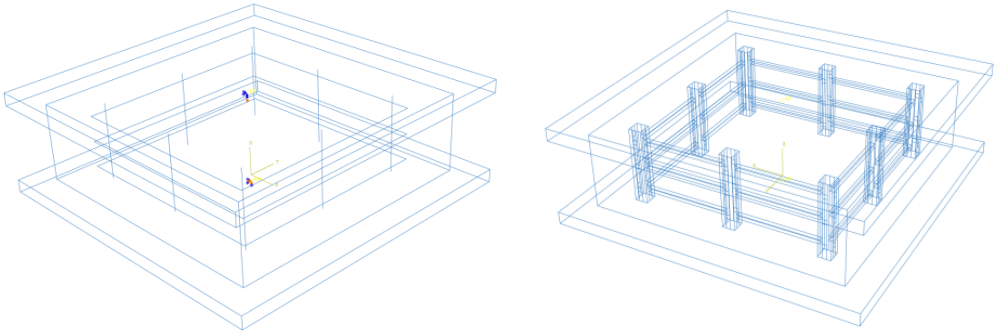

Figure 3-10: Wire-Frame View of the Whole Model for A) Approach 2 B) Approach 3.

With the models fully prepared, analyses were then conducted. For each approach, the stress contour plots (in ksi) at the compressive strength were obtained for the concrete (Figure 3-11) and the steel cage (Figure 3-12).

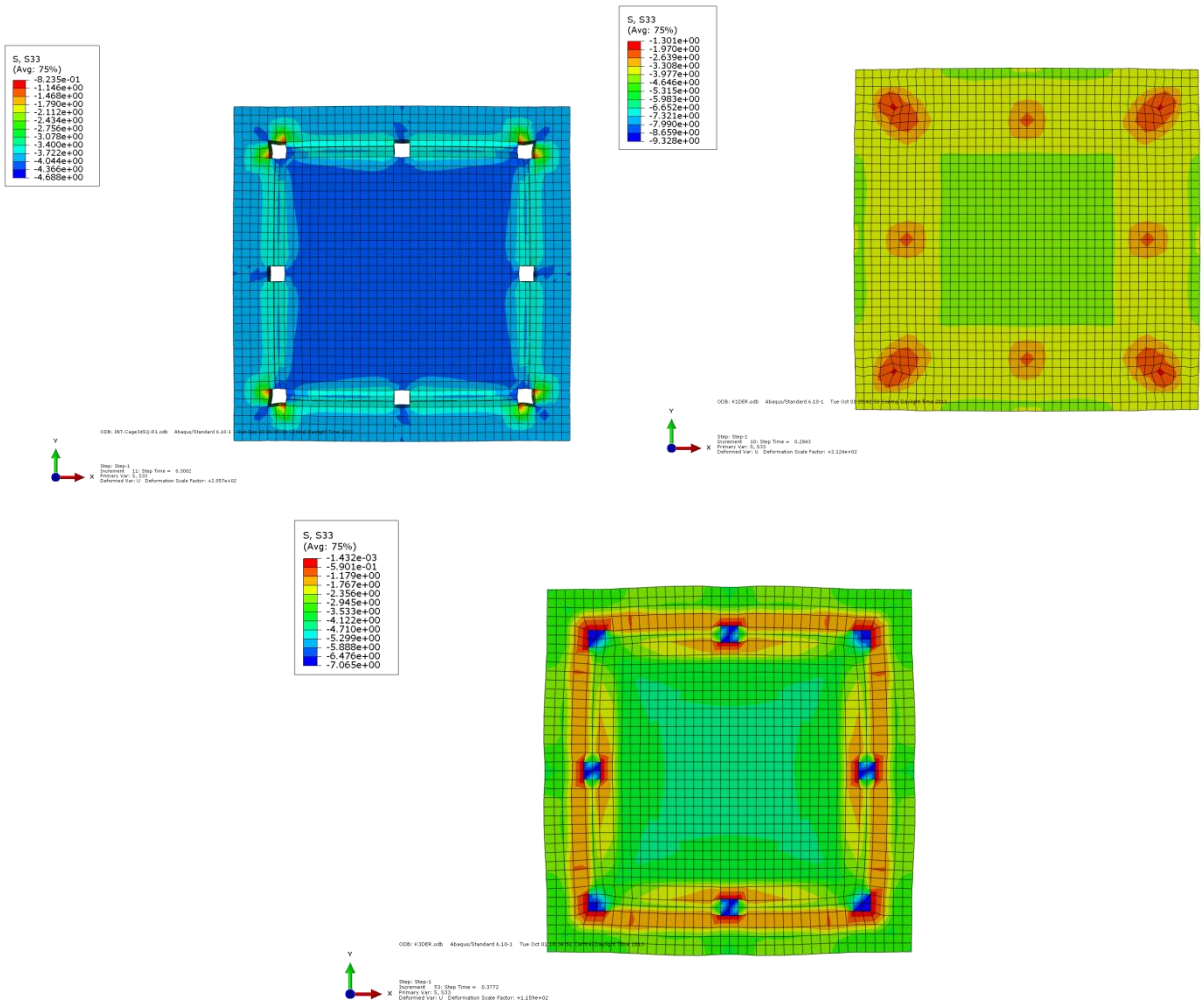

Figure 3-11: Concrete Stress Contour Plots for A) Approach 1 B) Approach 2 C) Approach 3.

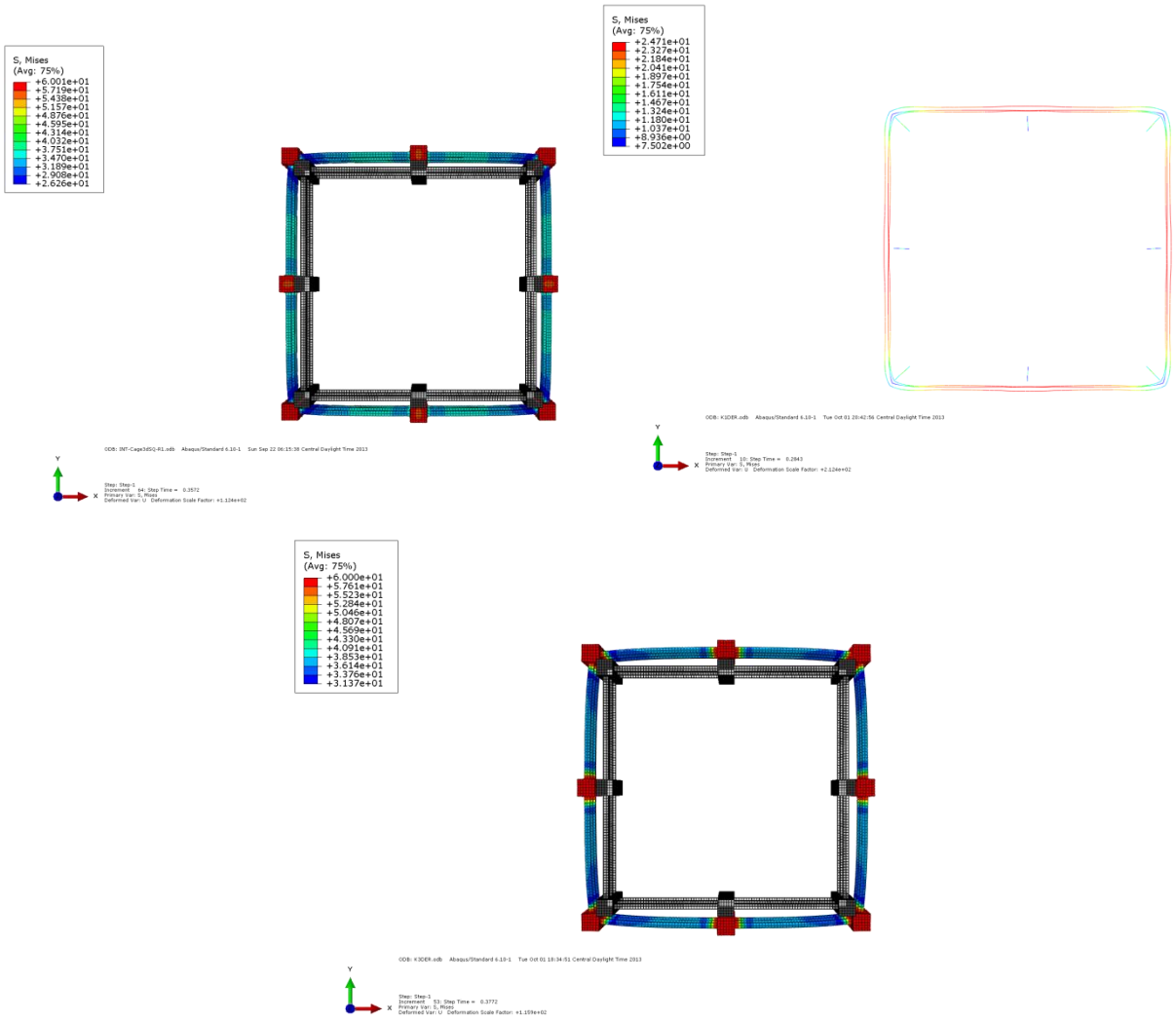

Figure 3-12: Steel Cage Stress Contour Plots for A) Approach 1 B) Approach 2 C) Approach 3

Figure 3-11 shows that similar behavior is observed in the three approaches. As expected, the core exhibited the largest stresses due to the confinement effect. It is also observed that arching action is more evident in approaches 1 and 3 i.e. when solid elements were used. The three plots were obtained at similar strains with an average value of 0.002. Figure 3-12 shows that in the three approaches, yielding has yet to occur in the lateral steel ties. Additionally, the axial stress-strain curves for the concrete core were plotted for the three approaches in Figure 3-13 below. The compressive strength values obtained from each approach were very close, and their average was 4.29 ksi. It is observed that approaches 1 and 2 are very close, while approach 3 reaches the compressive strength at a higher strain. Another observation is that the increase in

strength due to steel confinement is lower than expected. The unconfined strength was taken to be 4 ksi, while the average confined strength was obtained to be 4.29 ksi earlier. This is due to the fact that Concrete Damage Plasticity model (CDP) does not lend itself well to analyses with large confinement as per the Abaqus online documentation (2010) and research conducted by Yu et al. (2010). As the modification of the model is beyond of the scope of this work, the analyses was performed with the available model and considered conservative compared to the actual behavior.

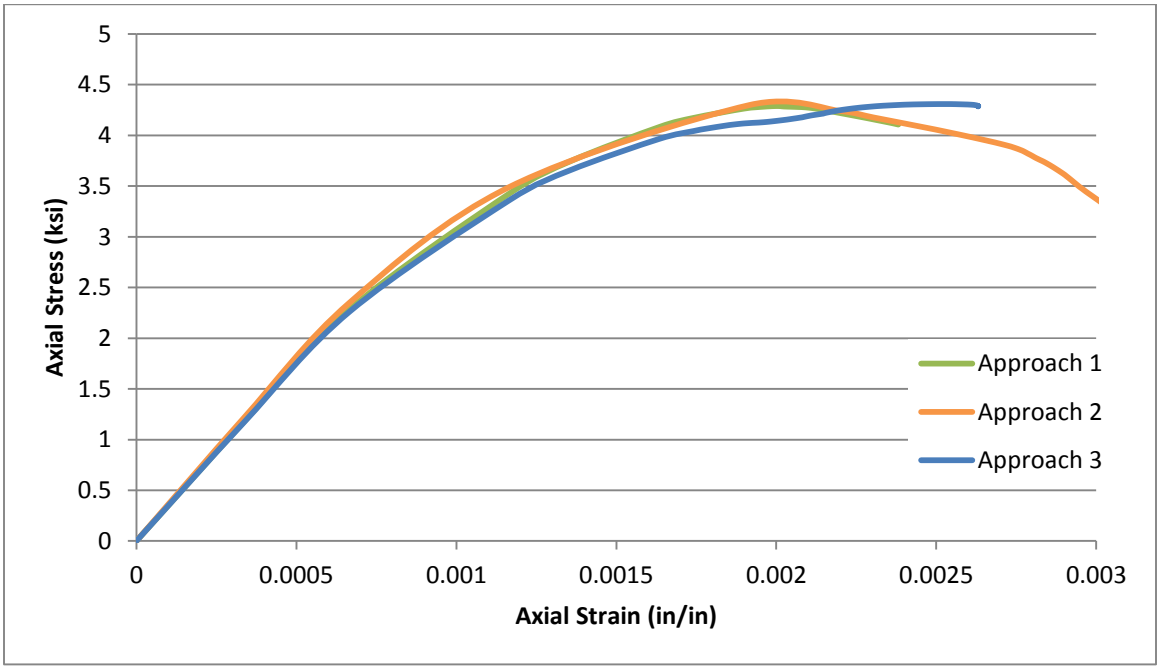

Figure 3-13: Axial Stress-Strain Curves Obtained from the FE Analysis.

From the results obtained, it was shown that the three approaches provided similar results. As all models provided reasonable results and did not differ from each other, the simplest approach, approach 2, would be used for the final model.

Final Finite Element Model

For the final model, the material models were the same as described for the preliminary models. As it was shown in the previous section, approach 2 with the truss elements for steel provided reasonable results and was chosen. Elements-wise, concrete was modeled using solid elements (C3D8r), while steel was modeled using truss elements (T3D2). The reinforcement was modeled using the embedded region technique. Further simplification was applied to this model based on the preliminary models' results. Displacement was applied to the upper surface directly.

Symmetry was also utilized about both the x and y-axes, thus only quarter of the specimen was modeled. Figure 3-14 below provides the wire-frame view, mesh, and boundary conditions used for this model.

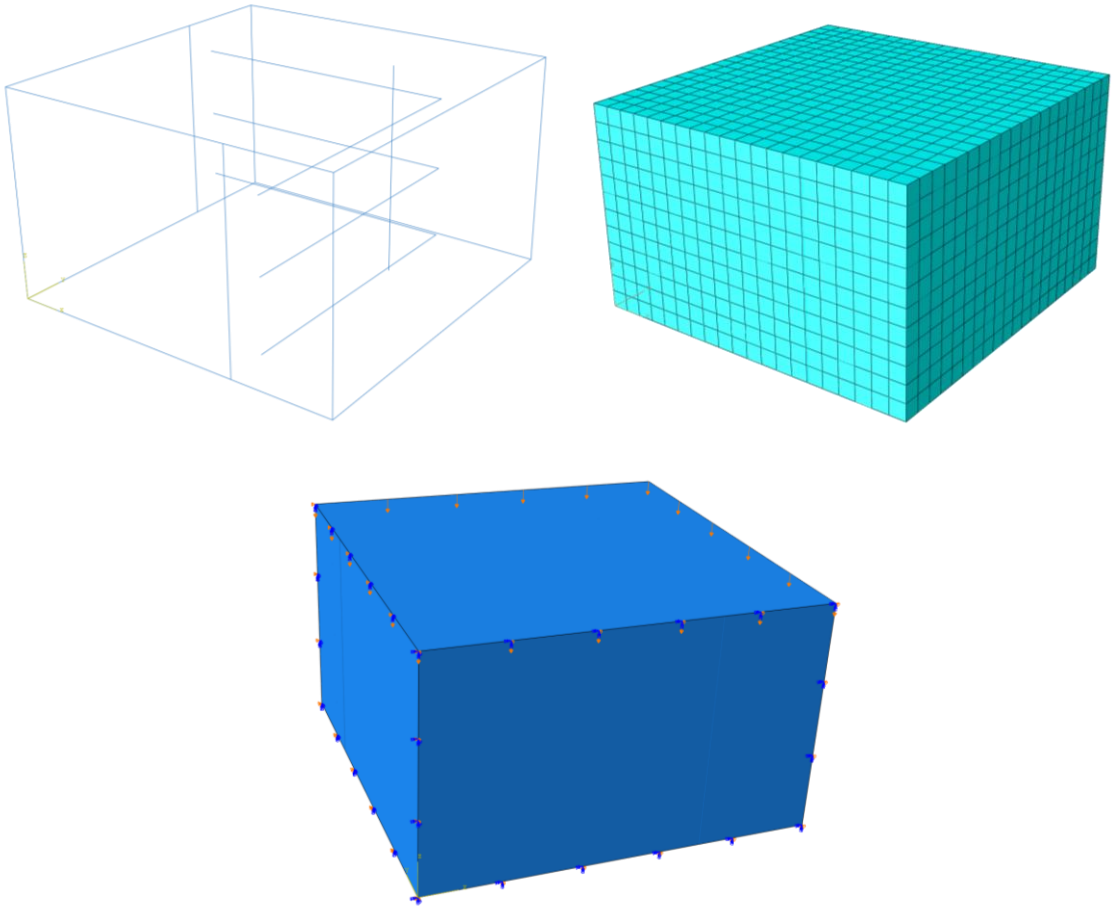

Figure 3-14: Final Model a) Wire-Frame View b) Mesh c) Boundary Conditions.

Multiple models were generated for the following aspect ratios (Width:Depth) that are shown in Figure 3-15:

- 1:1
- 1:2
- 1:3
- 1:4

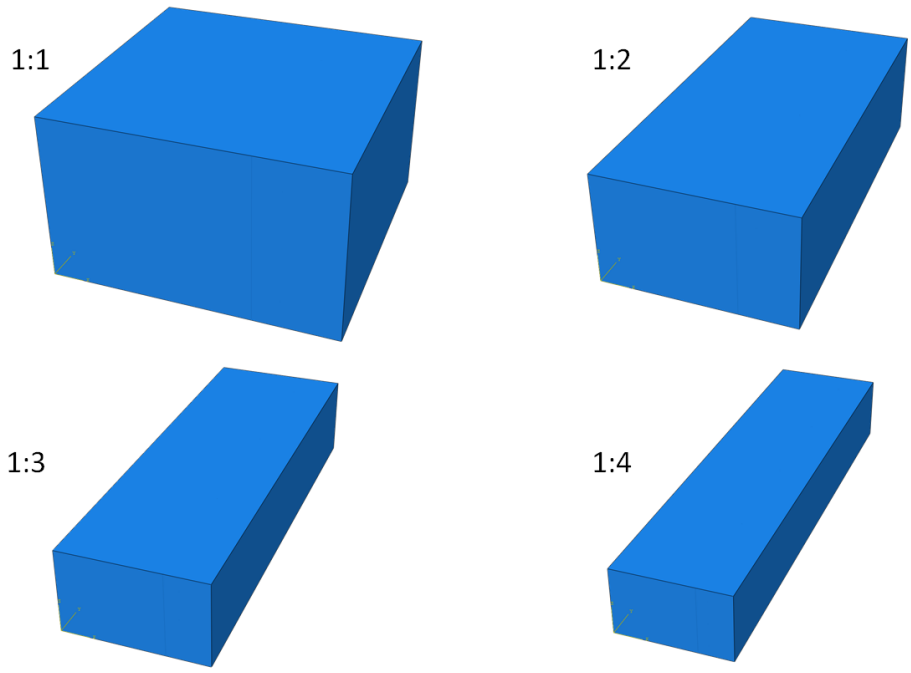

Figure 3-15: Final Model Aspect Ratios.

After running the analysis on the models, the core axial stress-strain curves were obtained as shown in Figure 3-16. The compressive strength values are summarized in Table 3-2. It is observed that the compressive strength decreases as the aspect ratio increases. This is reasonable as the effectiveness of confinement diminishes as the aspect ratio increases.

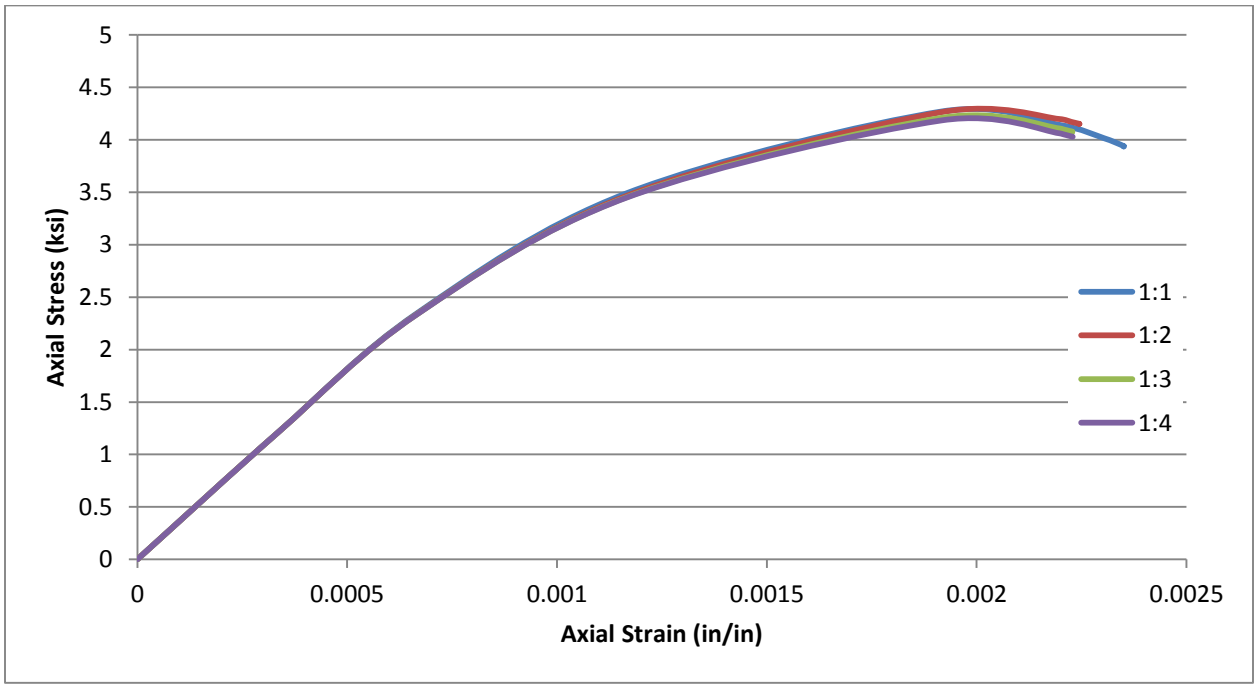

Figure 3-16: Final Model's Core Axial Stress-Strain Curves.

Table 3-2: Final Model Compressive Strength Values.

Aspect Ratio	1:1	1:2	1:3	1:4
f_{cc} (ksi)	4.27	4.26	4.21	4.19

Next, the stresses in the ties are shown in Figure 3-17. It is shown that the steel ties in all models have yielded by the end of the analysis. It is also observed that the stress in the ties along the x-axis did not vary with the aspect ratio. This is reasonable since the width was fixed in all models. Finally, it is noted that the stresses in the ties along the y-axis varied. In order to have a better view, a zoomed view of the later stages of loading is provided in Figure 3-18 for stresses in ties along the y-axis. It is observed that the ties in the model with the higher aspect ratios yielded first. Overall, for all aspect ratios, the ties yielded around the same time both along the x and y-axes. From this, it is concluded that steel ties will yield around the same time for aspect ratios up to four. Even though the concrete damage plasticity model did not fully capture the confinement effect in this case, the obtained results still hold, as it is expected that with the full effect of confinement accounted for, yielding will occur in the ties earlier.

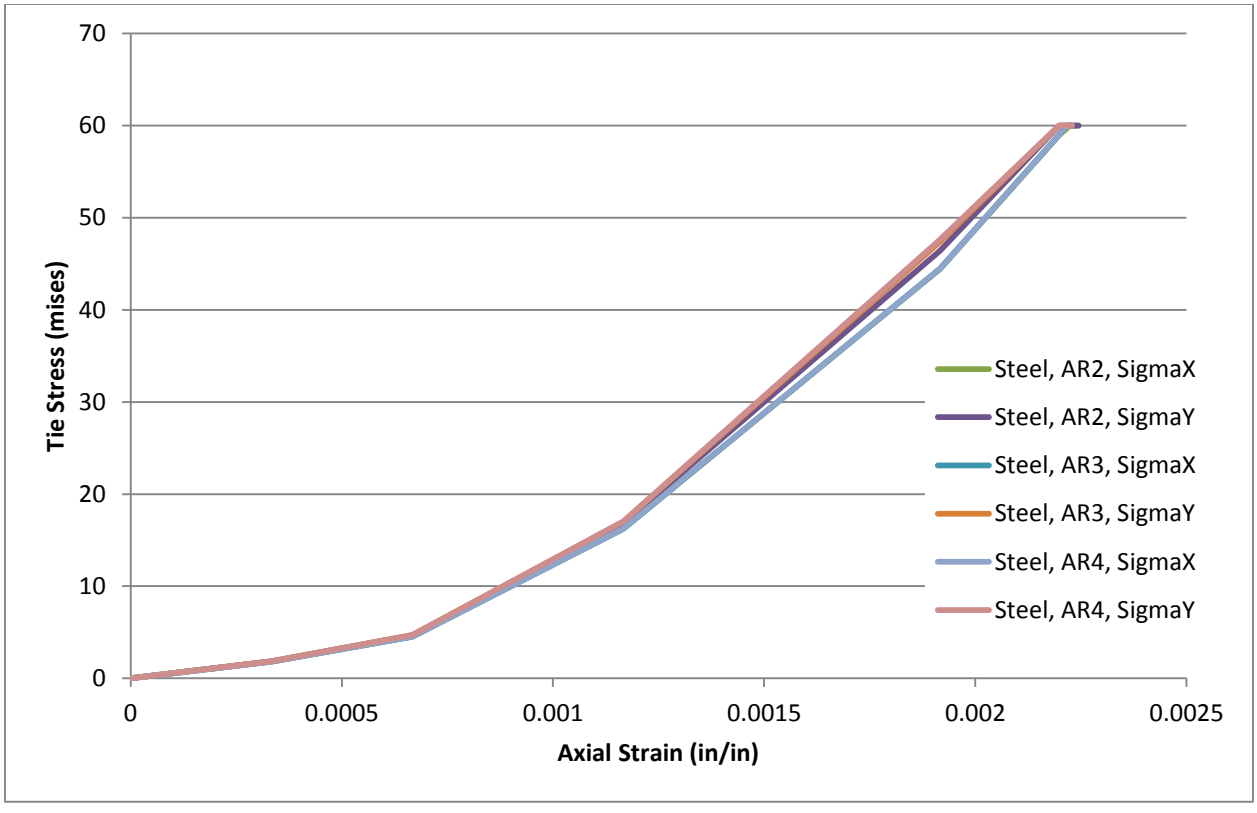

Figure 3-17: Final Model's Tie Stress vs. Axial Strain Curves.

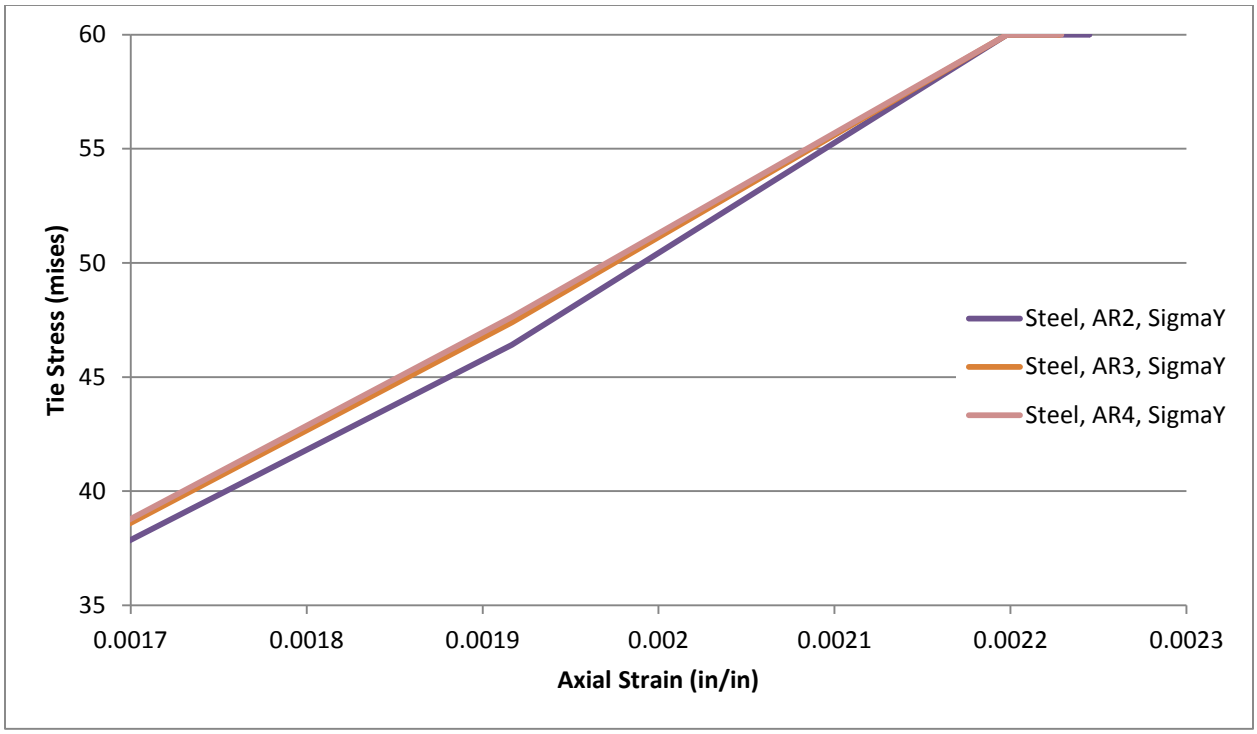

Figure 3-18: Zoomed View Of The Tie Stress Vs. Axial Strain Curves.

Chapter 4 - Rectangular Columns Subjected to Biaxial Bending and Axial Compression

Confined column analysis is a very involved process. Many studies in the literature investigated the confinement effect of transverse steel and FRP independently, but not as many accounted for the combined effect. For that to be accomplished, a new combined confinement model is proposed and discussed in this chapter. This new model necessitated modifications to existing models, and the implementation of an updated procedure to obtain the confined compressive strength using the triaxial state of stress analysis. This shall be presented as well in this chapter.

Confinement Models for Concrete

Mander Model for Concrete Confined with Transverse Steel

Mander et al. (1988) developed a stress-strain model for concrete confined with transverse steel. The model can be applied for members under static or dynamic loading that is applied either monotonically or cyclically. The model is based on effective lateral pressures which can be equal or unequal. This allows the model to accounts for the section's geometry, and in turn renders it applicable to both circular and rectangular sections.

Mander et al. based the stress-strain curve on equations suggested by Popovics (1973). The equations are as follows:

$$f_c = \frac{f_{cc} x r}{r - 1 + x^r} \quad \textbf{(4-1)}$$

$$x = \frac{\varepsilon_c}{\varepsilon_{cc}} \quad \textbf{(4-2)}$$

$$r = \frac{E_c}{E_c - E_{sec}} \quad \textbf{(4-3)}$$

$$E_{sec} = \frac{f_{cc}}{\varepsilon_{cc}} \quad \textbf{(4-4)}$$

$where\ f_c = longitudinal\ compressive\ concrete\ stress$

$f_{cc} = compressive\ strength\ of\ confined\ concrete$

$\varepsilon_{cc} = strain\ at\ the\ compressive\ strength\ of\ confined\ concrete$

The strain at the compressive strength of confined concrete is obtained according to the following equation suggested by Richart et al (1928):

$$\varepsilon_{cc} = \varepsilon_{co}\left(1 + 5\left(\frac{f_{cc}}{f_c'} - 1\right)\right) \quad \textbf{(4-5)}$$

$where\ f_c' = unconfined\ concrete\ strength$

$\varepsilon_{co} = strain\ corresponding\ to\ the\ unconfined\ concrete\ strength$

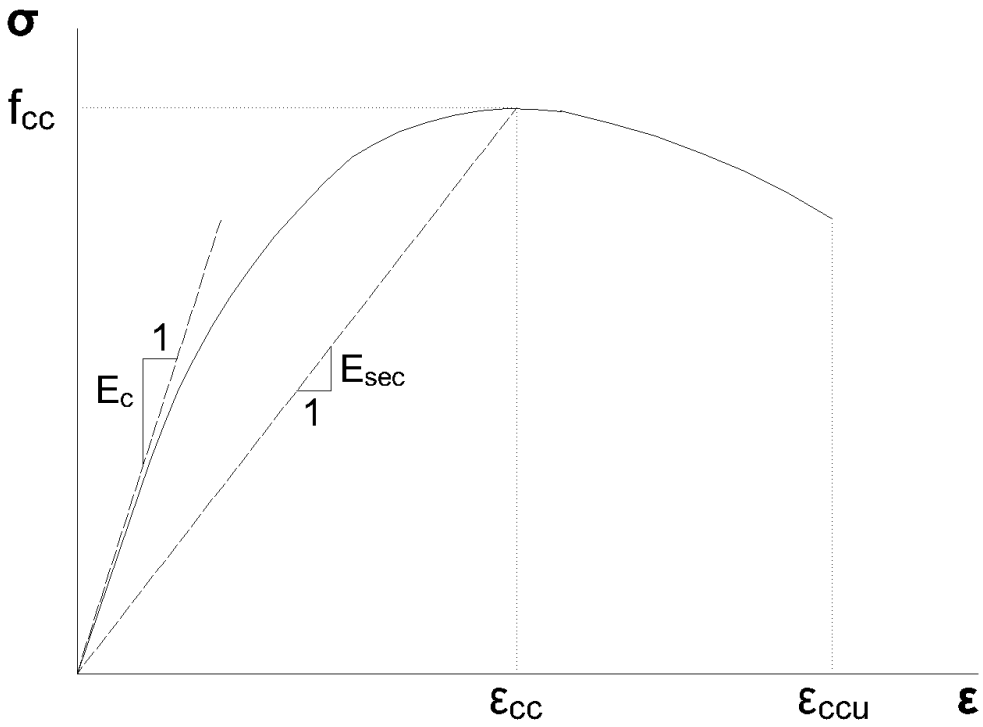

Figure 4-1: Stress-strain model proposed by Mander et al. (1988) for confined concrete.

Figure 4-1 illustrates the proposed stress-strain model. The confined concrete curve illustrates the behavior under concentric axial loading. The ascending branch has an initial slope equal to the modulus of elasticity of concrete (E_c) that decreases as the stress increases until the stress reaches its peak at the confined compressive strength (f_{cc}). The slope becomes negative and the stress decreases until the occurrence of the first hoop fracture. The descending branch represents the ductile region of the curve.

As stated earlier, effective lateral pressures were employed in this model. This approach was similar to the one used by Sheikh and Uzumeri (1982). Arching action leads to the development of portions of concrete in which confining stress is fully developed. Only on these portions can the maximum transverse pressure from the confining steel be exerted effectively.

The area of the confined concrete is assumed to be the area within the centerlines of the perimeter hoop (A_{cc}). Figure 4-2 shows the effective confinement regions in rectangular sections. It assumed that the arching action acts in the form of parabolas with an initial slope of 45°. This action occurs vertically between the transverse steel layers and horizontally between longitudinal bars.

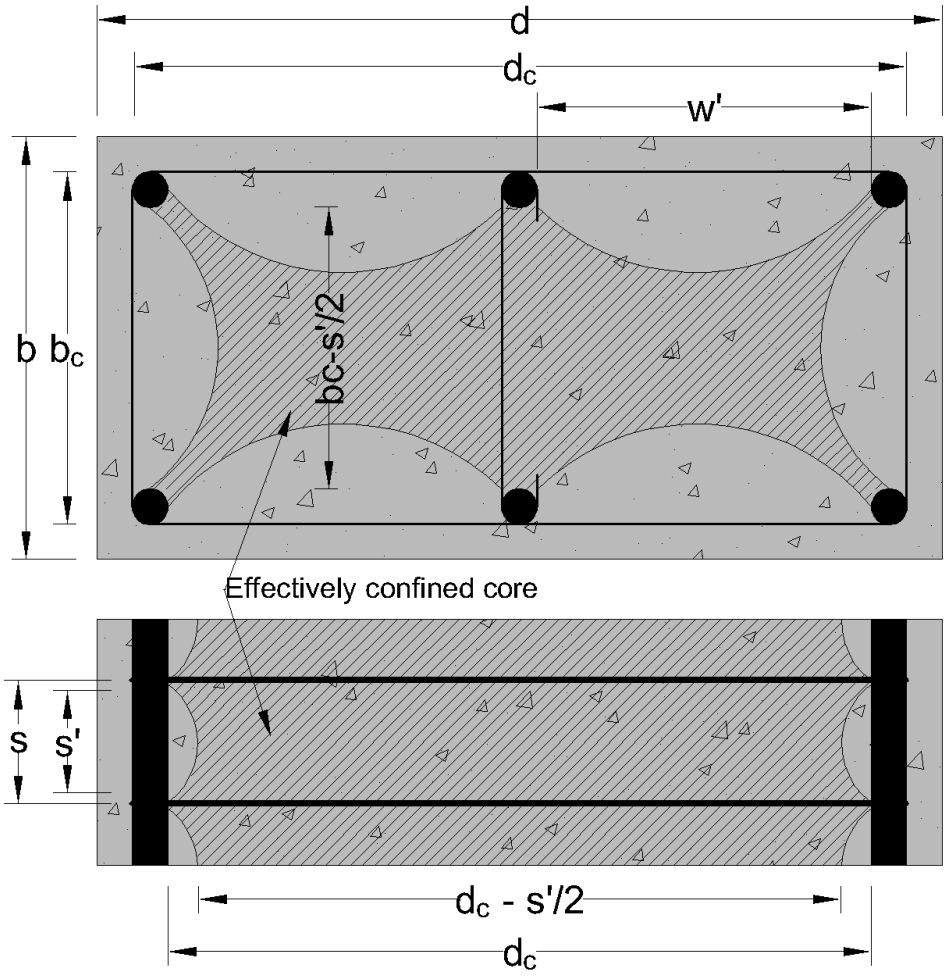

Figure 4-2: Effectively Confined Core for Rectangular Hoop Reinforcement Proposed by Mander et al. (1988).

Figure 4-2 above shows that the effective confined area is smaller than the core area, thus the effective lateral pressure (f_l') is obtained as a percentage of the lateral pressure from the transverse reinforcement (f_l) as follows:

$$f_l' = k_e f_l \quad \textbf{(4-6)}$$

$$k_e = \frac{A_e}{A_{cc}} \quad \textbf{(4-7)}$$

$$A_{cc} = A_c(1 - \rho_{cc}) = area\ of\ concrete\ core \quad \textbf{(4-8)}$$

$where\ k_e = confinement\ effectiveness\ coefficient$

$A_e = area\ of\ effectively\ confined\ concrete\ core$

$\rho_{cc} = ratio\ of\ longitudinal\ steel\ to\ the\ area\ of\ the\ core$

The effectively confined core area is obtained by deducting the area of the horizontal and vertical parabolas shown in Figure 4-2. The effective area (A_e) is obtained as follows:

$$A_e = \left(b_c d_c - \sum_{i=1}^{n} \frac{(w_i')^2}{6}\right)\left(1 - \frac{s'}{2b_c}\right)\left(1 - \frac{s'}{2d_c}\right) \quad \textbf{(4-9)}$$

$where\ w_i' = ith\ clear\ distance\ between\ adjacent\ longitudinal\ bars$

$n = number\ of\ longitudinal\ bars$

Substituting back in the equation for the confinement effectiveness coefficient, the following equation is obtained:

$$k_e = \frac{\left(1 - \sum_{i=1}^{n} \frac{(w_i')^2}{6b_c d_c}\right)\left(1 - \frac{s'}{2b_c}\right)\left(1 - \frac{s'}{2d_c}\right)}{(1 - \rho_{cc})} \quad \textbf{(4-10)}$$

The steel ratios in each transverse direction are obtained as follows:

$$\rho_x = \frac{A_{sx}}{sd_c} \quad \textbf{(4-11)}$$

$$\rho_y = \frac{A_{sy}}{sb_c} \quad \textbf{(4-12)}$$

Next, the lateral confining pressures are obtained by:

$$f_{lx} = \rho_x f_{yh} \quad \textbf{(4-13)}$$

$$f_{ly} = \rho_y f_{yh} \quad \textbf{(4-14)}$$

Finally, the effective pressures are obtained as follows:

$$f_{lx}' = k_e \rho_x f_{yh} \quad \textbf{(4-15)}$$

$$f_{ly}' = k_e \rho_y f_{yh} \quad \textbf{(4-16)}$$

For strength determination, the constitutive model proposed by Willam and Warnke (1975) is used. Further details are provided in the Formulations section.

Finally, for the determination of the ultimate confined strain Scott et al. (1982) proposed to set it at the point which first hoop fracture occurs. This is the point when the lateral pressure provided by the steel drops and in turn is the end of the meaningful region of the confined curve.

Mander (1984) proposed an energy balance approach to predict the ultimate confined strain. This is done by equating the ultimate strain energy capacity of the confining reinforcement per unit volume of concrete core (U_{sh}) to the difference in area between the confined (U_{cc}) and the unconfined (U_{co}) concrete stress-strain curves, in addition to the energy required to maintain the yielding of the longitudinal steel (U_{sc}). This is expressed in the following equation:

$$U_{sh} = U_{cc} + U_{sc} - U_{co} \quad \textbf{(4-17)}$$

Below are the expressions for each energy term. All equations are provided in SI units. The expressions for U_{sh} and U_{co} were estimated from experiments by Mander et al:

$$U_{sh} = \rho_s A_{cc} \int_0^{\varepsilon_{sf}} f_s d\varepsilon_s = \rho_s A_{cc} * 110\ MJ/m^3 \quad \textbf{(4-18)}$$

$$U_{cc} = A_{cc} \int_0^{\varepsilon_{cu}} f_c d\varepsilon_c \quad \textbf{(4-19)}$$

$$U_{sc} = \rho_{cc} A_{cc} \int_0^{\varepsilon_{cu}} f_{sl} d\varepsilon_c \quad \textbf{(4-20)}$$

$$U_{co} = A_{cc} \int_0^{\varepsilon_{sp}} f_c d\varepsilon_c = 0.017\sqrt{f'_{co}}\ MJ/m^3 \quad \textbf{(4-21)}$$

Substituting back in the first equation, it simplifies to:

$$110\ \rho_s = \int_0^{\varepsilon_{cu}} f_c d\varepsilon_c + \int_0^{\varepsilon_{cu}} f_{sl} d\varepsilon_c - 0.017\sqrt{f'_{co}}\ MJ/m^3 \quad \textbf{(4-22)}$$

Lam and Teng Model for Concrete Confined with FRP Wraps

Lam and Teng (2003) developed a stress-strain model for concrete confined with Fiber Reinforced Polymer (FRP) wraps. Assessment performed by an ACI committee 440 task group (2007) showed that this model was the most reliable for predicting the ultimate compressive strength and strain for circular and rectangular columns. The equations for this model are as follows:

$$f_c = \begin{cases} E_c\varepsilon_c - \dfrac{(E_c - E_2)^2}{4f'_c}\varepsilon_c^2, & for\ 0 \le \varepsilon_c \le \varepsilon'_t \\ f'_c + E_2\varepsilon_c, & for\ \varepsilon'_t \le \varepsilon_c \le \varepsilon_{ccu} \end{cases} \quad \textbf{(4-23)}$$

$$E_2 = \frac{f_{cc} - f'_c}{\varepsilon_{ccu}} \quad \textbf{(4-24)}$$

$$\varepsilon'_t = \frac{2f'_c}{E_c - E_2} \quad \textbf{(4-25)}$$

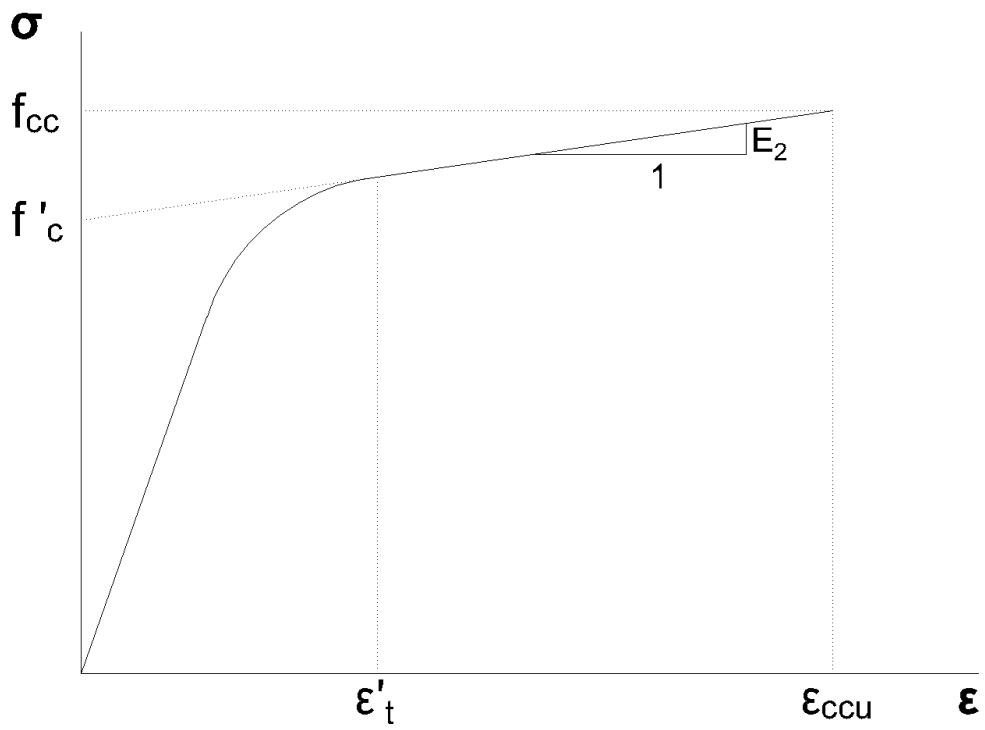

Figure 4-3: Stress-strain model proposed by Lam and Teng (2003) for confined concrete.

Figure 4-3 illustrates Lam and Teng stress-strain model. The upper curve illustrates the behavior under concentric axial loading. The first branch is parabolic and its initial slope equal to the modulus of elasticity of concrete (E_c). The second branch is linear and starts at the transition strain (ε_t') calculated above. The curve is continuous at the transition point as there is no sudden change in the slope there. This behavior has been observed under sufficient FRP confinement. For that to hold, Lam and Teng (2003) set a minimum confinement ratio limit (f_{lf}/f_c') of 0.07, while the ACI committee 440 (2008) increased it to 0.08. Spoelstra and Monti (1999) were able to verify this limit for circular sections in their analytical model. In this work, ACI 440 provisions were followed, thus the limit was taken to be 0.08. If the confinement ratio is below the limit, Mander model (descending second branch) is used instead.

As for the ultimate axial strength and strain, Lam and Teng proposed the following equations:

$$f_{cc} = f_c' + \psi_f 3.3 \kappa_a f_l \quad \textbf{(4-26)}$$

$$\varepsilon_{ccu} = \varepsilon_c' \left(A + 12 k_b \frac{f_l}{f_c'} \left(\frac{\varepsilon_{fe}}{\varepsilon_c'} \right)^{0.45} \right) \leq 0.01 \quad \textbf{(4-27)}$$

$$where\ \psi_f = \begin{cases} 1\ (Lam\ and\ Teng) \\ 0.95\ (ACI\ 440.2R-08) \end{cases}$$

$$\kappa_a = \frac{A_e}{A_c}\left(\frac{b}{h}\right)^2 \quad \textbf{(4-28)}$$

$$\kappa_b = \frac{A_e}{A_c}\left(\frac{h}{b}\right)^{0.5} \quad \textbf{(4-29)}$$

$$\varepsilon_{fe} = 0.586\varepsilon_{fu} \quad \textbf{(4-30)}$$

$$A = \begin{cases} 1.75\ (Lam\ and\ Teng) \\ 1.5\ (ACI\ 440.2R-08) \end{cases}$$

ACI Committee 440 added an additional reduction factor to the strength equation (ψ_f) based on their judgment (2008). Similarly, a limitation on the value of ultimate strain was imposed by ACI 440.2R-08 to prevent excessive cracking which leads to the loss of concrete integrity. If this limit is exceeded, the ultimate strain will be set to 0.01, and the corresponding stress value will be set as the new ultimate strength.

In order to extend their model to rectangular sections, Lam and Teng proposed the addition of shape factors (κ_a and κ_b). They also converted the rectangular section to an equivalent circular section as shown in Figure 4-4. The equivalent diameter is calculated as follows:

$$D = \sqrt{b^2 + h^2} \quad \textbf{(4-31)}$$

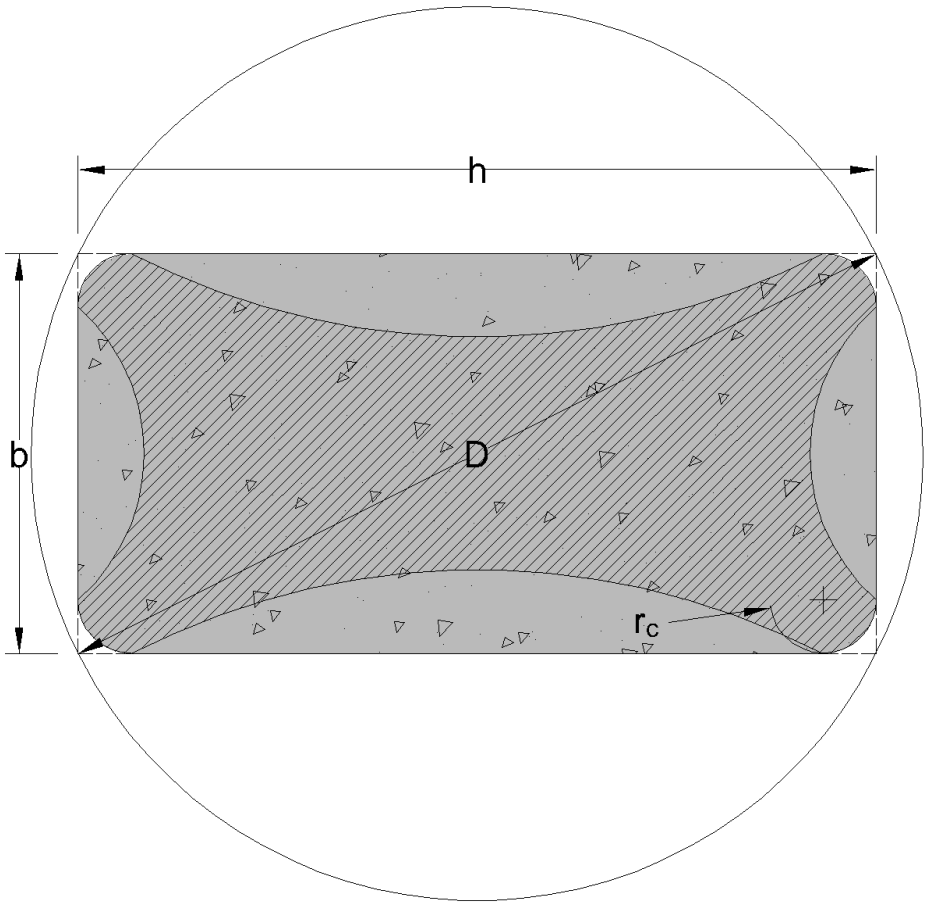

Figure 4-4: Lam and Teng Equivalent Circular Section.

The effectively confined concrete area was assumed to be transcribed by parabolas with an initial slope equal to that of the adjacent diagonal. The confined area ratio is obtained from the following expression:

$$\frac{A_e}{A_c} = \frac{1 - \frac{\left(\left(\frac{b}{h}\right)(h-2r_c)^2 + \left(\frac{h}{b}\right)(b-2r_c)^2\right)}{3A_g} - \rho_g}{1-\rho_g} \quad \textbf{(4-32)}$$

$where\ r_c = radius\ of\ rounded\ corners$

$\rho_g = longitudinal\ reinforcement\ ratio$

Lastly, the lateral pressure provided by the FRP confinement in the equivalent circular section is computed as follows:

$$f_l = \frac{2nt_f E_f \varepsilon_{fe}}{D} \quad \textbf{(4-33)}$$

Combined Confinement Model

As previously mentioned, Mander model (1988) was developed for concrete confined with transverse steel only, while Lam and Teng model (2003) was developed for concrete confined with FRP only. This limits their application in reinforced concrete columns in which both types of reinforcement exist. These columns are subjected to two different confining pressures from steel and FRP. To account for the interaction between the two confining systems, a model to estimate the combined behavior of the two systems is proposed. The proposed model combines the models proposed by Mander and Lam and Teng and allows for prediction of the confined strength of concrete columns confined with both transverse steel and FRP wraps.

The expression for the lateral confinement pressure is replaced with two lateral pressures in the x and y directions. This formulation accounts for the contribution of both transverse steel and FRP inside the core (f_{le}) and only FRP in the cover (f_{lf}) as shown in Figure 4-5. The expressions are as follows:

$$f_{lxf} = k_f \frac{2nt_f E_f \varepsilon_{fe}}{h} \quad \textbf{(4-34)}$$

$$f_{lyf} = k_f \frac{2nt_f E_f \varepsilon_{fe}}{b} \quad \textbf{(4-35)}$$

$$f_{lxe} = k_f \frac{2nt_f E_f \varepsilon_{fe}}{h} + k_e \rho_x f_{yh} \quad \textbf{(4-36)}$$

$$f_{lye} = k_f \frac{2nt_f E_f \varepsilon_{fe}}{b} + k_e \rho_y f_{yh} \quad \textbf{(4-37)}$$

$$k_f = \frac{1 - \frac{\left(\left(\frac{b}{h}\right)(h-2r_c)^2 + \left(\frac{h}{b}\right)(b-2r_c)^2\right)}{3A_g} - \rho_g}{1-\rho_g} \quad \textbf{(4-38)}$$

$$k_e = \frac{\left(1 - \sum_{i=1}^{n} \frac{(w_i')^2}{6b_c d_c}\right)\left(1 - \frac{s'}{2b_c}\right)\left(1 - \frac{s'}{2d_c}\right)}{(1-\rho_{cc})} \quad \textbf{(4-39)}$$

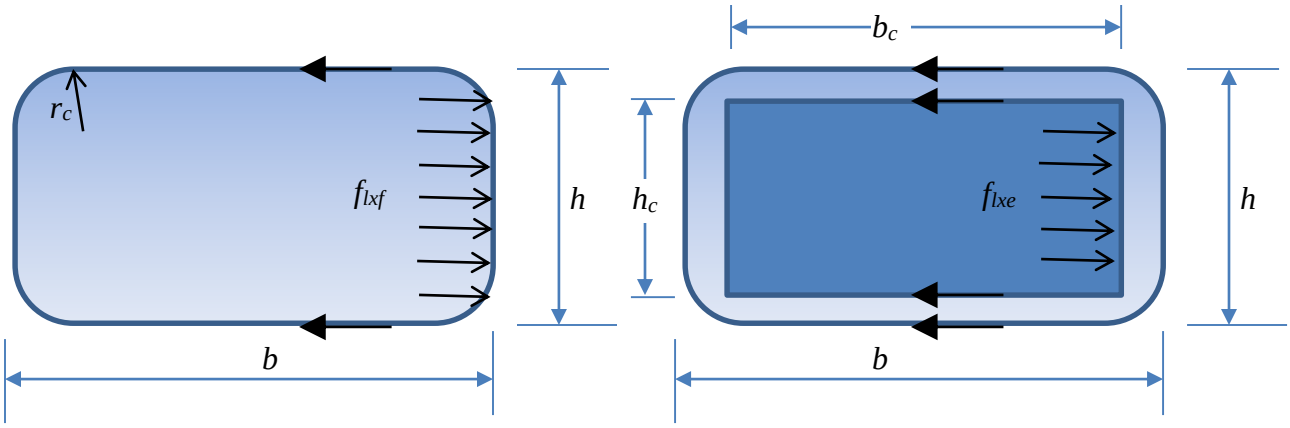

Figure 4-5: Effective Horizontal Pressure of Confined Rectangular Section.

The values of the ultimate confined strength of the core and the cover are then calculated based on the constitutive model developed by Willam and Warnke (1975). The procedure is described in detail in the next section.

Under the framework of the combined model, the appropriate model (Mander model or Lam and Teng model) for the specific case is applied based on the confinement ratio provided by the FRP. If the ratio (f_{lf}/f_c') is greater than or equal to 0.08, the ascending second branch is confirmed and Lam and Teng model will be used to calculate the stress-strain curve's parameters for the core and the cover. Otherwise, Mander model will be used to compute these parameters. The confinement ratio limit of 0.08 was provided by ACI 440.2R-08 (2008).

After computing the appropriate model's parameters, stresses are computed using the applied model's equation for both the core and the cover. As the cover will always have a lower ultimate strain value due to its lower confinement pressure, in a few cases, there will be a strain level at which cover stress will be zero while the core is still active and sound. This is not reasonable because the existence of the FRP prevents concrete cover spalling. Additionally, a sudden drop in the stresses could cause convergence issues. In order to avoid this, it is assumed that the stress-strain curve remains flat after reaching the ultimate strain, i.e., when ultimate strain for the cover is exceeded, cover stress remains constant from that point until the ultimate strain value for the core is reached. This is only applicable to cases where Lam and Teng model is used. For Mander model, the ultimate confined strain value is obtained from equation 4.21, and is not dependent on the confining pressure values. As a result, the ultimate strain for both core and cover is obtained to be the same. This behavior is illustrated in Figure 4-6.

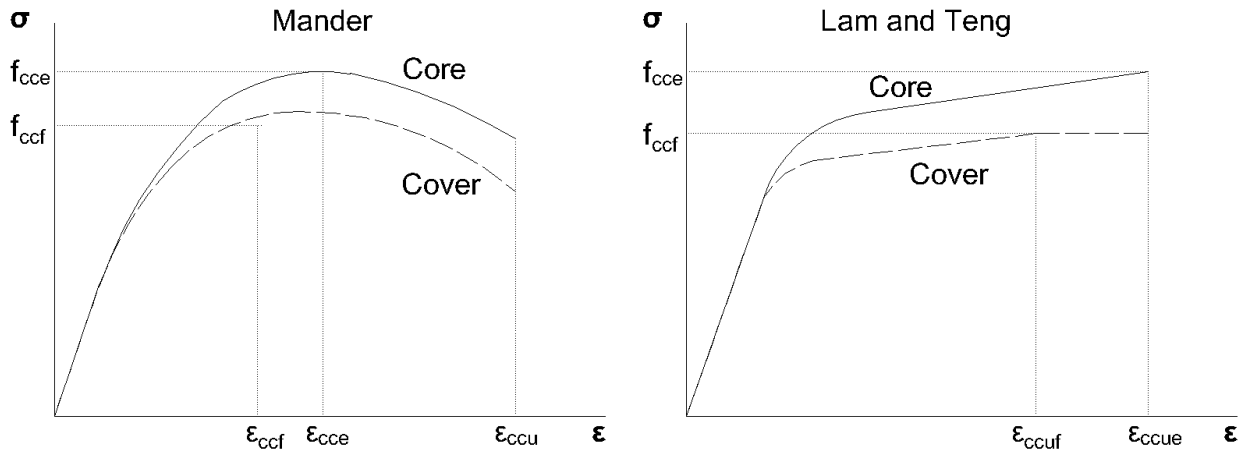

Figure 4-6: Confinement Models for Core and Cover.

Formulations

Generalized Moment of Area Theorem

First, the axial stress equation provided by Hardy Cross for an unsymmetric section subjected to an axial force and biaxial bending is as follows (1930):

$$\sigma_z = \frac{P}{A} + \frac{M_x I_y - M_y I_{xy}}{I_x I_y - I_{xy}^2} y + \frac{M_y I_x - M_x I_{xy}}{I_x I_y - I_{xy}^2} x \qquad \textbf{(4-40)}$$

$where: \sigma_z = normal\ stress\ at\ a\ point\ in\ the\ section$

$P = applied\ load$

$A = section\ area$

$M_x = bending\ moment\ about\ the\ x-axis$

$M_y = bending\ moment\ about\ the\ y-axis$

$I_x = moment\ of\ inertia\ about\ the\ x-axis$

$I_y = moment\ of\ inertia\ about\ the\ y-axis$

$I_{xy} = product\ moment\ of\ inertia\ in\ x-y\ plane$

$x = distance\ between\ the\ point\ and\ the\ x-axis\ of\ the\ inelastic\ centroid$

$y = distance\ between\ the\ point\ and\ the\ y-axis\ of\ the\ inelastic\ centroid$

The equation is then rewritten to obtain the axial strain as follows:

$$\varepsilon_z = \frac{P}{EA} + \frac{M_x EI_y - M_y EI_{xy}}{EI_x EI_y - EI_{xy}^2} y + \frac{M_y EI_x - M_x EI_{xy}}{EI_x EI_y - EI_{xy}^2} x \qquad \textbf{(4-41)}$$

$where: E = Young's\ modulus\ of\ elasticity$

In a linear elastic analysis, the modulus of elasticity is a constant. On the contrary, the modulus of elasticity varies along the section in the case of nonlinear analysis where the stress profile is nonlinear. As a result, Rasheed and Dinno (1994) proposed implementing the summation expressions $\sum E_i A_i$ and $\sum E_i I_i$ to account for this variation. The curvatures are obtained according to the following equations:

$$\phi_x = \frac{M_x EI_y - M_y EI_{xy}}{\beta^2} \quad \textbf{(4-42)}$$

$$\phi_y = \frac{M_y EI_x - M_x EI_{xy}}{\beta^2} \quad \textbf{(4-43)}$$

$$where: \beta = EI_x EI_y - EI_{xy}^2 \quad \textbf{(4-44)}$$

$\phi_x = x - curvature.$

$\phi_y = y - curvature.$

Now, the axial strain equation can be simplified to the following equation:

$$\varepsilon_z = \frac{P}{EA} + \phi_x y + \phi_y x \quad \textbf{(4-45)}$$

Using this equation, the stain at the geometric centroid ($\varepsilon_o \; at \; x = y = 0$) is obtained below:

$$\varepsilon_o = \frac{P}{EA} \quad \textbf{(4-46)}$$

From the axial strain equation, an equation to determine the load (P) at the geometric centroid is obtained below:

$$P = EA\bar{\varepsilon_o} - EA\bar{y}\phi_x - EA\bar{x}\phi_y \quad \textbf{(4-47)}$$

But:

$$EAM_x = EA\bar{y} \quad \textbf{(4-48)}$$

$$EAM_y = EA\bar{x} \quad \textbf{(4-49)}$$

$where: \bar{y} = y_g - y_c$

$\bar{x} = x_g - x_c$

$x_g: Horizontal \; distance \; to \; the \; geometric \; centroid \; measured \; from \; the \; left \; side$

$y_g: Vertical \; distance \; to \; the \; geometric \; centroid \; measured \; from \; the \; bottom \; side$

$x_g: Horizontal \; distance \; to \; the \; inelastic \; centroid \; measured \; from \; the \; left \; side$

$y_g: Vertical \; distance \; to \; the \; inelastic \; centroid \; measured \; from \; the \; bottom \; side$

Using the previous expressions, the axial load equation is now simplified to the following:

$$P = EA\bar{\varepsilon_o} - EAM_x\phi_x - EAM_y\phi_y \quad \textbf{(4-50)}$$

Next, the equation is generalized for moments of area about the geometric centroidal axes. Starting with moments about the x-axis, the moment is transferred from the inelastic centroid to the geometric centroid using the following equation:

$$\overline{M_x} = M_x - P\bar{y} \quad \textbf{(4-51)}$$

The coupled equations of moments about the inelastic centroid are as follows:

$$M_x = EI_x\phi_x + EI_{xy}\phi_y \quad \textbf{(4-52)}$$

$$M_y = EI_y\phi_y + EI_{xy}\phi_x \quad \textbf{(4-53)}$$

Substituting the moment about the inelastic equation and the axial load equation into the moment about the geometric centroid equation, the following is obtained:

$$\overline{M_x} = EI_x\phi_x + EI_{xy}\phi_y - \left(EA\bar{\varepsilon_o} - EAM_x\phi_x - EAM_y\phi_y\right)\bar{y} \quad \textbf{(4-54)}$$

$$\overline{M_x} = -EAM_x\bar{\varepsilon_o} + (EI_x + EAM_x\bar{y})\phi_x + \left(EI_{xy} + EAM_y\bar{y}\right)\phi_y \quad \textbf{(4-55)}$$

Similarly, the following expressions are obtained for the moment about the y-axis:

$$\overline{M_y} = M_y - P\bar{x} \quad \textbf{(4-56)}$$

$$\overline{M_y} = EI_y\phi_y + EI_{xy}\phi_x - \left(EA\bar{\varepsilon_o} - EAM_x\phi_x - EAM_y\phi_y\right)\bar{x} \quad \textbf{(4-57)}$$

$$\overline{M_y} = -EAM_y\bar{\varepsilon_o} + \left(EI_{xy} + EAM_x\bar{x}\right)\phi_x + \left(EI_y + EAM_y\bar{x}\right)\phi_y \quad \textbf{(4-58)}$$

In the previous final expressions, the terms $(EI_x + EAM_x\bar{y})$ and $\left(EI_y + EAM_y\bar{x}\right)$ are taken to represent $\overline{EI_x}$ and $\overline{EI_y}$, respectively. Also, the terms $\left(EI_{xy} + EAM_y\bar{y}\right)$ and $\left(EI_{xy} + EAM_x\bar{x}\right)$ are actually equal, since $EAM_y\bar{y} = EA\bar{x}\bar{y}$ and $EAM_x\bar{x} = EA\bar{y}\bar{x}$, thus the term $\overline{EI_{xy}}$ is taken to represent them. Now, assembling the equations for the axial load and moments about the centroidal axes, the following generalized system of equations is obtained:

$$\begin{bmatrix} P \\ \overline{M_x} \\ \overline{M_y} \end{bmatrix} = \begin{bmatrix} EA & -EAM_x & -EAM_y \\ -EAM_x & \overline{EI_x} & \overline{EI_{xy}} \\ -EAM_y & \overline{EI_{xy}} & \overline{EI_y} \end{bmatrix} \begin{bmatrix} \bar{\varepsilon_o} \\ \phi_x \\ \phi_y \end{bmatrix} \quad \textbf{(4-59)}$$

Applying the obtained system at the inelastic centroid, moments of area are canceled, and the final system becomes partially uncoupled as follows:

$$\begin{bmatrix} P \\ M_x \\ M_y \end{bmatrix} = \begin{bmatrix} EA & 0 & 0 \\ 0 & EI_x & EI_{xy} \\ 0 & EI_{xy} & EI_y \end{bmatrix} \begin{bmatrix} \varepsilon_o \\ \phi_x \\ \phi_y \end{bmatrix} \quad \textbf{(4-60)}$$

Either system of equations could be applied. Equation 4-59 is used if forces are to be tracked at the geometric centroid, while equation 4-60 is used if forces are to be tracked at the inelastic centroid.

Confined Concrete Compressive Strength Determination

Constitutive Model

The constitutive model developed by Willam and Warnke (1975) was chosen to determine the confined concrete compressive strength for rectangular columns in both Mander model and Lam and Teng model. Mander adopted the model and calibrated it using results from triaxial tests conducted by Schickert and Winkler (1977). The equations for the ultimate surface meridians are as follows:

$$T = 0.069232 - 0.661091\overline{\sigma_{oct}} - 0.04935(\overline{\sigma_{oct}})^2 \quad \textbf{(4-61)}$$

$$C = 0.122965 - 1.150502\overline{\sigma_{oct}} - 0.315545(\overline{\sigma_{oct}})^2 \quad \textbf{(4-62)}$$

On the other hand, Lam and Teng (2003) derived an empirical equation to determine the strength. ACI Committee 440 (2008) adopted this equation with the addition of a reduction factor ($\psi_f = 0.95$):

$$f_{cc} = f_c' + \psi_f 3.3 \kappa_a f_l \quad \textbf{(4-63)}$$

$$where\ \kappa_a = \frac{A_e}{A_c}\left(\frac{b}{h}\right)^2 \quad \textbf{(4-64)}$$

$f_l = equivalent\ circular\ section\ lateral\ pressure$

The equation above was extended to rectangular sections by implementing the shape factor (κ_a) and the equivalent circular section lateral pressure (f_l) as explained earlier. The problem with applying this approach for the analysis is that it causes a discontinuity in the combined model between having no FRP in the section and including FRP. The combined model utilizes Mander model when there is no FRP in the section. As stated earlier, Mander utilized the triaxial approach, which does not necessitate converting the section in an equivalent circular section. Upon including FRP, the combined model utilizes the Lam and Teng model if the confinement ratio exceeds 0.08, and at this time, using the equivalent circular section could

cause an unpredicted jump or drop in the ultimate strength. Additionally, as Lam and Teng model is based on analysis of a circular section, it is inherently limited to the C surface meridian ($\theta=60^o$) and assumes equal lateral stresses ($\sigma_2=\sigma_3=f_l$), which is not the case in non-square columns. This prevents the model from capturing all possible states of stress. In order to avoid these issues, it was decided to implement Willam and Warnke (1975) model for all cases in the combined model. In order to evaluate the applicability of this approach, the compressive strengths for two specimens were obtained using Lam and Teng empirical equation (2003) and Willam and Warnke model based on Schickert and Winkler data (1977). Specimen SC has a square section and was based on tests by Darby et al. (2011), while specimen CR has a rectangular section and was based on tests by Wang and Hsu (2007). The number of FRP plies was varied between zero and five. More details on these specimens can be found in Chapter 5. The results are plotted in Figure 4-7 and Figure 4-8.

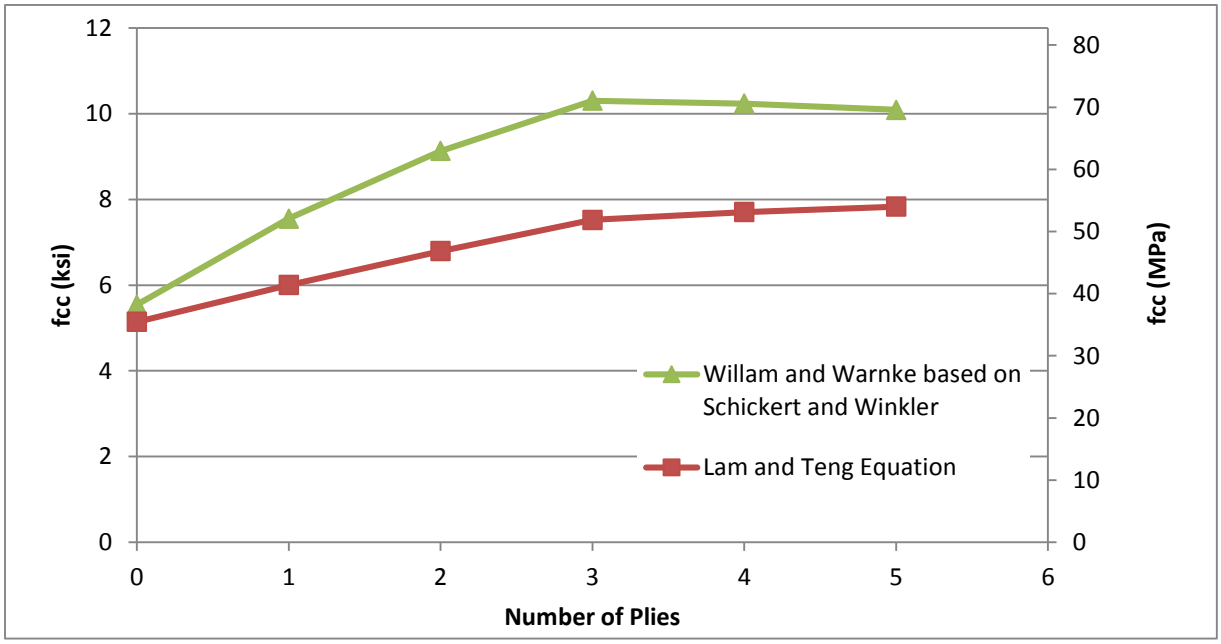

Figure 4-7: Compressive Strength vs. Number of Plies for Specimen SC.

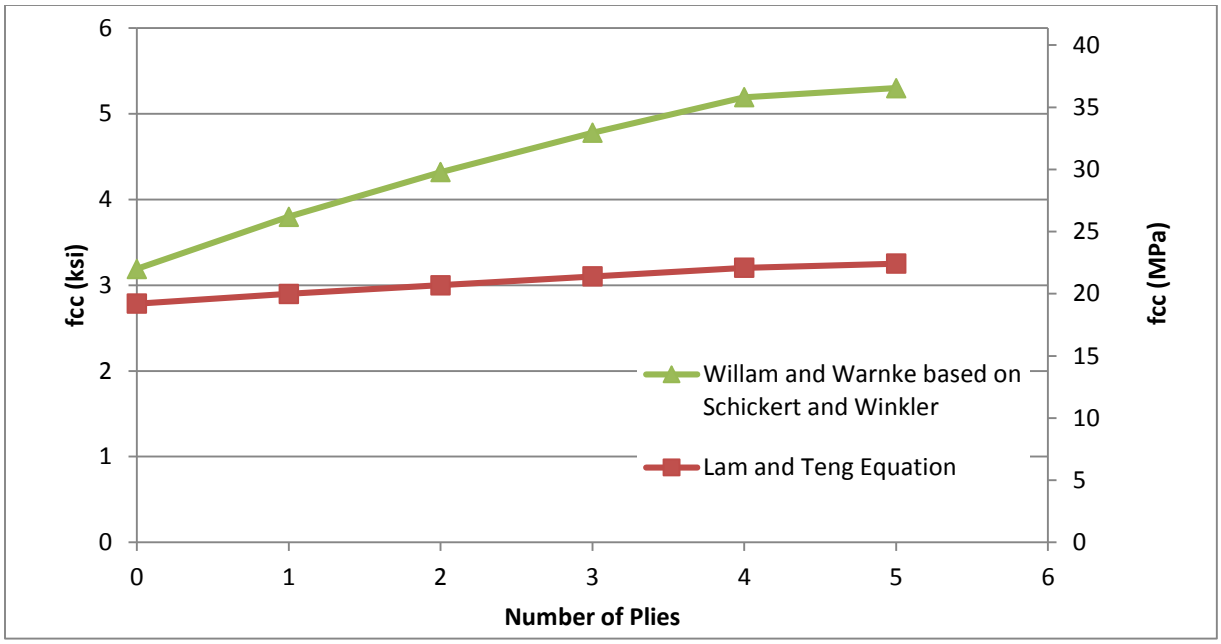

Figure 4-8: Compressive Strength vs. Number of Plies for Specimen CR.

From Figure 4-7 and Figure 4-8, it is observed that the triaxial constitutive model overestimated the confined compressive strength when compared with Lam and Teng model. In order to improve the results, the triaxial constitutive model was recalibrated using Lam and Teng's empirical equation for the square section case (SC). This is due to the fact that Lam and Teng empirical equation was heavily calibrated against experiments of columns wrapped with FRP. Next is an explanation of the procedure followed to recalibrate the model.

The model defines two ultimate strength meridian surfaces for concrete, compression (C) and tension (T). The failure surface is obtained using interpolation between the two ultimate meridian surfaces. Five control points are used to define the ultimate meridian surfaces, which are the uniaxial compressive strength (f'_{co}), the uniaxial tensile strength (f'_{t}), the biaxial compression point (f_{cb}), and the defined triaxial points on C and T curves. Calculation details for these points are provided by Elwi and Murray (1979) and are summarized in Table 4-1. Figure 4-9 illustrates the ultimate curves on the octahedral plane and provides the locations of the control points.

Table 4-1: Surface Meridians Control Points Summary.

Control Parameter	$\overline{\sigma_{oct}}$	$\overline{\tau_{oct}}$
f'_{co}	$-1/3$	$\sqrt{2}/3$
f'_{t}	$\alpha_t/3$	$\sqrt{2}\alpha_t/3$
f'_{cb}	$-2\alpha_c/3$	$\sqrt{2}\alpha_c/3$
Triaxial on C	User Defined	User Defined
Triaxial on T	User Defined	User Defined

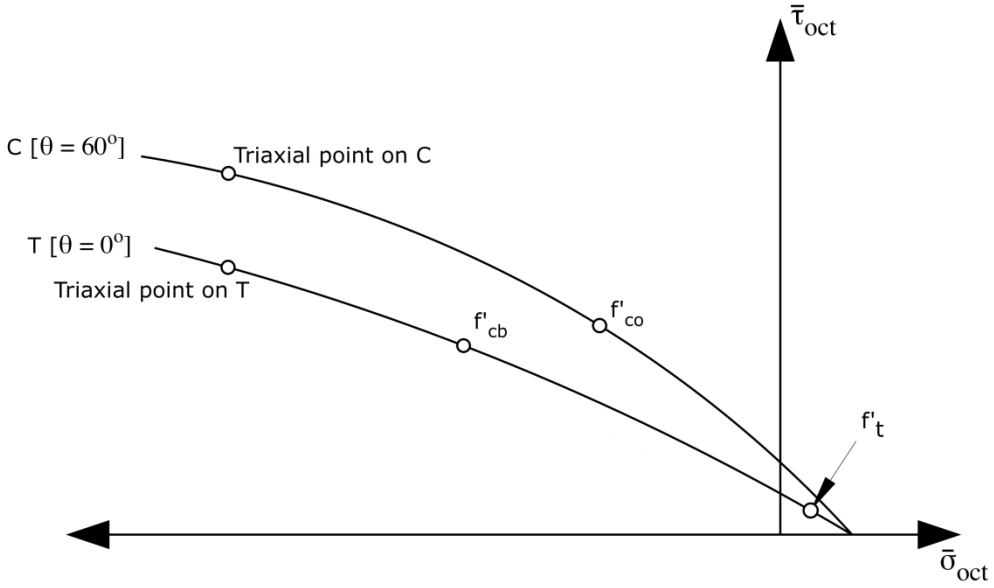

Figure 4-9: Ultimate Strength Curves C and T on the Octahedral Plane.

The present calibration was based on the experimental dataset KHR provided by Kupfer, Hilsdorf and Rüsch (1969).This dataset was chosen over Schickert and Winkler dataset (1977) because the specimens tested by Kupfer et al. had higher octahedral stresses, which is usually the case in FRP confined columns. FRP confinement effect is added to that of steel, which increases the octahedral stress. The properties and ultimate strength surfaces obtained by Elwi and Murray (1979) for this dataset are provided in Table 4-2.

Table 4-2: KHR data properties and ultimate surfaces.

$f'_{co} = 4.58\ ksi$	$\alpha_c = 1.15$	$\alpha_t = 0.091$
$T = 0.063046 - 0.662701\overline{\sigma_{oct}} - 0.049435(\overline{\sigma_{oct}})^2$		
$C = 0.11356 - 1.173709\overline{\sigma_{oct}} - 0.300524(\overline{\sigma_{oct}})^2$		

For recalibration, the user defined triaxial point was obtained from Lam and Teng ultimate strength equation. This point is located on the C curve, as Lam and Teng model utilizes the equivalent circular section concept in which the lateral pressures are equal. The obtained C strength surface is shown in Figure 4-10.

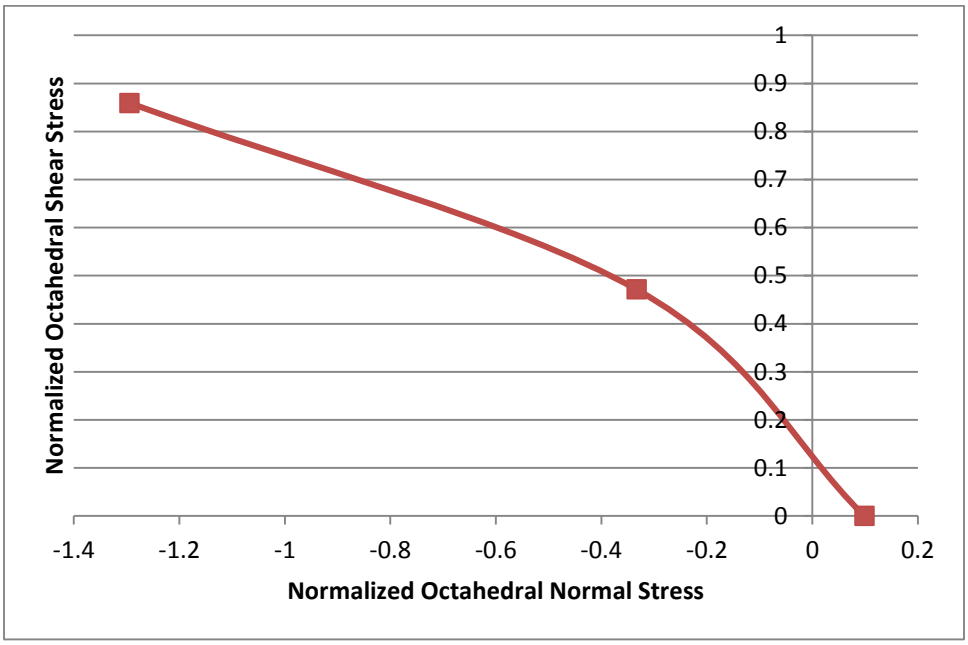

Figure 4-10: C Strength Surface Obtained Using Lam and Teng Equation.

It is observed in Figure 4-10 that the surface can be represented using a bilinear curve. As the final point on the T curve cannot be obtained directly from Lam and Teng's equation, the following procedure was formulated to obtain it:

1. Determine the intercept of the original KHR data T surface.
2. Fit the updated C surface based on the obtained T intercept, the uniaxial compressive strength and the triaxial point obtained from Lam and Teng's equation.
3. Calculate the new slope of the second branch of the C surface (m'_C)
4. Determine the new slope of the second branch of the T surface (m'_T) using the original KHR slope ratio (R) as follows:

$$m'_T = m'_C * R \quad \textbf{(4-65)}$$

$$where\ R = \frac{m_T}{m_C}$$

5. Fit the updated T surface based on the uniaxial tensile strength, biaxial compression point, and the obtained triaxial point on T.

6. Verify the new T intercept matches the original. If not, repeat steps 2-6 using the updated T intercept.

Based on the procedure above, the updated C and T surface equations were obtained. Figure 4-11 plots the following bilinear curves:

$$C = \begin{cases} 0.107795 - 1.09083\overline{\sigma_{oct}}\,, & for\ \overline{\sigma_{oct}} > -0.333 \\ 0.336883 - 0.40357\overline{\sigma_{oct}}\,, & for\ \overline{\sigma_{oct}} \leq -0.333 \end{cases} \quad \textbf{(4-66)}$$

$$T = \begin{cases} 0.061898 - 0.62637\overline{\sigma_{oct}}\,, & for\ \overline{\sigma_{oct}} > -0.767 \\ 0.229132 - 0.40824\overline{\sigma_{oct}}, & for\ \overline{\sigma_{oct}} \leq -0.767 \end{cases} \quad \textbf{(4-67)}$$

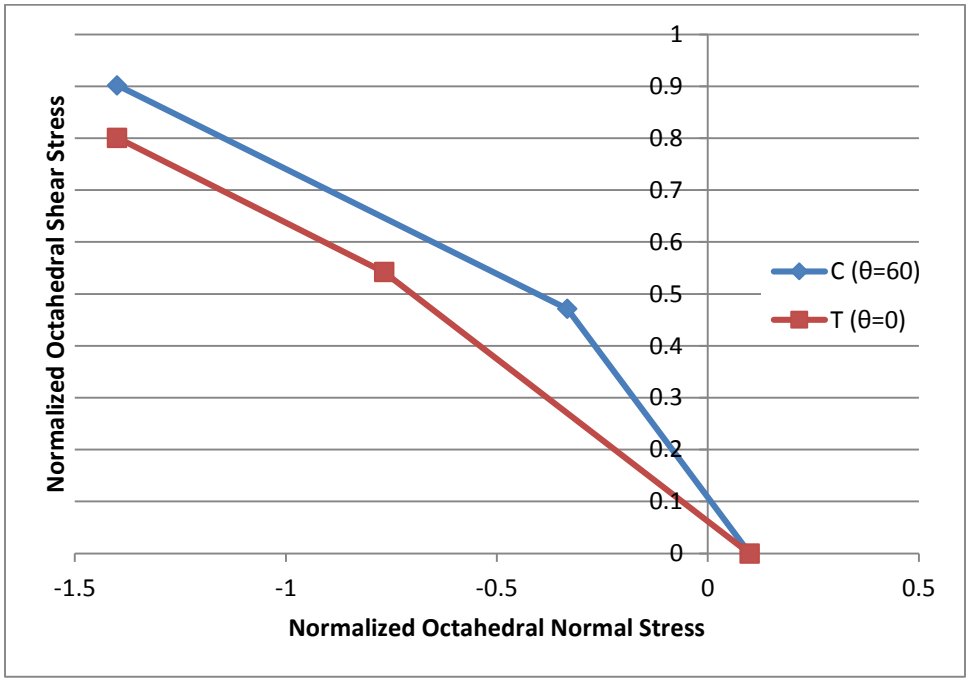

Figure 4-11: Recalibrated Ultimate Strength Surfaces C and T.

Next, using the updated model, the compressive strength was recalculated for the two specimens as shown in Figure 4-12 and Figure 4-13.

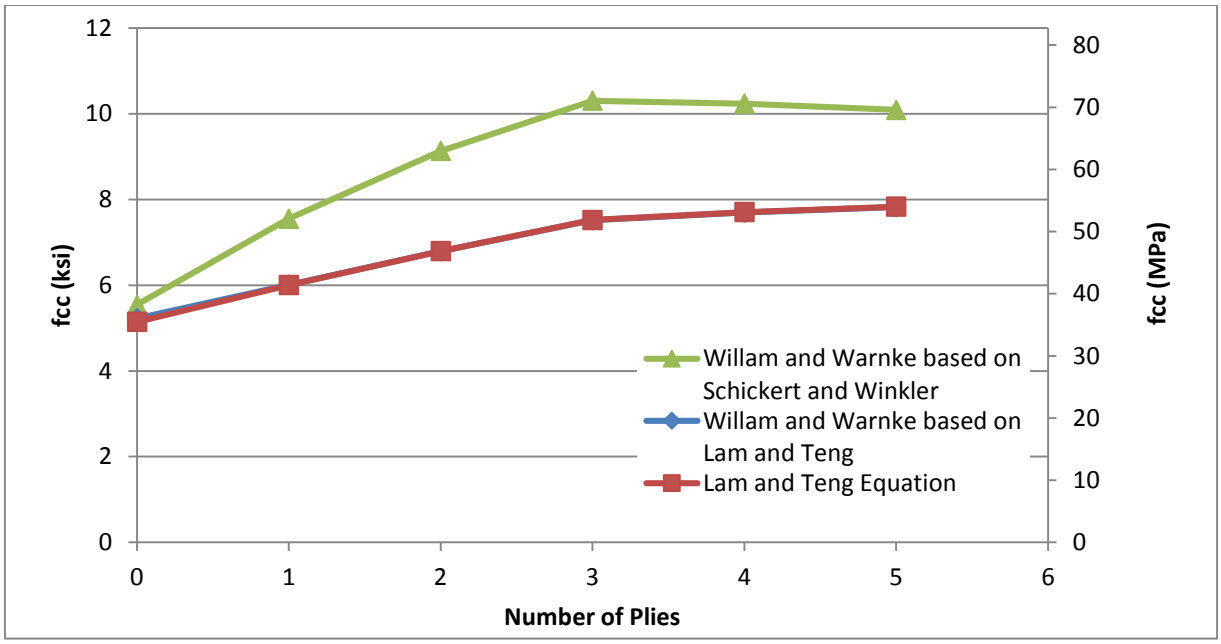

Figure 4-12: Updated Compressive Strength vs. Number of Plies for Specimen SC

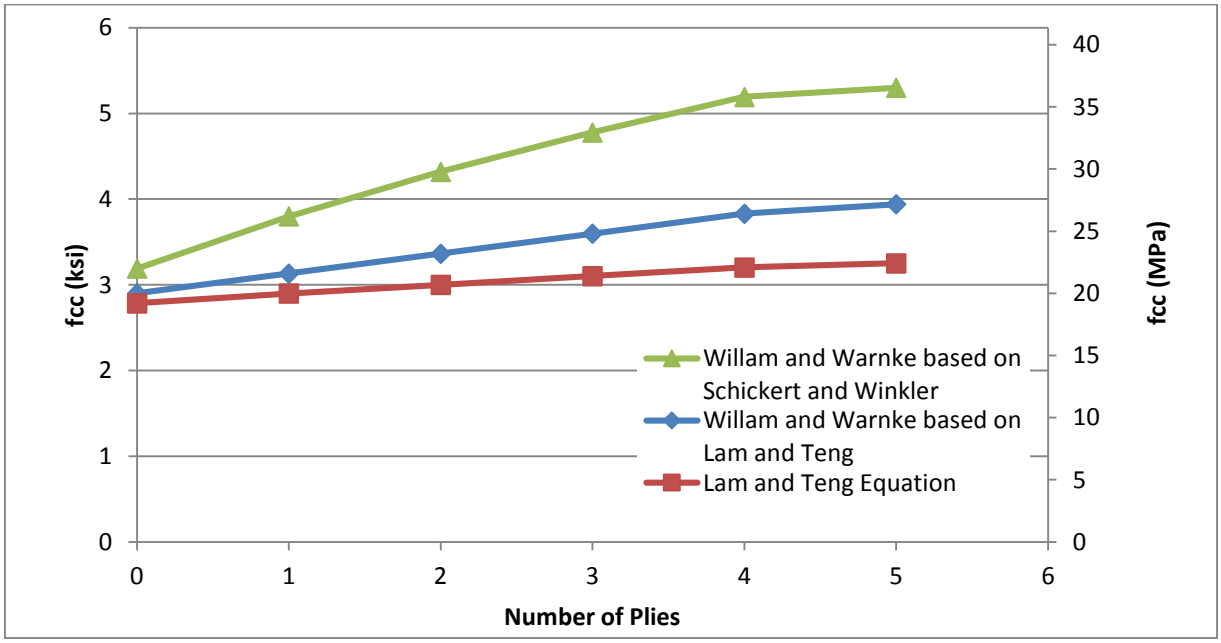

Figure 4-13: Updated Compressive Strength vs. Number of Plies for Specimen CR.

Figure 4-12 shows excellent matching between the updated constitutive model and Lam and Teng equation. This is expected as the calibration process was based on this section. Figure 4-13 shows an immense improvement in the new model when compared to the original. This new calibration was adopted in this study for use within the framework of the combined model.

Numerical Approach

For the purpose of this study, a numerical procedure was implemented to determine the confined concrete strength. The procedure is summarized in the following steps:

1. Determine f'_{lx} and f'_{ly} as described earlier. The values are then are converted to negative values that represent the major and intermediate principal stresses (σ_1, σ_2) so that $\sigma_{1>}\ \sigma_{2.}$
2. Assume an initial value for the confined compressive strength (f_{cc}), which represents the minor principal stress (σ_3).
3. Calculate the octahedral normal stress (σ_{oct}), octahedral shear stress (τ_{oct}), and the lode angle (θ) as follows:

$$\sigma_{oct} = \frac{1}{3}(\sigma_1 + \sigma_2 + \sigma_3) \quad \textbf{(4-68)}$$

$$\tau_{oct} = \frac{1}{3}[(\sigma_1 - \sigma_2)^2 + (\sigma_2 - \sigma_3)^2 + (\sigma_1 - \sigma_3)^2]^{\frac{1}{2}} \quad \textbf{(4-69)}$$

$$\cos\theta = \frac{\sigma_1 - \sigma_{oct}}{\sqrt{2}\tau_{oct}} \quad \textbf{(4-70)}$$

4. Determine the ultimate stress meridian surfaces, T (θ=0^o) and C (θ=60^o) using the equations for the bilinear curve derived in the previous section://DOLATER REFORMAT

$If\ |\overline{\sigma_{oct}}| < 0.333$:

$$C = 0.107795 - 1.09083\overline{\sigma_{oct}} \quad \textbf{(4-71)}$$

$Else$:

$$C = 0.336883 - 0.40357\overline{\sigma_{oct}} \quad \textbf{(4-72)}$$

$If\ |\overline{\sigma_{oct}}| < 0.767$:

$$T = 0.061898 - 0.62637\overline{\sigma_{oct}} \quad \textbf{(4-73)}$$

$Else$:

$$T = 0.229132 - 0.40824\overline{\sigma_{oct}} \quad \textbf{(4-74)}$$

$where\ \overline{\sigma_{oct}} = \sigma_{oct}/f'_c$

5. Determine the octahedral shear stress (τ_{oct}) using the interpolation function obtained by Willam and Warnke (1975):

$$\overline{\tau_{oct}} = C\frac{0.5D/\cos\theta + (2T - C)(D + 5T^2 - 4TC)^{\frac{1}{2}}}{D + (2T - C)^2} \quad \textbf{(4-75)}$$

$$D = 4(C^2 - T^2)\cos^2\theta \quad \textbf{(4-76)}$$

$$\tau_{oct} = f'_c\overline{\tau_{oct}} \quad \textbf{(4-77)}$$

6. Recalculate the confined compressive strength (f_{cc}) as follows:

$$f_{cc} = \sigma_3 = \frac{\sigma_1 + \sigma_2}{2} - \sqrt{4.5\tau_{oct}^2 - 0.75(\sigma_1 - \sigma_2)^2} \quad \textbf{(4-78)}$$

7. If the value obtained at the end matches that of the assumed initial value then convergence is achieved. Otherwise, the obtained value is set as the initial value and the process is repeated until convergence is attained.

Chapter 5 - Results and Discussion

The aforementioned procedure was implemented in KDOT Column Expert software, which was then used to generate interaction diagrams. The following two sections present the results obtained from the program for multiple cases. In the first section, experimental points found in the literature were used to compare with and validate the proposed approach. Then, in the second section, parametric studies were conducted and the results obtained are presented in this chapter.

Comparison with Experiments

Rocca et al. (2009) assembled a database with results for FRP-confined reinforced concrete columns obtained from the literature. From this database, results obtained by Bousias et al. (2004), Memon and Sheikh (2005), and Harajli and Rteil (2004) were used to verify the proposed approach. Additionally, specimens tested by Darby et al. (2011) and Wang and Hsu (2007) were also included in the comparison. The specifications for these specimens are provided in Table 5-1 and Table 5-2 below. It is noted that Wang and Hsu's rectangular specimens (CR) included an additional steel leg connecting the middle bars. Also, specimens SC3u and SC3 tested by Darby et al. had pairs of 25 mm (0.98 in) diameter bars. As it is not possible to input that to the program, they were replaced in the analysis with single bars that have an equivalent area of 1.52 in^2. Finally, in cases where some properties were not provided by the authors, reasonable assumptions were made for these values such as minimum lateral reinforcement (#3 bars at maximum spacing permitted by ACI 318-11 (2011)), minimum radius of curvature (0.5 in), and lateral steel properties (E=29000 ksi, f_y=60 ksi). The notations used for the specifications are provided in Table 5-3.

Table 5-1: Specimens' Geometric and FRP Properties.

Source	Code	FRP	b	h	cc	r_c	E_f	ε_{fu}	t_f	n	f_{lf}/f'_c	P_{max}	M_{max}
Units (if applicable)			in	in	in	in	ksi	%	in	ply		kip	kip.ft
Bousias et al. (2004)	BO1-a	None	9.84	19.69	2	0.52	-	-	-	0	-	193.95	224.35
	BO2-a	CFRP	9.84	19.69	2	0.52	33350	1.5	0.005	2	0.104	186.75	264.20
	BO3-a	CFRP	9.84	19.69	2	0.52	33350	1.5	0.005	5	0.263	194.63	279.70
	BO4-a	GFRP	9.84	19.69	2	0.52	10150	3.1	0.007	5	0.207	193.05	240.59
	BO1-b	None	19.69	9.84	2	0.52	-	-	-	0	-	189.68	81.18
	BO2-b	CFRP	19.69	9.84	2	0.52	33350	1.5	0.005	2	0.104	186.75	82.66
	BO3-b	CFRP	19.69	9.84	2	0.52	33350	1.5	0.005	5	0.263	194.63	90.04
	BO4-b	GFRP	19.69	9.84	2	0.52	10150	3.1	0.007	5	0.207	193.05	88.56
Harajli and Rteil (2004)	HR1-a	None	5.91	11.81	1	0.52	-	-	-	0	-	44.10	43.54
	HR2-a	CFRP	5.91	11.81	1	0.52	33350	1.5	0.005	1	0.074	44.10	47.97
	HR1-b	None	5.91	11.81	1	0.52	-	-	-	0	-	51.98	64.94
	HR2-b	CFRP	5.91	11.81	1	0.52	33350	1.5	0.005	1	0.074	51.98	69.37
Memon and Sheikh (2005)	MS1	None	12.01	12.01	1	0.64	-	-	-	0	-	552.15	143.91
	MS2	GFRP	12.01	12.01	1	0.64	2864.33	2.28	0.049	2	0.072	326.03	184.50
	MS3	GFRP	12.01	12.01	1	0.64	2864.33	2.28	0.049	4	0.143	555.08	185.98
	MS4	GFRP	12.01	12.01	1	0.64	2864.33	2.28	0.049	2	0.071	560.93	171.22
	MS5	GFRP	12.01	12.01	1	0.64	2864.33	2.28	0.049	1	0.035	332.78	173.43
	MS6	GFRP	12.01	12.01	1	0.64	2864.33	2.28	0.049	3	0.104	569.70	211.07
Wang and Hsu (2007)	CS0	GFRP	11.81	11.81	1.18	1.18	-	-	-	0	-	478.58	0
	CS2	GFRP	11.81	11.81	1.18	1.18	2972.5	2	0.05	2	0.151	568.13	0
	CS6	GFRP	11.81	11.81	1.18	1.18	2972.5	2	0.05	6	0.454	905.63	0
	CR0	GFRP	11.81	17.72	1.18	1.18	-	-	-	0	-	735.30	0
	CR2	GFRP	11.81	17.72	1.18	1.18	2972.5	2	0.05	2	0.119	809.55	0
	CR6	GFRP	11.81	17.72	1.18	1.18	2972.5	2	0.05	6	0.356	1011.15	0
Darby et al. (2011)	SC1u	None	5.91	5.91	1	0.79	-	-	-	0	-	172.35	0.06
	SC1	CFRP	5.91	5.91	1	0.79	31030	1.45	0.006	2	0.157	211.28	4.02

Source	Code	FRP	b	h	cc	r_c	E_f	ε_{fu}	t_f	n	f_{lf}/f'_c	P_{max}	M_{max}
	SC2u	None	11.81	11.81	1	1.57	-	-	-	0	-	547.43	3.23
	SC2	CFRP	11.81	11.81	1	1.57	31030	1.45	0.006	4	0.219	813.83	22.66
	SC3u	None	17.72	17.72	1	2.36	-	-	-	0	-	2050.20	16.16
	SC3	CFRP	17.72	17.72	1	2.36	31030	1.45	0.006	6	0.219	1656.90	40.77

Table 5-2: Specimens' Concrete and Steel Properties.

Source	Code	f'_c	f_y	f_{yt}	E_l	E_t	Bars in x	Bars in y	d_l	A_l	d_t	A_t	s'
Units (If applicable)		ksi	ksi	ksi	ksi	ksi			in	in^2	in	in^2	in
Bousias et al. (2004)	BO1-a	2.65	81.2	41.47	29000	29000	2	2	0.71	0.394	0.31	0.078	7.87
	BO2-a	2.62	81.2	41.47	29000	29000	2	2	0.71	0.394	0.31	0.078	7.87
	BO3-a	2.60	81.2	41.47	29000	29000	2	2	0.71	0.394	0.31	0.078	7.87
	BO4-a	2.71	81.2	41.47	29000	29000	2	2	0.71	0.394	0.31	0.078	7.87
	BO1-b	2.60	81.2	41.47	29000	29000	2	2	0.71	0.394	0.31	0.078	7.87
	BO2-b	2.62	81.2	41.47	29000	29000	2	2	0.71	0.394	0.31	0.078	7.87
	BO3-b	2.60	81.2	41.47	29000	29000	2	2	0.71	0.394	0.31	0.078	7.87
	BO4-b	2.71	81.2	41.47	29000	29000	2	2	0.71	0.394	0.31	0.078	7.87
Harajli and Rteil (2004)	HR1-a	2.94	77.43	60	29000	29000	2	3	0.50	0.200	0.31	0.078	5.91
	HR2-a	3.06	77.43	60	29000	29000	2	3	0.50	0.200	0.31	0.078	5.91
	HR1-b	2.94	81.93	60	29000	29000	2	3	0.63	0.310	0.31	0.078	5.91
	HR2-b	3.06	81.93	60	29000	29000	2	3	0.63	0.310	0.31	0.078	5.91
Memon and Sheikh (2005)	MS1	6.15	67.43	66.27	29314.65	30120.85	3	3	0.77	0.465	0.38	0.110	11.81
	MS2	6.16	67.43	66.27	29314.65	30120.85	3	3	0.77	0.465	0.38	0.110	11.81
	MS3	6.19	67.43	66.27	29314.65	30120.85	3	3	0.77	0.465	0.38	0.110	11.81
	MS4	6.28	67.43	66.27	29314.65	30120.85	3	3	0.77	0.465	0.38	0.110	11.81
	MS5	6.34	67.43	66.27	29314.65	30120.85	3	3	0.77	0.465	0.38	0.110	11.81
	MS6	6.41	67.43	66.27	29314.65	30120.85	3	3	0.77	0.465	0.38	0.110	11.81
Wang and Hsu (2007)	CS0	2.76	63.66	52.93	29000	29435	2	2	0.79	0.487	0.39	0.122	7.09

Source	Code	f'_c	f_y	f_{yt}	E_l	E_t	Bars in x	Bars in y	d_l	A_l	d_t	A_t	s’
	CS2	2.76	63.66	52.93	29000	29435	2	2	0.79	0.487	0.39	0.122	7.09
	CS6	2.76	63.66	52.93	29000	29435	2	2	0.79	0.487	0.39	0.122	7.09
	CR0	2.76	63.66	52.93	29000	29435	2	3	0.79	0.487	0.39	0.122	7.09
	CR2	2.76	63.66	52.93	29000	29435	2	3	0.79	0.487	0.39	0.122	7.09
	CR6	2.76	63.66	52.93	29000	29435	2	3	0.79	0.487	0.39	0.122	7.09
Darby et al. (2011)	SC1u	5.66	79.75	60	29000	29000	2	2	0.47	0.175	0.38	0.110	5
	SC1	5.08	79.75	60	29000	29000	2	2	0.47	0.175	0.38	0.110	5
	SC2u	3.63	79.75	60	29000	29000	2	2	0.98	0.761	0.38	0.110	11
	SC2	3.63	79.75	60	29000	29000	2	2	0.98	0.761	0.38	0.110	11
	SC3u	6.53	79.75	60	29000	29000	2	2	1.39	1.522	0.38	0.110	12
	SC3	3.63	79.75	60	29000	29000	2	2	1.39	1.522	0.38	0.110	12

Table 5-3: Notations for Specifications.

Symbol	Description	Symbol	Description
b	Section width	f_y	Longitudinal steel yield stress
h	Section height	f'_c	Concrete compressive strength
cc	Clear cover	f_{yt}	Transverse steel yield stress
r_c	Radius of rounded corners	E_l	Longitudinal steel modulus of elasticity
E_f	FRP modulus of elasticity	E_t	Transverse steel modulus of elasticity
ε_{fu}	FRP rupture strain	d_l	Longitudinal bar diameter
t_f	FRP ply thickness	A_l	Longitudinal bar area
n	Number of FRP plies	d_t	Transverse bar diameter
f_{lf}/f'_c	Confinement ratio	A_t	Transverse bar area
P_{max}	Maximum applied axial load	s’	Clear tie spacing
M_{max}	Maximum applied bending moment		

In the next part, for each specimen, a sketch of the cross-section will be shown, and the interaction diagram obtained from the proposed approach using KDOT Column Expert will be provided. The experimental results will be shown as a point on the interaction diagram.

Memon and Sheikh Specimens (2005)

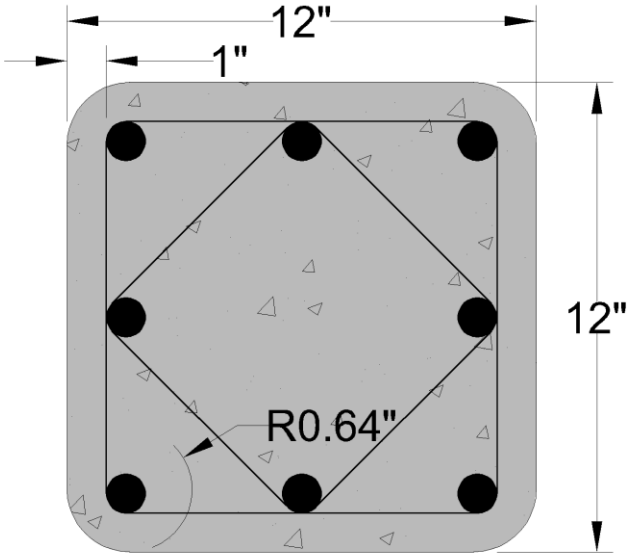

Figure 5-1: Cross-section of MS Specimens by Memon and Sheikh (2005).

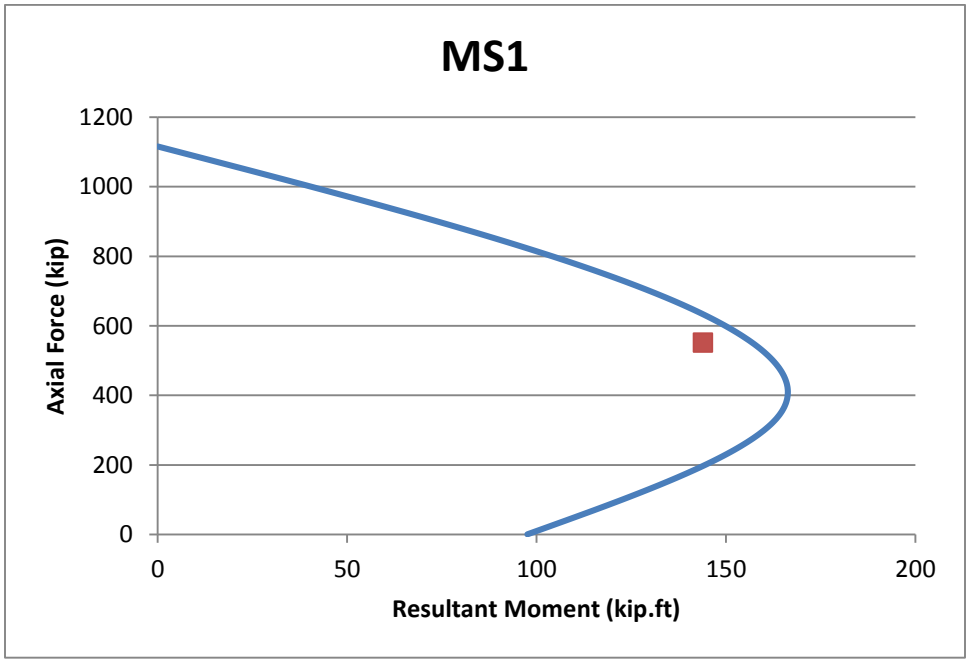

Figure 5-2: Interaction Diagram for Specimen MS1.

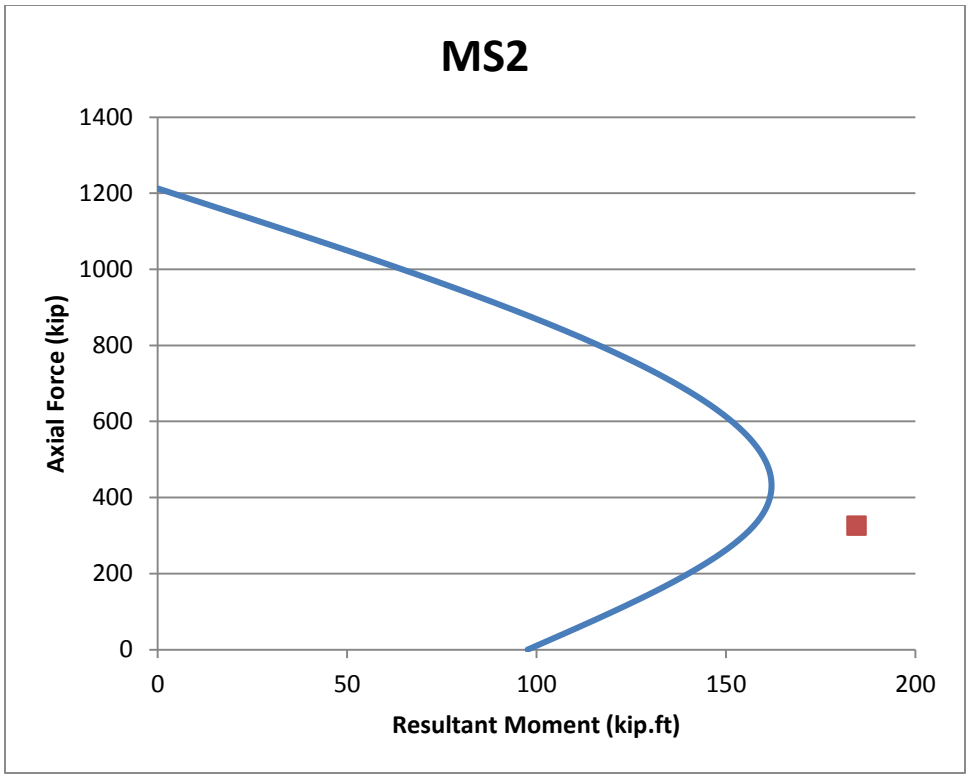

Figure 5-3: Interaction Diagram for Specimen MS2.

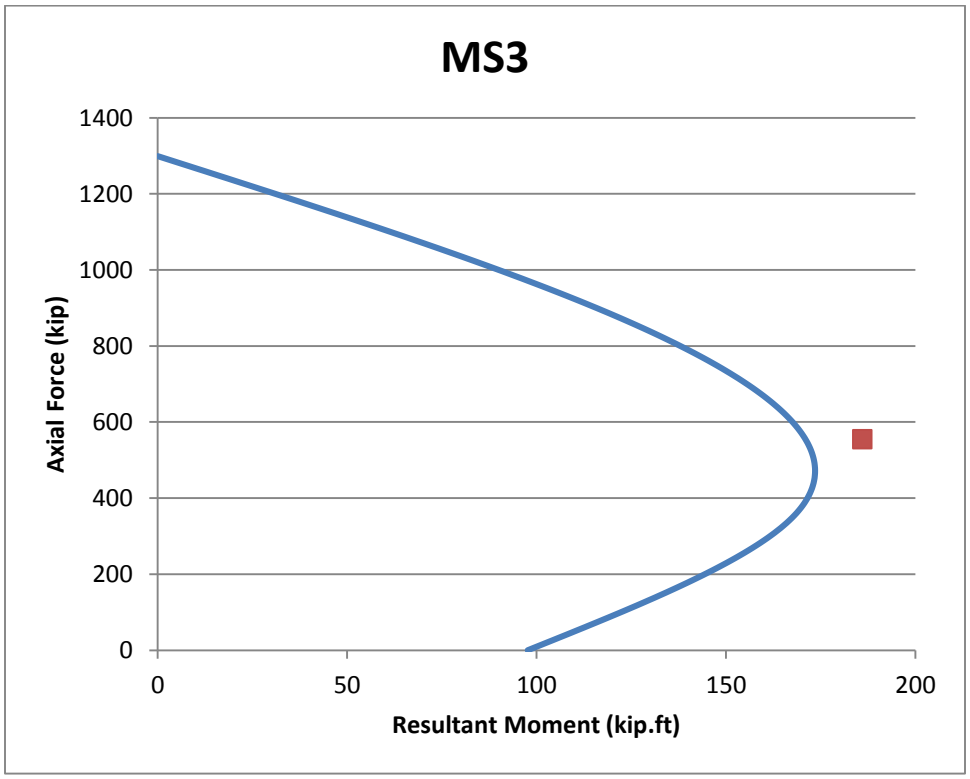

Figure 5-4: Interaction Diagram for Specimen MS3.

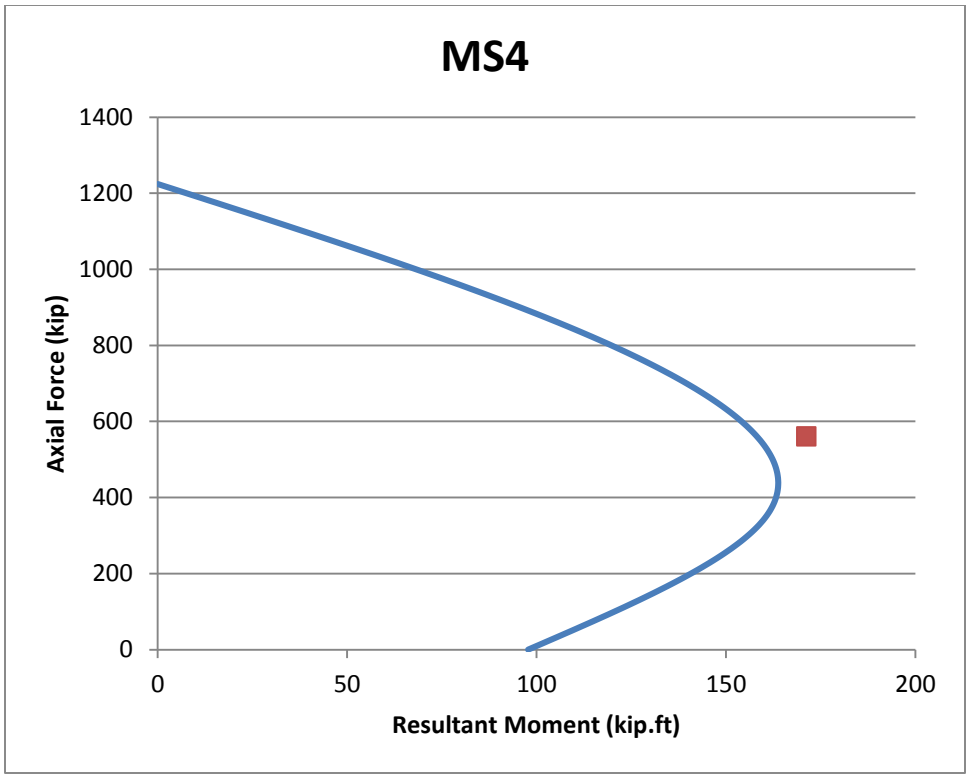

Figure 5-5: Interaction Diagram for Specimen MS4.

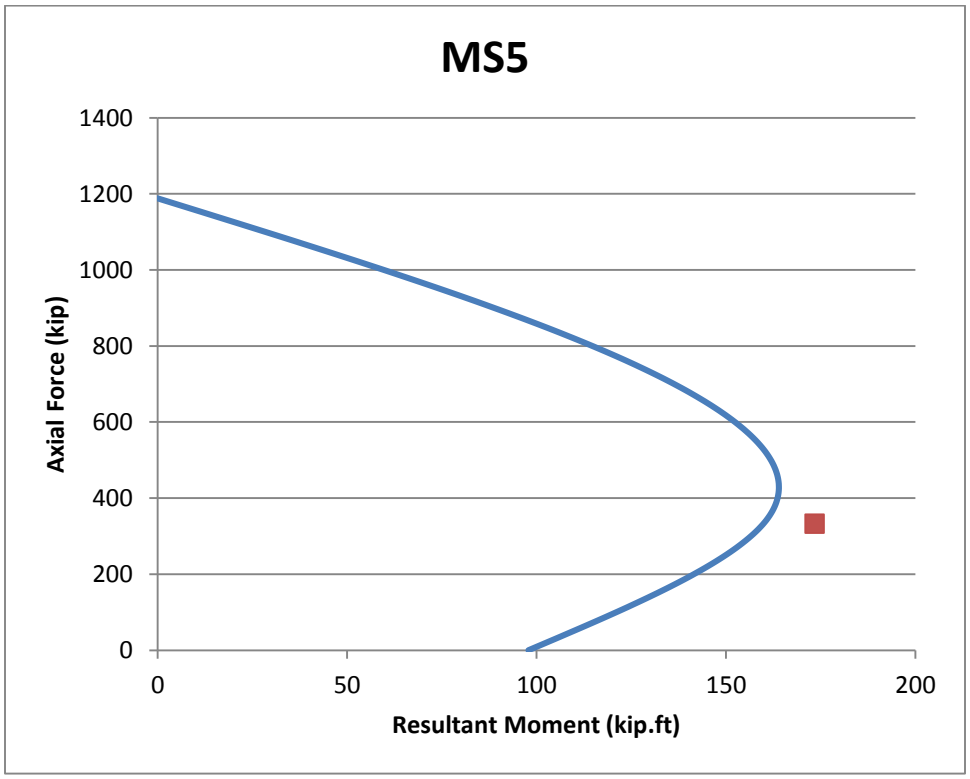

Figure 5-6: Interaction Diagram for Specimen MS5.

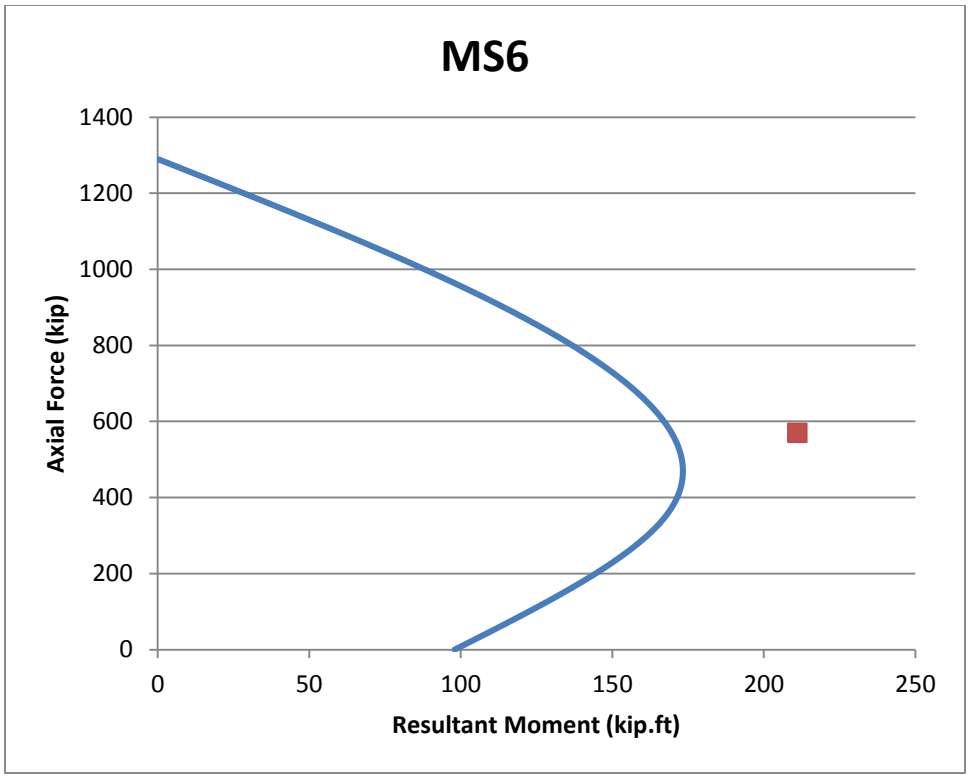

Figure 5-7: Interaction Diagram for Specimen MS6.

Figure 5-2-Figure 5-7 show the interaction diagrams obtained for specimens tested by Memon and Sheikh (2005). These specimens fell in the balanced failure region of the interaction diagram. The capacity was overestimated only in the case of MS1. For the remaining cases, the program provided conservative results. Overall, the results obtained showed good agreement and the proposed approach provided conservative estimates for the capacity.

Bousias et al. Specimens (2004)

Figure 5-8: Cross-section of B0x-a Specimens by Bousias et al. (2004).

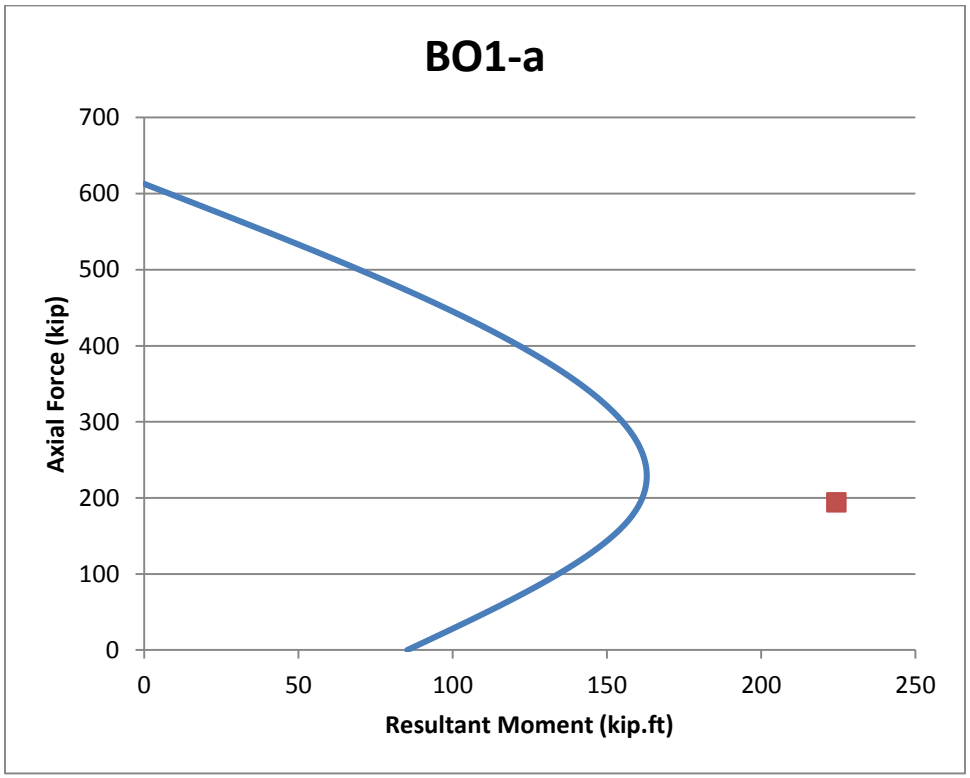

Figure 5-9: Interaction Diagram for Specimen B01-a.

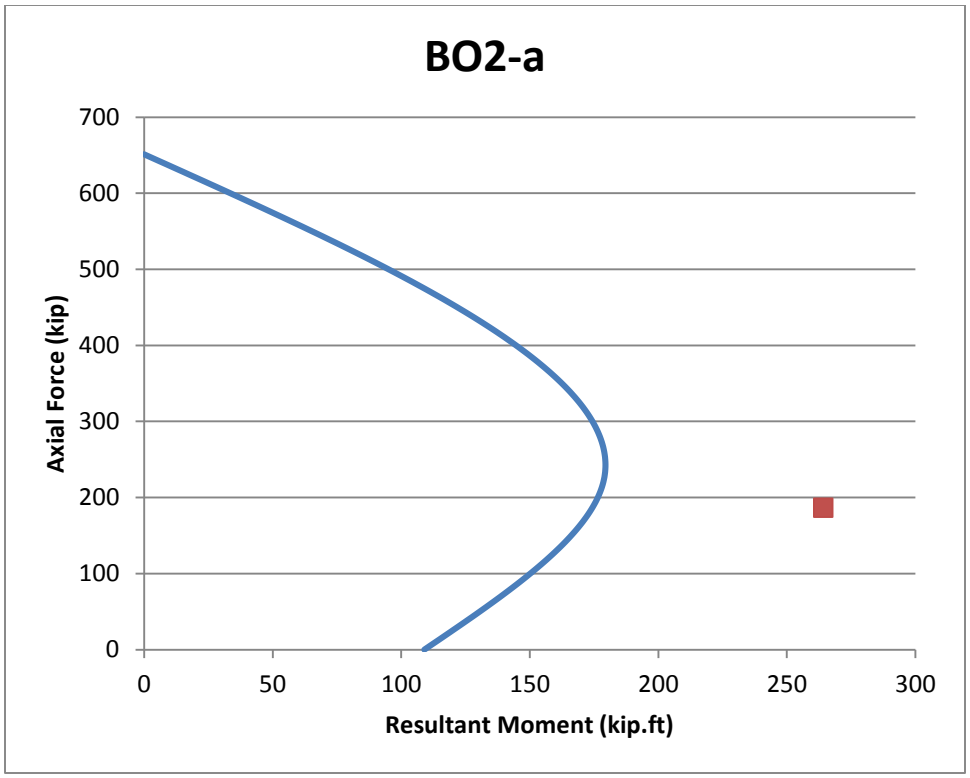

Figure 5-10: Interaction Diagram for Specimen B02-a.

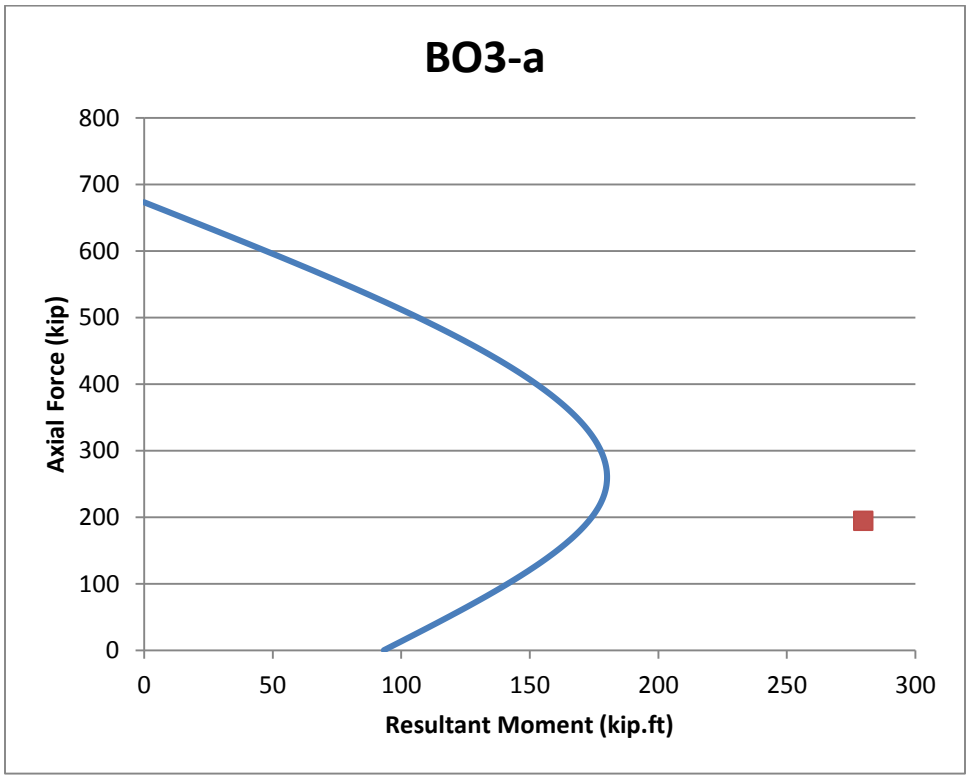

Figure 5-11: Interaction Diagram for Specimen B03-a.

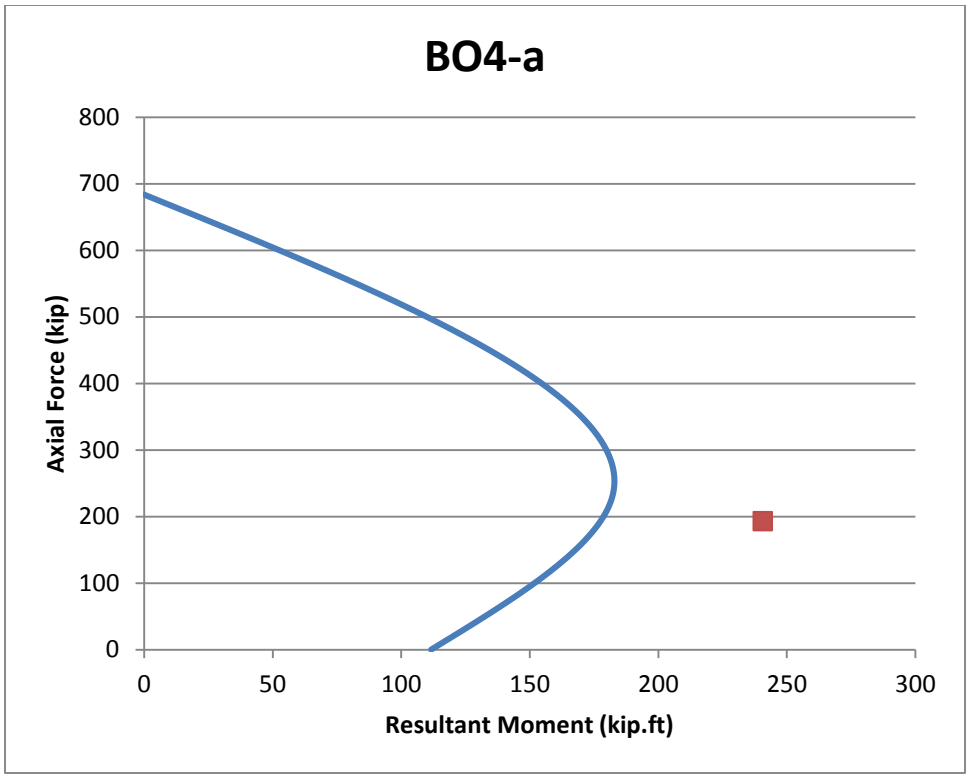

Figure 5-12: Interaction Diagram for Specimen B04-a.

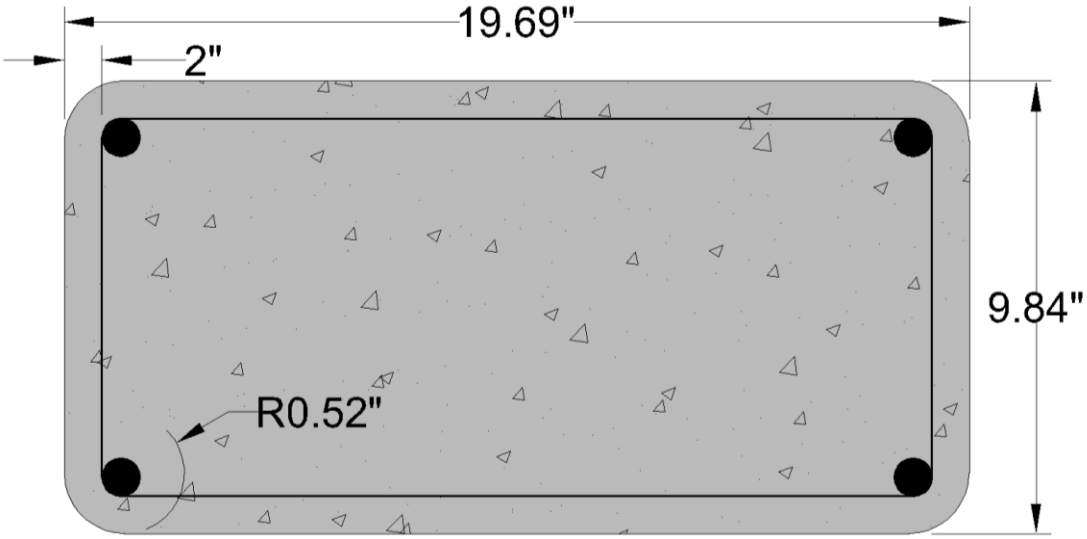

Figure 5-13: Cross-section of B0x-b Specimens by Bousias et al. (2004).

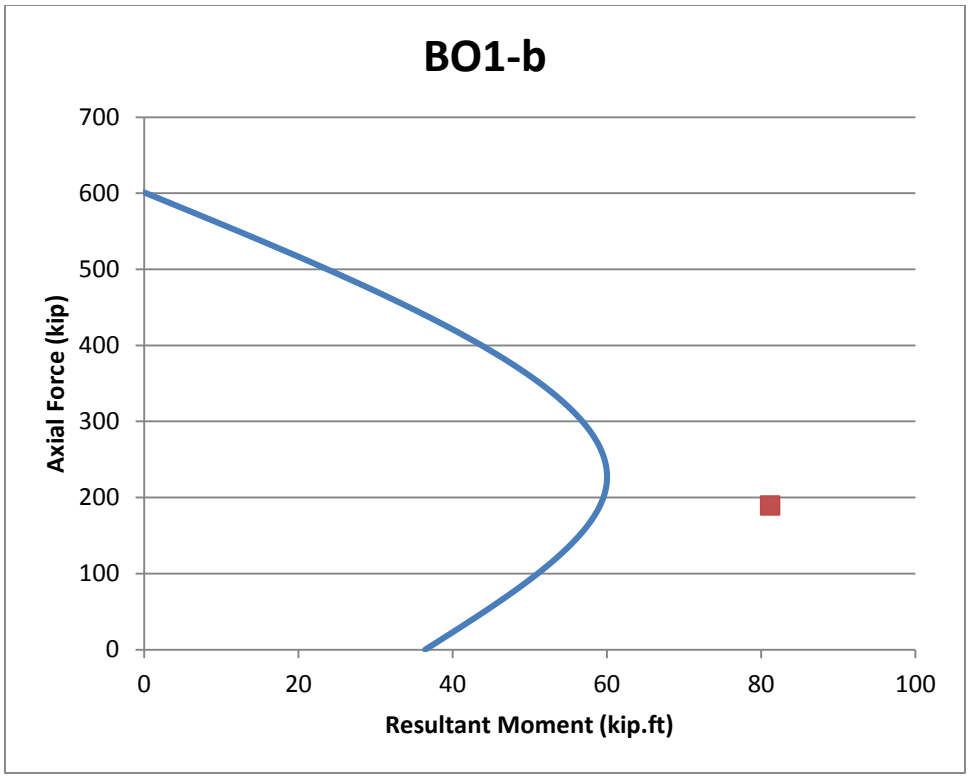

Figure 5-14: Interaction Diagram for Specimen B01-b.

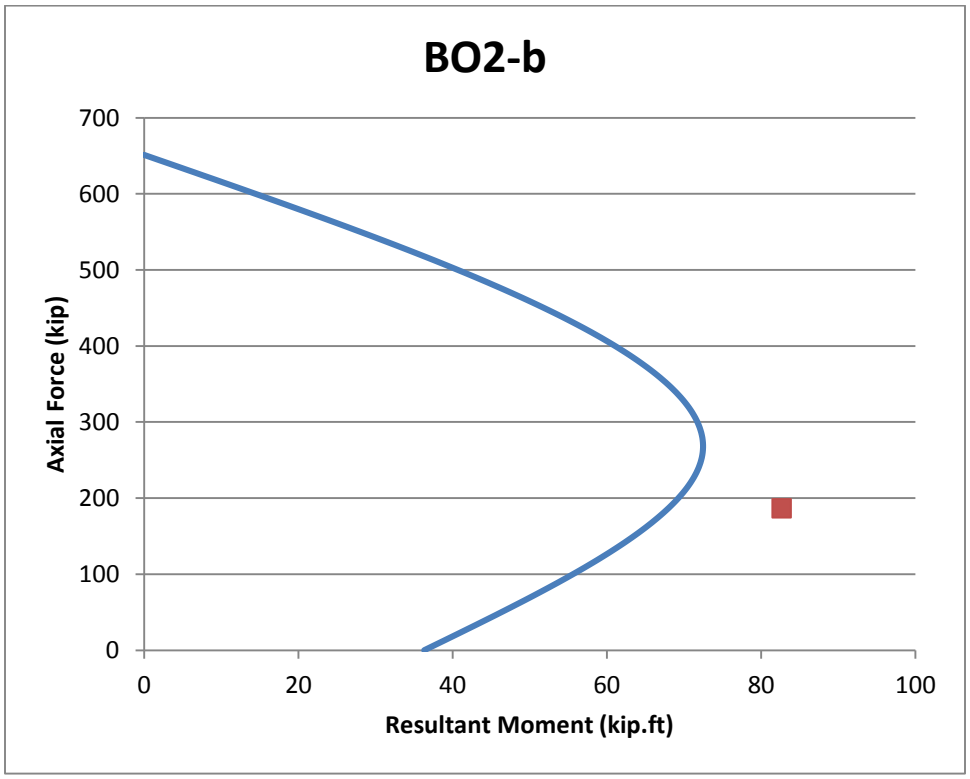

Figure 5-15: Interaction Diagram for Specimen B02-b.

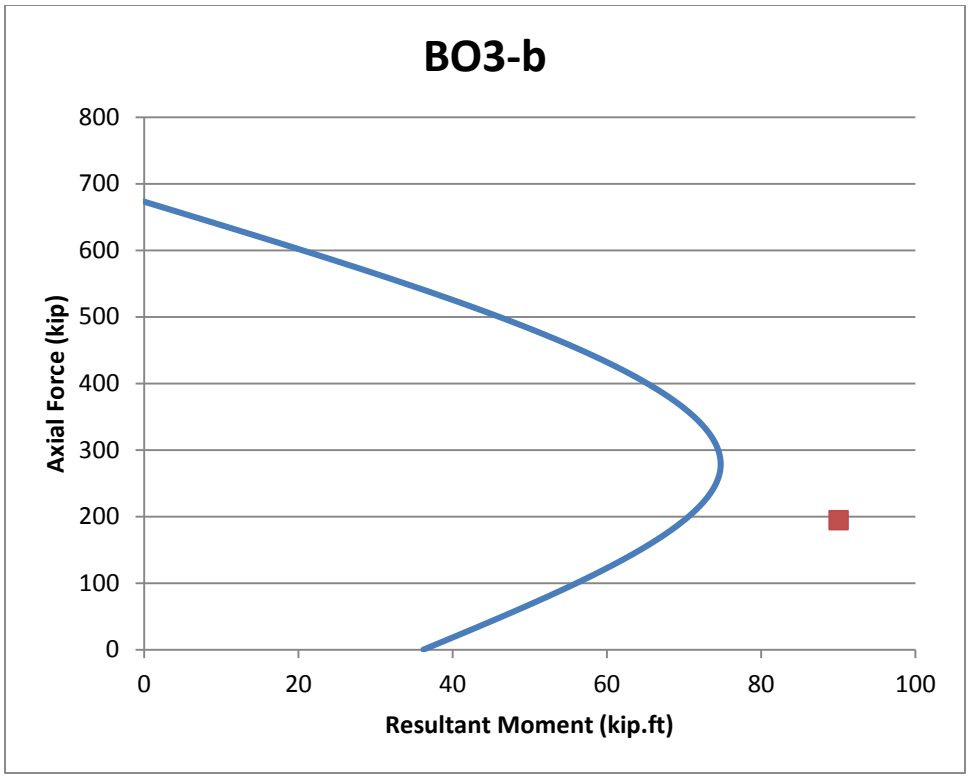

Figure 5-16: Interaction Diagram for Specimen B03-b.

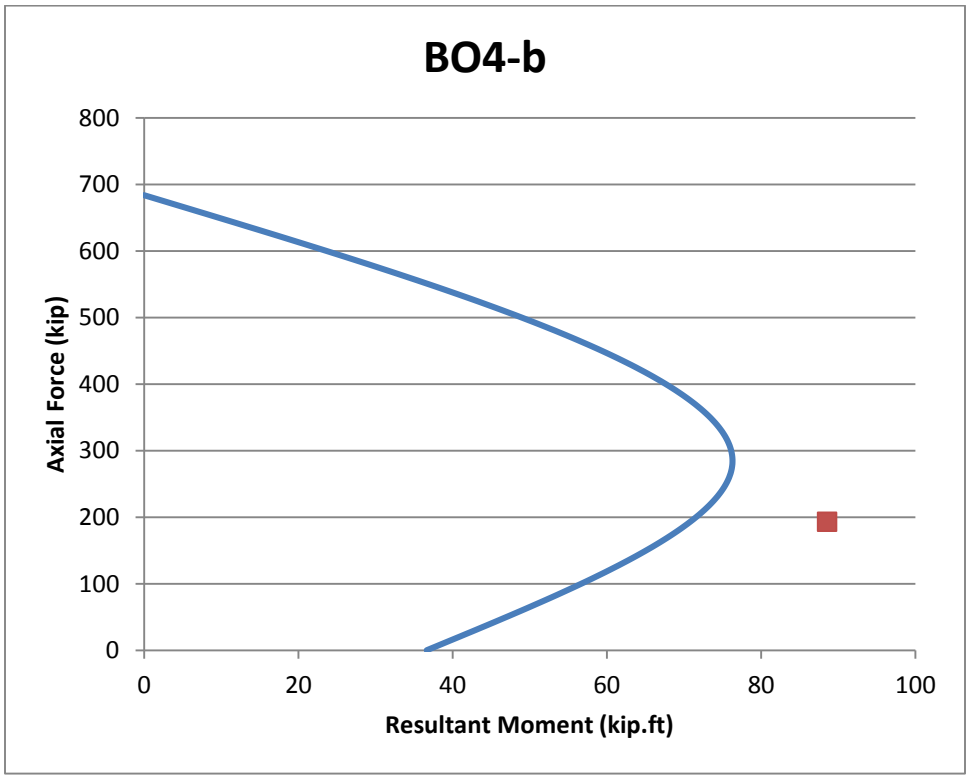

Figure 5-17: Interaction Diagram for Specimen B04-b.

Figure 5-9 to Figure 5-17 show the interactions diagrams obtained for specimens tested by Bousias et al (2004). These specimens were tested about both the strong (B0x-a) and weak (B0x-b) axes. As the program does not allow the width to exceed the height, the Alpha angle (α) between the resultant moment and the moment about the x-axis was taken to be 90^{o} for B0X-b specimens. All specimens fell in the balanced failure region of the interaction diagram. The program provided conservative results for all tested cases. Overall, the results obtained showed good agreement and the proposed approach provided conservative estimates for the capacity.

Harajli and Rteil Specimens (2004)

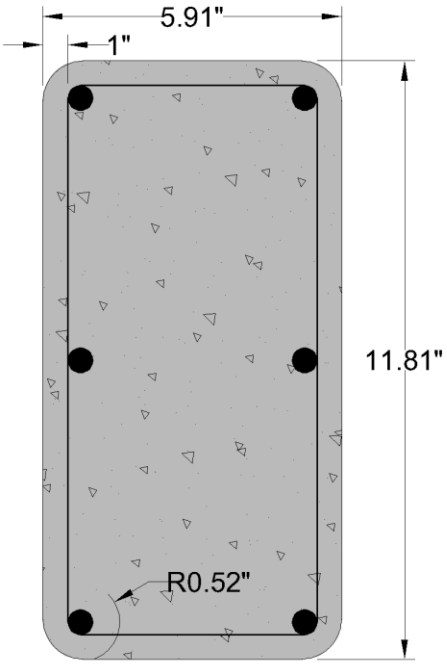

Figure 5-18: Cross-section of HRx-a Specimens by Harajli and Rteil (2004).

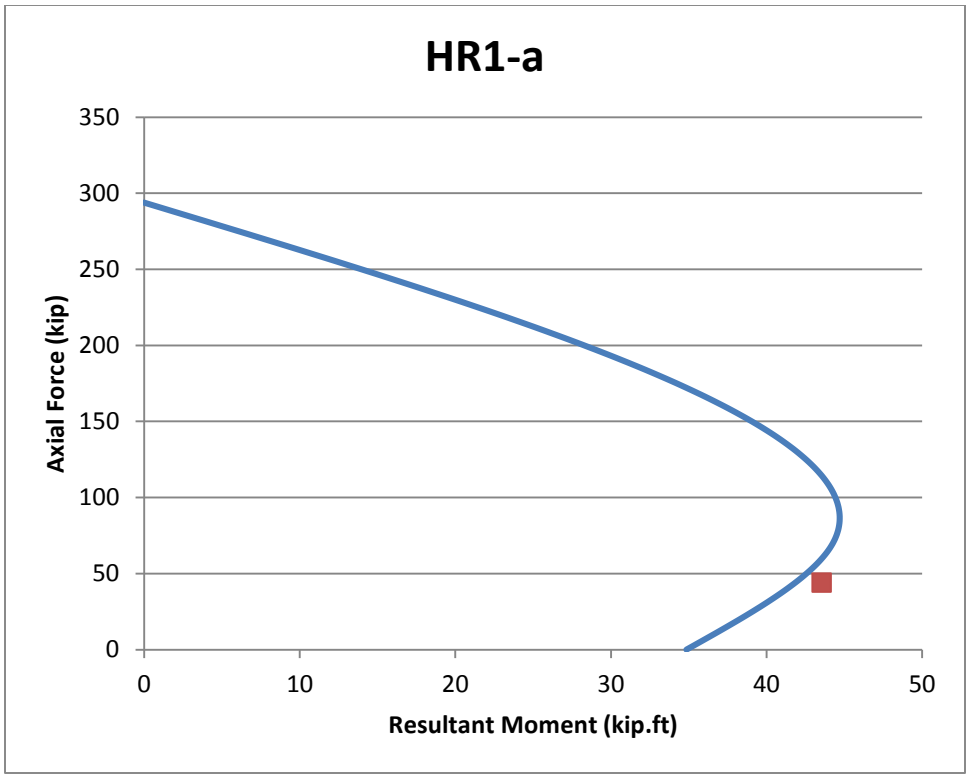

Figure 5-19: Interaction Diagram for Specimen HR1-a.

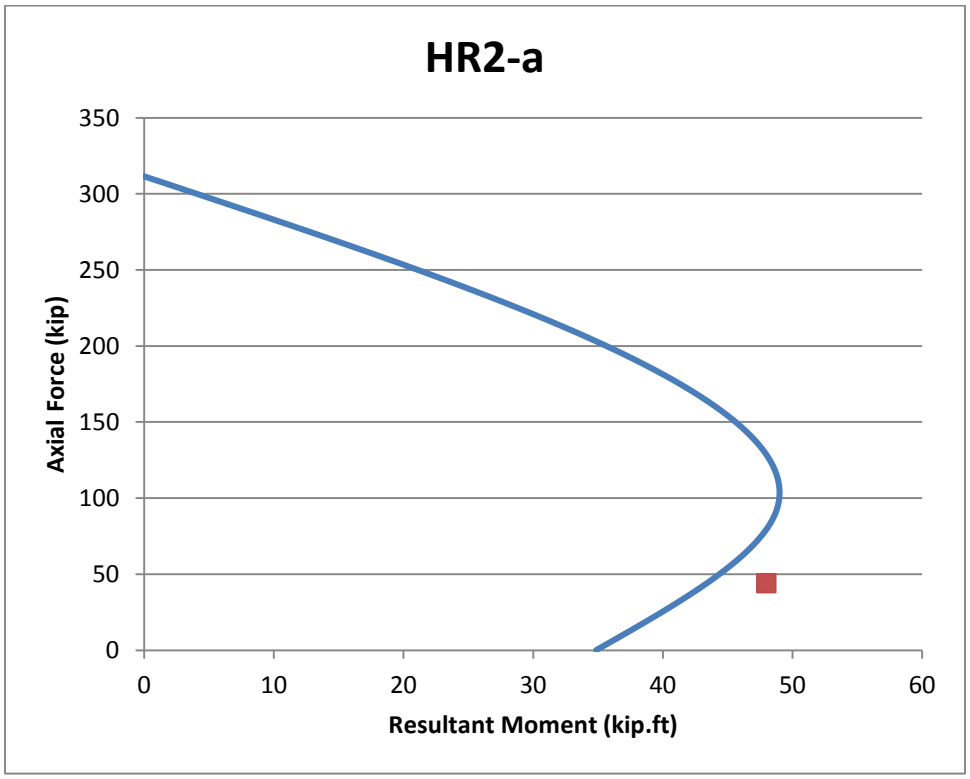

Figure 5-20: Interaction Diagram for Specimen HR2-a.

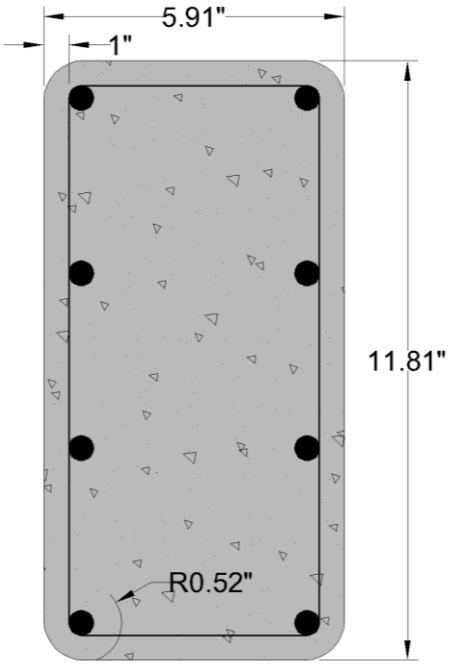

Figure 5-21: Cross-section of HRx-b Specimens by Harajli and Rteil (2004).

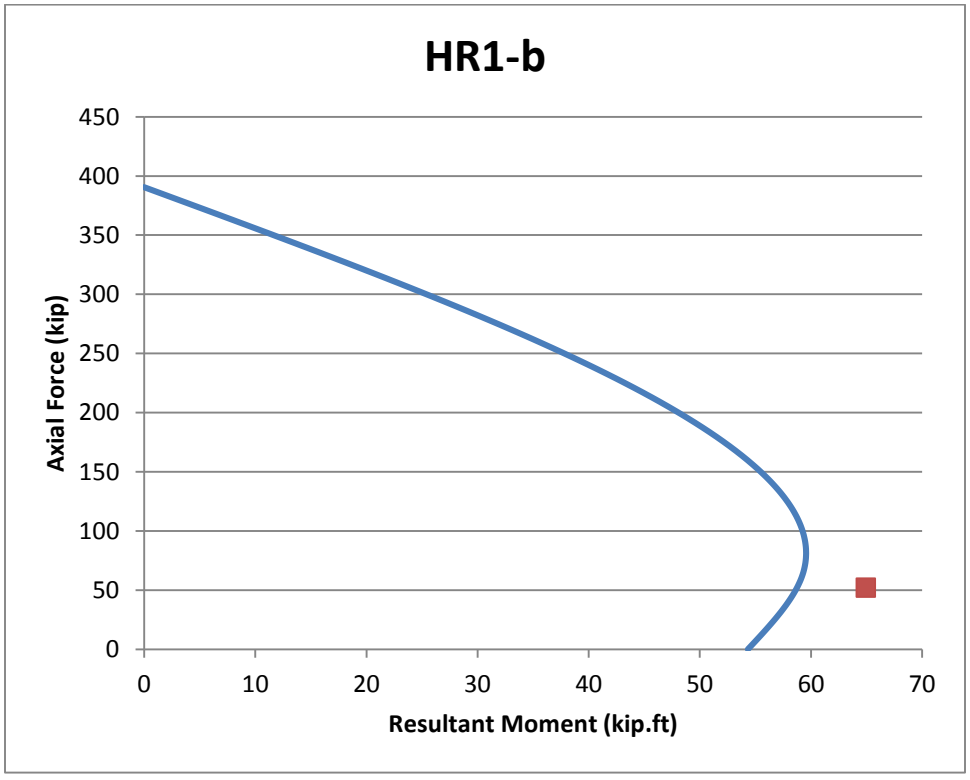

Figure 5-22: Interaction Diagram for Specimen HR1-b.

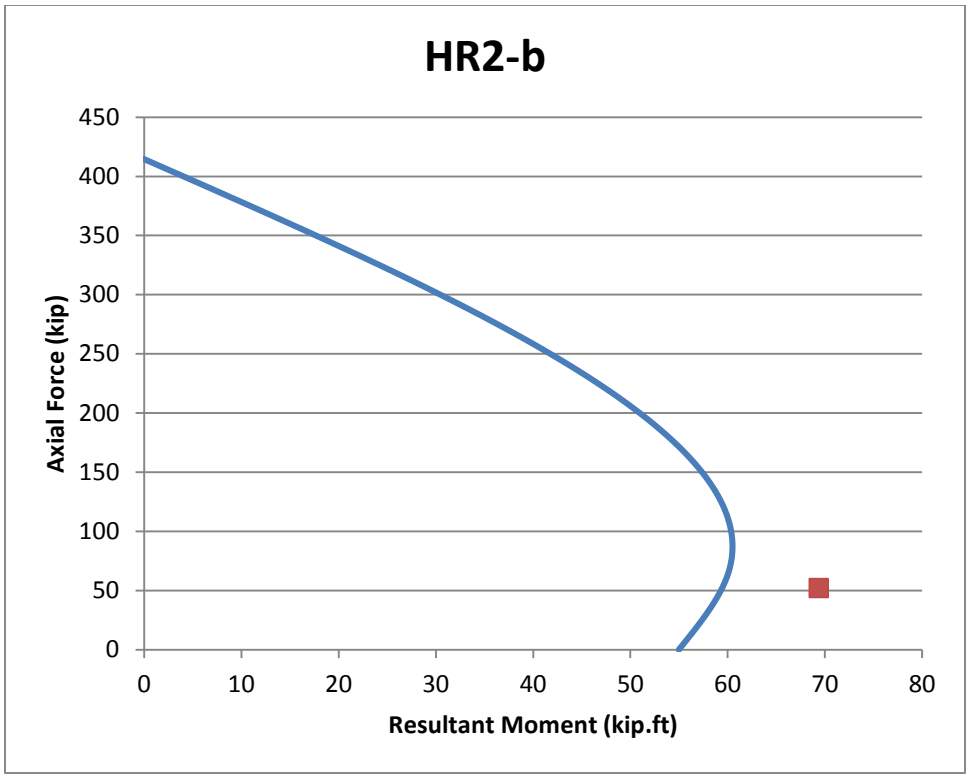

Figure 5-23: Interaction Diagram for Specimen HR2-b.

Figure 5-19 to Figure 5-23 show the interaction diagrams obtained for specimens tested by Harajli and Rteil (2004). These specimens fell in the tension failure region of the interaction diagram. The program provided conservative results for all tested cases. Overall, the results obtained showed good agreement and the proposed approach provided conservative estimates for the capacity.

Darby et al. Specimens (2011)

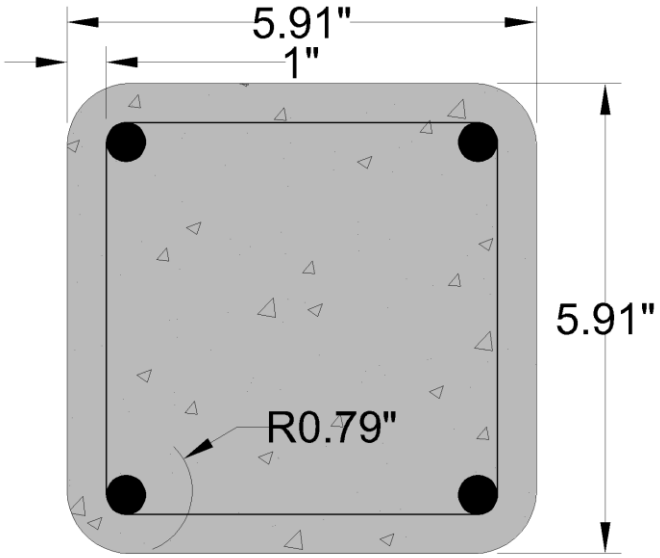

Figure 5-24: Cross-section of SC1 Specimens by Darby et al. (2011).

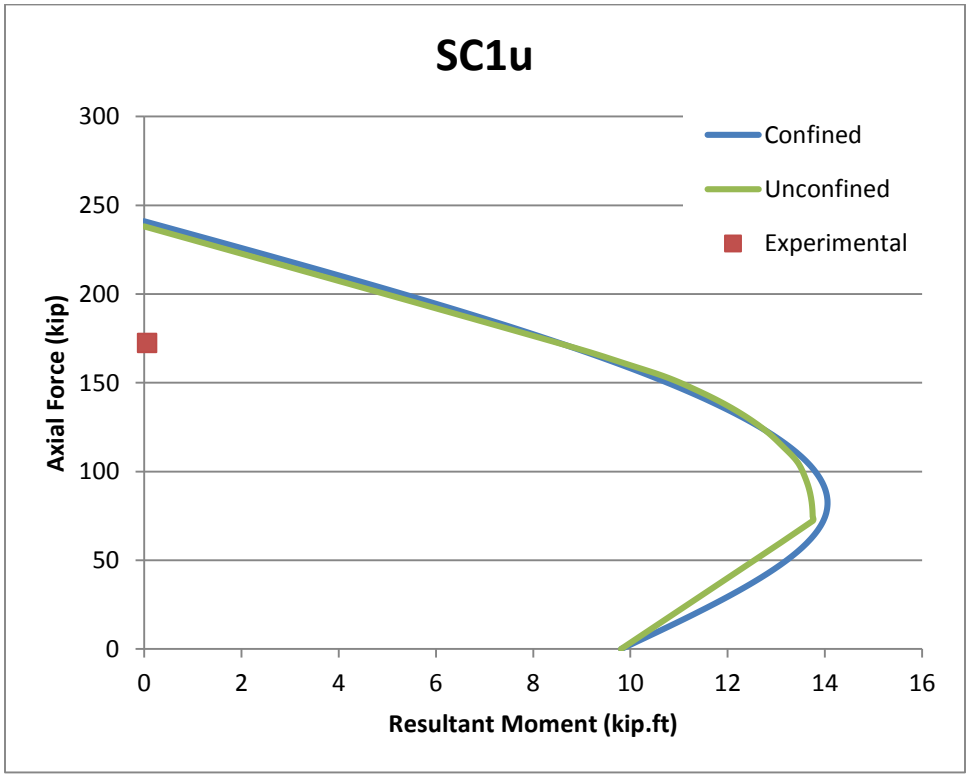

Figure 5-25: Interaction Diagram for Specimen SC1u.

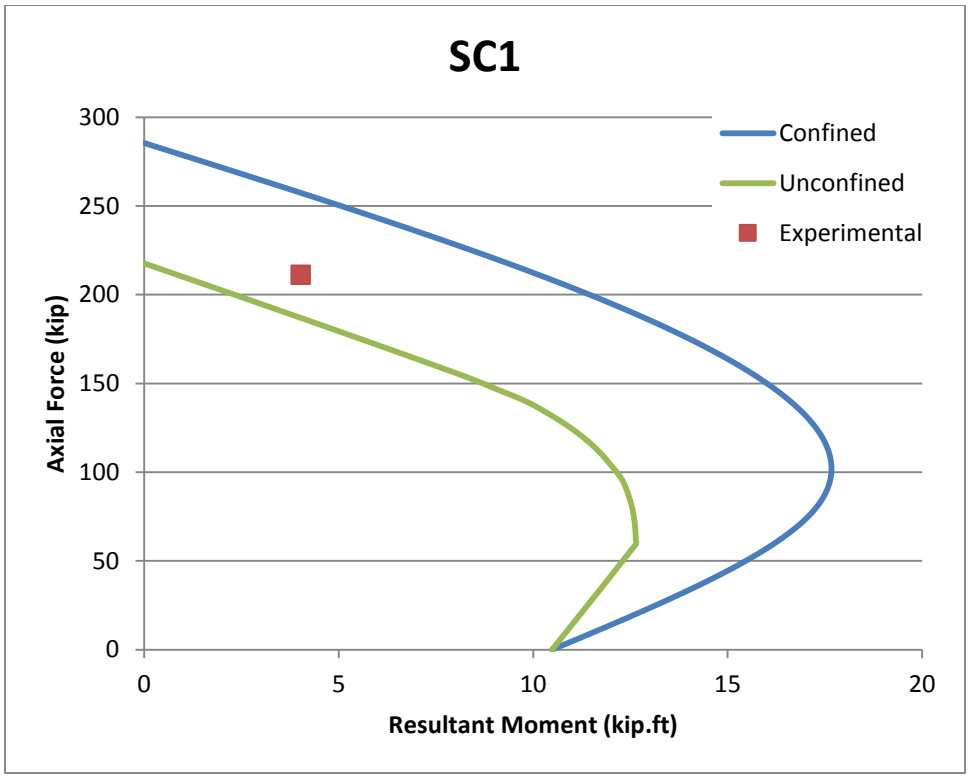

Figure 5-26: Interaction Diagram for Specimen SC1.

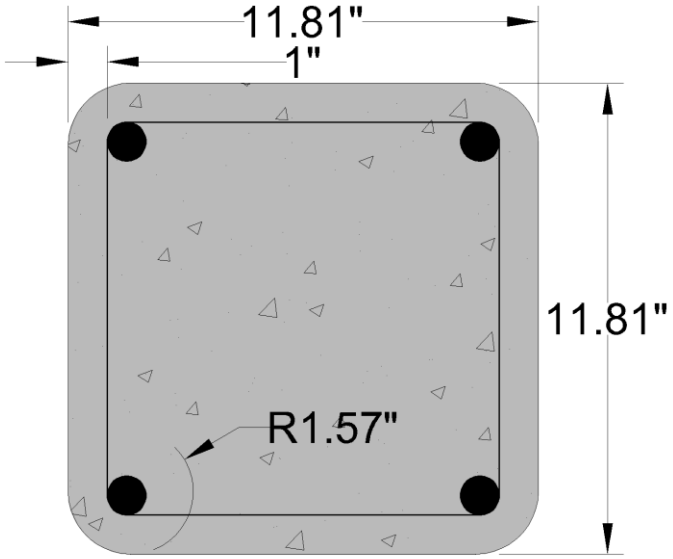

Figure 5-27: Cross-section of SC2 Specimens by Darby et al. (2011).

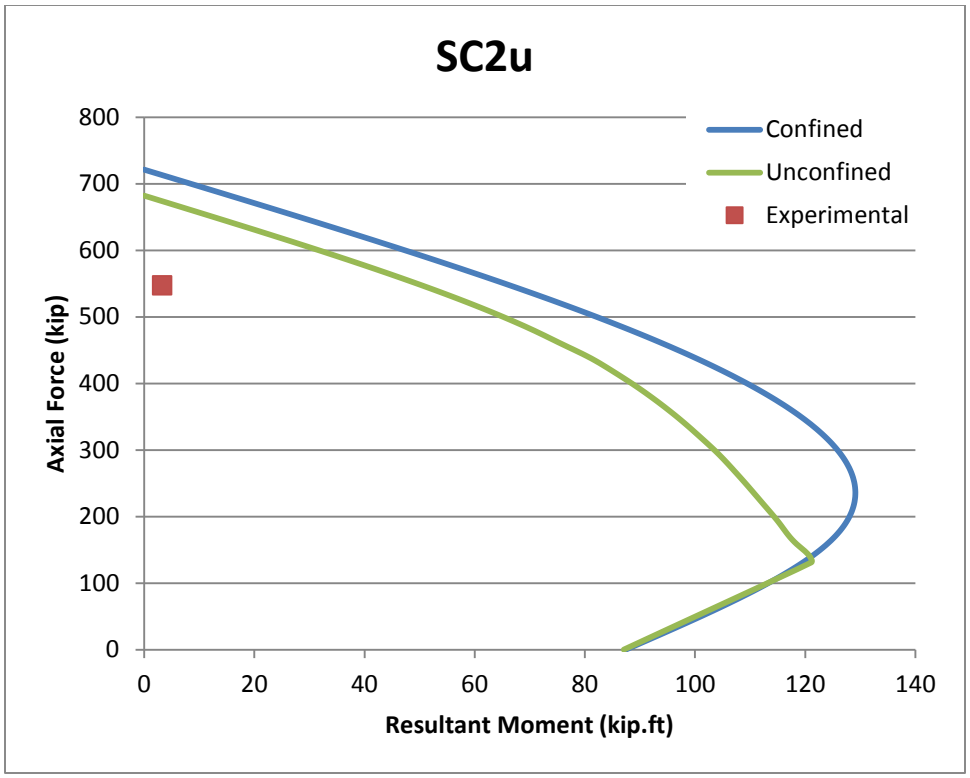

Figure 5-28: Interaction Diagram for Specimen SC2u.

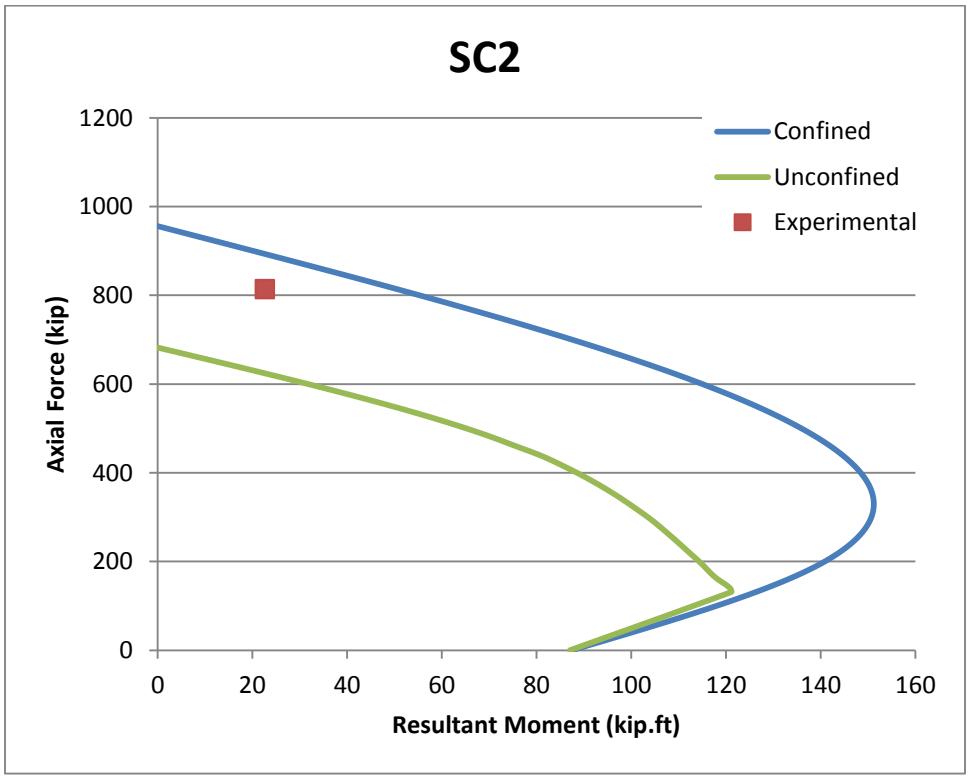

Figure 5-29: Interaction Diagram for Specimen SC2.

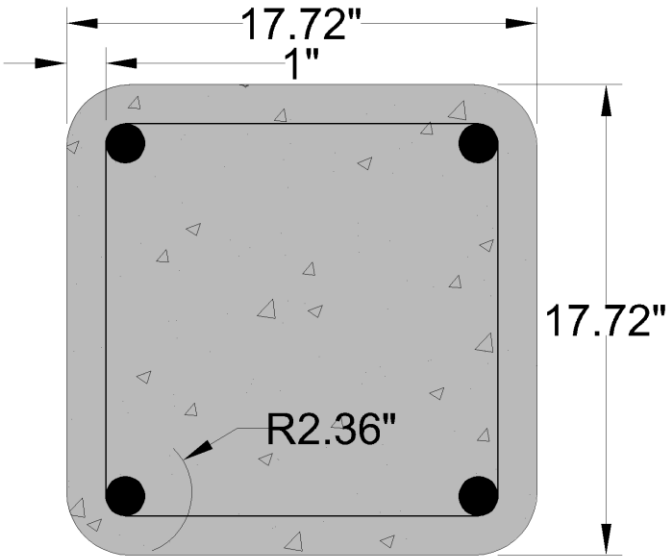

Figure 5-30: Cross-section of SC3 Specimens by Darby et al. (2011).

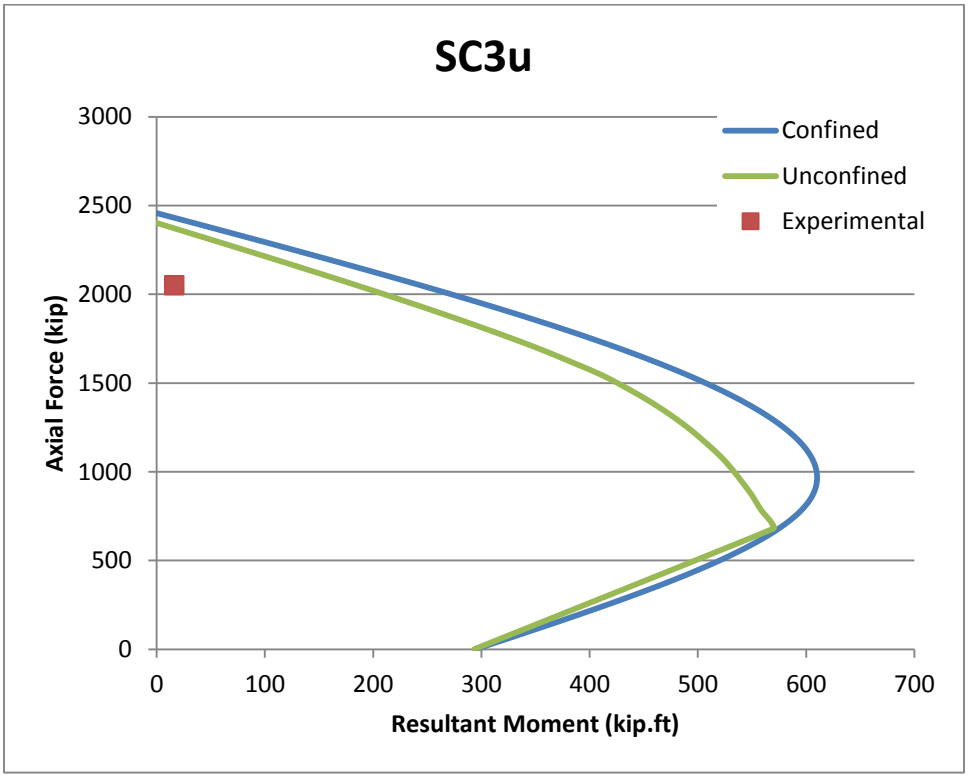

Figure 5-31: Interaction Diagram for Specimen SC3u.

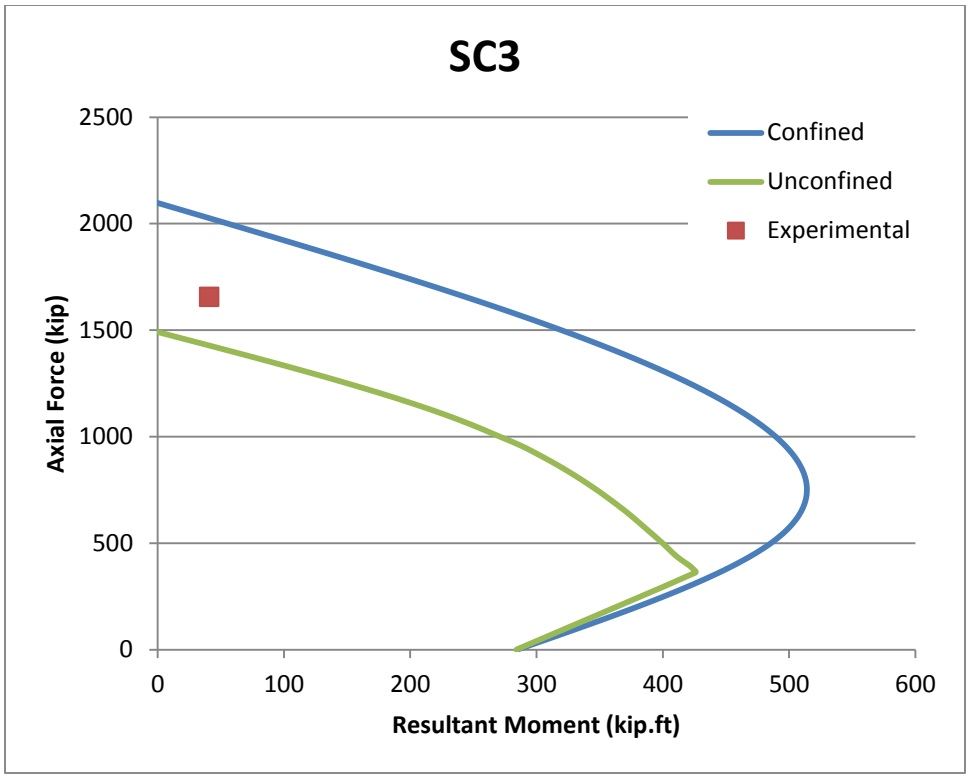

Figure 5-32: Interaction Diagram for Specimen SC3.

Figure 5-25 to Figure 5-32 show the interaction diagrams obtained for specimens tested by Darby et al. (2011). For these specimens, the authors did not provide details about lateral steel reinforcement and only stated that the minimum required reinforcement was provided. Because of that, bar size #3 was assumed and used in the analysis. ACI 318-11 provisions state that for a ties in a compression member, the spacing of the bars shall not exceed 16 times the longitudinal bar diameter, 48 times the tie bar diameter, or the least dimension of the section (2011). For all sections, the controlling value was determined to be the smaller dimension, and the clear spacing values for each section were accordingly assumed. These specimens fell in the compression failure region of the interaction diagram. For these specimens, the results obtained from the program were not conservative, even for cases where no FRP wraps were used. In order to investigate this, the interaction diagram for the sections excluding the confinement effect was obtained. The procedure to obtain this curve has been detailed by Abd El Fattah (2012). Even after ignoring the confinement effect, the point was below the interaction diagram. Even though the lateral reinforcement used in analysis was assumed, it is not expected that the assumption affected the results negatively. As the ties' clear spacing obtained was the maximum allowed by the ACI 318-11 code provisions (2011), increases in this value are not allowed. On the other

hand, decreasing the tie spacing will increase the effect of confinement. This will shift the confined curve upward, which will introduce even less conservative results. This issue could be due to an error in the provided specimens' parameters. It could also be attributed to the experiments themselves; however, given the current information, a conclusion cannot be reached.

Wang and Hsu Specimens (2007)

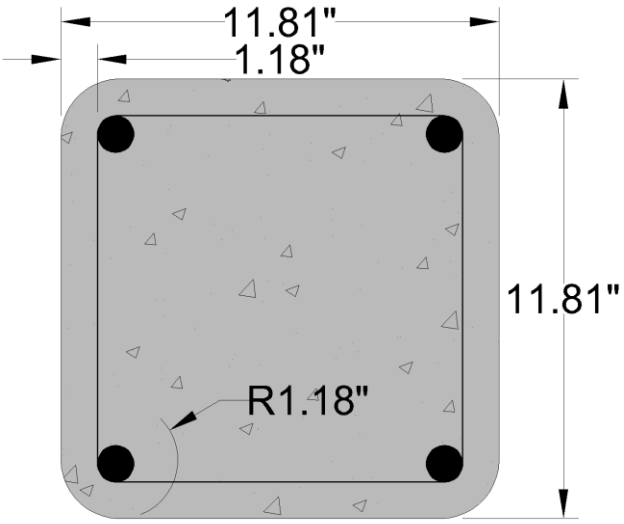

Figure 5-33: Cross-section of CS Specimens by Wang and Hsu (2007).

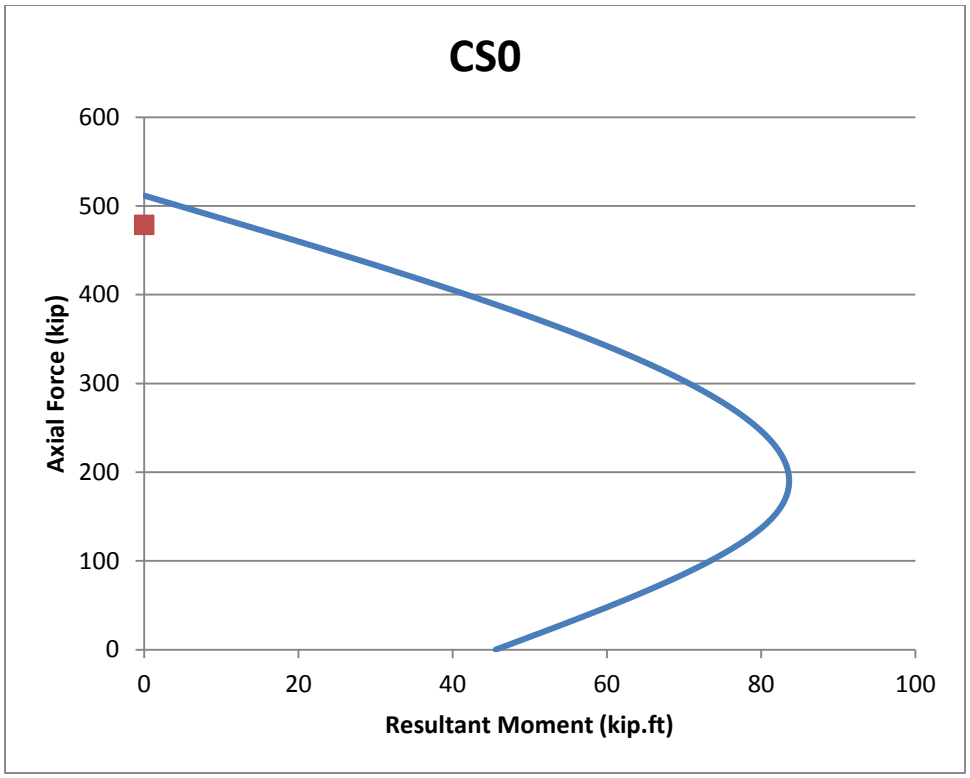

Figure 5-34: Interaction Diagram for Specimen CS0.

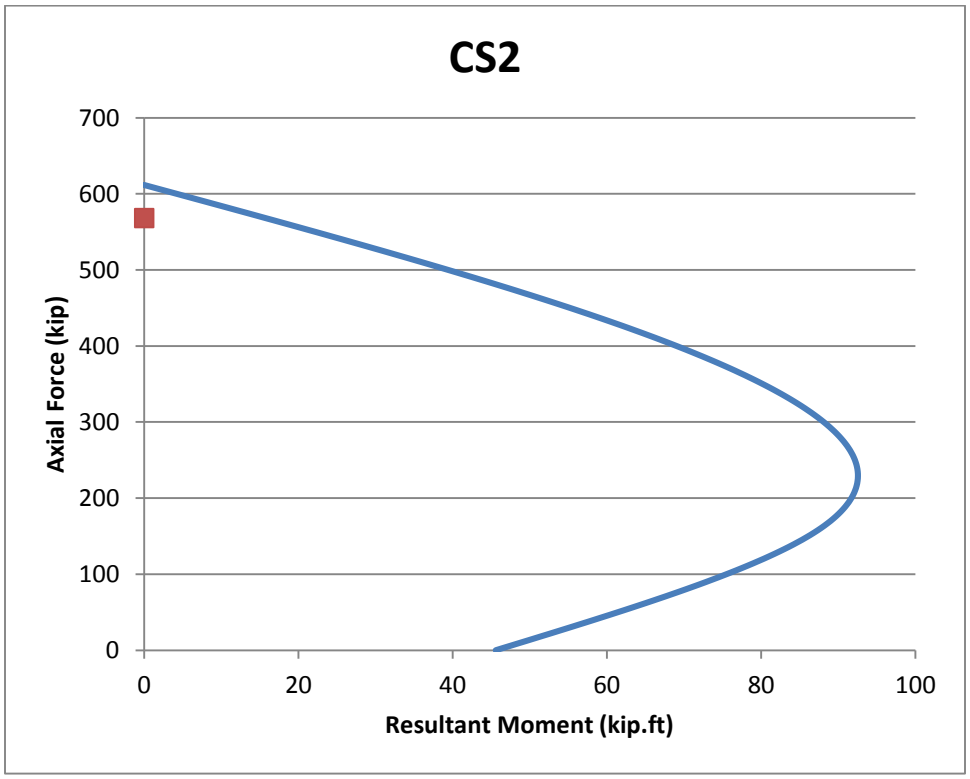

Figure 5-35: Interaction Diagram for Specimen CS2.

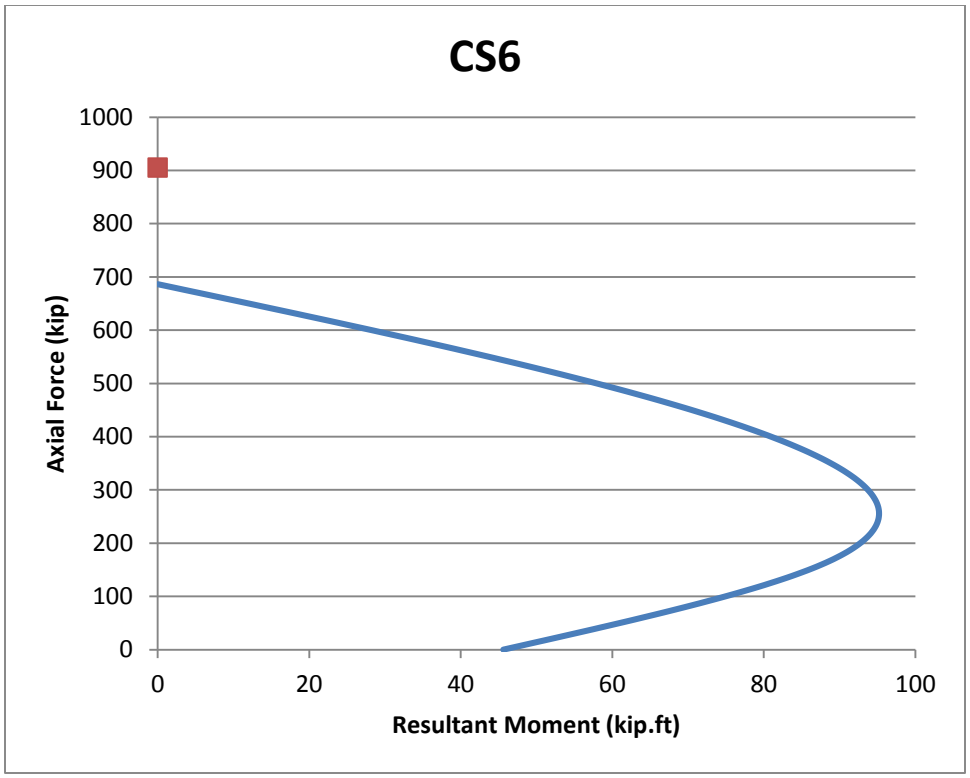

Figure 5-36: Interaction Diagram for Specimen CS6.

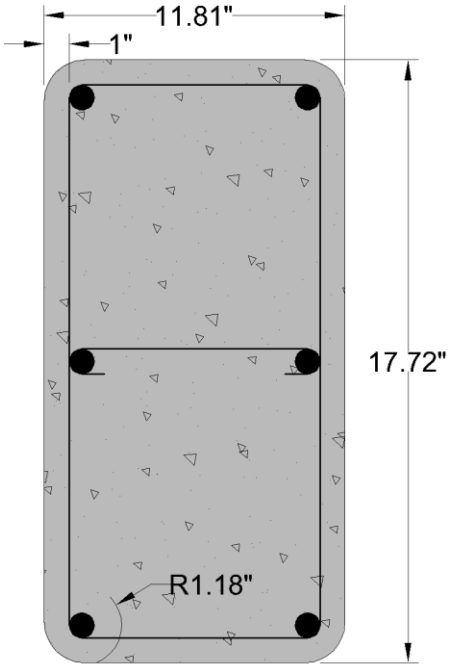

Figure 5-37: Cross-section of CR Specimens by Wang and Hsu (2007).

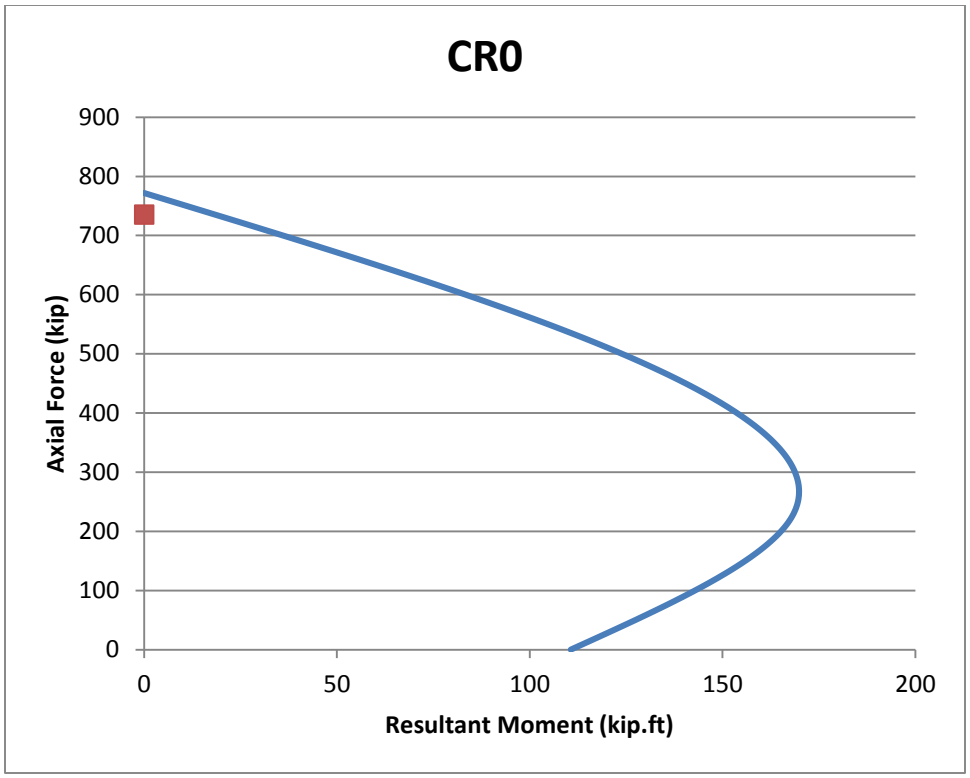

Figure 5-38: Interaction Diagram for Specimen CR0.

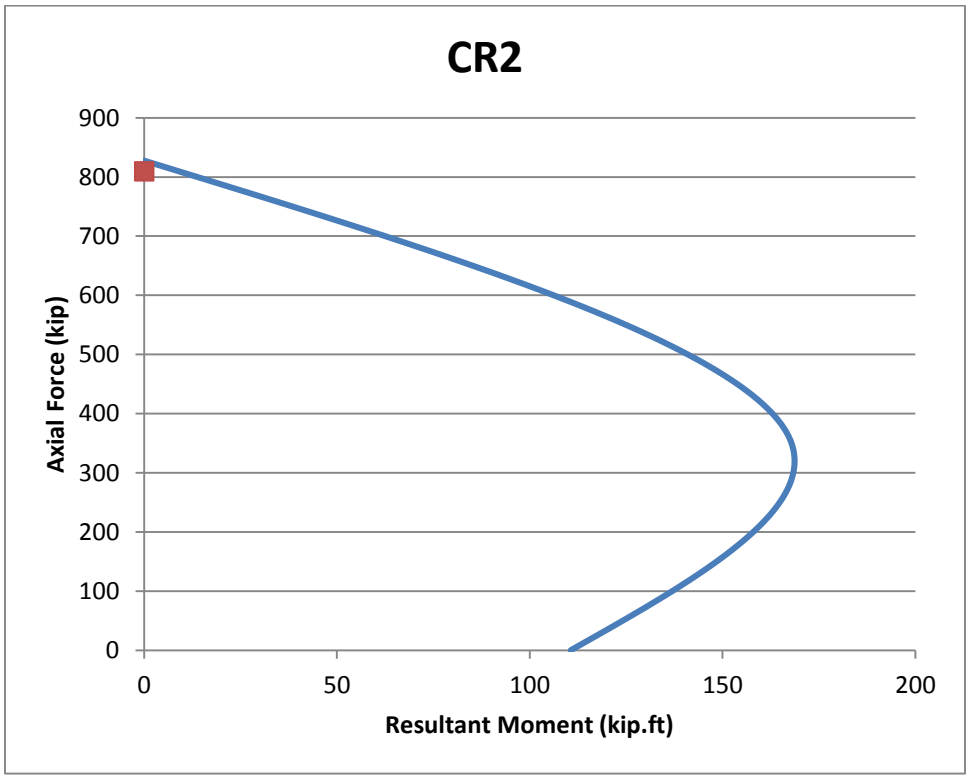

Figure 5-39: Interaction Diagram for Specimen CR2.

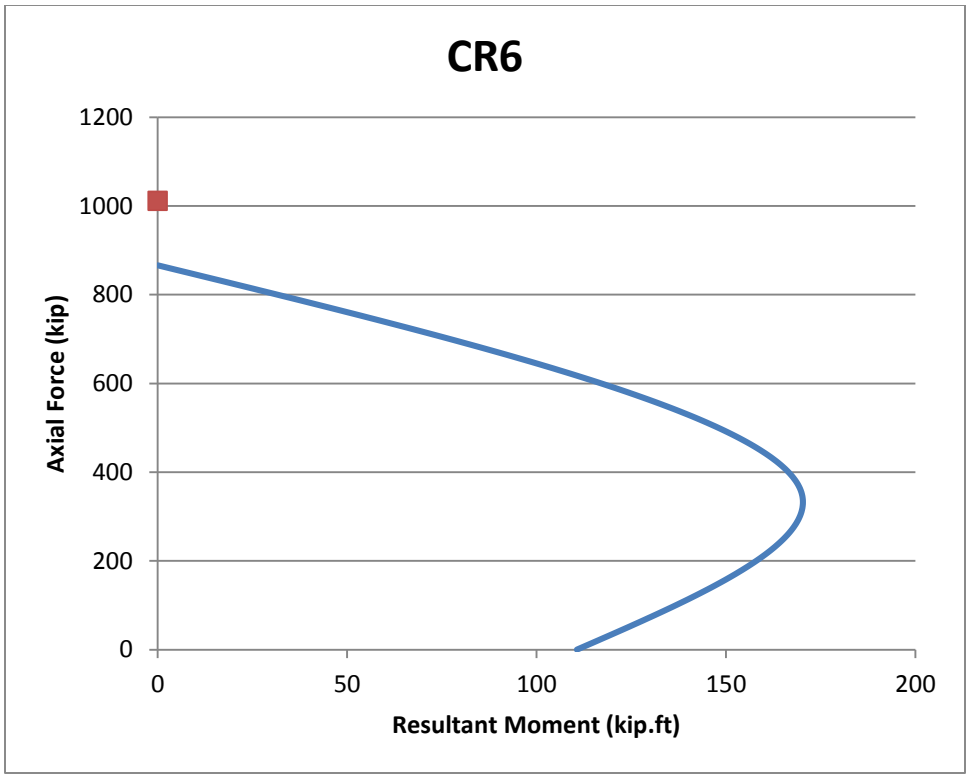

Figure 5-40: Interaction Diagram for Specimen CR6.

Figure 5-34 to Figure 5-40 show the interaction diagrams obtained for specimens tested by Wang and Hsu (2007). Their experimental program included both square and rectangular sections. These specimens fell in the compression failure region of the interaction diagram. For specimens with number of FRP plies below six, the program results were very close to these obtained from the experiments. The program provided conservative results in the cases of CS6 and CR6. Overall, the results obtained showed good agreement with the experiments.

Parametric Studies

In order to validate the proposed approach and observe the behavior of the combined model and the programmed algorithm, a parametric study was conducted. The common properties are provided in Table 5-4. They include the compressive strength (f'_c), clear cover (cc), radius of rounded corners (r_c), ties bar size and their clear spacing (s'), yield strength (f_y) and modulus of elasticity (E_s) for both longitudinal and lateral reinforcement, FRP properties such as modulus of elasticity (E_f), rupture strain (ε_{fu}), ply thickness (t_f).

Table 5-4: Common Properties for the Parametric Study.

Property	f'_c (ksi)	cc (in)	r_c (in)	Tie size	s' (in)	f_y (ksi)	E_s (ksi)	E_f (ksi)	ε_{fu}	t_f (in)
Value	4	1	1	#3	1.5	60	29000	33350	0.0015	0.005

The properties for the longitudinal reinforcement, which was one of the variables, are provided in Table 5-5. This table provides the sections' dimensions, their bar sizes, their count along the x and y-axes and the steel ratio (ρ).

Table 5-5: Section Geometry and Longitudinal Reinforcement Details.

Section	Bar size	Bars in x	Bars in y	ρ
12x12	#5	4	4	0.0258
12x24	#4	4	5	0.0292
12x36	#8	4	6	0.0293
12x48	#8	4	8	0.0312
16x16	#6	5	5	0.0275
16x32	#8	5	6	0.0278
16x48	#9	5	8	0.0286
20x20	#6	6	6	0.022
20x40	#8	6	8	0.0237
20x48	#9	6	8	0.025
25x25	#7	7	7	0.02
25x48	#9	7	9	0.0233
30x30	#8	8	8	0.0246
30x48	#10	8	9	0.0265
36x36	#10	8	8	0.0274
36x48	#11	8	9	0.0271

All sections listed above were analyzed while varying the number of FRP layers from zero to five. Detailed confined interaction diagram data was then obtained from the software. These data was then parsed for three key values, the ultimate axial capacity (P_n), the maximum moment at balance condition (M_{max}), and the moment at pure tension (M_n). Additionally, the percentage increase in sections with FRP relative to the section with steel only (PD) was calculated. The results are provided in Table 5-6.

Table 5-6: Parametric Study Results.

Section	n	P_n	M_{max}	M_n	PD	Section	n	P_n	M_{max}	M_n	PD
12x12	0	932.37	128.70	84.02	-	20x40	0	4617.73	2357.62	1615.77	-
	1	986.80	130.86	84.02	0.06		1	4666.66	2359.46	1615.77	0.01
	2	1027.62	131.55	84.02	0.10		2	4691.12	2360.42	1615.77	0.02
	3	1050.30	134.16	84.02	0.13		3	4715.59	2361.43	1615.77	0.02
	4	1063.90	134.42	84.02	0.14		4	4715.59	2361.43	1615.77	0.02
12x24	0	1828.88	551.13	407.26	-	20x48	0	5650.52	3515.81	2461.67	-
	1	1857.33	551.76	407.26	0.02		1	5680.42	3517.15	2461.67	0.01
	2	1876.30	552.19	407.26	0.03		2	5710.31	3518.52	2461.67	0.01
	3	1885.78	552.41	407.26	0.03		3	5710.31	3518.52	2461.67	0.01
	4	1885.78	552.41	407.26	0.03		4	5740.20	3519.91	2461.67	0.02
12x36	0	2646.28	1239.29	936.23	-	25x25	0	3694.99	1172.10	752.84	-
	1	2660.52	1239.63	936.23	0.01		1	3789.67	1126.77	752.84	0.03
	2	2674.76	1239.98	936.23	0.01		2	3846.48	1128.49	752.84	0.04
	3	2674.76	1239.98	936.23	0.01		3	3922.22	1130.90	752.84	0.06
	4	2689.01	1240.34	936.23	0.02		4	3979.03	1197.27	752.84	0.08
12x48	0	3517.01	2114.78	1543.64	-	25x48	0	6825.60	4314.82	2897.03	-
	1	3535.55	2115.81	1543.64	0.01		1	6898.61	4319.91	2897.03	0.01
	2	3535.55	2115.81	1543.64	0.01		2	6898.61	4319.91	2897.03	0.01
	3	3535.55	2115.81	1543.64	0.01		3	6935.12	4306.41	2897.03	0.02
	4	3535.55	2115.81	1543.64	0.01		4	6935.12	4363.39	2897.03	0.02
16x16	0	1613.75	323.26	218.31	-	30x30	0	5300.90	2092.43	1404.09	-

Section	n	P_n	M_{max}	M_n	PD	Section	n	P_n	M_{max}	M_n	PD
	1	1679.72	310.29	218.31	0.04		1	5412.35	2027.20	1404.09	0.02
	2	1729.20	311.46	218.31	0.07		2	5495.94	2029.89	1404.09	0.04
	3	1778.68	332.95	218.31	0.10		3	5579.53	2032.68	1404.09	0.05
	4	1828.17	334.18	218.31	0.13		4	5635.25	2034.60	1404.09	0.06
16x32	0	3121.07	1306.10	951.75	-	30x48	0	8518.73	5606.59	3931.47	-
	1	3170.73	1307.50	951.75	0.02		1	8610.21	5612.78	3931.47	0.01
	2	3170.73	1307.50	951.75	0.02		2	8610.21	5612.78	3931.47	0.01
	3	3187.28	1307.98	951.75	0.02		3	8655.96	5615.93	3931.47	0.02
	4	3220.39	1308.96	951.75	0.03		4	8701.70	5619.10	3931.47	0.02
16x48	0	4699.66	2969.89	2184.09	-	36x36	0	7747.06	3876.23	2716.40	-
	1	4724.78	2963.56	2184.09	0.01		1	7872.20	3729.71	2716.40	0.02
	2	4749.89	2962.35	2184.09	0.01		2	7955.63	3732.34	2716.40	0.03
	3	4749.89	2962.35	2184.09	0.01		3	8039.06	3735.05	2716.40	0.04
	4	4749.89	3002.44	2184.09	0.01		4	8122.49	3737.84	2716.40	0.05
20x20	0	2396.97	586.49	360.65	-	36x48	0	10235.32	6793.56	4809.55	-
	1	2480.55	557.91	360.65	0.03		1	10346.03	6641.11	4809.55	0.01
	2	2528.32	559.24	360.65	0.05		2	10401.39	6723.33	4809.55	0.02
	3	2588.02	560.97	360.65	0.08		3	10456.75	6725.91	4809.55	0.02
	4	2647.72	595.78	360.65	0.10		4	10512.10	6728.52	4809.55	0.03

At the first glance, it appears from the data shown in Table 5-6 that adding more FRP layers to some cases (shaded in gray in the table) does not increase the axial capacity of the section. In order to investigate, compressive strength values for both the core (f_{cce}) and the cover

(f_{ccf}) were computed for two sample cases of 12x24 and 12x48. Extracted parameters are listed in Table 5-7.

Table 5-7: Extracted Analysis Parameters.

Section	12x24		12x48			
n_f	3	4	1	2	3	4
f_{lf}/f'_c	0.082	0.109	0.015	0.03	0.044	0.059
f_{cce} (ksi)	5.19	5.16	4.65	4.657	4.664	4.66
f_{ccf} (ksi)	4.13	4.17	4.009	4.018	4.026	4.034

Before proceeding, it is observed that the confined compressive strength has dropped for the first case from 5.19 ksi to 5.16 ksi, and for the second case from 4.664 ksi to 4.66 ksi as the number of FRP layers has increased from 3 to 4 layers in each case. This occurred even though the confining pressure has increased since the number of FRP layers increased. The cause of this issue is the restriction on the ultimate strain imposed by ACI 440.2R-08 (2008). In these two instances, the strain obtained exceeded 0.01, and thus a new f_{cc} value corresponding to this ultimate strain is calculated.

For the first case, as the confinement ratio (f_{lf}/f'_c) is greater than 0.08, the model used is Lam and Teng model with an ascending second branch. Detailed calculations will be provided to verify the results obtained from the program for this case. The areas are calculated as follows:

$b_c = b - 2cc - d_t = 12 - 2 - 0.375 = 9.625\ in$

$h_c = h - 2cc - d_t = 24 - 2 - 0.375 = 21.625\ in$

$A_{core} = b_c * h_c - n * A_s = 208.141 - 14 * 0.6 = 199.741\ in^2$

$A_{cover} = b * h - b_c * h_c = 288 - 208.141 = 79.859\ in^2$

$where\ b_c = confined\ core\ width$

$h_c = confined\ core\ depth$

$cc = clear\ cover$

$d_t = tie\ diameter$

$n = number\ of\ longitudenal\ bars$

$A_s = longitudenal\ bar\ area$

$f_y = yield\ stress\ for\ longitudenal\ reinforcement$

Using the extracted value from Table 5-7 and the calculated areas, the axial capacity is calculated as follows:

$P_n = f_{cce} * A_{core} + f_{ccf} * A_{cover} + f_y * n * A_s$

$P_3 = 5.19 * 199.741 + 4.13 * 79.859 + 60 * 14 * 0.6 = 1870.47\ kip$

$P_4 = 5.16 * 199.741 + 4.17 * 79.859 + 60 * 14 * 0.6 = 1867.68\ kip$

$where\ P_3 = axial\ capacity\ of\ specimen\ with\ 3\ layers$

$P_4 = axial\ capacity\ of\ specimen\ with\ 4\ layers$

As it can be seen from the calculation, the capacity has actually dropped when the number of FRP layers was increased. The values are very close (percentage difference is 0.15%), and are smaller than the step size used by the incremental solver, which caused the program to provide the same results for both sections. Similarly, for the second case, the change in f_{cc} values is very small due to the high aspect ratio. In this case, Mander model is used since the confinement ratio is below 0.08. The small change in f_{cc} is not significant enough for solver, and results in an axial capacity difference that is smaller than the step size. This again causes the program to output the same interaction diagram for all sections under this case. Calculation details for the second case are shown below:

$b_c = b - 2cc - d_t = 12 - 2 - 0.375 = 9.625\ in$

$h_c = h - 2cc - d_t = 48 - 2 - 0.375 = 45.625\ in$

$A_{core} = b_c * h_c - n * A_s = 439.141 - 20 * 0.79 = 423.341\ in^2$

$A_{cover} = b * h - b_c * h_c = 576 - 439.141 = 136.859\ in^2$

$P_3 = 4.664 * 423.341 + 4.026 * 136.859 + 60 * 20 * 0.79 = 3473.457\ kip$

$P_4 = 4.66 * 423.341 + 4.034 * 136.859 + 60 * 20 * 0.79 = 3472.858\ kip$

It is concluded that this is not an issue with the program, and is just part of the process. This occurrence is expected in section with high aspect ratio, where the addition of FRP layers does not immensely increase the confined compressive strength of the section.

Additionally, for the sections with width of 12 in, the interaction diagrams were obtained for multiple Alpha angles (α). For illustration purposes, two interaction diagrams are provided. Figure 5-41 and Figure 5-42 correspond to section 12x12 and 12x36, respectively. For the square section, the interaction diagrams for α=0^o and α=90^o were identical, which is reasonable for a square section where the width and the height are equal. For α=45^o, the interaction diagram was inside the previous two. This is again reasonable due to the existence of two moment

components in this case. As for the 12x36 section, it was observed that the moment at pure tension decreased as the angle Alpha increased, which was expected. This shows that the program behavior is consistent with different angles.

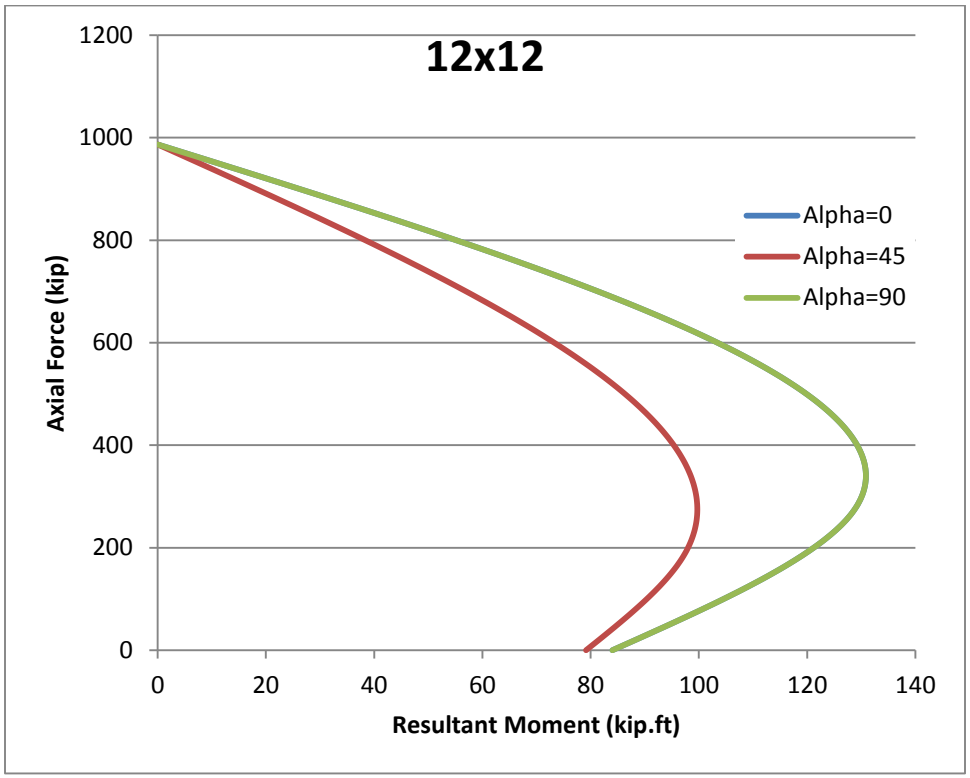

Figure 5-41: Interaction Diagram for Multiple Alpha Angles for Section 12x12.

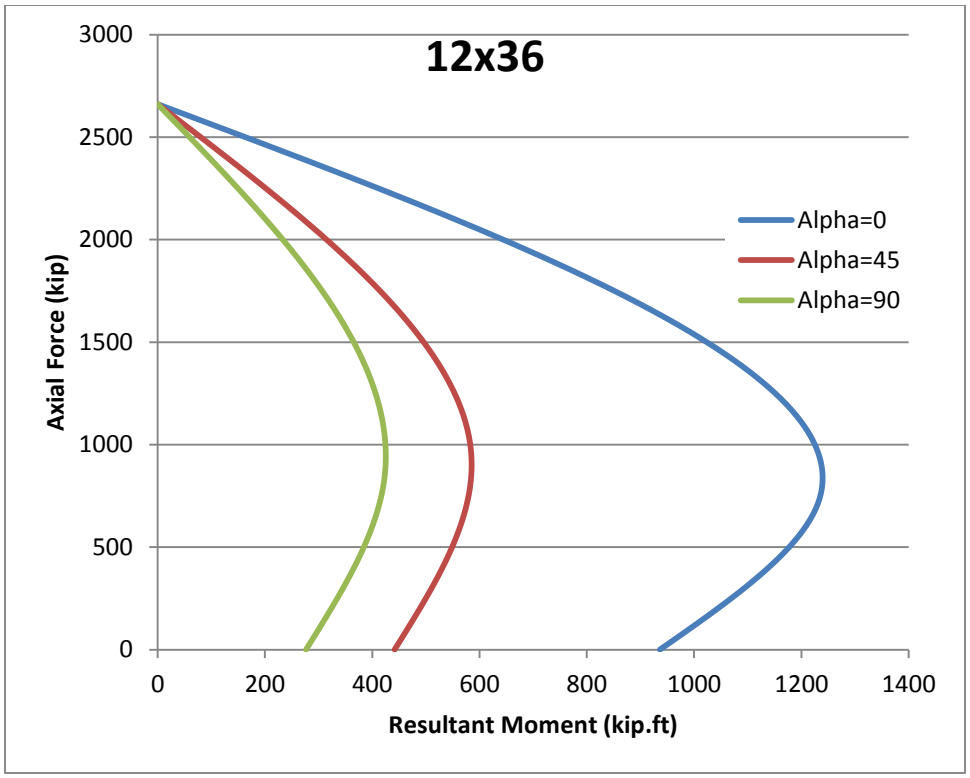

Figure 5-42: Interaction Diagram for Multiple Alpha Angles for Section 12x36.

Overall, the obtained results shown in Table 5-6 were reasonable. Generally, the axial capacity has mostly increased as the number of FRP layers increased. It is observed that the increase in axial capacity due to the addition of FRP is diminished in sections with higher aspect ratios. This is expected because the FRP confinement effect is highly dependent on the aspect ratio. It is concluded that the program is functioning properly and the proposed approach provides reasonable results. Additional interaction diagrams are provided hereafter for illustration purposed (Figure 5-43 to Figure 5-47).

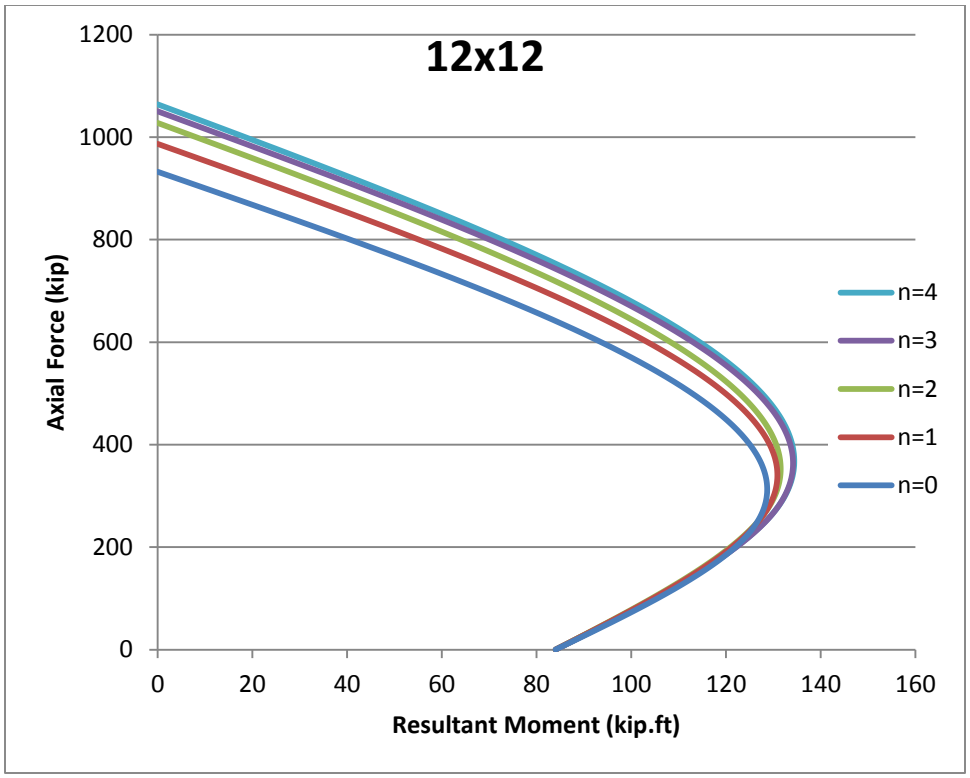

Figure 5-43: Interaction Diagrams for Section 12x12.

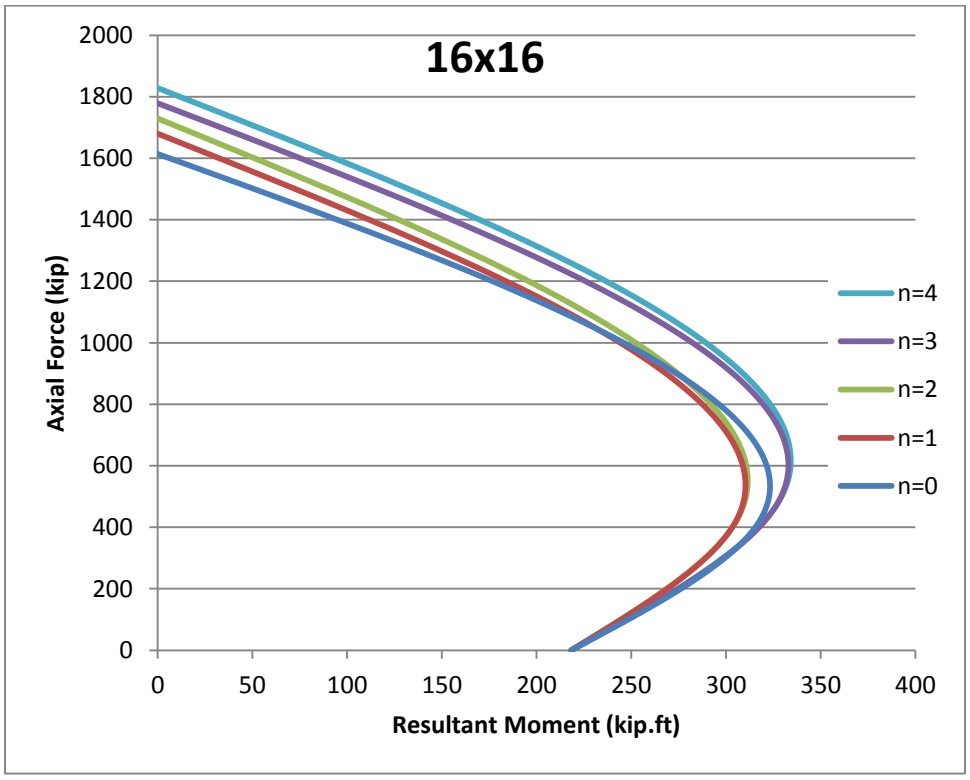

Figure 5-44: Interaction Diagrams for Section 16x16.

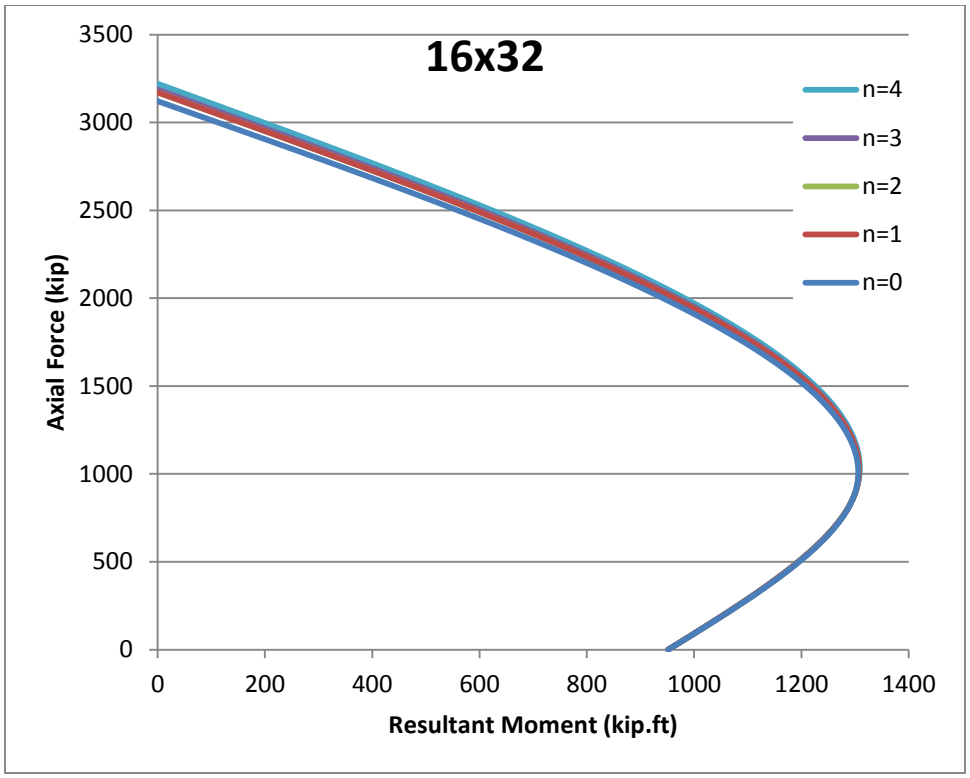

Figure 5-45: Interaction Diagrams for Section 16x32.

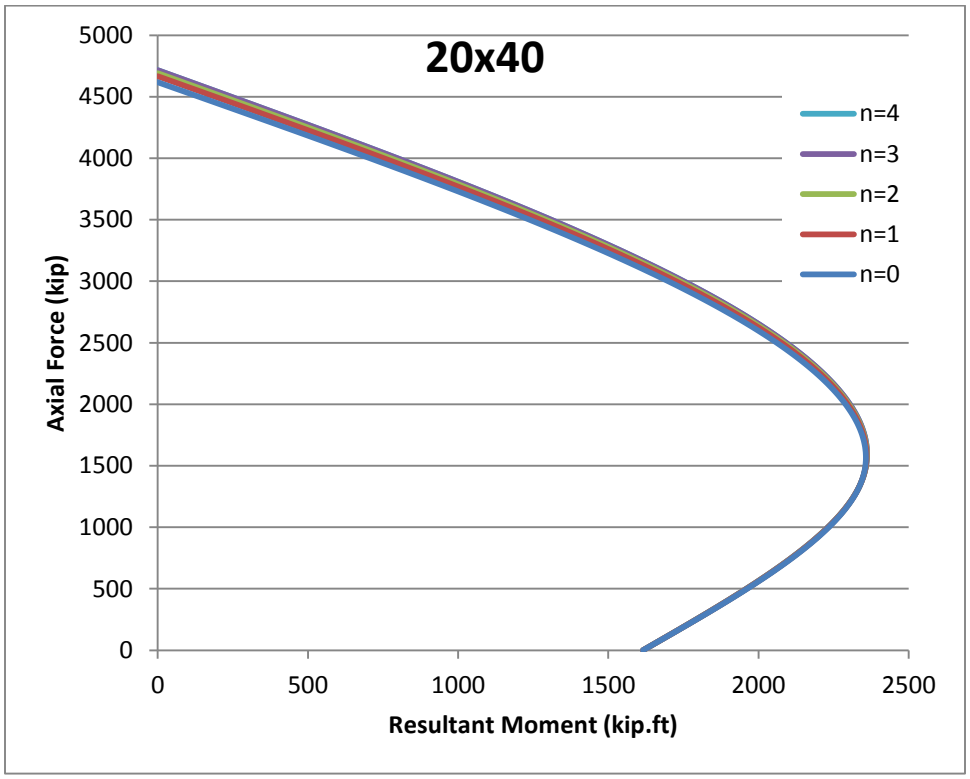

Figure 5-46: Interaction Diagrams for Section 20x40.

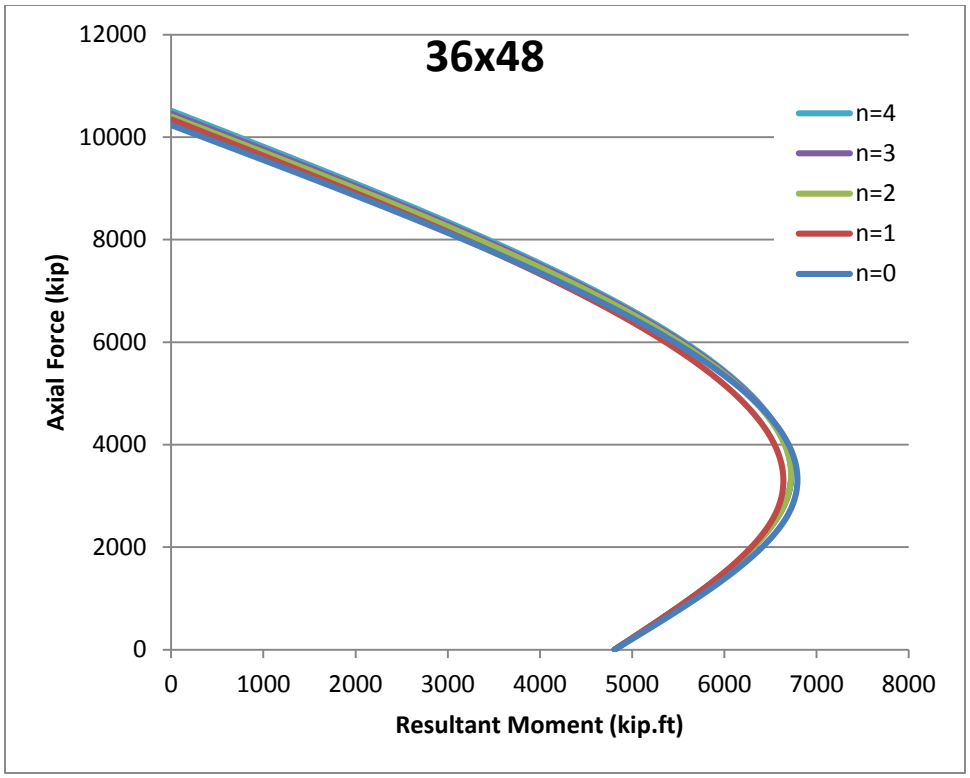

Figure 5-47: Interaction Diagrams for Section 36x48.

Chapter 6 - Computer Software Development

Introduction

In order to facilitate the involved process of confined analysis of reinforced concrete columns, Abd El Fattah (2012) developed KDOT Column Expert computer software. This software was developed using C# programming language for use in Microsoft Windows operating system environment. Object Oriented Programming (OOP) principles were applied in the development of this software to enhance flexibility and facilitate future expansions. The program capabilities include confinement analysis for circular columns with FRP, and confinement analysis for rectangular columns with steel only.

The author implemented the previously described proposed approach to confinement analysis of rectangular concrete columns with FRP into KDOT Column Expert version 5.0. Next, the general interface and new additions to the rectangular module will be presented.

Graphical User Interface (GUI)

When the program is first started, the user is presented with the section selection dialog box. The program is divided into two modules, circular and rectangular analysis modules. This dialog is shown in Figure 6-1.

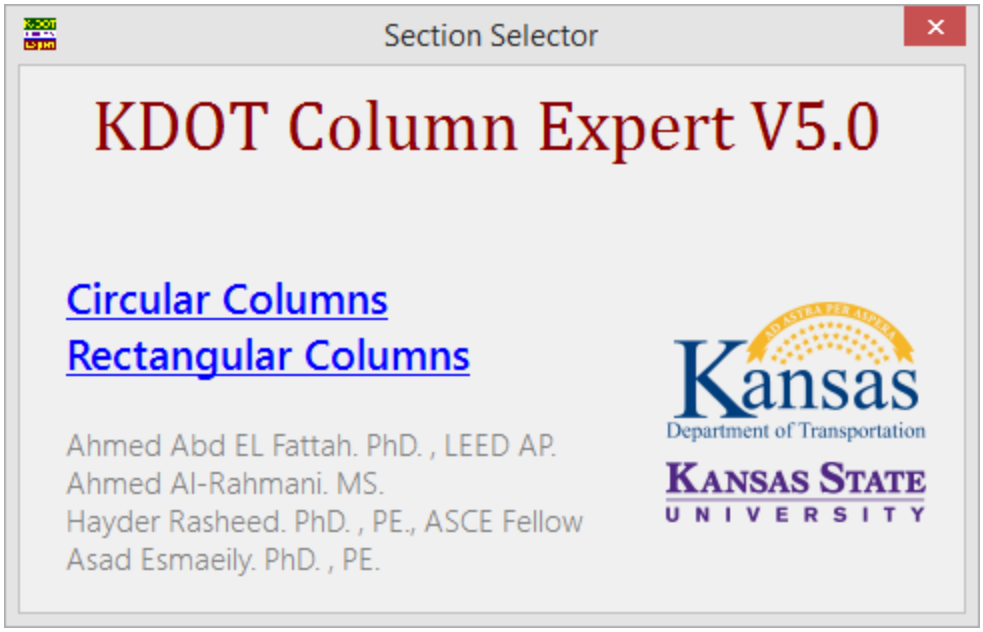

Figure 6-1: Section Selection Dialog Box.

After the user makes the selection, the appropriate interface is then loaded. As this report involved square and slightly rectangular sections, only the rectangular module will be presented hereafter. Figure 6-2 shows the interface running after the program is loaded.

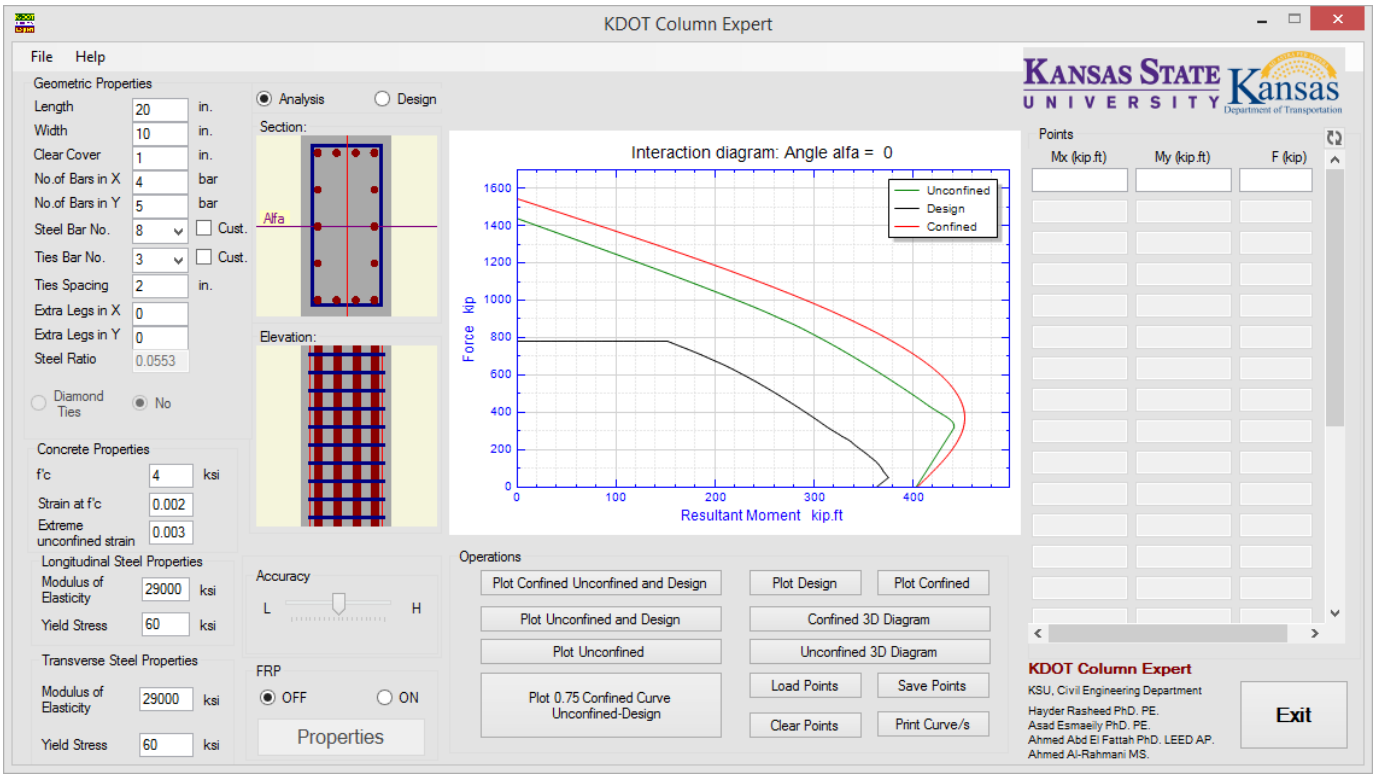

Figure 6-2: KDOT Column Expert Rectangular Module Interface.

The program interface is divided into four columns. The first column has input boxes for all necessary inputs, including geometric, concrete and steel properties. A new addition to this version is an option to use custom bars for both longitudinal and lateral steel. Upon checking the "Cust." Option, the user is presented with a dialog box requesting the custom bar's diameter and area. Due to the structure of the program, custom longitudinal bars will override bar size #18, while custom ties will override bar size #3. This was necessitated by the structure of the program. The selection of these bar sizes was done to minimize the chance for conflicts.

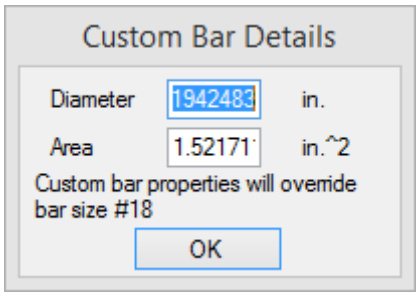

Figure 6-3: Custom Bar Dialog Box.

Column two provides sketches for the cross-section and elevation views. These graphics aid in the visualization of the analyzed columns and can help in detecting mistakes in data input. Next, a seek bar (slider) is provided to specify required accuracy. It works by varying the number of filament layers used in the analysis. The seek bar allows adjustment between 15 and 35 layers. The default setting is set at middle with 25 layers. The final setting available on this column, which is a new addition to this version, is the FRP switch. Setting this to "ON" opens a dialog box for the user to input the FRP properties into. The dialog box is shown in Figure 6-4.

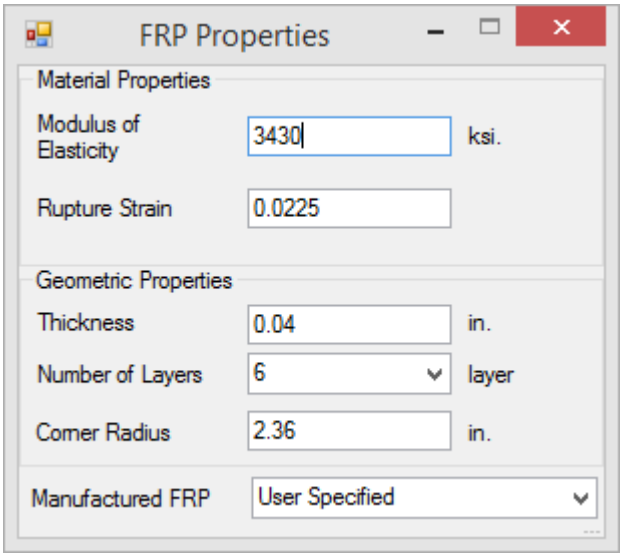

Figure 6-4: FRP Properties Dialog Box.

The user is required to input the modulus of elasticity, rupture strain, thickness, number of layer, and the radius of rounded corners. The user also has the option of choosing predefined FRP properties for several commercially available FRP products.

The third column has the main plot and the action buttons. The plotting area shows the interaction diagrams obtained from the analysis as requested. The action buttons specify which interaction diagrams are plotted. The program can plot the confined, unconfined, and design

interaction diagrams. Upon the completion of the new analysis, the user is prompted to select an angle Alpha (α) to display the interaction diagram for. This angle is defined as the angle between the resultant moment and the moment about the x-axis. The program can also plot a 3D interaction diagram, which is shown in a new window (Figure 6-5). Finally, the last column allows the user to input data points to plot on the interaction diagram. The points are immediately plotted on the interaction diagram corresponding to the appropriate angle (α). Up to 25 points can be plotted on the same diagram. These points can be saved to an external file and loaded using the action buttons.

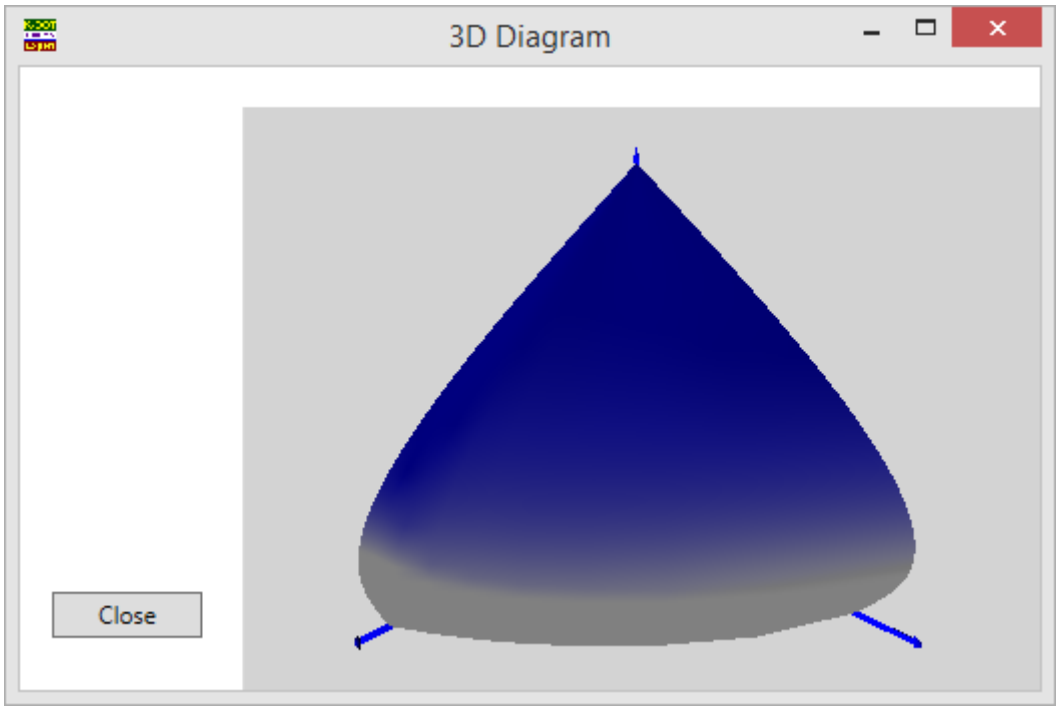

Figure 6-5: 3D Diagram Window.

Chapter 7 - Conclusions and Recommendations

Conclusions

In this study, a model was proposed to combine FRP and steel confinement in rectangular reinforced concrete columns. From previously conducted research, Mander model was found to be the most suitable confinement model for steel. Based on the conducted literature review and the recommendations of ACI committee 440 (2007), Lam and Teng model was found to be the most suitable confinement model for FRP. The eccentricity-based modeling approach was applied to the developed combined model. The proposed model and procedure were then implemented in "KDOT Column Expert" software version 6.0. The software was then used to generate interaction diagrams, which were compared with experiments found in the literature. The proposed model results showed good agreement with the experimental data. Additionally, the results were shown to be conservative for many of the cases tested. Furthermore, a parametric study was conducted after validating the proposed model. The objective of the parametric study was to examine the behavior of the model for cases beyond what was validated with experiments, and ensure its consistency. The model provided reasonable results, and its consistency was validated based on them. It is concluded that the combined confinement model and the software in which it was implemented, KDOT Column Expert, are viable tools to accurately model confinement in rectangular concrete columns with both transverse steel and FRP.

Recommendations

The following points could be done to extend this research, address some of the issues encountered, and improve the quality of the results:

- It is recommended that more experimental studies be conducted on reinforced concrete sections with high aspect ratios, as literature is currently lacking these results.
- As a few of the specimens tested had points very close to the generated interaction diagram, it is recommended that a factor for design purposes is introduced in order to generate more conservative curves.

- For future work, the proposed model could be expanded to include columns with multispiral lateral reinforcement configuration.

References

Abaqus 6.10 Online Documentation. (2010). Dassault Systèmes.

Abd El Fattah, A. M., (2012). *Behavior of concrete columns under various confinement effects.* (Doctoral dissertation). Kansas State University, Manhattan, KS.

ACI Committee 318, (2011). *Building code requirements for structural concrete (ACI 318-11) and commentary*. Farmington Hills, MI.

ACI Committee 440 Subcommittee F – REPAIR, (2007). *Task Group on FRP Confinement Report*. Farmington Hills, MI.

ACI Committee 440, (2008). *Guide for the design and construction of externally bonded FRP systems for strengthening concrete structures (ACI 440.2R-08)*. Farmington Hills, MI.

Ahmad, S. H., and Shah, S. P., (1982). Stress-strain curves of concrete confined by spiral reinforcement. *ACI Journal Proceedings*, *79*(6), 484-490.

Bank, L. C., 2006, *Composites for construction: Structural design with FRP materials*, John Wiley and Sons, Hoboken, NJ, 560 pp.

Bousias, S., Triantafillou, T., Fardis, M., Spathis, L, and O'Regan, B., (2004). "Fiber-reinforced polymer retrofitting of rectangular reinforced concrete columns with or without corrosion." ACI Struct J;101(4): 512–20.

Campione, G., and Miragia, N., (2003). "Strength and strain capacities of concrete compression members reinforced with FRP." *Cement and Concrete Composites*, 25(1), 31–41.

Chun, S. S., and Park, H. C., (2002). "Load carrying capacity and ductility of RC columns confined by carbon fiber reinforced polymer." *Proceedings of the Third International Conference on Composites in Infrastructure* (San Francisco, CA). Tucson, AZ: University of Arizona.

Cross, H., (1930). "The column analogy: Analysis of elastic arches and frames". *University of Illinois Engineering Experiment Station Bulletin Series No. 215.* University of Illinois, Urbana, IL.

Darby, A., Coonan, R., Ibell, T., and Evernden, M., (2011). "FRP confined square columns under concentric and eccentric loading." *Proceedings of the 5th international Advanced Composites in Construction 2011 conference.* 264-275. Chesterfield: NetComposites.

Elwi, A. A., and Murray, D. W., (1979). "A 3D hypoelastic concrete constitutive relationship." *ASCE Journal of the Engineering Mechanics Division*, *105*(4), 623-641.

Harajli, M, and Rteil, A., (2004). “Effect of confinement using fiber-reinforced polymer or fiber-reinforced concrete on seismic performance of gravity load-designed columns.” *ACI Struct J*., 101(1): 47–56.

Hognestad, E., (1951). “A study of combined bending and axial load in reinforced concrete members.” *University of Illinois Engineering Experiment Station Bulletin Series No. 399.* University of Illinois, Urbana, IL.

Kupfer, H. B., Hilsdorf, H. K., and Rüsch, H., (1969). “Behaviour of concrete under biaxial stresses.” *ACI Journal*, 66(8), 656-666.

Lam, L., and Teng J. G., (2003). “Design-oriented stress-strain model for FRP-confined concrete in rectangular columns.” *Journal of Reinforced Plastics and Composites*, 22(13), 1149-1186.

Mander, J. B., Priestley, M. J. N., and Park, R., (1984)."Seismic design of bridge piers." *Research Report No. 84-2*, Univ. of Canterbury, New Zealand.

Mander, J. B., Priestley, M. J. N., and Park, R., (1988). “Theoretical stress-strain model for confined concrete.” *Journal of Structural Engineering*, ASCE, 114(8), 1827-1849.

Memon, M., Sheikh, S., (2005). “Seismic resistance of square concrete columns retrofitted with glass fiber-reinforced polymer.” *ACI Struct J*., 102(5): 774–83.

Mirmiran, A., Shahawy, M., Samaan, M., and El Echary, H., (1998). “Effect of column parameters on FRP-confined concrete.” *Journal of Composite for Construction*, ASCE, 2(4), 175–185.

Pinto PE, Giuffre A. Comportamento del cemento armato per sollecitazioni cicliche di forte intensita. Giornale del Genio Civile 1970;5 (in Italian).

Popovics, S., (1973). “A numerical approach to the complete stress-strain curves of concrete.” Cem. Concr. Res., 3(5), 583-59.

Pulido, C., Saiidi, M. S., Sanders, D., and Itani, A., (2002). “Experimental validation and analysis of a CFRP-retrofit of a two-column bent.” *Proceedings of the Third International Conference on Composites in Infrastructure* (San Francisco, CA). Tucson, AZ: University of Arizona.

Rasheed, H. A., and Dinno, K. S., (1994). “An efficient nonlinear analysis of RC sections.” *Computers and Structures*, 53(3): 613-623.

Restrepol, J. I., and DeVino, B., (1996). “Enhancement of the axial load carrying capacity of reinforced concrete columns by means of fiberglass-epoxy jackets.” *Second International Conference on Advanced Composite Materials in Bridges and Structures*. Montreal, Canada.

Richard, R. M., and Abbott, B. J., (1975). “Versatile elastic-plastic stress-strain formula.” *Journal of the Engineering Mechanics Division*, *101*(4), 511-515.

Richart, F. E., Brandtzaeg, A., and Brown, R. L., (1929). “The failure of plain and spirally reinforced concrete in compression.” *Engineering Station Series Bulletin No. 190*, University of Illinois, Urbana.

Rocca S., Galati N., and Nanni, A., (2009). "Interaction diagram methodology for design of FRP-confined reinforced concrete columns." *Construction and Building Materials*, 23(4), 1508-1520.

Samaan, M., Mirmiran, A., and Shahawy, M., (1998). "Model of concrete confined by fiber composites." *J. Struct. Eng*., 124(9), 1025-1031.

Schickert, G., and Winkler, H., (1977). “Results of tests concerning strength and strain of concrete subjected to multiaxial compressive stresses.” *Deutscher Ausschuss fur Stahlbeton*, Heft 277, Berlin, West Germany.

Scott, B. D., Park, R., and Priestley, N., (1982). “Stress-strain behavior of concrete confined by overlapping hoops at low and high strain rates.” *ACI J.*, 79(1), 13-27.

Sheikh, S. A., and Uzumeri, S. M., (1982). “Analytical model for concrete confinement in tied columns.” *Journal of Structural Engineering*, ASCE, 108(12), 2703-2722.

Spoelstra, M. R., and Monti, G., (1999). “FRP-confined concrete model.” *Journal of Composites for Construction*, ASCE, 3(3), 143-150.

Ugural, A. C., and Fenster, S. K., (2003). “*Advanced strength and applied elasticity.”* 4th ed, Prentice Hall: New Jersey.

Wang, Y. C., and Hsu, K., (2007). “Design of FRP-wrapped reinforced concrete columns for enhancing axial load carrying capacity.” *Composite Structures*, 82(1), 132-139.

Wang, Y. C., and Restrepo, J. I., (2001). “Investigation of concentrically loaded reinforced concrete columns confined with glass fiber-reinforced polymer jackets” *ACI Structural Journal*, 98(3), 377-385.

Willam, K. J., and Warnke, E. P., (1975). "Constitutive model for the triaxial behavior of concrete." *International Association for Bridge and Structural Engineering Proceedings*, 19, 1-15.

Yu, T., Teng, J. G., Wong, Y. L., and Dong, S. L., (2010). “Finite element modeling of confined concrete-II: Plastic-damage model.” *Engineering Structures*, 32(3), 680-691.

Section II: Shear Force-Flexure-Axial Force Interaction in Rectangular Concrete Columns

Chapter 8 - Introduction

Background

Columns are structural members that are essential to most structures. Columns transfer loads mainly through axial compression. Under extreme conditions, columns can be subjected to the effect of combined axial load, bending moment, and shear. The knowledge of the full interaction domain is very important in light of the extreme load event imposed by AASHTO LRFD. The analysis of columns under extreme loading events requires accounting for all possible factors that contribute to the column's ultimate capacity, including the confinement effect. This necessitates the extension of the developed confined analysis procedure to account for shear interaction. There is a need to develop a tool that provides engineers with reliable prediction for the ultimate capacity of confined concrete columns under these extreme loading conditions.

Objectives

This part of the study aims to estimate the shear capacity of rectangular reinforced concrete columns under axial load and bending moment. To achieve that, a procedure based on AASHTO LRFD Bridge Design Specifications (2014) provisions and the simplified modified compression field theory (Bentz et al., 2006) is formulated. The developed procedure shall provide predictions for axial load-shear-bending moment interaction domain. The procedure will then be implemented in "KDOT Column Expert" analysis software to facilitate the process of obtaining the full interaction domain.

Scope

This section consists of five chapters that cover all the aspects involved in this part of the study. Chapter eight provides a brief introduction to the background and objectives of the study, in addition to the scope. Chapter nine comprises reviews of building codes and experimental work found in the literature. Chapter ten includes the formulation part, in which all equations used in the procedure are provided and described, and the implementation part, in which the proposed procedure is explained in detail. Chapter eleven reports on the results obtained from this study, including comparisons with experiments and sectional analysis software "Response-

2000" (Bentz, 2000), in addition to the discussion. Chapter twelve summarizes the conclusions of this study and provides recommendations for further future research work.

Chapter 9 - Literature Review

Review of Building Codes

In this section, a review of the shear analysis provisions from selected building codes is presented. The focus of this review will be on guidelines for rectangular non prestressed reinforced concrete columns subjected to combined axial, shear and flexure.

Japanese Code (2007)

The JSCE code (2007) assumes the shear resistance is provided by concrete (V_c) and steel (V_s). The steel contribution is calculated based on the truss theory assuming 45_o inclined compression struts. The equations provided next all utilize SI units (i.e. MPa for stresses, Newton for forces, mm for distances). The equations are as follows:

$$V = V_c + V_s \quad \textbf{(9-1)}$$

$$V_c = \frac{\beta_d \beta_p \beta_n f_{vcd} b d}{1.3} \quad \textbf{(9-2)}$$

$where\ f_{vcd} = 0.2\sqrt[3]{f_c'} \leq 0.72$

$$\beta_d = \sqrt[4]{\frac{1000}{d}}$$

$$\beta_p = \sqrt[3]{100\rho_w}$$

$$\rho_w = \frac{A_s}{bd}$$

$$\beta_n = \begin{cases} 1 + \frac{2M_o}{M} \leq 2, if\ P \geq 0 \\ 1 + \frac{4M_o}{M} \geq 0, if\ P < 0 \end{cases}$$

$M_o = moment\ necessary\ to\ cancel\ stress\ due\ to\ axial\ force\ at\ extreme\ tension\ fiber.$

$$V_s = \frac{A_v f_{yt} (\sin(\alpha) + \cos(\alpha)) d}{1.1 * 1.15} \quad \textbf{(9-3)}$$

$where\ \alpha = angle\ between\ stirrups\ and\ longitudinal\ axis.$

The code specifies that for cases where shear reinforcement is necessary, the spacing between stirrups shall not exceed neither half the effective depth, nor 300 mm.

Additionally, the code specifies an amount of shear reinforcement, which is required even if calculations deem shear reinforcement unnecessary. The minimum amount of shear reinforcement is obtained according to the following equation:

$$A_{v,min} = 0.0015(b.s) \quad \textbf{(9-4)}$$

For this case, the spacing should not exceed neither three quarters of the effective depth, nor 400 mm.

Eurocode 2 (2004)

The Eurocode 2 part 1 provides separate procedures for shear design in members based on the need for shear reinforcement. The equations provided next all utilize SI units (i.e. MPa for stresses, Newton for forces, mm for distances). For members no requiring shear reinforcement, the shear resistance is obtained as follows:

$$V = \left(0.12k\left(100\rho_l(f_c' - 1.6)\right)^{\frac{1}{3}} - 0.15\sigma_{cp}\right)bd \quad \textbf{(9-5)}$$

$$where\ \rho_l = \frac{A_{sl}}{bd} \leq 0.02$$

$$\sigma_{cp} = \frac{P}{A_c}$$

$$k = 1 + \sqrt{\frac{200}{d}} \leq 2$$

$$A_{sl} = area\ of\ tensile\ reinforcement$$

For this case, the shear value should not be taken less than the minimum obtained as follows:

$$V_{min} = \left(0.035\left(1 + \sqrt{\frac{200}{d}}\right)^{\frac{3}{2}}(f_c' - 1.6)^{\frac{1}{2}} - 0.15\sigma_{cp}\right)bd \quad \textbf{(9-6)}$$

For members requiring shear reinforcement, the code utilizes a truss model with variable angles. The angle of inclined struts is limited as follows:

$$1 \leq \cot(\theta) \leq 2.5 \quad \textbf{(9-7)}$$

The shear resistance is calculated as follows:

$$V = \frac{A_v}{s} z f_{yt} \cot(\theta) \leq \frac{v_1 f_{yt}}{\cot(\theta) + \tan(\theta)} bz \quad \textbf{(9-8)}$$

$$where\ v_1 = 0.6\left(1 - \frac{f_c' - 1.6}{250}\right)$$

$$z = inner\ lever\ arm\ corresponding\ to\ the\ maximum\ bending\ moment.$$

The maximum spacing of legs in a series of shear links should not exceed the value obtained from the following equation:

$$s_{max} = 0.75d \leq 600\ mm \quad \textbf{(9-9)}$$

It should be noted that the German code DIN 1045-1(2001) had been compiled in parallel to the Eurocode (Hawkins et al., 2005)). As a result, the provisions in both are similar. Some differences exist as the national values for some parameters might differ from those recommended in the Eurocode.

ACI 318-11 (2011)

The ACI 318-11 building code (2011) provisions determines the shear strength based on an average shear stress on the full effect cross section. For transversely reinforced members, it is assumed that a portion of the shear strength (V_n) is provided by the concrete (V_c), with the remainder provided by the transverse steel (V_s), as per the following equation:

$$V_n = V_c + V_s \quad \textbf{(9-10)}$$

The concrete contribution (V_c) for members subjected to combined axial (P), shear (V) and flexure (M) is obtained from the following equation:

$$V_c = 2\left(1 + \frac{P}{2000A_g}\right)\lambda\sqrt{f_c'}bd \quad \textbf{(9-11)}$$

Additionally, the code allows for a more detailed calculation of the shear in concrete, as per the following equations:

$$V_c = \left(1.9\lambda\sqrt{f_c'} + 2500\rho_w \frac{Vd}{M_m}\right)bd \quad \textbf{(9-12)}$$

$$M_m = M - P\frac{4h - d}{8} \quad \textbf{(9-13)}$$

$$V_c \leq 3.5\lambda\sqrt{f_c'}bd\sqrt{1 + \frac{P}{500A_g}} \quad \textbf{(9-14)}$$

The steel contribution is calculated from the following equation below. The limit on the maximum value was established to prevent concrete crushing. A larger section should be selected if this limit is exceeded.

$$V_s = \frac{A_v f_{yt}(\sin(\alpha) + \cos(\alpha)\, d}{s} \leq 8\sqrt{f_c'}bd \qquad \textbf{(9-15)}$$

where $\alpha = angle\ between\ stirrups\ and\ longitudinal\ axis.$

The code provisions specify a minimum amount of transverse reinforcement to prevent sudden failure due to rapid formation of inclined cracking. The minimum amount required is computed from the following equation:

$$A_{v,min} = 0.75\sqrt{f_c'}\frac{bs}{f_{yt}} \leq \frac{50bs}{f_{yt}} \qquad \textbf{(9-16)}$$

The code imposes limits on the maximum spacing of transverse reinforce, which depends on the shear resistance portion resisted by steel. The spacing limits are provided next:

$$s_{max} = \begin{cases} \min\left(\frac{d}{2}, 24\ in\right)\ if\ V_s \leq 4\sqrt{f_c'}bd \\ \min\left(\frac{d}{4}, 12\ in\right)\ if\ V_s > 4\sqrt{f_c'}bd \end{cases} \qquad \textbf{(9-17)}$$

AASHTO LRFD Bridge Design Specifications (2014)

The provisions adopted by AASHTO LRFD Bridge Design Specifications (2014) are based on the simplified modified compression field theory (Bentz et al., 2006). In their paper, Bentz and his coauthors proposed their method, and compared it with experimental results and predictions from ACI equations. They showed excellent matching with the experimental data, and that the predictions from the ACI equations were inconsistent. Hawkins and his coauthors (2005) evaluated multiple shear models, and found that the overall performance of the AASHTO LRFD provisions were good to reasonable in all evaluation categories. Their recommended method based purely on performance was the AASHTO LRFD approach. As the theory proved to be very accurate, it was the method of choice to determine the shear capacity of rectangular concrete columns in this study. It is noted that the Canadian Standards Association's Design of concrete structures CSA A23.3-04 standard (2004) is also based on the simplified compression field theory, and thus provides similar provisions. Further details on this theory will be provided in Chapter 10.

Experimental Studies

In this section, a review of selected experiments conducted on square and rectangular reinforced concrete columns is presented. Further details on the selected specimens' parameters and the experimental results can be found in Table 11-1 and Table 11-2, respectively.

Umehara and Jirsa (1982)

Umehara and Jirsa (1982) investigated shear failure in short reinforced concrete columns. In their study, a series of ten short columns with rectangular cross-section of 9 x 16 in section were tested and compared with square columns with 12 x 12 in cross-section tested previously. The main variables in their experiments were the loading direction, history and level of axial load. The cross-section was a 2/3 scale model of a prototype column. Longitudinal reinforcement consisted of ten #6 bars in order to ensure that the flexural capacity in both the strong and weak directions were in excess of the shear capacity. The capacity calculations were performed in accordance to the ACI 1977 building code. Transverse reinforcement was provided by deformed 6 mm bars (diameter = 0.24 in) spaced at 3.5 in. Large blocks monolithically casted bounded the ends of the test specimens. These blocks provided anchorage for the longitudinal bars and facilitated the attachment of loading systems to the specimens. High slump concrete was used to allow it to fill all voids due to the congestion of reinforcement. To compare with previous studies, an axial load of 120 kip, which corresponds to 40% of the axial load at balanced strain condition was applied. Two loading rams were used to apply lateral loads, and one for axial load. Loads cells attached to the rams measured the loads applied. The authors observed that for short columns, the angle of shear cracks at failure was less than 45^{o}. They stated that for specimens with diagonal unidirectional loading, the capacity could be estimated by an interaction line between the maximum capacities of columns under unidirectional loading along the principal axes.

Aboutaha et al. (1999)

Aboutaha et al. (1999) conducted an experimental program on the use of rectangular steel jackets to rehabilitate shear critical concrete columns. A total of 11 large rectangular columns with a cross-section of 18 x 36 in were tested. Eight columns were loaded in the weak direction and three columns were loaded in the strong axis. Four of these specimens were prepared as reference specimens; thus, they were not retrofitted with steel jackets. The longitudinal

reinforcement consisted of 16 #8 bars. For ties, #3 bars were spaced at 16 in. For the selected specimens, three transverse cross ties were provided at every other longitudinal bar along the height of the columns. Lateral loads were applied in increment of 10 kip. These columns were not subjected to axial loading. The detailing of the columns' reinforcement was based on ACI 318-56 and ACI-63 building codes. Testing showed that all unretrofitted specimens demonstrated shear failure. Column SC3, loaded in the weak direction, developed major shear cracks over the full height of the column at a lateral load of 90 kip. The column lost its lateral resistance due to the diagonal shear failure followed by concrete compression shear failure. Column, SC9, loaded in the strong direction, developed major shear cracks at 110 kip. The column exhibited compression shear failure at 130 kip. Both columns did not develop their nominal flexural capacity by failure.

Priestley et al. (1994)

Priestley et al. (1994a and 1994b) conducted two test programs. The first program included four reference circular columns and four columns retrofitted with steel jackets. The second program included three reference rectangular columns and three steel jacketed columns. As the scope defined for this research covers rectangular columns, the focus will be on the second test program. The rectangular columns had a cross- section of 16 x 24 in. Longitudinal reinforcement consisted of 22 #6 bars. Transverse reinforcement was provided by #2 ties at spacing of 5 in. The columns were subjected to an axial load of 114 kip. The columns exhibited brittle shear failure. Column R3A did not achieve its flexural strength. The angle of shear cracks reached 29^{o} from the column's axis at failure. Column R5A developed flexure shear cracks from both top and bottom of the column. The major shear crack was inclined at an angle of 25^{o} to the column's axis. Comparisons with prediction provided from ACI 318-89 design equations showed that actual shear capacity was more than 100% higher than these predictions.

Ousalem et al. (2003)

Ousalem et al. (2003) conducted an experimental program that consisted of seven rectangular concrete columns. The specimens were scaled to 1/3 of the actual columns. All specimens had a square cross-section with a side length of 11.81 in. The selected specimens had a total of 16 D13 (diameter = 0.5 in) bars. Transverse reinforcement provided by ties of D6 (diameter = 0.25 in) spaced at 1.97 in. The selected specimens were design to fail in shear.

Independent axial and lateral loads were applied to the specimens. For all specimens, the axial load was fixed at 121.4 kip. The failure in the selected specimens was based on truss mechanism. Collapse was observed to occur along inclines planes. Ousalem et al. investigated the effect of the lateral load pattern on the response of the columns. The observed that a larger number of cracks developed, and that the shear strength degradation was more pronounced under lateral loading with many hysteretic reversals.

Wight and Sozen (1973)

Wight and Sozen (1973) conducted experiments to investigate the mode of failure for reinforced concrete columns subjected to several reversals of loading. Twelve specimens were prepared with a cross-section of 6 x 12 in. The longitudinal reinforcement consisted of 4 #6 deformed bars. Transverse reinforcement was provided by either plain #2 bars or deformed #3 bars. Ties spacing varied between 2.5 in to 5 in depending on the specimen. The main variables in testing were the axial load, transverse reinforcement ratio, and required deflection ductility. A servoram was attached to the end of the specimen to apply a constant axial load. The axial load varied between 0 and 40 kip, depending on the specimen. A pair of hydraulic jacks applied the lateral displacement. It was observed that specimens with axial loads had higher ultimate shear capacities. Failure mechanism observed included yielding of the transverse reinforcement, spalling of the concrete cover, and crushing of concrete along inclined shear cracks.

Yarandi (2007)

Yarandi (2007) conducted an experimental program to evaluate the use of an external prestressing retrofitting system for concrete columns. The experiments included five unstrengthened rectangular concrete columns. The cross-section for the selected specimens was 13.78 x 27.56 in. Longitudinal reinforcement consisted of 12 #20 (diameter = 0.77 in) bars. Transverse reinforcement was provided by ties made of 6.35 mm bars (diameter = 0.25 in) for specimen RRC, and #10 hoop (diameter = 0.44 in) for specimen SRC. The transverse reinforcement was spaced at 11.81 in for all specimens. Axial loads applied were 291 kip and 339 kip for specimens RRC and SRC, respectively. Specimen SRC developed flexural cracks perpendicular to the direction of loading, followed by propagation of inclined shear cracks into the sides. Concrete cover spalled off near the base of the column. Shear cracks propagation continues into the sides with the formation of new diagonal cracks. Both longitudinal and

transverse reinforcement yielded. Specimen RRC developed flexural cracks that propagated towards the sides with an angle of inclination. The angle of inclination for one crack was obtained to be 45^{o}. New cracks formed as the propagation continued towards the sides. Both types of reinforcement reached yielding in this specimen. Failure was attributed to insufficient transverse reinforcement.

Wehbe et al. (1998)

Wehbe et al. (1998) performed experimental testing to examine the ductility capacity of rectangular reinforced concrete bridge columns. Four model bridge columns specimens were designed and tested. The variables considered in their study were the amount of transverse steel reinforcement, and the axial load applied. All specimens had a rectangular cross-section of 15 x 24 in. Longitudinal reinforcement consisted of 18 #6 rebars in each specimen. Transverse reinforcement was provided by #2 perimeter hoop, #2 cross ties in the long direction, and #3 cross ties in the weak direction. The specimens were divided into two groups based on the transverse reinforcement spacing. Group A had a tie spacing of 4.25 in, while group B had a tie spacing of 3.25 in. Specimens were subjected to a constant axial load and lateral load reversals in the strong direction. The specified axial load was applied first, then unidirectional lateral loading in the strong direction was then applied. The axial loads varied between 135 kip and 340 kip.

Pujol (2002)

Pujol (2002) conducted an experimental program that consisted of eight assemblies. Each test assembly consisted of two specimens joined by a center stub. Each specimen represented a cantilever column under axial load and a point transverse load applied at its end. All specimens had a rectangular cross-section of 6 x 12 in. Longitudinal reinforcement consisted of four #6 bars. Transverse reinforcement was provided by #2 hoops. The main variables in the tests were the spacing of transverse reinforcement, axial load, and displacement history. Spacing of transverse reinforcement was varied between 1.5 in and 3 in. The specimens were subjected to an axial load of either 30 kip or 60 kip. All specimens initially developed cracks perpendicular to the column axis. As the lateral load increased, the flexural cracks started deviating from the vertical. Yielding and light spalling of the concrete were observed. Columns with higher axial loads exhibited concrete spalling over a larger area. Failure was characterized by expansion and disintegration of the concrete close to the column base. It was observed that concrete within the

plastic hinge region was reduced to broken fragments. These fragments could still carry some loads due to the friction between them and the confinement supplied from the reinforcement cage.

Melek and Wallace (2004)

Melek and Wallace (2004) conducted an experimental program to investigate the behavior of full-scale columns with lap splices subjected to axial load and cyclic lateral load. Six square cantilever columns with a side length of 18 in were designed and tested. Longitudinal reinforcement consisted of eight #8 bars distributed uniformly along the sides of the section. Transverse reinforcement was provided by #3 hoops spacing at 18 in. The main test variables were the axial load level, column shear demand, and applied displacement history. The specimens were subjected to an axial load of either 120 kip, 240 kip, or 360 kip. From the test results, it was observed that flexural cracking initiated at the base of the column. These cracks propagated to the middle of the height of the column. Initial hairline shear cracks were observed, which increased as the load increased. Concrete crushing and concrete cover spalling were observed at failure.

Chapter 10 - Formulation and Implementation

In this chapter, the developed procedure based on the simplified modified compression field theory (Bentz et al., 2006) as adopted by AASHTO LRFD Bridge Design Specifications (2014) is presented. In the formulation part, the equations used will be presented and explained. In the implementation part, the procedure followed will be presented and clarified in detail. It should be noted that the equations presented are for non prestressed rectangular concrete columns.

Formulation

This section includes the equations provided in AASHTO LRFD (2014) that were used in the procedure. The limits imposed by the specification will also be presented and discussed.

Effective Section Dimensions

The simplified modified compression field theory assumes that the concrete shear stresses are uniformly distributed over an effective area defined by the two effective section dimensions. The effective web width (b_v) is defined as the minimum web width parallel to the neutral axis. For rectangular sections, which are the focus of this work, the effective web width is taken equal to the section width (b).

$$b_v = b \quad \textbf{(10-1)}$$

As for the effective shear depth, it is defined as the distance perpendicular to the neutral axis between the resultants of tensile and compressive forces induced in the section due to flexure only. The effective shear depth is obtained as follows:

$$d_v = \frac{M_n}{A_s f_y} > \max(0.9d_e, 0.72h) \quad \textbf{(10-2)}$$

$$d_e = d_s \ (for\ nonprestressed\ sections) \quad \textbf{(10-3)}$$

$where\ M_n = pure\ moment\ capacity.$

$A_s = area\ of\ tension\ reinforcement\ (below\ the\ geometric\ centroid).$

$f_y = yield\ strength\ of\ reinforcing\ bars.$

$h = section\ height.$

$d_s = distance\ from\ extreme\ compression\ fiber\ to\ the\ centroid\ of\ tensile\ reinf.$

Minimum Transverse Reinforcement

In order to control the propagation of diagonal cracks and improve the ductility of the section, a minimum amount if transverse reinforcement is necessary. This amount increases as the concrete strength (f'_c) increases, as is obtained from the following equation:

$$A_{v,min} = 0.0316\sqrt{f_c'}\frac{b_v s}{f_{yt}} \quad \textbf{(10-4)}$$

$where\ A_{v,min} = minimum\ area\ of\ transverse\ reinvofrcement\ within\ distance\ s.$

$f_c' = unconfined\ concrete\ compressive\ strength.$

$s = spacing\ of\ transverse\ reinforcement.$

$f_{yt} = yield\ strength\ of\ transverse\ bars.$

$f_{yt} \leq 100\ ksi.$

The amount of the transverse reinforcement affects the calculations. The case where transverse reinforcement available is greater than the minimum will be referred to as Case I. Otherwise, sections with less than the minimum will be referred to as Case II.

Maximum Spacing of Transverse Reinforcement

In order to provide sufficient crack control, sections with high shear stress (v_u) require closely spaced transverse reinforcement. The maximum allowable transverse reinforcement spacing (s_{max}) is determined as follows:

$$s_{max} = \begin{cases} \min(0.8d_v, 24\ in) & if\ v_u < 0.125f_c' \\ \min(0.4d_v, 12\ in) & if\ v_u \geq 0.125f_c' \end{cases} \quad \textbf{(10-5)}$$

$$v_u = \frac{V}{b_v d_v} \quad \textbf{(10-6)}$$

$where\ V = shear\ force\ at\ section.$

This limit is known as the spacing limit hereafter, and shall be checked to ensure that the section satisfies AASHTO LRFD (2014) requirements.

Determination of the Longitudinal Tensile Strain

Longitudinal tensile strain (ε_s) is obtained for the section at the centroid of tension reinforcement. Its value is obtained from the following expression:

$$\varepsilon_s = \frac{\frac{|M|}{d_v} + 0.5N + V}{E_s A_s} \leq 0.006 \quad \textbf{(10-7)}$$

$where\ M = applied\ bending\ moment.$

$N = applied\ axial\ force.$

$V = applied\ shear\ force\ (from\ previous\ step\ or\ iteration).$

$E_s = modulus\ of\ elasticty\ of\ steel.$

If the longitudinal strain value is obtained to be negative, this indicates that the section is in compression, and concrete area can be included in the calculations as follows:

$$\varepsilon_s = \frac{\frac{|M|}{d_v} + 0.5N + V}{E_s A_s + E_c A_{ct}} \geq -0.0004 \quad \textbf{(10-8)}$$

$where\ E_c = modulus\ of\ elasticity\ of\ concrete.$

$A_{ct} = concrete\ area\ on\ the\ tension\ side\ (below\ the\ geometric\ centroid).$

A limit on the value of moment is enforced for this equation, hereafter known as the minimum moment limit. The minimum value of moment to be taken in the analysis is expressed in the following equation:

$$M_{min} = V.d_v \quad \textbf{(10-9)}$$

Determination of Diagonal Compressive Stress Inclination

The angle of inclination of diagonal compressive stresses (θ), also taken as the angle between a strut and the longitudinal axis of the member, is obtained according to the following expression:

$$\theta = 29 + 3500\varepsilon_s \leq 75\ (in\ degrees) \quad \textbf{(10-10)}$$

This angle corresponds to inclination of the shear cracks developed in the section.

Determination of Cracked Concrete's Ability to Transmit Tension and Shear

The parameter (β) indicates the ability of diagonally cracked concrete to transfer tension and shear. Determining this parameter depends on the amount of transverse reinforcement, equation (10-1). For case I, the following equation can be used:

$$\beta = \frac{4.8}{1 + 750\varepsilon_s} \quad \textbf{(10-11)}$$

In Case II, where the transverse reinforcement is below the minimum required by AASHTO LRFD (2014), the crack spacing parameter (s_{xe}) is added to the equation as follows:

$$\beta = \frac{4.8}{(1+750\varepsilon_s)}\frac{51}{(39+s_{xe})} \quad \textbf{(10-12)}$$

$$s_{xe} = s_x \frac{1.38}{a_g + 0.63} \quad \textbf{(10-13)}$$

$$s_x = \min(d_v, s_l) \quad \textbf{(10-14)}$$

$where\ a_g = maximum\ aggregate\ size.$

$s_l = maximum\ spacing\ between\ layers\ of\ longitudenal\ crack\ control\ reinforcement.$

For longitudinal crack control reinforcement, the area in each layer (A_l) is limited by the following equation:

$$A_l \geq 0.003 b_v s_x \quad \textbf{(10-15)}$$

Nominal Shear Resistance

The shear resistance of a concrete member is obtained by summing the concrete component (V_c) and the steel component (V_s). The shear resistance may not exceed an upper limit, in order to prevent crushing of concrete before yielding of transverse reinforcement. This limit will be referred to as the crushing limit hereafter.

$$V_n = V_c + V_s \leq 0.25\, f_c' b_v d_v \quad \textbf{(10-16)}$$

The concrete contribution relies on the tensile and shear stresses induced in the concrete, while the shear contribution relies on the tensile stresses that develop in the transverse reinforcement. These components are obtained as follows:

$$V_c = 0.0316\beta\sqrt{f_c'} b_v d_v \quad \textbf{(10-17)}$$

$$V_s = \frac{A_v f_y d_v \big(\cot(\theta) + cot(\alpha)\big)\sin(\alpha)}{s} \quad \textbf{(10-18)}$$

$where\ \alpha = angle\ of\ inclination\ of\ transverse\ reinforcement.$

$A_v = area\ of\ shear\ reinfocement\ within\ distance\ s.$

For sections with closed stirrups, the steel component expression simplifies to:

$$V_s = \frac{A_v f_y d_v \cot(\theta)}{s} \quad \textbf{(10-19)}$$

Yielding Limit

The shear resistance was obtained from equation (10-16). This value does not consider the stress in longitudinal reinforcement bars. In order to determine the force induced in these bars, the equilibrium in the free body diagram (Figure 10-1) was examined by taking moments about point O.

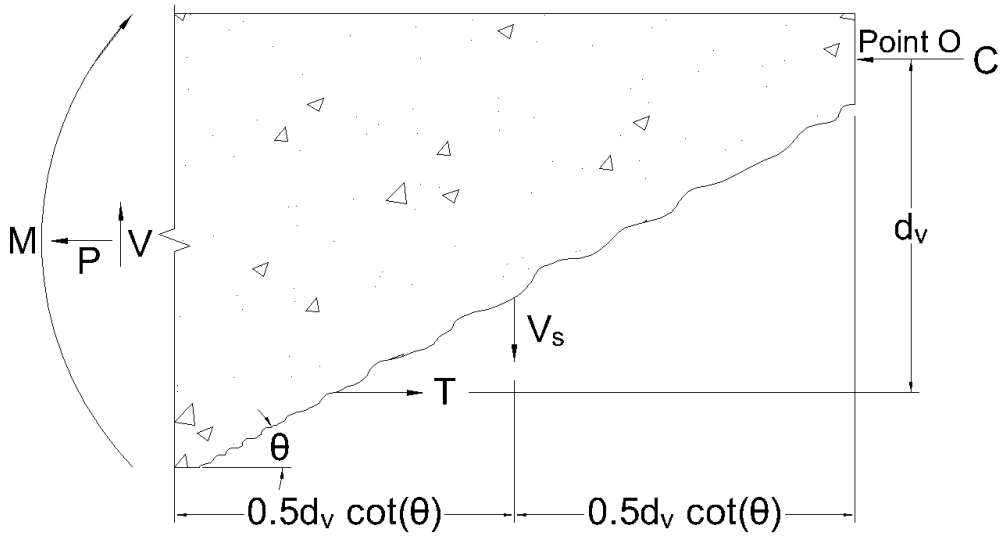

Figure 10-1: Free Body Diagram for Yielding Limit Derivation.

The resulting expression for the force in the longitudinal bars (F_l) after simplification is as follows:

$$F_l = T = \frac{M}{d_v} + \frac{P}{2} + V\cot(\theta) - 0.5V_s\cot(\theta) \leq A_s f_y \qquad \textbf{(10-20)}$$

If the force computed exceeds the yielding force, the shear is recalculated so that this limit is not exceeded per the following expression:

$$V = \frac{\left(A_s f_y - \frac{M}{d_v} - \frac{P}{2} + 0.5V_s\cot(\theta)\right)}{\cot(\theta)} \qquad \textbf{(10-21)}$$

Implementation

In this section, the procedure implemented will be described in light of the equations provided in the formulation part. First, an overview of the procedure will be presented. This part will explain how everything ties together. Then, details on calculations involved in each part will be presented in their respective sections.

Overview of the Procedure

To start the analysis, specific input parameters are required. These include parameters related to the section geometry, concrete, and longitudinal and transverse steel reinforcement. The parameters required are listed below:

- Geometric properties: This includes the width (b), height (h), clear cover (cc).
- Concrete properties: This includes the compressive strength (f'_c).
- Longitudinal steel properties: This includes the modulus of elasticity (E_s), yield strength (f_y), number of bars along the width, number of bars along the height, and steel bar diameter (d_l).
- Transverse steel properties: This includes the modulus of elasticity (E_s), yield strength (f_{yt}), ties spacing (s'), number of extra legs along the width, number of extra legs along the height, and tie bar diameter (d_t).

After providing the input parameters, the axial load (P_{inp}), which the section is subjected to, and for which the shear analysis is required, is input. The section is then analyzed under axial load and bending moment to obtain its interaction diagram at zero shear based on the procedure described by Abd El Fattah (2012). This procedure was developed to predict the axial force-bending moment interaction domain for confined sections, in which the moment is equal or greater than that in unconfined sections. The procedure implemented in KDOT Column Expert has been validated extensively. Two critical points are extracted from this analysis, which are the pure axial point (P_{max}) and the maximum moment at the input axial point level (M_{max}). The input axial load value must not exceed the maximum pure axial capacity of the section, as expressed below:

$$P_{inp} \leq P_{max} \qquad \textbf{(10-22)}$$

Next, the effective shear area is determined. These parameters include the effective web width (b_v) and the effective shear depth (d_v), which are evaluated according to equations (10-1) and (10-2), respectively. After that, the minimum amount of transverse reinforcement ($A_{v,min}$) is computed from equation (10-4), and compared to the amount of transverse reinforcement available in the section. Based on the comparison, the case number, which mainly affects the calculation of the factor (β), is determined. The concrete crushing limit is calculated from equation (10-16) at this stage as its value does not change for the same section. Next, the maximum value of shear (V_{max}) is determined. The minimum moment limit is crucial in this part

of the calculation which controls the first segment of the interaction diagram (Figure 10-2). Further details about the calculation of the maximum shear will be provided in the next section. If from the analysis, the moment value (M_{min}) specified by the AASHTO LRFD (2014) provisions exceeds the maximum moment capacity of the section at the applied axial load level (M_{max}), the analysis is stopped here, and the interaction diagram will consists of a straight line until the maximum moment value is reached. Otherwise, moment is incremented between the initial moment and maximum values, and the shear capacity is obtained at each increment. This calculation affects the inclined segment of the interaction diagram. The slope of this segment could change depending whether analysis limits are reached. As mentioned earlier, analysis is stopped when the moment applied reaches the maximum moment capacity of the section at the applied axial load level. Detailed explanation of the calculations involved in this step will be provided later in this chapter. A flowchart of this overview is provided in Figure 10-3.

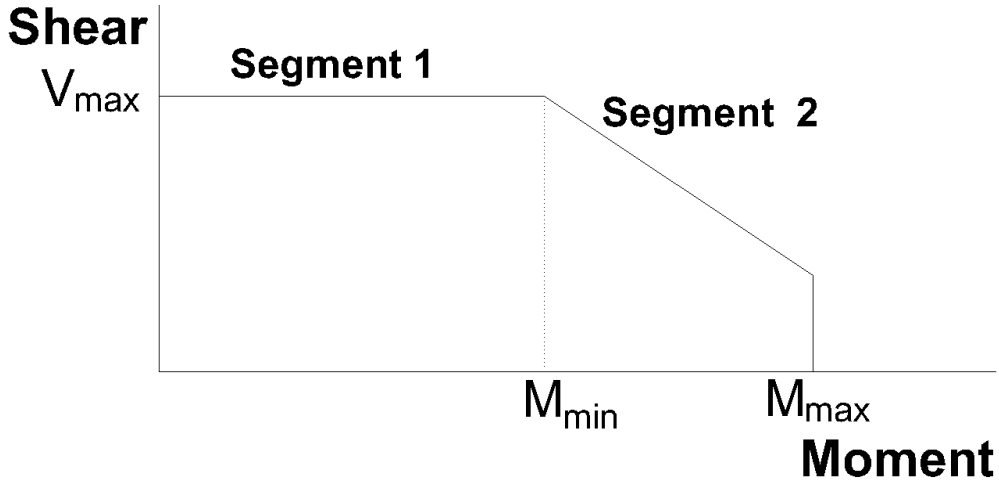

Figure 10-2: Sample Shear-Bending Moment Interaction Diagram.

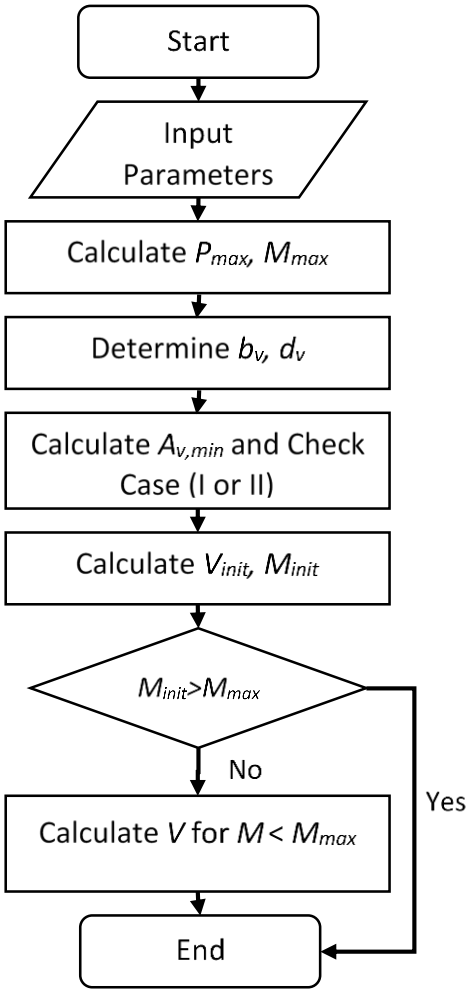

Figure 10-3: Flowchart for Overview of Shear Calculation Procedure.

General Shear Capacity Calculation Procedure

This procedure applies for all points after the moment applied exceeds the minimum moment (M_{min}) obtained from equation (10-9). The analysis is initiated with the last point obtained from the initial shear capacity procedure (M_{min}, V_{max}). The moment (M) is incremented between the minimum moment and the maximum moment for the section. This moment in addition to the previous shear value (V_{inp}) and the applied axial load (P_{inp}) are used to determine the axial strain from equation (10-8). After that, the inclination angle (θ) is computed from equation (10-10).Next, the amount of transverse reinforcement is compared to the minimum specified by AASHTO from equation (10-4). Case I corresponds to sections with an amount greater than the minimum, and for that, the transmissibility factor (β) is computed from equation

(10-11). Otherwise, Equations (10-12), (10-13) and (10-14) are used. In this case, the maximum aggregate size (a_g) is required as an input in equation (10-13). With the parameters θ and β known, the shear resistance provided by the concrete (V_c) and steel (V_s) can be calculated from equations (10-17) and (10-18), respectively. The shear resistance is then obtained from equation (10-16). The equation sets a maximum limit on the shear capacity to prevent premature crushing of concrete before yielding has occurred in the transverse reinforcement. The next limit to check for is the yielding tension limit. The force in the longitudinal bars (F_l) is calculated from equation (10-20), and compared to the maximum force at yielding. If the force computed exceeds the limit, the shear is recalculated so that the limit is not exceeded according to equation (10-21). The value obtained for shear (V_{out}) is compared with the input shear (V_{inp}). It is said that the calculation converges when the difference between the two shears does not exceed the specified tolerance.

$$\left|V_{out} - V_{inp}\right| \leq tolerance \qquad \textbf{(10-23)}$$

If convergence is achieved, the final shear value is taken as the section's shear capacity in combination with the current moment increment and the applied axial force. The moment is then increased, and the analysis is repeated until the maximum moment (M_{max}) is reached. In the case convergence is not achieved, the last output shear value is taken to be the new input value, and the analysis is then repeated until convergence is reached for that point. The resulting set of points is then used to plot the bending moment-shear force interaction diagram under the applied axial force. The described procedure is summarized in the flowchart shown in Figure 10-4.

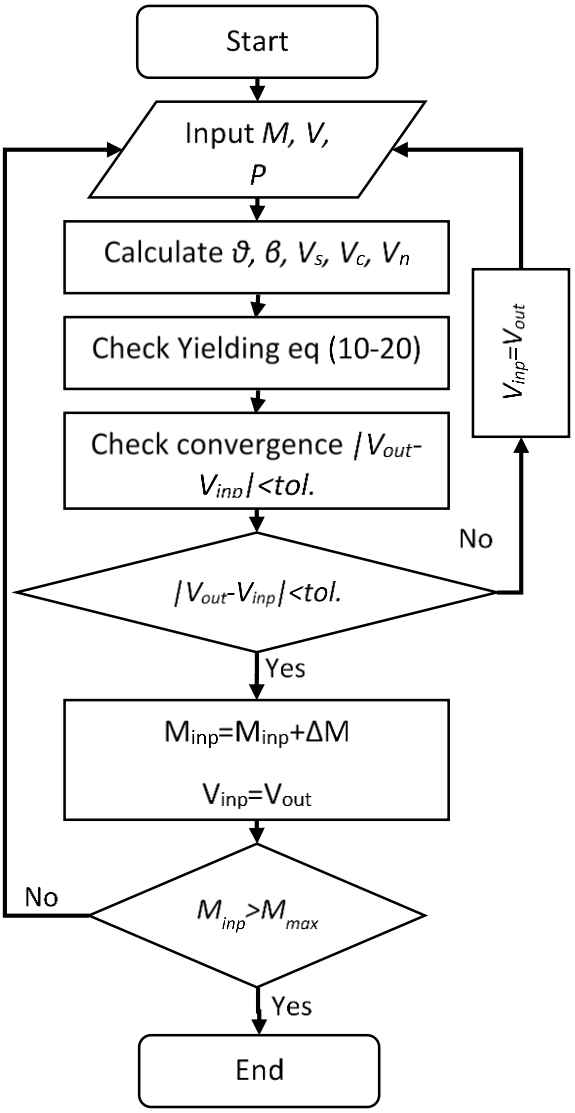

Figure 10-4: Flowchart for General Procedure.

Maximum Shear Capacity Calculation Procedure

For the first segment of the interaction diagram, the procedure to calculate the shear capacity differs from the general procedure due to the fact that no initial estimate for the shear capacity is available to calculate the longitudinal strain (ε_s) and base the new shear value on it. To accommodate that, the inclination angle is assumed (θ) to be 45°. This value is plugged into equation (10-10) to obtain the axial strain as follows:

$$\varepsilon_s = \frac{\theta - 29}{3500} = 4.57 \times 10^{-3} \qquad \textbf{(10-24)}$$

Next, depending on the present case, the shear transmission factor (β) is determined. For case I, it is obtained from equation (10-11) as follows:

$$\beta = \frac{4.8}{1 + 750\varepsilon_s} = 1.084 \qquad \textbf{(10-25)}$$

Otherwise, the factor is obtained from equation (10-12) accounting for the effect of bar spacing and aggregate size. The concrete's and steel's contributions to the shear capacity are then obtained from equations (10-17) and (10-18), respectively. The obtained shear capacity is then compared with the crushing limit as shown in equation (10-16). The minimum of the two is then taken to be the initial estimate of the shear capacity. This value is then taken as an input for the general procedure explained earlier, and a new axial strain value is computed. From that, a new estimate for the shear capacity is obtained after comparing with all of the applicable limits explained earlier. The iterations continue until the difference between the input and output shear values is within the defined tolerance. The value obtained after convergence is taken to be initial shear value (V_{init}). Using this value, the minimum moment (M_{min}) to be considered in the analysis is calculated from equation (10-9). This minimum moment is compared against the pure moment capacity of the section to ensure it does not exceed it. Now, the general procedure is applied to obtain the shear capacity at the minimum moment, using the initial shear value as the input shear. Iterations are performed until convergence is reached, and the new shear capacity is then taken to be the maximum shear capacity of the section (V_{max}). The initial shear value is then discarded. With this, two points have been calculated on the interaction diagram: (0, V_{max}) and (M_{min}, V_{max}). If the maximum moment capacity is reached, the analysis is then halted and the interaction diagram will consist of a horizontal line connecting the two points and a vertical line going down to (M_{max}, 0). Otherwise, the maximum shear is then taken as the input shear in the general procedure for the first point on the inclined portion of the interaction diagram. The calculations involved have been detailed in the previous section. Figure 10-5 provides a flowchart that summarizes the procedure.

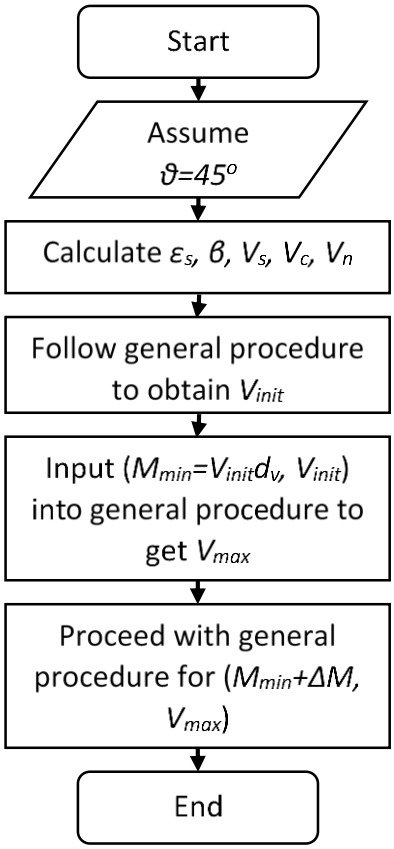

Figure 10-5: Flowchart for Maximum Shear Capacity Calculation

Chapter 11 - Results and Discussion

The aforementioned procedure was implemented in KDOT Column Expert software, which was then used to generate axial force-shear force-bending moment interaction diagrams. In the first section, a brief overview of the analysis program Response-2000 is provided (Bentz, 2000).The second section includes the validation of the proposed approach against Response-2000 and experimental points found in the literature.

Response-2000

Response-2000 is a sectional analysis program that was developed by Evan C. Bentz in a project supervised by Professor Michael P. Collins. (2000). The GUI-based software was written for Windows and is provided for free by the author. The software can calculate the strength and ductility of a reinforced concrete cross-section subjected to shear, moment, and axial load. The interaction domain is obtained based on the modified compression field theory (Vecchio and Collins, 1986). The program provides the shear-flexure interaction diagram based on AASHTO 1999 provisions under a constant axial load. In this work, the proposed procedure was based on the simplified modified compression field theory (Bentz, 2006) and AASHTO LRFD (2014) provisions. The interaction diagrams obtained were compared to those obtained from Response-2000 in the following section.

Experimental Validation

Sivaramakrishnan (2010) assembled a database of rectangular concrete columns based on the Pacific Earthquake Engineering Research center (PEER) structural database (Berry et al., 2004) and based on additional reports and manuscripts. From this database (Ghannoum and Sivaramakrishnan, 2012), the results obtained by Umehara and Jirsa (1982), Aboutaha et al. (1999), Priestley et al. (1994a and 1994b), Ousalem et al. (2003), Wight and Sozen (1973), Yarandi (2007), Wehbe et al. (1998), Pujol (2002), and Melek and Wallace (2004) were used to verify the proposed approach. The specifications for these specimens are provided in Table 11-1, while the experimental results are shown in Table 11-2. It should be noted that the x-axis was taken parallel to the width of the section, lateral loads were applied perpendicular to the x-axis, and only extra transverse reinforcement legs parallel to the lateral load (along y-axis) were reported, as traverse reinforcement in the other direction does not contribute to the shear

capacity. Finally, the database included columns that were tested in different configurations including single cantilever, double cantilever and double curvature. The induced bending moment for every configuration was calculated as follows:

$M_{max} = V_{max} * a$

$where\ M_{max} = maximum\ induced\ moment$

$V_{max} = maximum\ applied\ lateral\ load\ (shear)$

$a = shear\ span$

Table 11-1: Specimens' Properties.

Source	Code	b	h	cc	a	d_l	Bars in x	Bars in y	d_t	s'	Extra legs in x	f'_c	f_y	f_{yt}
Units (If Applicable)		in	in	in	in	in			in	in		psi	ksi	ksi
Umehara and Jirsa (1982)	CUS	9.00	16.00	0.98	17.91	0.75	2	5	0.24	3.50	0	5060.50	63.95	60.03
	CUW	16.00	9.00	0.98	17.91	0.75	5	2	0.24	3.50	2	5060.50	63.95	60.03
Aboutaha et al. (1999)	SC3	36.00	18.00	1.50	48.00	0.98	8	2	0.37	16.00	3	3175.50	62.93	58.00
	SC9	18.00	36.00	1.50	48.00	0.98	2	8	0.37	16.00	0	2320.00	62.93	58.00
Priestley et al. (1994a)	UnitR3A	24.00	16.00	0.87	48.00	0.75	8	5	0.25	5.00	0	5001.05	68.01	47.00
	UnitR5A	24.00	16.00	0.87	48.00	0.75	8	5	0.25	5.00	0	4700.90	68.01	47.00
Ousalem et al. (2003)	D13	11.81	11.81	1.08	17.72	0.50	5	5	0.25	1.97	0	3784.50	64.82	57.71
	D14	11.81	11.81	1.08	17.72	0.50	5	5	0.25	1.97	0	3784.50	64.82	57.71
Wight and Sozen (1973)	WI_40_033aE	6.00	12.00	1.38	34.49	0.75	2	2	0.25	5.00	0	5031.50	71.92	50.03
	WI_40_048E	6.00	12.00	1.38	34.49	0.75	2	2	0.25	3.50	0	3784.50	71.92	50.03
	WI_25_033_E	6.00	12.00	1.38	34.49	0.75	2	2	0.25	5.00	0	4872.00	71.92	50.03
	WI_0_048W	6.00	12.00	1.38	34.49	0.75	2	2	0.25	3.50	0	3749.70	71.92	50.03
	WI_40_147_E	6.00	12.00	1.25	34.49	0.75	2	2	0.37	2.52	0	4857.50	71.92	45.97
	WI_40_092_E	6.00	12.00	1.25	34.49	0.75	2	2	0.37	4.02	0	4857.50	71.92	45.97
Yarandi (2007)	RRC	13.78	27.56	1.77	59.06	0.77	4	4	0.25	11.81	0	5075.00	58.00	58.00
	SRC	13.78	27.56	1.78	59.06	0.77	4	4	0.44	11.81	0	6090.00	58.00	58.00
Wehbe et al. (1998)	A1	15.00	24.00	1.10	91.93	0.75	4	7	0.24	4.25	2	3944.00	64.96	62.06
	A2	15.00	24.00	1.10	91.93	0.75	4	7	0.24	4.25	2	3944.00	64.96	62.06
	B1	15.00	24.00	0.98	91.93	0.75	4	7	0.24	3.25	2	4074.50	64.96	62.06
	B2	15.00	24.00	0.98	91.93	0.75	4	7	0.24	3.25	2	4074.50	64.96	62.06
Pujol (2002)	10-2-3N	6.00	12.00	1.00	27.00	0.75	2	2	0.25	3.00	0	4888.73	65.68	59.58
	10-3-1.5N	6.00	12.00	1.00	27.00	0.75	2	2	0.25	1.50	0	4658.79	65.68	59.58
	10-3-3N	6.00	12.00	1.00	27.00	0.75	2	2	0.25	3.00	0	4338.87	65.68	59.58
	10-3-2.25N	6.00	12.00	1.00	27.00	0.75	2	2	0.25	2.25	0	3968.97	65.68	59.58
	20-3-3N	6.00	12.00	1.00	27.00	0.75	2	2	0.25	3.00	0	5278.63	65.68	59.58

Source	Code	b	h	cc	a	d_l	Bars in x	Bars in y	d_t	s'	Extra legs in x	f'_c	f_y	f_{yt}
	10-1-2.25N	6.00	12.00	1.00	27.00	0.75	2	2	0.25	2.25	0	5292.50	65.69	59.58
Melek and Wallace (2004)	S10MI	18.00	18.00	1.50	72.00	1.00	3	3	0.38	18.00	0	5255.00	74.00	69.70
	S20MI	18.00	18.00	1.50	72.00	1.00	3	3	0.38	18.00	0	5255.00	74.00	69.70
	S30MI	18.00	18.00	1.50	72.00	1.00	3	3	0.38	18.00	0	5255.00	74.00	69.70
	S20HI	18.00	18.00	1.50	66.00	1.00	3	3	0.38	18.00	0	5125.00	74.00	69.70
	S20HIN	18.00	18.00	1.50	66.00	1.00	3	3	0.38	18.00	0	5125.00	74.00	69.70
	S30XI	18.00	18.00	1.50	60.00	1.00	3	3	0.38	18.00	0	5125.00	74.00	69.70

Table 11-2: Experimental Results.

Source	Code	P	V_{max}	M_{max}
Units (If Applicable)		kip	kip	kip.ft
Umehara and Jirsa (1982)	CUS	120.15	72.53	108.27
	CUW	120.15	59.16	88.31
Aboutaha et al. (1999)	SC3	0.00	101.19	404.76
	SC9	0.00	144.49	577.97
Priestley et al. (1994b)	UnitR3A	114	141.10	564.40
	UnitR5A	114	169.70	678.80
Ousalem et al. (2003)	D13	121.39	59.77	88.25
	D14	121.39	66.47	98.14
Wight and Sozen (1973)	WI_40_033aE	42.49	22.20	63.81
	WI_40_048E	40.01	23.51	67.57
	WI_25_033_E	24.95	19.76	56.78
	WI_0_048W	0.00	22.11	63.54
	WI_40_147_E	40.01	26.92	77.38
	WI_40_092_E	40.01	27.24	78.29
Yarandi (2007)	RRC	290.89	116.24	572.07
	SRC	339.00	128.50	632.36

Source	Code	P	V_{max}	M_{max}
Wehbe et al. (1998)	A1	138.25	82.82	634.50
	A2	338.32	89.98	689.34
	B1	135.10	85.41	654.32
	B2	340.35	96.87	742.07
Pujol (2002)	10-2-3N	30.00	25.52	57.42
	10-3-1.5N	30.00	26.08	58.69
	10-3-3N	30.00	25.52	57.42
	10-3-2.25N	30.00	25.65	57.70
	20-3-3N	60.00	29.38	66.11
	10-1-2.25N	30.00	26.47	59.56
Melek and Wallace (2004)	S10MI	120.00	45.60	273.60
	S20MI	240.00	52.50	315.00
	S30MI	360.00	64.10	384.60
	S20HI	240.00	60.60	333.30
	S20HIN	240.00	60.10	330.55
	S30XI	360.00	76.60	383.00

Table 11-3: Notations for Specifications and Results.

Symbol	Description	Symbol	Description
b	Section width	f'_c	Concrete compressive strength
h	Section height	f_y	Longitudinal steel yield stress
cc	Clear cover	f_{yt}	Transverse steel yield stress
a	Shear span	P	Applied axial load
d_l	Longitudinal bar diameter	V_{max}	Maximum applied lateral load
d_t	Transverse bar diameter	M_{max}	Maximum induced bending moment
s’	Clear tie spacing		

In the next part, the shear-moment interaction diagram for each specimen at a constant axial load obtained from KDOT Column Expert and Response-2000 will be provided. The experimental data point corresponding to each specimen will be plotted as a point on the interaction diagram.

Umehara and Jirsa (1982)

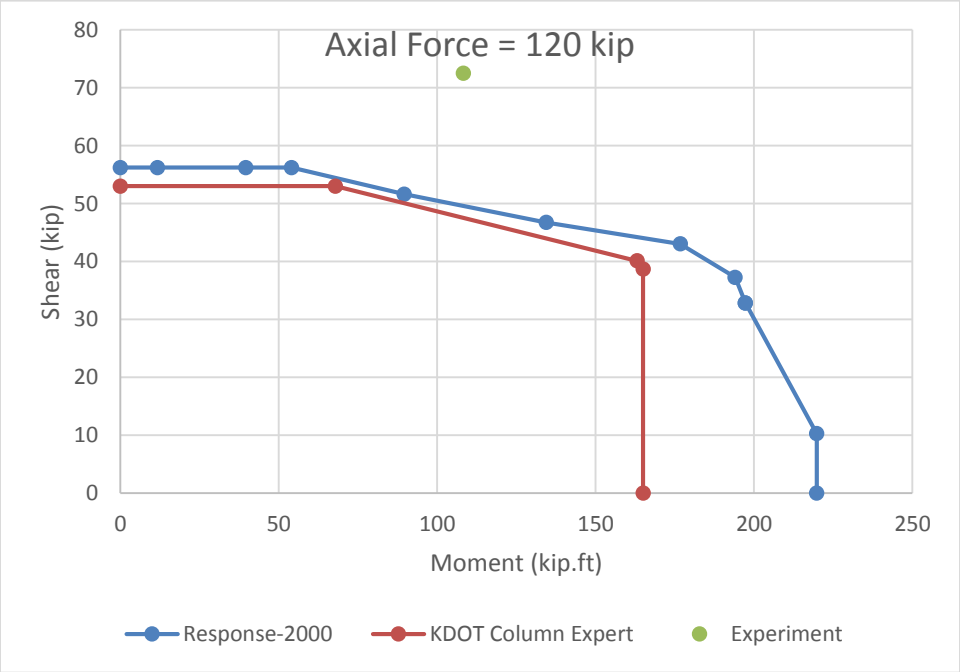

Figure 11-1: Interaction Diagram for Specimen CUS by Umehara and Jirsa (1982).

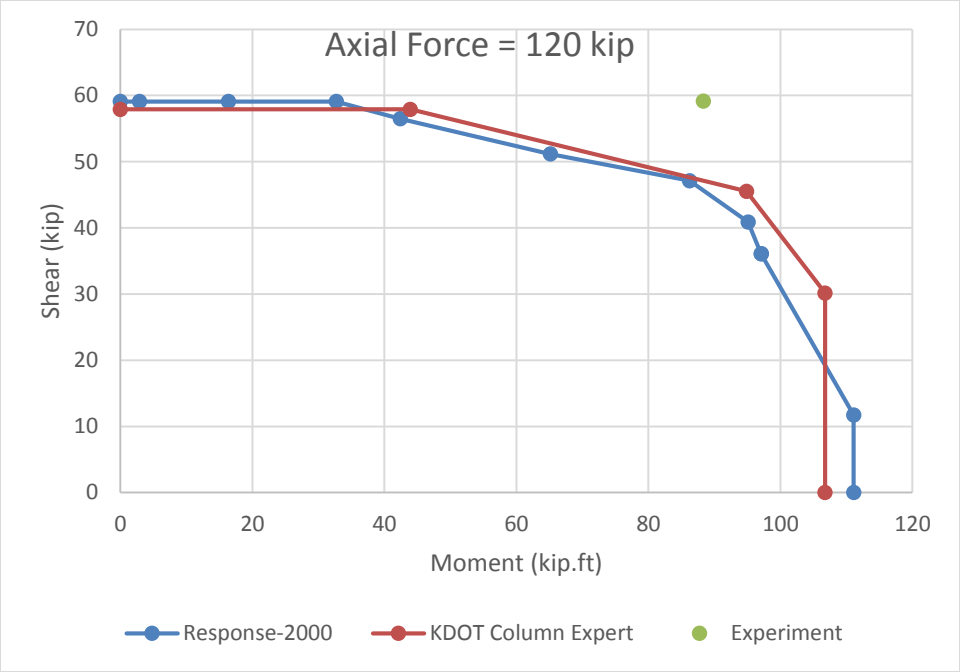

Figure 11-2: Interaction Diagram for Specimen CUW by Umehara and Jirsa (1982).

Figure 11-1 and Figure 11-2 show the shear-moment interaction diagrams obtained for specimens tested by Umehara and Jirsa (1982) using both Response-2000 and KDOT Column Expert. The axial load level was maintained at 120 kip for these specimens. The two specimens had identical properties, with the only difference being the direction of loading. Specimen CUS was loaded so that moment was induced about the strong axis, while specimen CUW was loaded so that moment was induced about the weak axis. For both specimens, the results from the two programs were conservative. It is observed that the curves were close to each other, except at the level of zero shear for specimen CUS. Response-2000 predicted higher moment capacity (219 k.ft) compared to the value obtained from KDOT Column Expert (165 k.ft). As described in , the formulation chapter, KDOT Column Expert was initially developed to predict the axial force-bending moment interaction domain for confined sections, in which the moment is equal or greater than that in unconfined sections. The procedure implemented in KDOT Column Expert has been validated extensively. Unfortunately, as the source code of Response-2000 was not available, further investigation was not possible. Overall, this case showed good agreement between the present procedure and experimental results.

Aboutaha et al. (1999)

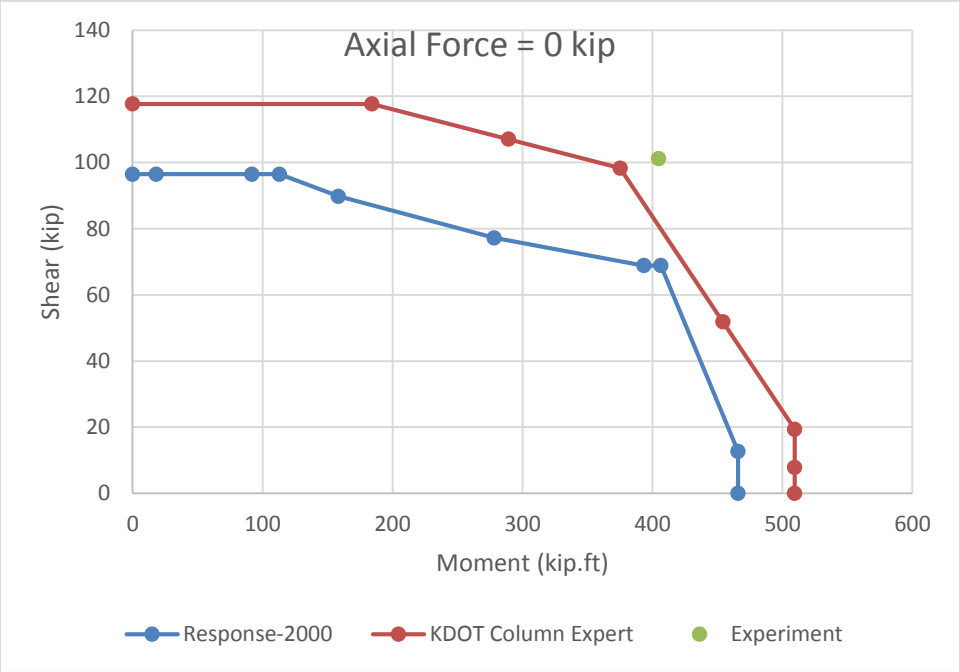

Figure 11-3: Interaction Diagram for Specimen SC3 by Aboutaha et al. (1999).

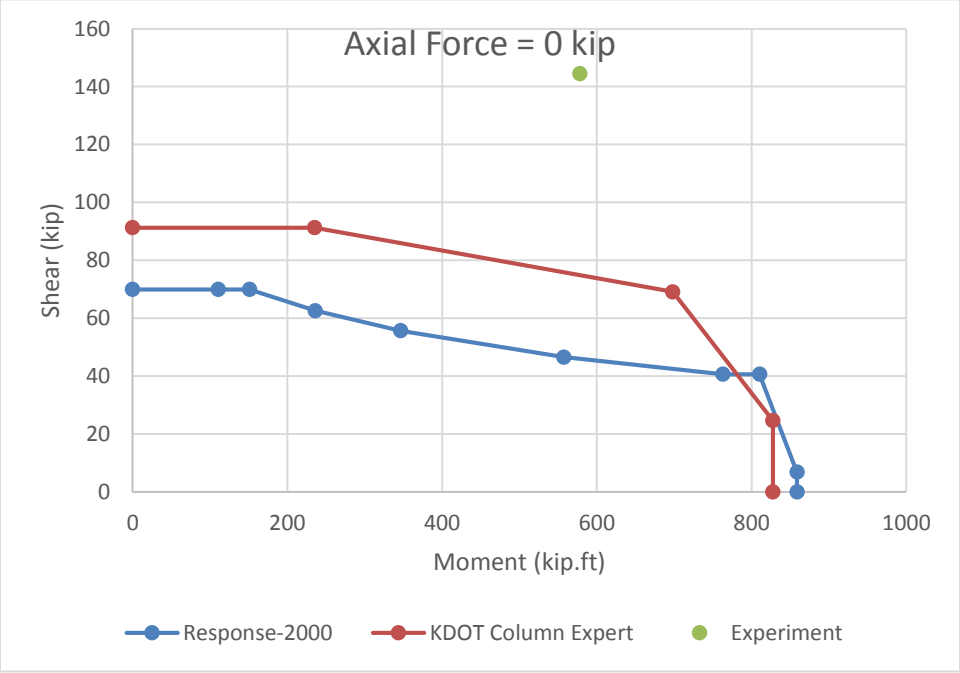

Figure 11-4: Interaction Diagram for Specimen SC9 by Aboutaha et al. (1999).

Figure 11-3 and Figure 11-4 show the shear-moment interaction diagrams obtained for specimens tested by Aboutaha et al. (1999) using both Response-2000 and KDOT Column Expert. No axial loads were applied to these specimens. The two specimens had identical

properties except for their compressive strength. Specimen SC3 was loaded so that moment was induced about the weak axis, while specimen SC9 was loaded so that moment was induced about the strong axis. For both specimens, the results from the two programs were conservative, especially for specimen SC9 as shown in Figure 11-4. KDOT Column Expert provided higher values for both shear and moment compared to Response-2000. Overall, this case showed good agreement between the present procedure and experimental results.

Priestley et al. (1994b)

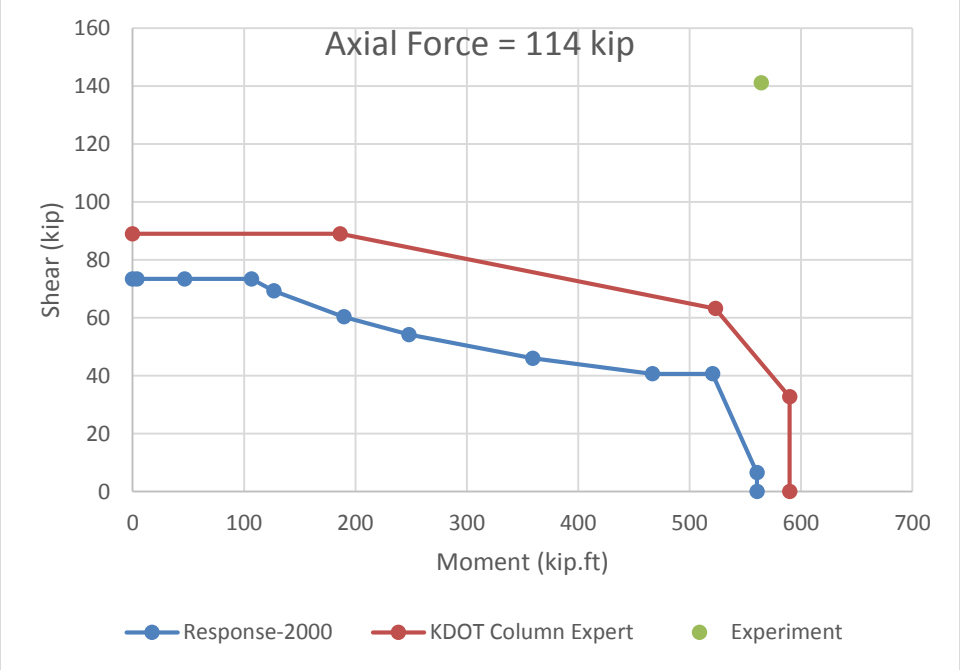

Figure 11-5: Interaction Diagram for Specimen UnitR3A by Priestley et al. (1994b).

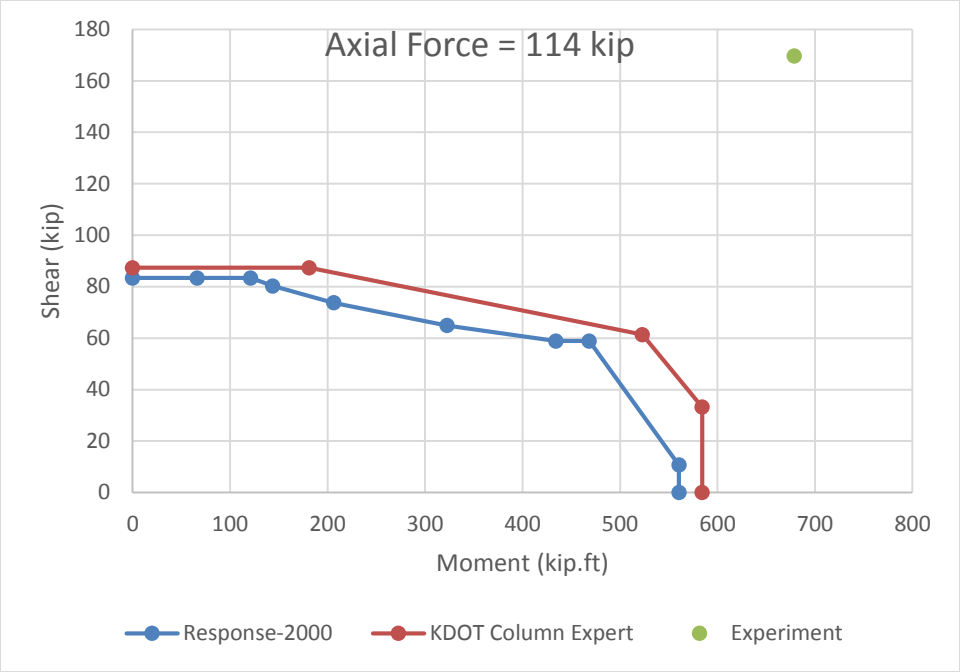

Figure 11-6: Interaction Diagram for Specimen UnitR5A by Priestley et al. (1994b).

Figure 11-5 and Figure 11-6 show the shear-moment interaction diagrams obtained for specimens tested by Priestley et al. (1994b) using both Response-2000 and KDOT Column Expert. The axial load was fixed at 114 kip for these specimens. The two specimens had identical properties except for their compressive strength. Both specimens were loaded so that moment was induced about the weak axis. For both specimens, the results from the two programs were conservative. KDOT Column Expert provided marginally higher values for both shear and moment compared to Response-2000. Overall, this case showed good agreement between the present procedure and experimental results.

Ousalem et al. (2003)

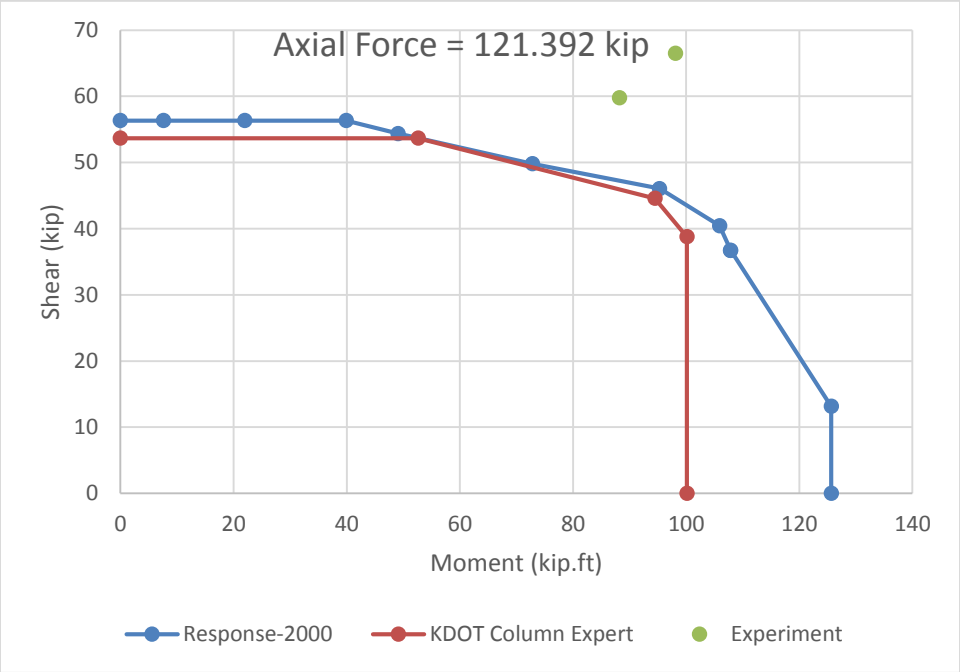

Figure 11-7: Interaction Diagram for Specimens D13 and D15 by Ousalem et al. (2003).

Figure 11-7 shows the shear-moment interaction diagrams obtained for specimens tested by Ousalem et al. (2003) using both Response-2000 and KDOT Column Expert. The axial load was fixed at 121.39 kip for these specimens. As the two specimens had identical properties, the experimental points are shown on the same figure. For both specimens, the results from the two programs were conservative. Again, a discrepancy in the moment capacity at zero shear is observed. Response-2000 predicted higher moment capacity (125 k.ft) compared to the value obtained from KDOT Column Expert (100 k.ft). Further investigation was not possible as the source code for Response-2000 was not available. Overall, this case showed good agreement between the present procedure and experimental results.

Wight and Sozen (1973)

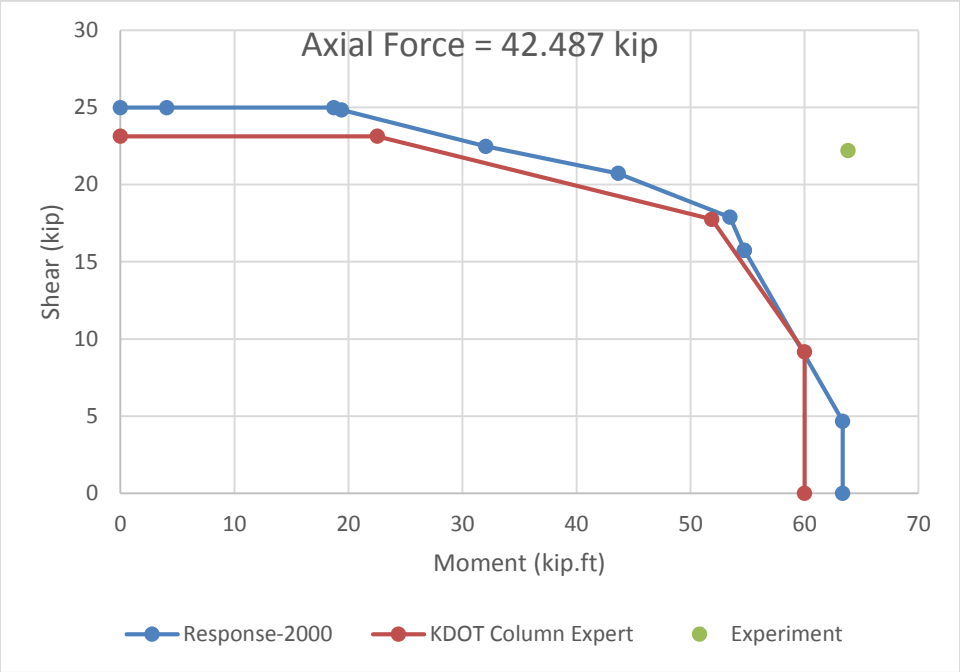

Figure 11-8: Interaction Diagram for Specimen WI_40_033aE by Wight and Sozen (1973).

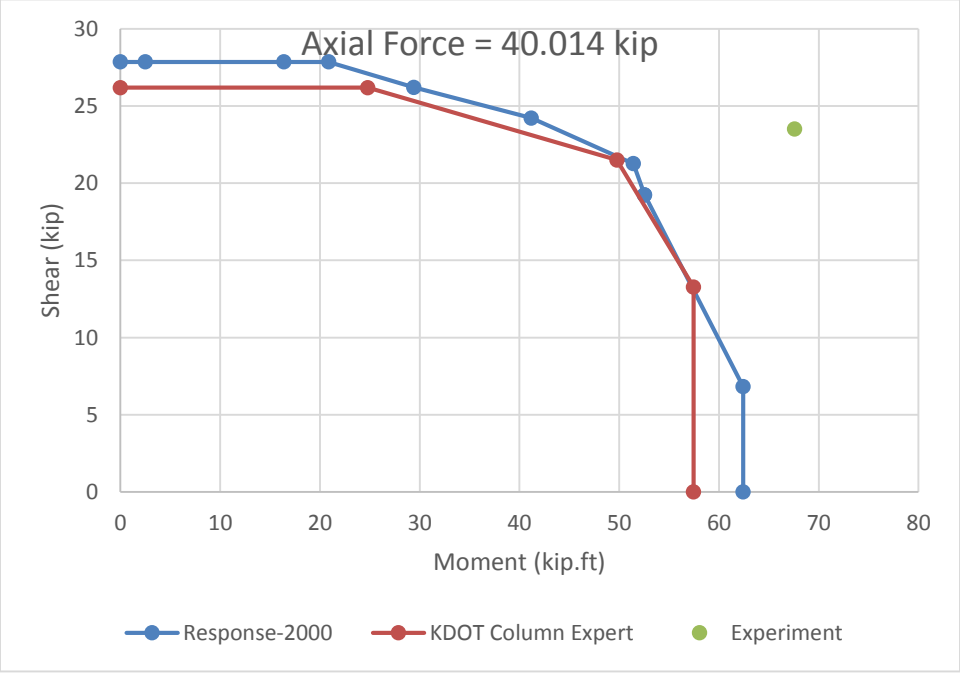

Figure 11-9: Interaction Diagram for Specimen WI_40_048E by Wight and Sozen (1973).

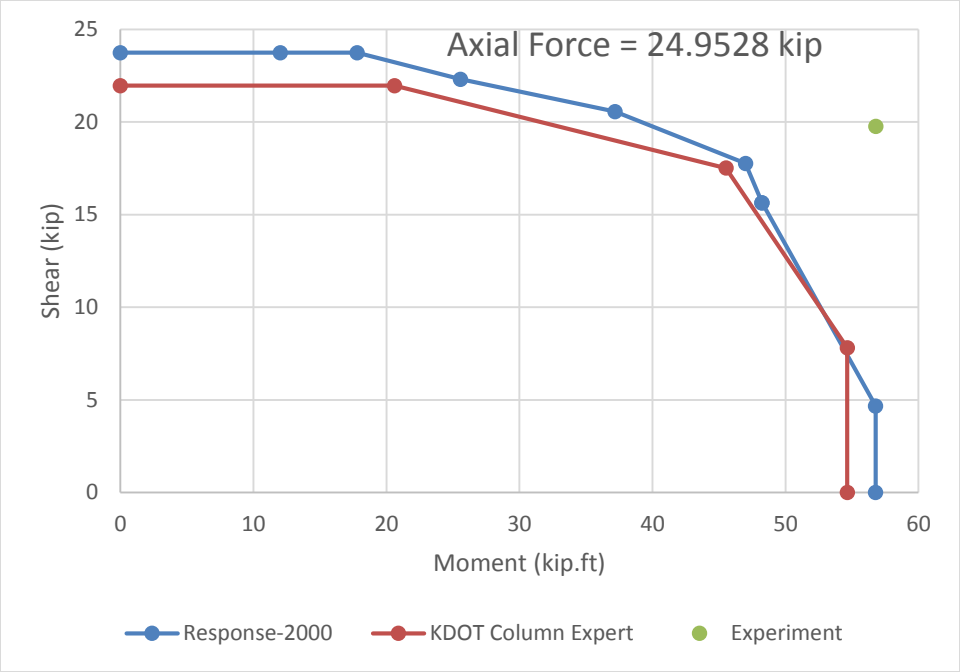

Figure 11-10: Interaction Diagram for Specimen WI_25_033_E by Wight and Sozen (1973).

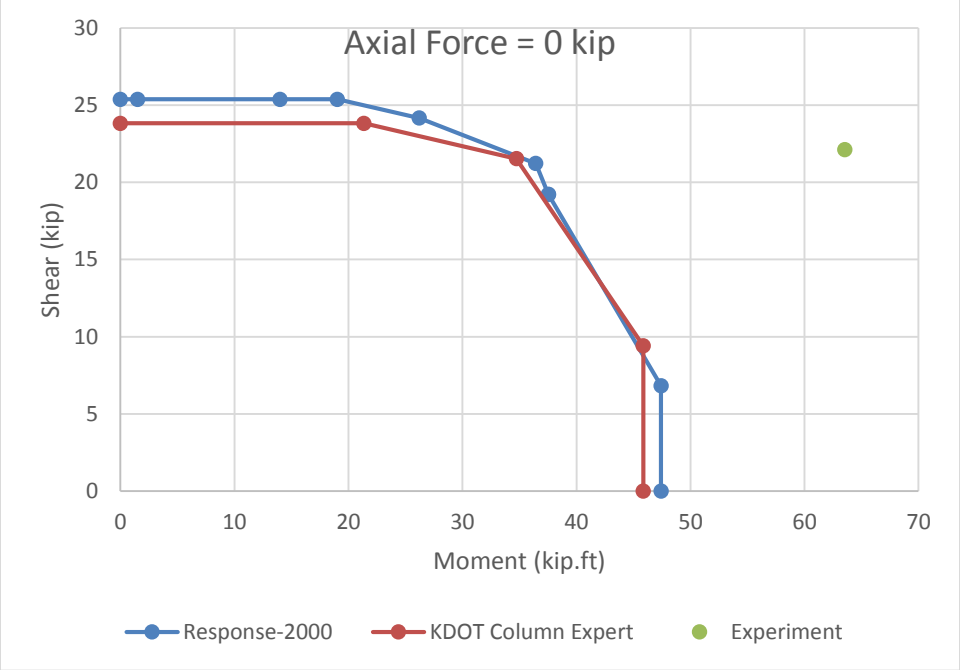

Figure 11-11: Interaction Diagram for Specimen WI_0_048W by Wight and Sozen (1973).

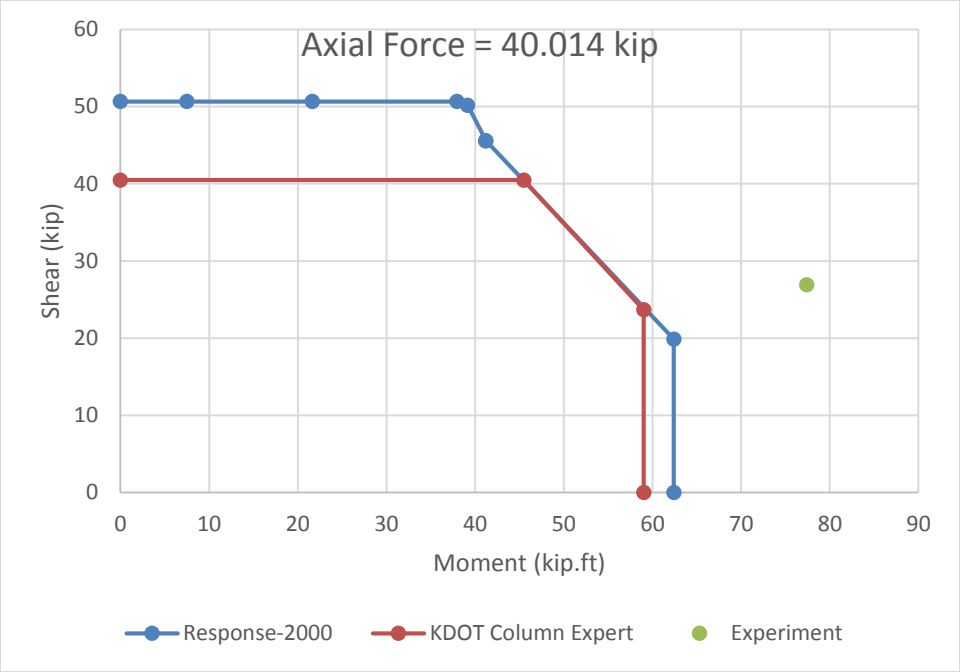

Figure 11-12: Interaction Diagram for Specimen WI_40_147_E by Wight and Sozen (1973).

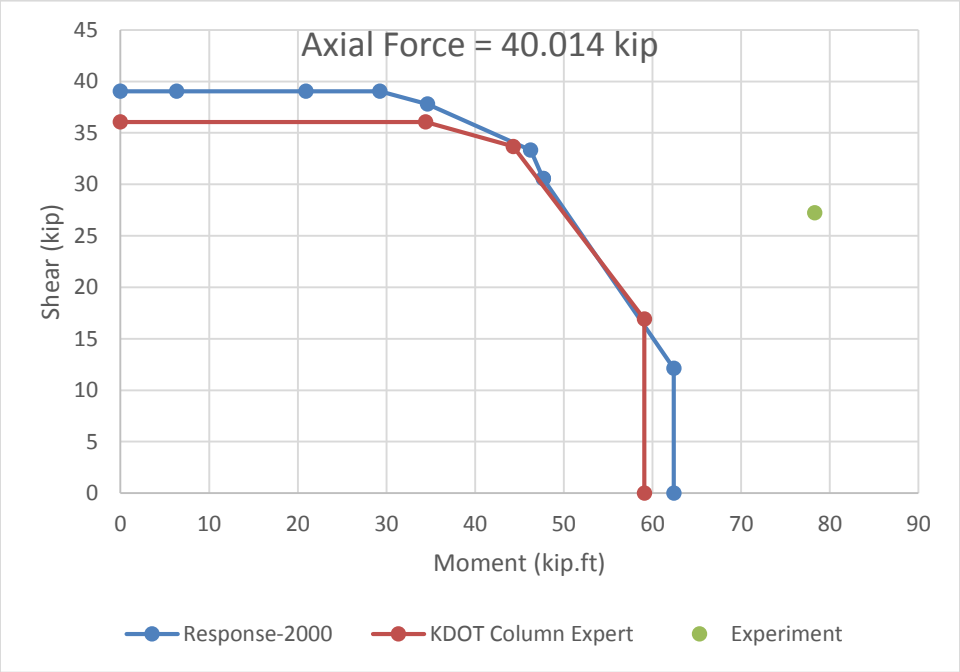

Figure 11-13: Interaction Diagram for Specimen WI_40_092_E by Wight and Sozen (1973).

Figure 11-8 to Figure 11-13 show the shear-moment interaction diagrams obtained for specimens tested by Wight and Sozen (1973) using both Response-2000 and KDOT Column Expert. The six specimens had the same geometric properties. The specimens could be divided in to two groups based on transverse reinforcement. The first group includes specimens

WI_40_033aE, WI_40_048E, WI_25_033_E, and WI_0_048W. The stirrups for the first group were made of #2 bars. The second group includes specimens WI_40_147_E and WI_40_092_E, and their stirrups were made of #3 bars. All specimens were loaded so that moment was induced about the strong axis. The axial load applied was different for each specimen and ranged from zero (specimen WI_0_048W) to 42.5 kip (specimen WI_40_033aE). The aforementioned figures show that the results from both programs were conservative. For these specimens, the curves obtained were close to each other, with Response-2000 values being marginally higher for both shear and moment compared to KDOT Column Expert. The only considerable difference is observed in the first portion of the curve for specimen WI_40_147_E. The shear value obtained from KDOT Column Expert was 40.47 kip, while the value obtained from Response-2000 was 50.65 kip. Further investigation into the discrepancy is provided next.

As described earlier in the implementation chapter, the first step is to determine an initial value for the shear at the prescribed axial load level with zero bending moment applied. This value was determined to be 60.65 kip. The effective shear depth was calculated to be 9 in, which agreed with the value provided by Response-2000. The minimum moment was then calculated per equation (10-9) as follows:

$$M_{min} = 60.65 * 9 = 545.85\ k.in = 45.49\ k.ft$$

The procedure is repeated with the new moment value included in the calculations. The shear for this case was obtained as 46.66 kip, however, the force induced in the longitudinal steel due to this combination per equation (10-20) was 70.41 kip, which was higher than the maximum force of 63.29 kip obtained in the yielding case. Due to the yielding limit, the shear had to be decreased to the value provided by equation (10-21), which came out to be 40.47 kip. This point is on both curves provided by KDOT Column Expert and Response-2000. As this point is the one that corresponds to the minimum value of moment (45.49 k.ft) specified by AASHTO LRFD (2014), the shear value cannot exceed the one obtained from this calculation. It appears that Response-2000 is allowing the moment to drop until the value of 39.15. As the source code is not available, further examination is not possible. Overall, this case showed good agreement between the proposed procedure and experimental results.

Yarandi (2007)

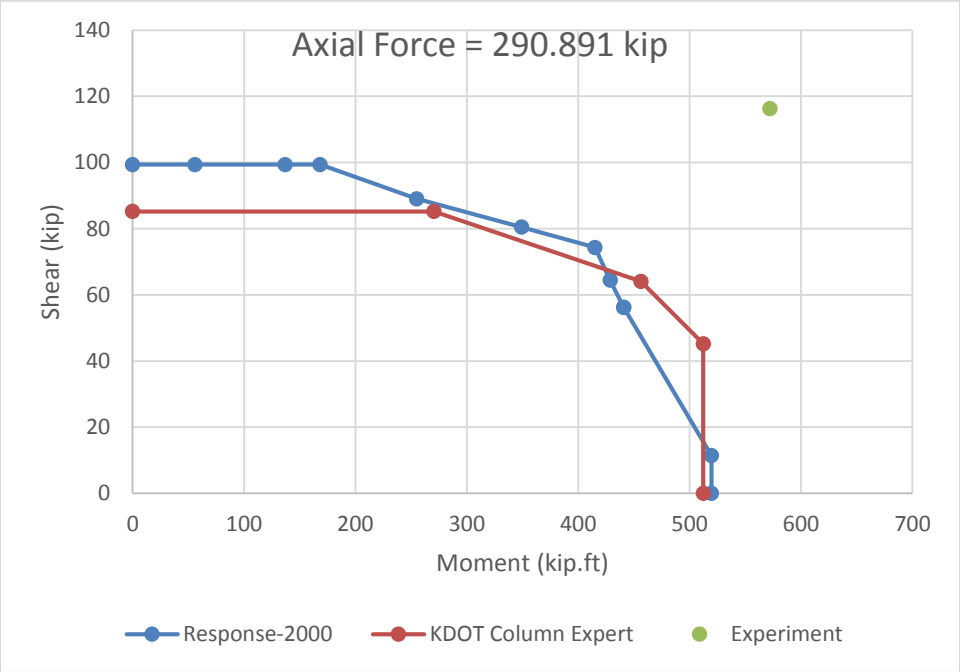

Figure 11-14: Interaction Diagram for Specimen RRC by Yarandi (2007).

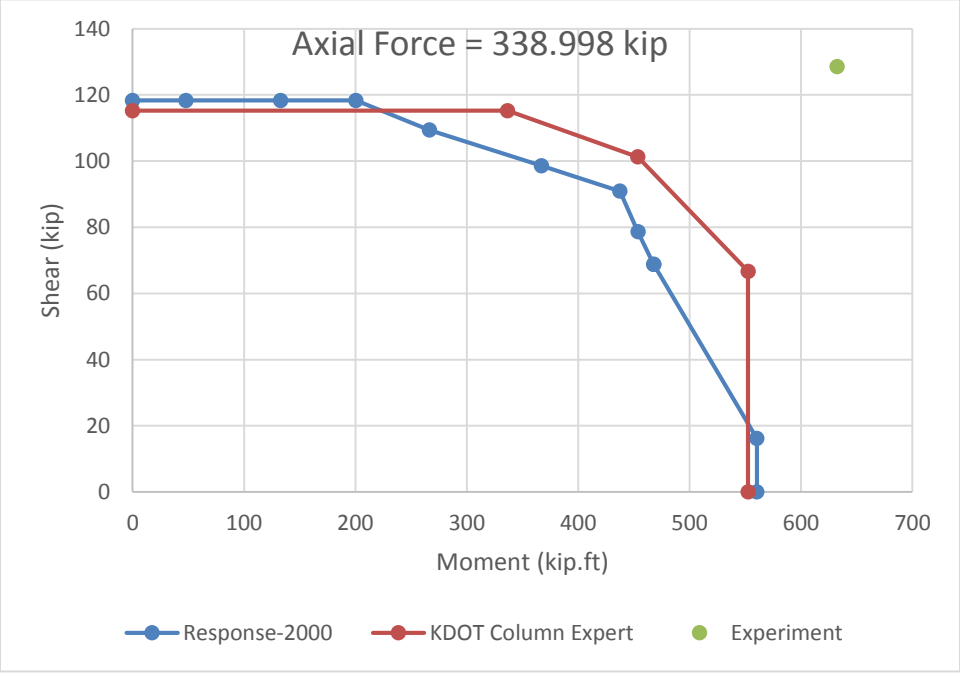

Figure 11-15: Interaction Diagram for Specimen SRC by Yarandi (2007).

Figure 11-14 and Figure 11-15 show the shear-moment interaction diagrams obtained for specimens tested by Yarandi (2007) using both Response-2000 and KDOT Column Expert. All specimens had the same geometry and rebar layout, but differed in the tie bar diameter and

compressive strength. Specimen RRC and specimen SRC were subjected to axial load of 291 kip and 339 kip, respectively. The curves for both specimen showed similar behavior and were conservative. Response-2000 provided higher values for shear capacity before the minimum moment limit imposed by AASHTO LRFD (2014) was reached, after which KDOT Column Expert provided higher predictions for the shear capacity. Overall, these cases showed good agreement between the present procedure and experimental results.

Wehbe et al. (1998)

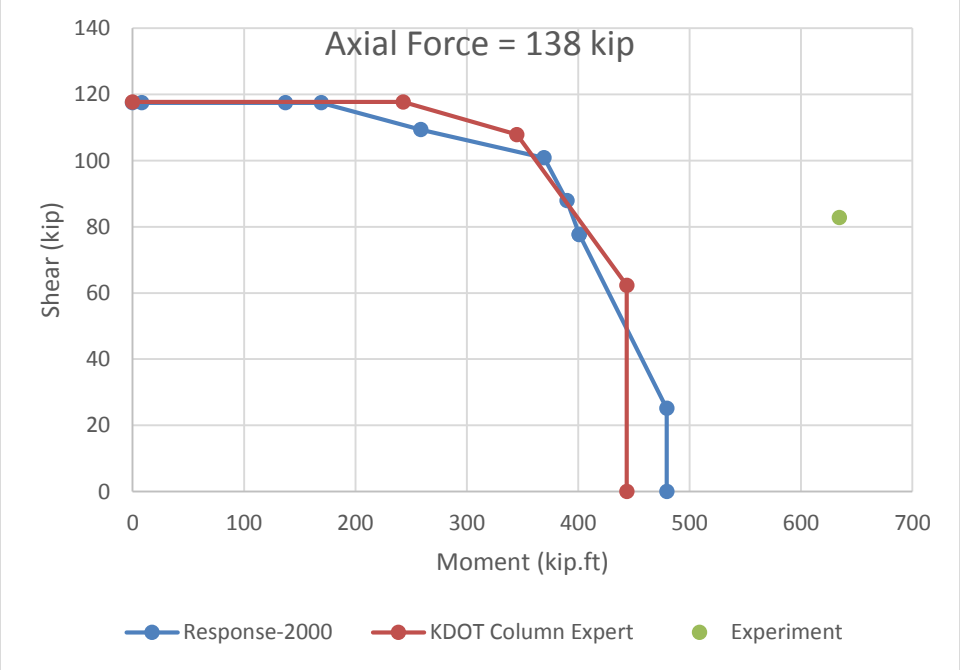

Figure 11-16: Interaction Diagram for Specimen A1 by Wehbe et al. (1998).

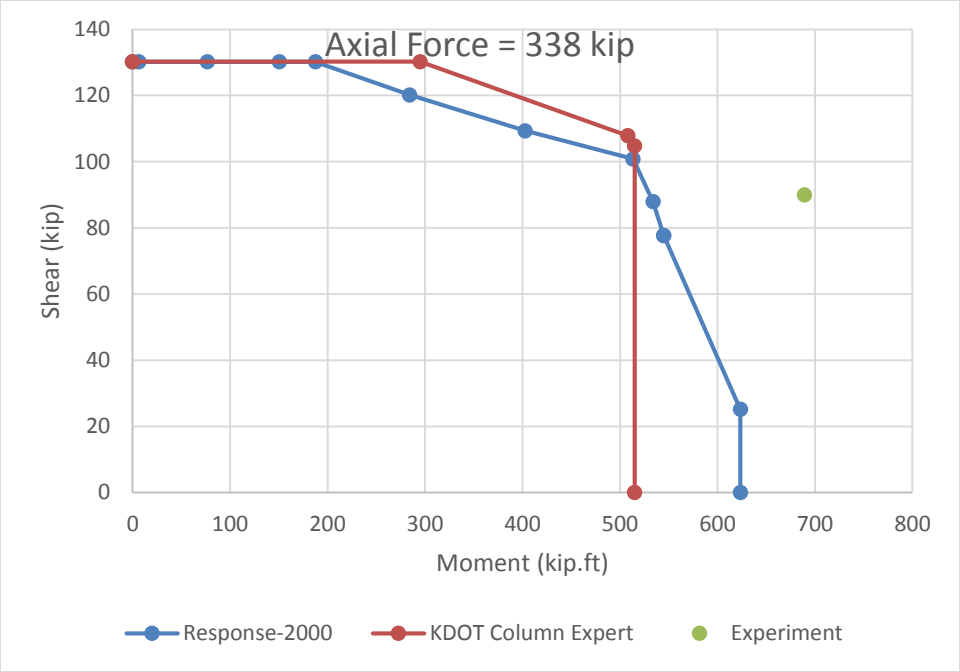

Figure 11-17: Interaction Diagram for Specimen A2 by Wehbe et al. (1998).

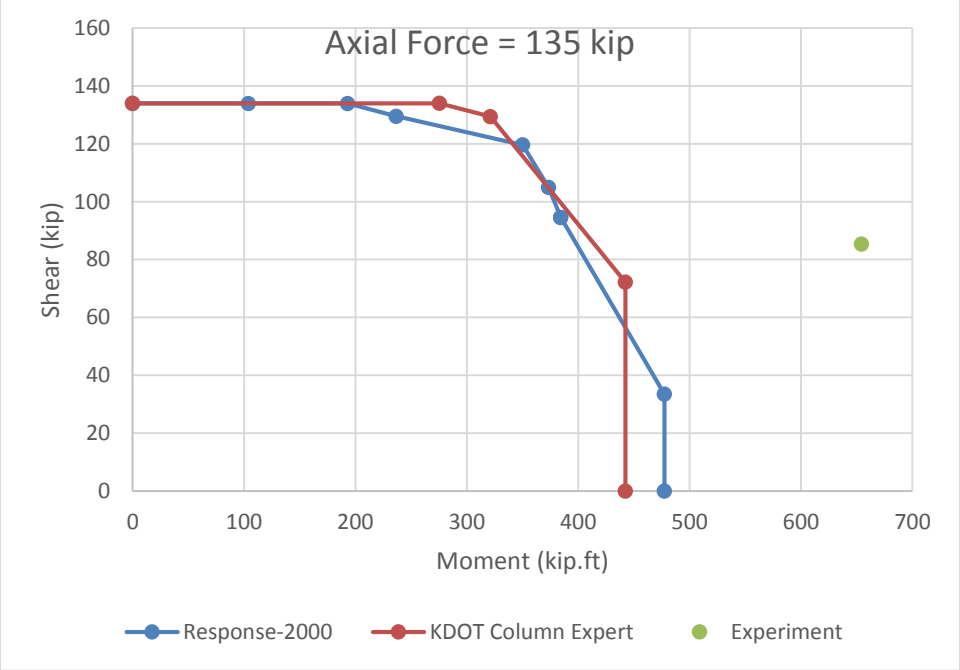

Figure 11-18: Interaction Diagram for Specimen B1 by Wehbe et al. (1998).

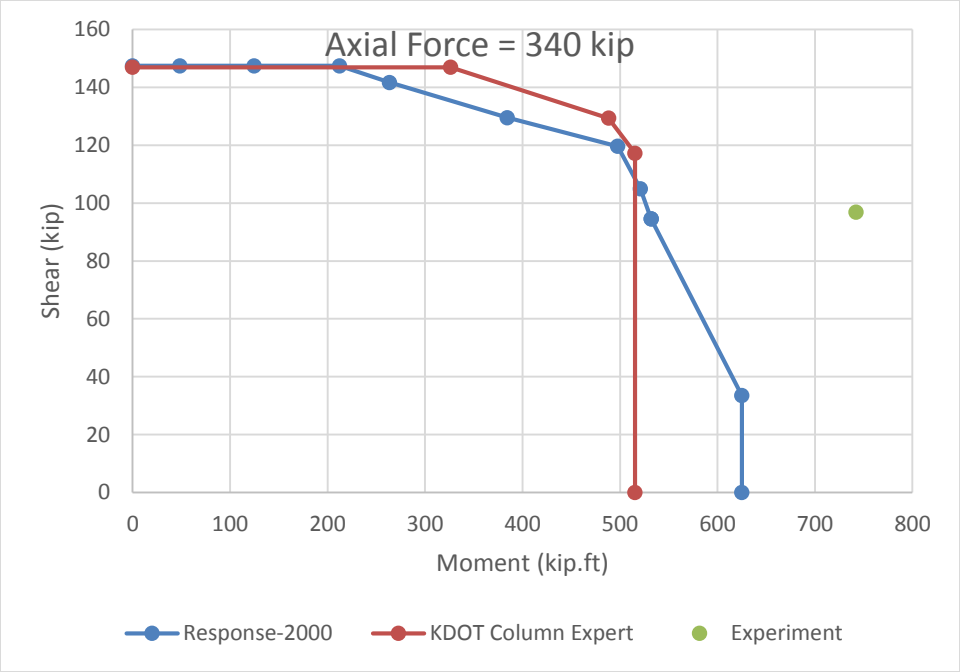

Figure 11-19: Interaction Diagram for Specimen B2 by Wehbe et al. (1998).

Figure 11-16 to Figure 11-19 show the shear-moment interaction diagrams obtained for specimens tested by Wehbe et al. (1998) using both Response-2000 and KDOT Column Expert. Specimens A1, A2, B1 and B2 were subjected to initial axial loads of 138 kip, 338 kip, 135 kip and 340 kip, respectively. The tie spacing for Group A and Group B was 4.25 in and 3.25 in, respectively. For all test specimens, the results from the two programs were mostly moment-dominated and they were conservative. The curves match well except for specimens A2 and B2, where the discrepancy in the moment capacity at zero shear is observed. Response-2000 predicted higher moment capacity (~625 k.ft for both specimens) compared to the value obtained from KDOT Column Expert (~515 k.ft for both specimens). Further investigation was not possible as the source code for Response-2000 was not available. Overall, this case showed good agreement between the present procedure and experimental results.

Pujol (2002)

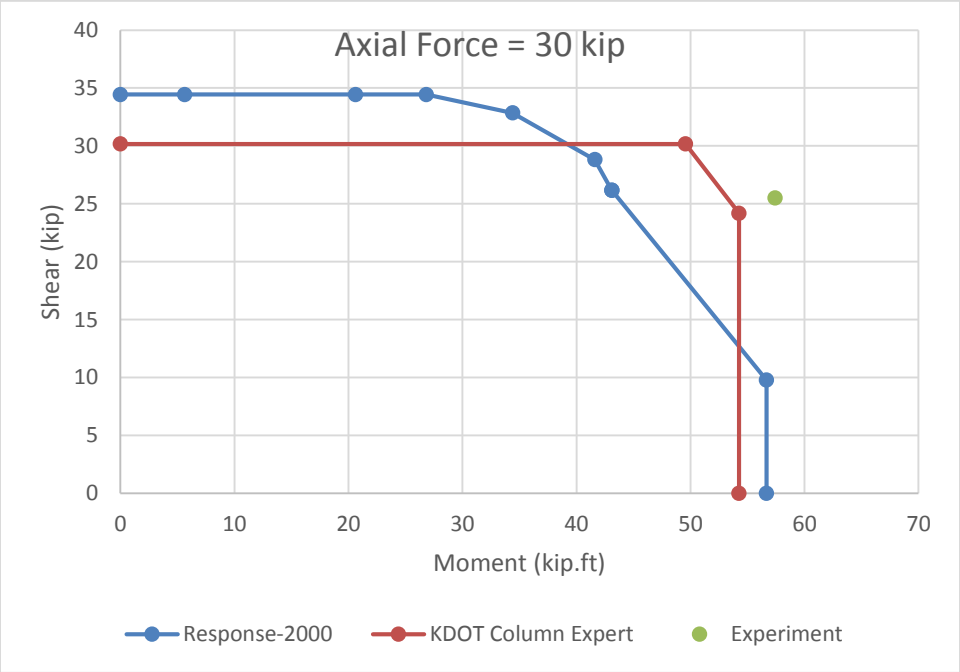

Figure 11-20: Interaction Diagram for Specimen 10-2-3N by Pujol (2002).

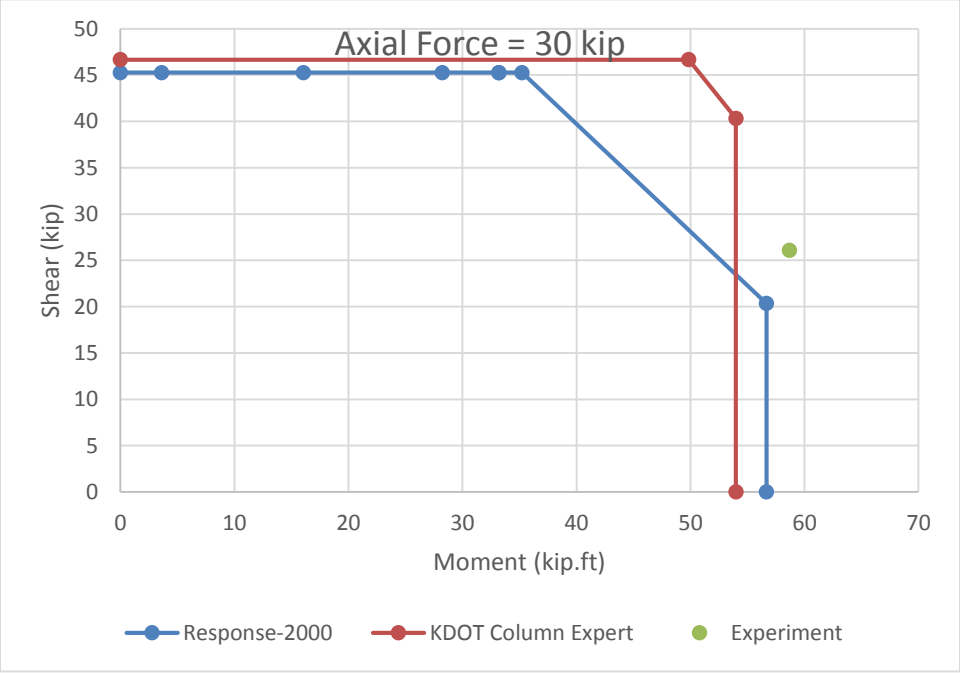

Figure 11-21: Interaction Diagram for Specimen 10-3-1.5N by Pujol (2002).

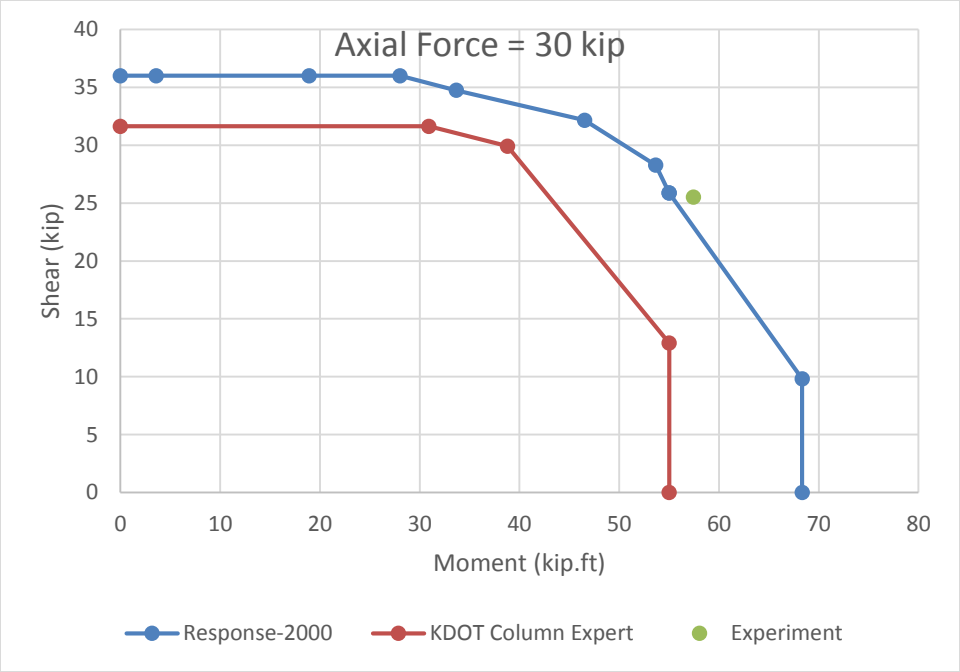

Figure 11-22: Interaction Diagram for Specimen 10-3-3N by Pujol (2002).

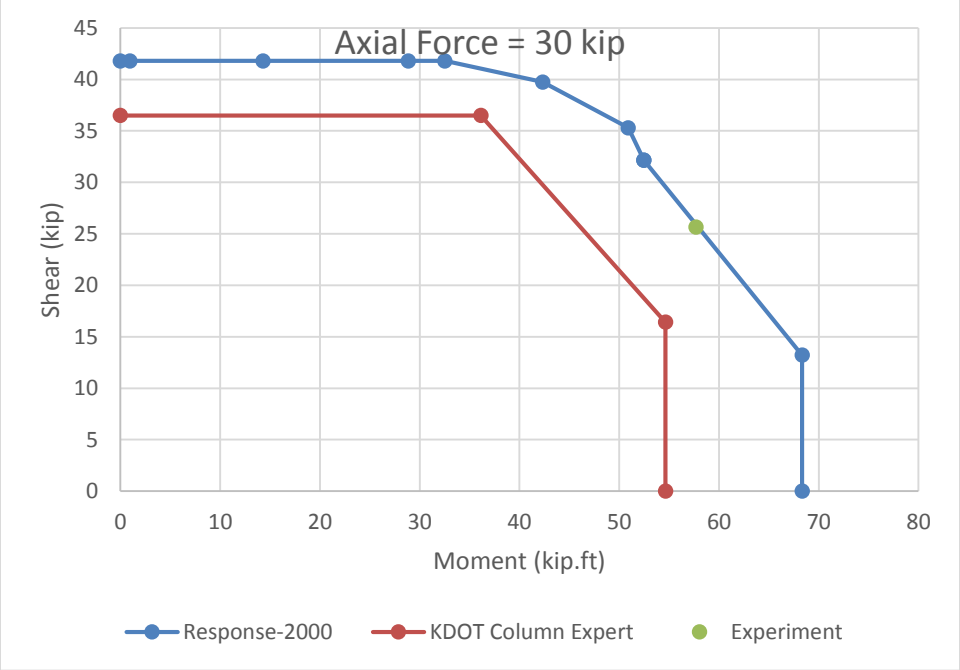

Figure 11-23: Interaction Diagram for Specimen 10-3-2.25N by Pujol (2002).

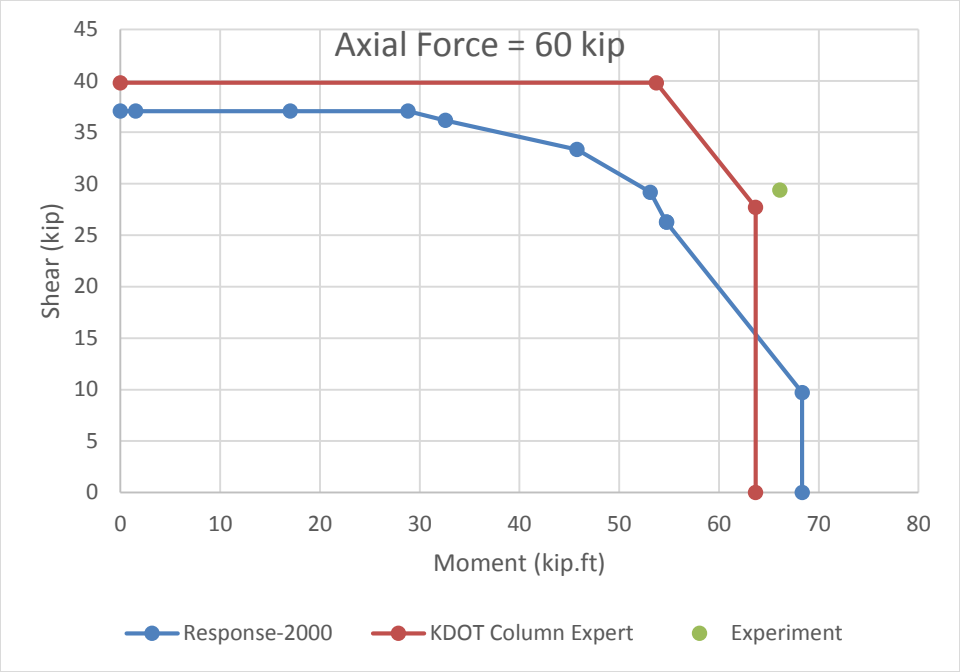

Figure 11-24: Interaction Diagram for Specimen 20-3-3N by Pujol (2002).

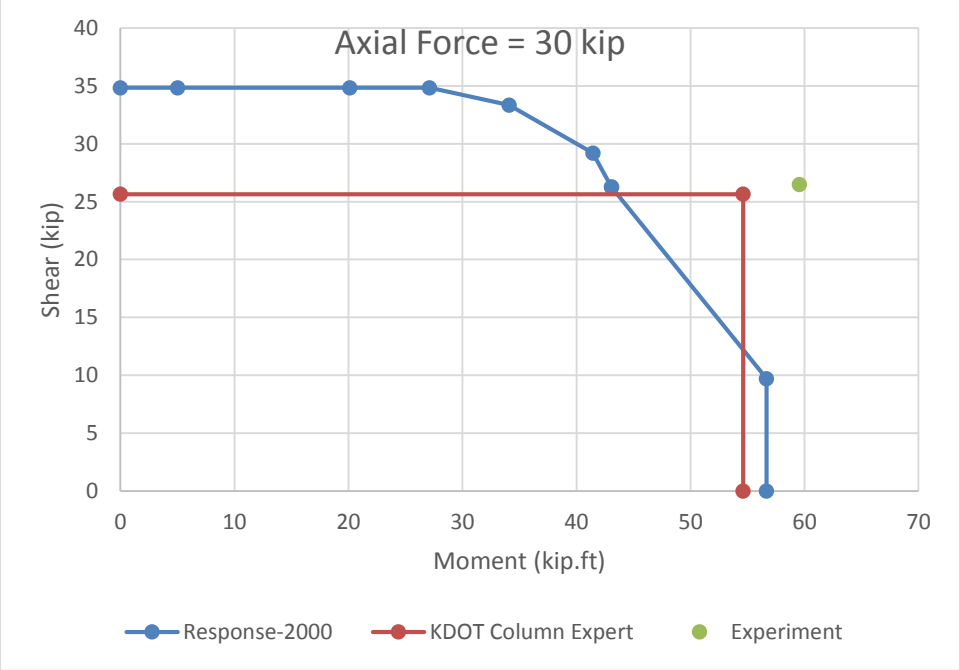

Figure 11-25: Interaction Diagram for Specimen 10-1-2.25N by Pujol (2002).

Figure 11-20 to Figure 11-25 show the shear-moment interaction diagrams obtained for specimens tested by Pujol (2002) using both Response-2000 and KDOT Column Expert. All specimens had the same geometry and rebar layout, but differed in the stirrup spacing and compressive strength. Specimen 20-3-3N was subjected to an axial load of 60 kip, while the

other specimens were subjected to an axial load of 30 kip. For all the specimens, the curves obtained were conservative. The curves for specimen 10-2-3N and specimen 10-3-1.5N (Figure 11-20 and Figure 11-21) behaved similarly. It was observed that the behavior close to zero moment level and zero shear level was close between KDOT Columns Expert and Response-2000. The major difference was observed after the moment exceeded the minimum allowed by AASHTO LRFD (2014). At this point the shear values provided by KDOT Column Expert were higher, however, they were still in agreement with the experimental results. Next, curves for specimen 10-3-3N and specimen 10-3-2.25N (Figure 11-22 and Figure 11-23) exhibited similar behavior. In this case, the results obtained from Response-2000 were higher. The experimental points were very close to the Response-2000 curve, and actually on the curve for specimen 10-3-2.25N. KDOT Column Expert provided more conservative results. The moment at zero shear demonstrated the discrepancy pointed out earlier in previous cases. Specimen 20-3-3N (Figure 11-24) showed similar behavior to the first two specimens, and both curves were conservative, with KDOT Column Expert predicting higher values for shear capacity. Finally, Figure 11-25 for specimen 10-1-2.25N showed that both curves were conservative, with KDOT Column Expert calculating larger values for the maximum moment on the section, which correlated very well with the experimental. For this case, the moment capacity of the section was reached before this value. Further examination showed similar behavior to that encountered in Wight and Sozen (1973) specimens, where the constant shear calculated as per AASHTO LRFD (2014) provisions induced a force in longitudinal bars that exceeded the yielding limit. This necessitated lowering the shear value so that the stress in the longitudinal bars would not exceed the yield stress. Overall, these cases showed good agreement between the present procedure and experimental results.

Melek and Wallace (2004)

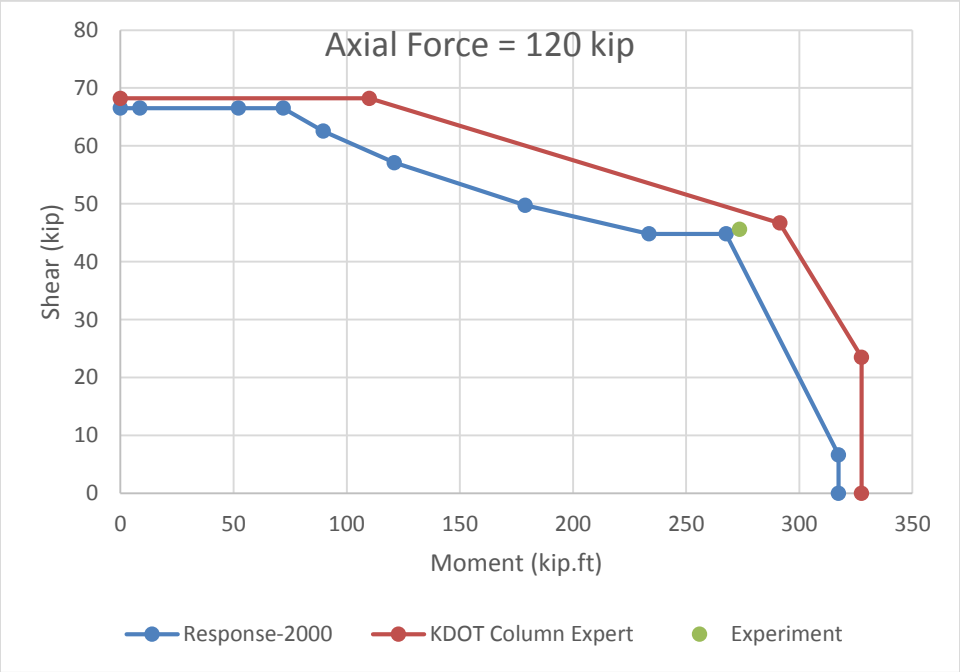

Figure 11-26: Interaction Diagram for Specimen S10MI by Melek and Wallace (2004).

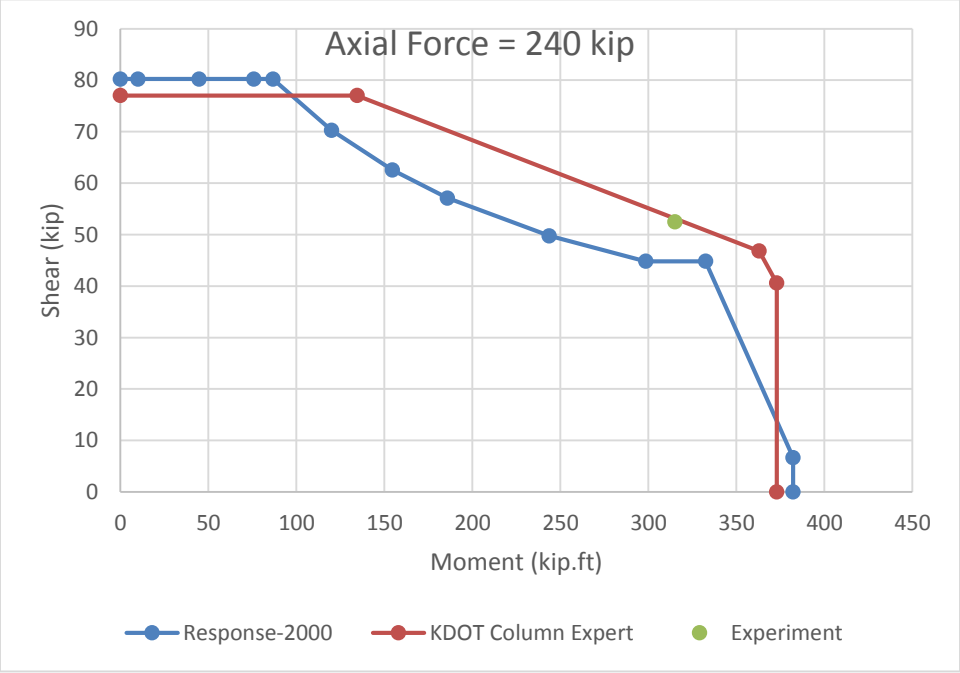

Figure 11-27: Interaction Diagram for Specimen S20MI by Melek and Wallace (2004).

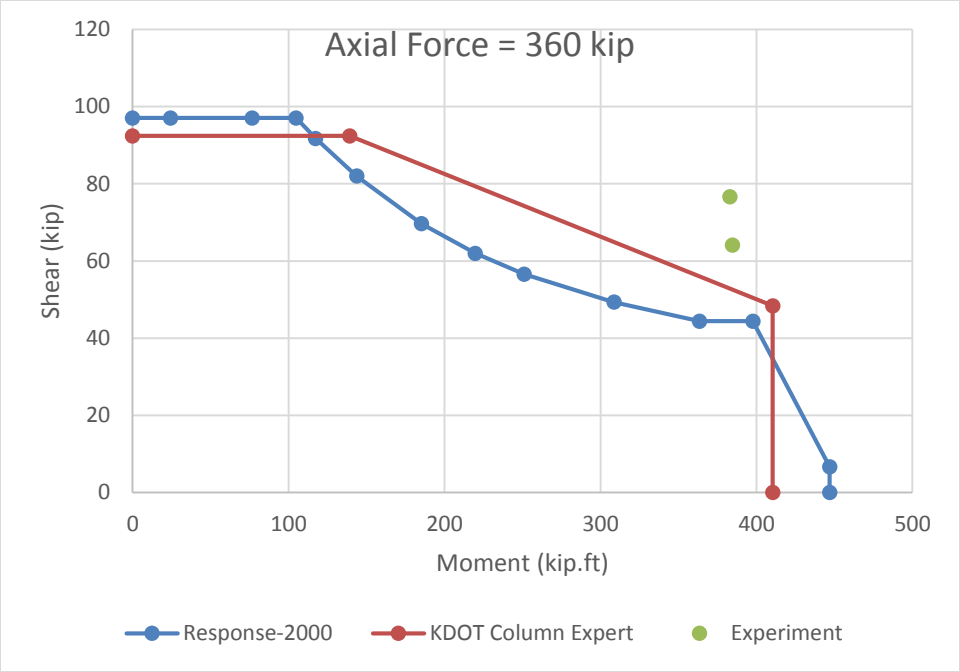

Figure 11-28: Interaction Diagram for Specimens S30MI and S30XI by Melek and Wallace (2004).

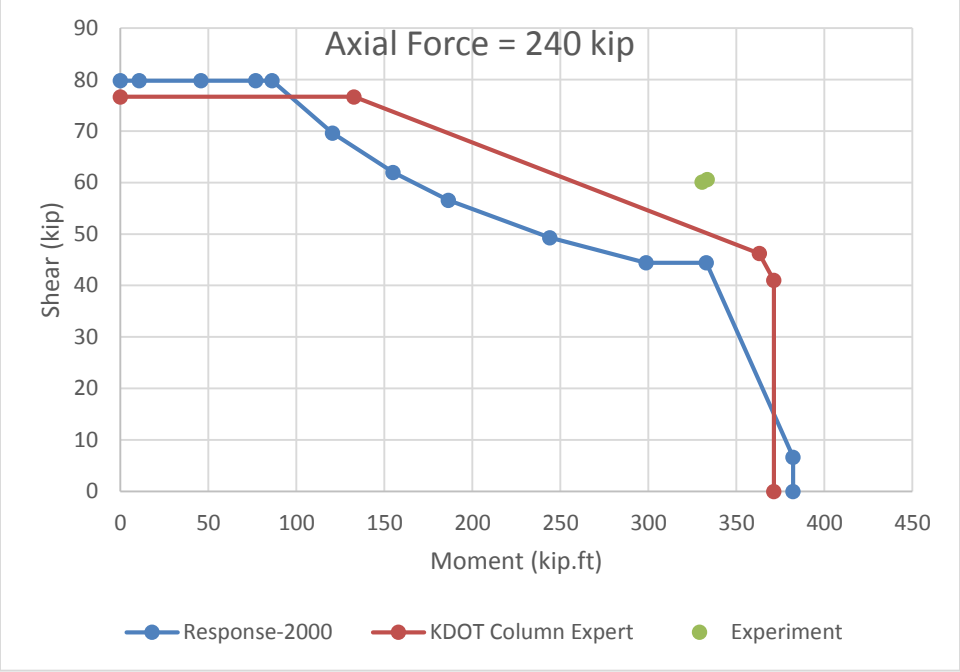

Figure 11-29: Interaction Diagram for Specimens S20HI and S20HIN by Melek and Wallace (2004).

Figure 11-26 to Figure 11-29 show the shear-moment interaction diagrams obtained for specimens tested by Melek and Wallace (2004) using both Response-2000 and KDOT Column

Expert. These specimens had the same cross-section and reinforcement, but differed in the compressive strength. S10, S20, S30 specimens were subjected to axial force of 120 kip, 240 kip, 360 kip, respectively. All curves showed similar behavior. As it can be seen in Figure 11-26 and Figure 11-27 S10MI and S20MI, the results provided from KDOT Column Expert were slightly on the unconservative side for these cases, however, the experimental points were close to the present curve. For the rest of the figures, every two specimens that shared the same axial loading are shown on the same figure. As it can be seen in Figure 11-28 and Figure 11-29, the results obtained from both Response-2000 and KDOT Column Expert were reasonably conservative, with KDOT Column Expert providing higher values for shear capacity. Overall, these cases showed good agreement between the present procedure and experimental results.

Chapter 12 - Conclusions and Recommendations

Conclusions

In this study, a procedure to determine the shear capacity of rectangular reinforced concrete columns under combined axial load and bending moment was formulated. The procedure was based on AASHTO LRFD (2014) provisions, which were established according to the simplified modified compression field theory. The developed procedure was then implemented in "KDOT Column Expert" confined analysis software version 6.0. The software is currently capable of generating the axial load-shear force-bending moment interaction domain. The software was then used to generate interaction diagrams, which were compared to "Response-2000" software (Bentz, 2000) and experimental values. The present model's results showed good agreement with the experimental data. Additionally, the results were shown to be conservative for many of the cases tested. It is concluded that the present procedure and the software in which it was implemented, KDOT Column Expert, are viable tools to accurately predict the combined axial load, shear and bending moment behavior in rectangular concrete columns.

Recommendations

The following topics could be extended to the augment of this research, address some of the issues encountered, and improve the quality of the results:

- It is recommended that more experimental studies be conducted on reinforced concrete sections with high aspect ratios, as literature is currently lacking these results.
- For future work, the present procedure could be extended to account for biaxial shear and bending moment. Currently, the simplified modified compression field theory does not account for that.
- Fore future work, the proposed procedure could be extended to include sections confined with FRP with regards to shear capacity contribution. As FRP confinement does not affect the shear capacity of the section, it is postulated that the simplified compression field theory would still apply, pending experimental verification.

References

AASHTO, (2014). *AASHTO LRFD bridge design specifications*. 7th edition, Washington, DC.

Abd El Fattah, A. M. (2012). *Behavior of concrete columns under various confinement effects.* (Doctoral dissertation). Kansas State University, Manhattan, KS.

Aboutaha, R. S., Engelhardt, M. D.; Jirsa, J. O., and Kreger, M. E., (1999). "Rehabilitation of shear critical concrete columns by use of rectangular steel jackets." *ACI Structural Journal* 96(1): 68-78.

ACI Committee 318, (2011). *Building code requirements for structural concrete (ACI 318-11) and commentary*. Farmington Hills, MI.

Bentz, C. E., Vecchio, J. F., and Collins, P. M. (2006). "Simplified modified compression field theory for calculating shear strength of reinforced concrete elements." *ACI Structural Journal*, (103)4, 614-624.

Bentz, E. C., (2000). *Sectional analysis of reinforced concrete members*. (Doctoral dissertation). University of Toronto, Ontario, Canada.

Berry, M., Parrish, M., and Eberhard, M. (2004). "PEER structural performance database user's manual." Pacific Earthquake Engineering Research Center, University of California, Berkeley.

Building and Civil Engineering Standards Committee, (2001). *Concrete, reinforced and prestressed concrete structures—Part 1: Design and construction, DIN 1045-1*. Berlin, Germany.

Commission of the European Communities, (2004). *Eurocode 2: Design of concrete structures—Part 1-1: General rules and rules for buildings*. Brussels, Belgium.

CSA Committee A23.3 (2004), *Design of Concrete Structures, CSA A23.3-04*. Rexdale, Ontario, Canada.

Ghannoum, W., and Sivaramakrishnan, B., (2012). "ACI 369 rectangular column database." Network for Earthquake Engineering Simulation (database), Dataset, DOI:10.4231/D36688J50.

Hawkins, N. M., Kuchma, D. A., Mast, R. F., Marsh, M. L., and Reineck, K., *Simplified shear design of structural concrete members: Appendexes*. NCHRP Web-Only Document 78. National Cooperative Highway Research Program, Washington, DC.

Japan Society of Civil Engineers, (2007). *Specification for design and construction of concrete structures: Design*. Tokyo, Japan.

Melek, M., and Wallace, J. W., (2004). "Cyclic behavior of columns with short lap splices", *ACI Structural Journal*, 101(6), 802-811.

Ousalem, H., Kabeyasawa, T., Tasai, A., (2003). "Effect of hysteretic reversals on lateral and axial capacities of reinforced concrete columns." *The Fifth US-Japan Workshop on Performance-Based Earthquake Engineering Methodology for Reinforced Concrete Structures*. Hakone, Japan. Pacific Earthquake Engineering Research Center (UC Berkeley): 211-221.

Priestley, M. J. N., Seible; F.; Xiao, Y., and Verma, R., (1994a). "Steel jacket retrofitting of reinforced concrete bridge columns for enhanced shear strength - Part 1: Theoretical considerations and test design." *ACI Structural Journal* 91(5): 394-405.

Priestley, M. J. N., Seible; F.; Xiao, Y., and Verma, R., (1994b). "Steel jacket retrofitting of reinforced concrete bridge columns for enhanced shear strength - Part 2: Test results and comparison with theory." *ACI Structural Journal* 91(5): 537-551.

Pujol; S., (2002). *Drift capacity of reinforced concrete columns subjected to displacement reversals.* (Doctoral dissertation). Purdue University, West Lafayette, IN.

Sivaramakrishnan, B., (2010). *Non-linear modeling parameters for reinforced concrete columns subjected to seismic loads*. (Master thesis). University of Texas, Austin, TX.

Umehara, H. and Jirsa, J. O., (1982). *Shear strength and deterioration of short reinforced concrete columns under cyclic deformations.* University of Texas, Austin, TX.

Vecchio, F. J., and Collins, M. P., (1986). "The modified compression field theory for reinforced concrete elements subjected to shear." *ACI Journal*, 83(2), 219-231.

Wehbe; N., Saiidi; M. S.; and Sanders, D., (1998). "Confinement of rectangular bridge columns for moderate seismic areas." *National Center for Earthquake Engineering Research (NCEER) Bulletin*. 12(1).

Wight, J. K., Sozen, M. A., (1973). "Shear strength decay in reinforced concrete columns subjected to large deflection reversals." *Structural Research Series SRS-403*. University of Illinois Engineering Experiment Station, Urbana, IL.

Yarandi, M. S., (2007). *Seismic retrofit and repair of existing reinforced concrete bridge columns by transverse prestressing*. (Doctoral dissertation). University of Ottawa, Ontario, Canada.